Towards High Performance Robotic Actuation

Thesis by

Nikola Zlatkov Georgiev

In Partial Fulfillment of the Requirements for the

Degree of

Doctor of Philosophy

CALIFORNIA INSTITUTE OF TECHNOLOGY

Pasadena, California

2019

Defended May 15th, 2019

Nikola Zlatkov Georgiev
ORCID: 0000-0002-7997-5577

ABSTRACT

The main objective of this thesis is to enable development of high performance actuation for legged, limbed and mobile robots. Such robots need to support their own weight, therefore, their actuators need to be light weight, compact, and efficient. In addition, these actuators need to exhibit significant shock tolerance and backdrivability due to the robots physical contact with the environment. A dynamics analysis also shows that the actuators' design may have significant impact on a robot's dynamics sensitivity. These consideration motivate improvements in all actuator design aspects compared to current approaches.

First, the application-specific design of outer rotor motors with concentrated windings is considered for three main categories: electric vehicles, drones and robotic joints. It is shown that an intrinsic design trade-off exists between a motor's copper loss, core loss and mass, which allows development of motors with superior performance for each application. In particular, it is shown that outstanding torque density may be reached with high pole count outer rotor motors and the design and optimization of such motors is outlined in terms of robotic applications. Analytic motor design scaling modes are also derived to highlight implementation challenges of high torque motors in robotics.

Next, the design of gearboxes for robotic actuation is discussed. A novel type of high reduction Bearingless Planetary Gearbox is introduced that allows a large range of reduction ratios to be achieved in a compound planetary stage. In the concept, all gear components float in an unconstrained manner as the planet carrier is substituted with a secondary sun gear. This is achieved by introducing an additional kinematic constraint that allows the planets to be uniform. The advantages of the Bearingless Planetary Gearbox over current approaches in terms of improved robustness, load distribution, manufacturability, and assembly are outlined.

Finally, analysis, design, and prototyping of rotary planar springs for rotary series elastic actuators is described. A model based on curved beam theory that allows rapid iteration and comparison between design parameters of rotary springs is developed. Mass reduction techniques based on composite arm structures are introduced and internal arm contact modeling is presented. Motivated by strain energy density analysis, an optimization based spring design approach is developed that allows significant increase in the torque and torque density.

PUBLISHED CONTENT AND CONTRIBUTIONS

[1] Travis Brown et al. "Series Elastic Tether Management for Rappelling Rovers." In: *2018 IEEE/RSJ International Conference on Intelligent Robots and Systems (IROS)*. IEEE. 2018, pp. 2893–2900. DOI: 10.1109/IROS.2018.8594134.

Development of the dual integrated spring design (Sec. 5.2.7) and gearbox with assembled planets (Sec. 4.3.4).

[2] Nikola Georgiev and Joel Burdick. "Optimization-based Design and Analysis of Planar Rotary Springs." In: *2018 IEEE/RSJ International Conference on Intelligent Robots and Systems (IROS)*. IEEE. 2018, pp. 927–934. DOI: 10.1109/IROS.2018.8594186.

Optimization-based planar rotary spring design (Sec. 5.4).

[3] Nikola Georgiev and Joel Burdick. "Design and analysis of planar rotary springs." In: *Intelligent Robots and Systems (IROS), 2017 IEEE/RSJ International Conference on*. IEEE. 2017, pp. 4777–4784. DOI: 10.1109/IROS.2017.8206352.

Planar rotary spring modeling and analysis (Sec. 5.2).

[4] Nikola Georgiev and Joel Burdick. "Design and analysis of the bearingless planetary gearbox." In: *Intelligent Robots and Systems (IROS), 2017 IEEE/RSJ International Conference on*. IEEE. 2017, pp. 1987–1994. DOI: 10.1109/IROS.2017.8206018.

Bearingless planetary gearbox design and analysis (Sec. 4.3).

CONTENTS

LIST OF FIGURES

LIST OF TABLES

NOMENCLATURE

(F_x^{end}, F_y^{end}). Ch. 5: Spring arm end forces.

(F_x, F_y). Ch. 5: Spring arm loading. May have superscripts if spring deformation in both directions is concerned.

(x_c, y_c). Ch. 5: Coordinates of spring arm centroid surface in the plane.

(x_n, y_n). Ch. 5: Coordinates of spring arm neutral surface in the plane.

(x_{dis}, y_{dis}). Ch. 5: Displacement of spring arm distal end.

$[\sigma]$. Ch. 5: Spring material maximum admissible stress.

α. Ch. 5: Tangent angle of spring arm neutral surface.

β_0. Ch. 5: Angular position of spring arm distal end.

$\delta\beta$. Ch. 5: Incremental angle in spring displacement simulation.

Δd. Ch. 5: Spring primary material layer thickness.

ΔE. Ch. 5: Spring stiffness reduction due to composite structure.

ΔM. Ch. 5: Spring mass reduction due to composite structure.

$\Delta\beta$. Ch. 5: Spring displacement.

$\Delta\beta_{max}$. Ch. 5: Spring specified maximum displacement.

δ^{coord},δ^{dir}. Ch. 5: Termination constants for spring arm contact locations update.

η_H, η_F. Ch. 4: bearingless planetary gearbox strength dertating constants.

γ. Ch. 5: Spring arm neutral surface displacement. May have subscript if spring deformation in both directions is concerned.

μ. Ch. 5: Spring material coefficient of friction.

μ_i^j. Ch. 1: joint friction coefficient of the i^{th} joint in the j^{th} limb.

μ_0. Ch. 3: Permeability of free space.

μ_R. Ch. 3: Relative permeability of rare earth magnets.

ν_a. Ch. 4: tangential velocity of driving sun gear in gearbox.

ω_a. Ch. 4: angular velocity of driving sun gear in gearbox.

ω_m. Ch. 3: Motor rotor rotational speed.

ω_{rated}. Ch. 3: Motor rated rotational speed.

Φ_c. Ch. 3: Amplitude of armature reaction flux.

Ψ. Ch. 3: Amplitude of motor phase flux linkage.

$\psi(.)$. Ch. 3: Motor phase flux linkage.

ρ. Ch. 5: Spring material density.

ρ_s. Ch. 5: Spring secondary material density.

ρ_{cu}. Ch. 3: Density of copper.

ρ_{fe}. Ch. 3: Density of steel.

σ. Ch. 3: Motor winding resistivity.

σ. Ch. 5: Spring arm bending stress.

σ_F,σ_H. Ch. 4: bending/Hertz stress in gearbox.

σ_y. Ch. 5: Spring material yield strength.

$\sigma_{[F]}$,$\sigma_{[H]}$. Ch. 4: maximum admissible bending/Hertz stress of gear material in gearbox.

σ_{cv}. Ch. 5: Spring arm bending stress on concave surface.

σ_{cx}. Ch. 5: Spring arm bending stress on convex surface.

σ_{max}. Ch. 5: Spring arm maximum bending stress.

τ. Ch. 5: Spring torque.

τ_a, τ_l, τ_f, τ_g. Ch. 4: gear meshing torques in bearingless planetary gearbox.

τ_i. Ch. 1: i^{th} joint torque in manipulator or limb.

τ_{des}. Ch. 5: Spring specified maximum torque.

θ. Ch. 5: Polar location of spring arm centroid surface, $\theta \in [\theta_{min}, \theta_{max}]$.

θ_i. Ch. 1: i^{th} joint angle in manipulator or limb.

Θ_i^j. Ch. 1: actuator output angle of the i^{th} joint in the j^{th} limb.

θ_m. Ch. 3: Motor rotor mechanical angle of rotation.

ξ_i. Ch. 1: i^{th} joint twist in manipulator or limb.

ζ_i^j. Ch. 1: actuator friction coefficient of the i^{th} joint in the j^{th} limb.

A. Ch. 5: Spring arm cross-sectional area.

a. Ch. 5: Radius of curvature of pring arm inner (convex) surface.

A_g. Ch. 1: floating base acceleration.

a_g. Ch. 3: Motor air gap thickness.

A_{slot}. Ch. 3: Motor slot area.

A_{tot}. Ch. 3: Combined area of a slot and tooth of motor stator.

b. Ch. 4: gear out-of-plane thickness in gearbox.

b. Ch. 5: Radius of curvature of spring arms outer (concave) surface.

B_c. Ch. 3: Amplitude of armature reaction flux density.

B_g. Ch. 3: Motor air gap flux density.

B_q. Ch. 3: Peak flux density in the motor stator tooth.

B_r. Ch. 3: Motor magnet residual flux density.

c, q. Ch. 5: Spring archimedean spiral arm coefficients.

C_0. Ch. 1: floating base frame.

c_f. Ch. 3: Motor slot fill factor.

C_F,C_H. Ch. 4: gear strength factors in gearbox.

C_i. Ch. 1: frame fixed to link i in manipulator or limb.

c_l. Ch. 3: Motor lamination fill factor.

$C_q(q)$. Ch. 3: Motor slot factor.

C_R, C_{k_c}, C_{A_q}, C_{A_s}. Ch. 3: Motor slot analysis related geometric constants.

C_s. Ch. 3: Motor scaling factor.

C_w. Ch. 3: Motor winding factor.

d. Ch. 5: Spring arm in-plane thickness.

d_e. Ch. 4: gearbox ring gear diameter.

d_f. Ch. 4: gearbox planet gear diameter.

d_s. Ch. 5: Spring secondary material layer thickness.

d_{in}. Ch. 3: Motor stator inner diameter.

d_{out}. Ch. 3: Motor stator outer diameter.

d_{wire}. Ch. 3: Motor bare copper wire diameter.

dm. Ch. 5: Mass of spring arm differential element.

E. Ch. 5: Young's modulus of spring material.

e. Ch. 5: Spring arm eccentricity.

E_s. Ch. 5: Spring secondary material Young's modulus.

f^{coord},f^{dir}. Ch. 5: Discrete recursive filters for spring arm contact locations update.

f_e. Ch. 3: Motor electrical frequency.

F_f,F_g,F_a. Ch. 4: gear meshing forces in gearbox.

F_i. Ch. 1: wrench between link i and link $i-1$ in manipulator or limb.

g. Ch. 4: greatest common divider of $z_e z_g - z_b z_f$ and z_g in gearbox.

$g_{i-1,i}$. Ch. 1: rigid body transformation of frame C_i relative to frame $C_i - 1$ in manipulator or limb.

h. Ch. 4: gearbox carrier.

I_i. Ch. 1: i^{th} joint reflected inertia in manipulator or limb.

I_m. Ch. 3: Motor synchronous current.

J_m. Ch. 3: Motor rotor inertia.

K. Ch. 5: Spring stiffness.

k_A. Ch. 3: Motor axial scaling coefficient.

k_c. Ch. 3: Motor winding coefficient.

K_d. Ch. 5: Spring arm scaled thickness.

K_h, K_e, K_a. Ch. 3: Motor core loss coefficients.

k_P. Ch. 3: Motor pole scaling coefficient.

k_q. Ch. 3: Motor topology family order.

k_R. Ch. 3: Motor radial scaling coefficient.

k_s. Ch. 3: Motor slot-pole symmetry.

k_s. Ch. 5: Spring composite structure design trade-off.

K_t. Ch. 3: Motor torque constant.

k_W. Ch. 3: Motor rewinding coefficient.

k_{area}. Ch. 3: Ratio of motor tooth body area to slot area.

k_{cu}. Ch. 3: Windings mass coefficient.

K_{des}. Ch. 5: Spring specified stiffness.

k_{fe}. Ch. 3: Ratio of the combined mass of the rotor, the stator teeth and yoke to the mass of the body of the teeth of a motor.

K_{ph}. Ch. 3: Motor phase bEMF constant.

L. Ch. 5: Spring arm length along the neutral surface.

l_m. Ch. 3: Motor out-of-plane thickness.

l_t. Ch. 3: Length of motor tooth.

L_{kg}. Ch. 3: Motor phase leakage inductance.

L_{ph}. Ch. 3: Motor phase inductance.

L_{sf}. Ch. 3: Motor phase self inductance.

L_s. Ch. 3: Motor synchronous inductance.

M. Ch. 5: Moment in spring arm.

m. Ch. 4: module of gears.

M_i. Ch. 1: i^{th} link generalized inertia matrix in manipulator or limb.

M_{cen}. Ch. 1: robot generalized inertia matrix in the given configuration.

M_{dyn}. Ch. 1: generalized inertia matrix of manipulator or robot (neglecting actuator reflected inertia).

M_m. Ch. 3: Motor mass.

M_{rob}. Ch. 1: generalized inertia matrix of manipulator or robot.

N. Ch. 5: Spring arm shear force.

n. Ch. 1: number of links in manipulator or limb.

n. Ch. 5: Spring arm count.

N^{coord}. Ch. 5: Spring arm contact locations.

N^{dir}. Ch. 5: Spring arm contact force direction.

N_c. Ch. 5: Spring arm contact force.

$N_{strands}$. Ch. 3: Motor wire strands.

N_{turns}. Ch. 3: Motor number of winding turns per stator tooth.

P. Ch. 3: Motor base topology pole count.

p. Ch. 3: Motor pole count.

P_h, P_e, P_a. Ch. 3: Motor core loss components.

p_L. Ch. 3: motor pole count threshold value at which $L_{sf} = L_{kg}$.

p_n. Ch. 4: number of planets in gearbox.

P_{co}. Ch. 3: Motor core loss.

P_{cu}. Ch. 3: Motor rated copper loss at stall.

Q. Ch. 3: Motor base topology slot count.

q. Ch. 3: Motor slot count.

Q_{pp}. Ch. 3: Motor slot per pole per phase.

R. Ch. 5: Location of spring arm centroid surface in polar coordinates.

r. Ch. 5: Spring arm radius of curvature $r \in [a, b]$.

r_c. Ch. 5: Radius of curvature of spring arm centroid surface.

R_n. Ch. 5: Radius of spring arm distal end.

r_n. Ch. 5: Radius of curvature of spring arm neutral surface.

R_s. Ch. 3: Motor synchronous resistance.

r_w. Ch. 3: Motor average winding radius.

R_{ae}. Ch. 4: gearbox reduction ratio.

R_{ag}. Ch. 3: Motor air gap reluctance.

R_{in}. Ch. 5: Radius of spring inner circle.

R_m. Ch. 3: Motor magnet reluctance.

R_{out}. Ch. 5: Radius of spring outer circle.

R_{phase}. Ch. 3: Motor phase resistance.

R_{slot}. Ch. 3: Motor slot resistance.

R_{term}. Ch. 3: Motor terminal resistance.

s. Ch. 5: Arc-length parameterization of spring arm neutral surface.

s_1, s_2. Ch. 5: Spring arm contact positions along the neutral surface.

S_i^j. Ch. 1: the compliant element spring constant of the i^{th} joint in the j^{th} limb.

t. Ch. 5: Spring out-of-plane thickness.

T_e. Ch. 4: gearbox output torque.

T_f. Ch. 4: gearbox planet torque at output ring gear.

T_m. Ch. 3: Motor torque.

t_m. Ch. 3: Motor magnet thickness.

t_r. Ch. 5: Spring transformed section thickness.

t_s. Ch. 5: Spring arm secondary material layer thickness.

T_ρ. Ch. 3: Motor torque density.

T_{peak}. Ch. 3: Motor peak torque.

t_{tip}. Ch. 3: Motor stator tooth tip thickness.

U. Ch. 5: Strain energy of spring arm differential element.

U_m. Ch. 5: Strain energy density of spring arm differential element.

V_i. Ch. 1: i^{th} link velocity in manipulator or limb.

V_{rated}. Ch. 3: Motor rated voltage.

w_t. Ch. 3: In-plane thickness of the motor stator teeth.

w_{tip}. Ch. 3: Width of the tips of the teeth of a motor stator.

y_r. Ch. 3: Motor rotor yoke.

y_s. Ch. 3: Motor stator yoke thickness.

z_a. Ch. 4: driving sun gear or number of teeth of the driving sun gear in gearbox.

z_e,z_b,. Ch. 4: ring gear or number of teeth of ring gear in gearbox.

z_f,z_g,. Ch. 4: planet gear or number of teeth of planet gear in gearbox.

z_l. Ch. 4: secondary sun gear or number of teeth of the secondary sun gear in gearbox.

Chapter 1

INTRODUCTION

1.1 Robotics Actuation

The majority of robotic systems are actuated using electric motors. Hydraulically and pneumatically actuated robots also exist, however, these are rare due to their control challenges, high cost and lower efficiency as a pump or compressor needs to supply constant fluid pressure during operation. Furthermore, the usually high pressures require regular maintenance and pose safety concerns during operation. The design of a robot that features partial hydraulic actuation is described in [1]. A pneumatically actuated bipedal is described in [2]. A classical comparative study of robotics actuator technology is available in [3]. This thesis is concerned with the design of robotic actuators featuring electric motors.

It is well known that electric motors with high power density that significantly exceeds biological muscle may be readily designed. However, such power levels are achieved only at very high rotational speed as motor torque density is quite low [3, 4]. The electro-magnetic torque limitations of motors are fundamental, thus, reaching the high torque levels needed for robotic joints requires the introduction of a speed reducer between the motor and the load.

Outstanding torque amplification may be achieved with compact and light gearboxes such as harmonic drives and cycloidal drives (their advantageous and disadvantages are outlined in Ch. 4). Even though actuators consisting of electric motors coupled with high reduction gearboxes are very common, they suffer from very high reflected inertia and no backdrivability, therefore, these actuators may not tolerate unexpected shocks, and robot impacts with the environment may lead to permanent damage.

A popular approach to increase the shock tolerance of an actuator that features a high reduction gearbox is to include a compliant element between the gearbox output and the load. The result is a series elastic actuator (SEA) [5]. Since the introduction of the idea, many prismatic [6–8] and rotary [9–16] series elastic actuator designs have been presented. Fig. 1.1 shows examples of prismatic and rotary SEA designs.

The rotation of the screw or gearbox output causes deformation of the elastic element that may be measured using encoders, potentiometers, etc. Then, knowledge of the

spring stiffness allows for an accurate estimation of the actuator force or torque to be obtained so that joint level force control may be implemented. Furthermore, significant energy may be stored in the elastic element deformation, thus, improving the robot operational efficiency during cyclic motion. These advantages of SEAs come at the price of significantly reduced achievable force or torque control bandwidth, typically not exceeding $10Hz$. SEA robot design, control, implementation

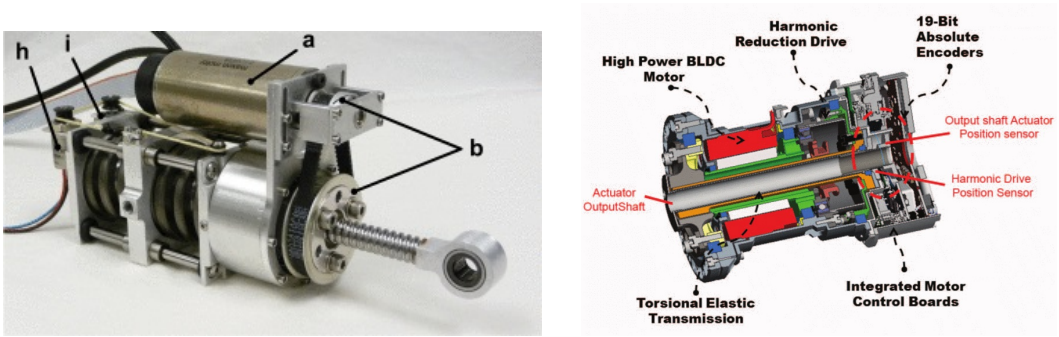

Figure 1.1: Examples of prismatic [8] ©2014 IEEE and rotary [17] ©2015 IEEE series elastic actuator designs.

and prototyping are described in [6, 7, 18–29].

SEA humanoid robots are predominantly controlled under static equilibrium. High performance controlled dynamic manipulation and locomotion using SEAs has not been shown to date.

SEA quadruped robots are either controlled under static equilibrium, similar to SEA humanoids, or using dynamic trot gaits where the feet placement accuracy is low and the actuators inject energy every cycle to maintain a bouncing-like locomotion.

It is the author's opinion that the SEA robot performance limitations are intrinsic and related to increased dynamics sensitivity caused by the actuators' elasticity, which may not be overcome using advanced control strategies. Ch. 2 shows how the actuator reflected inertia impacts the dynamic sensitivity of robots, and in particular, shows that series elasticity eliminates its potential dynamics benefits.

Recently, an alternative approach to robot actuation design has been developed. Rather than using small motors running at high speed coupled with high reduction gearboxes, large torque-optimized motors are coupled with low to mid reduction ratio gearboxes. The resulting actuators may have good gearbox transparency and backdrivability with much higher bandwidth than SEAs. However, due to the lower motor torque amplification, such actuators exhibit lower efficiency as they

need to dissipate significantly higher amount of heat to deliver the same amount of static torque compared to SEAs of the same size. As shown in Ch. 2, low to mid reduction ratio geared actuators may also reduce a robot's intrinsic dynamics sensitivity to a minimum level. MIT's Cheetah [4, 30] is an example of a quadruped robot design which is actuated with low reduction gearboxes (one stage planetary) coupled with high torque (off-the-shelf frameless) motors. Unmatched dynamic capability with great robustness has been demonstrated with this robotic system. A possibly improved actuator design that features mid reduction ratio gearbox (one stage compound planetary) with high torque (off-the-shelf frameless) motors is introduced in [31, 32].

Of main interest in this thesis are limbed or legged robots that have more than two limbs so that some of the limbs are used for manipulation or locomotion (or both). The primary motivation is RoboSimian (Fig. 1.2) which is DARPA Robotics Challenge (DRC) entry of NASA Jet Prop. Lab. RoboSimian has 28 degree-of-freedom (DOF) and four limbs that are capable of both mobility and manipulation [33]. All robot actuators are identical and each feature a harmonic drive with $1 : 160$ reduction ratio with no added elasticity. Thus, RoboSimian is mainly designed for stable, quasi-static locomotion and manipulation with limited shock tolerance and impacts with the environment may result in permanent damage. Furthermore, the harmonic drive nonlinearities and friction (Sec. 4.1) prevent implementation of joint-level force control. An objective of this thesis is to investigate alternative approaches to the actuation of multi-limbed robots (such as RoboSimian) that feature improved shock tolerance and allow joint-level force control so that dynamic locomotion and manipulation may be implemented on systems of this complexity.

Figure 1.2: Robosimina: NASA Jet Prop. Lab. entry to DRC [33] ©2015 Wiley.

1.2 Dual Robotic Actuation

The SEA shortcomings may be overcome by introducing a new robotic joint architecture that couples a low to mid reduction ratio geared motor to the SEA in parallel. In the resulting dual actuator:

- the SEA would store energy, and produce static and low bandwidth torque efficiently with low heat dissipation.
- the low to mid reduction ratio geared motor would produce high bandwidth torque and reduce robot dynamics sensitivity. The high frequency torque would generally be of lower amplitude, thus, the contribution of the low to mid reduction ratio geared motor to the total loss is expected to be low, despite its generally lower torque production efficiency.

The novel dual actuator can potentially preserve the shock tolerance of SEAs, provided the low to mid reduction ratio gearbox has high efficiency and backdrivability.

A dual actuation approach has been proposed in the past [34, 35]. In this previous work, the SEA is positioned away from the robotic joint at the base and is cable coupled in parallel to a direct drive joint motor. The main disadvantage of this approach is that the direct drive motor does not contribute with reflected inertia, and thus, does not reduce the robot dynamics sensitivity (see Ch. 2). Also due to the lack of a gearbox, the direct drive motor may only deliver limited torque with high energy dissipation.

The main motivation and goal of the work presented in this thesis is to enable the development of high performance actuation for legged, limbed and mobile robots. Due to the fact that such robots need to support their own weight, their actuators need to be light weight, compact and efficient. Towards this goal high torque density electric motors are developed in Ch. 3, a novel light weight and compact bearingless planetary gearbox is introduced in Ch. 4 and torque density optimized SEA rotary planar springs are developed in Ch. 5.

1.3 Thesis Structure and Contributions

Ch. 2 provides an analysis of robot dynamics sensitivity and shows how actuator reflected inertia impacts it in manipulators, and limbed and legged robots. The analytic results motivate the proposed dual actuation approach. Open chain manipulators (Sec. 2.2), and limbed/legged robots (Sec. 2.3) designed with geared actuators are considered. Series elastic actuators are considered in Sec. 2.4. Example robot models are analyzed in Sec. 2.5.

Ch. 3 is concerned with the design and prototyping of high performance permanent magnet motors. Sec. 3.2 discusses the application-specific motor design requirements for electric vehicles (Sec. 3.2.1), drones (Sec. 3.2.2) and robotic joint actuators (Sec. 3.2.3). Sec. 3.3 describes the structure of permanent magnet motors and outlines the advantages of outer rotor motors with concentrated windings. Sec. 3.3.3 describes a flux linkage model for these motors which is used in the derivation of the analytic design trade-offs and guidelines of Sec. 3.4. Sec. 3.4.1 describes how a motor's slot count affects its performance, Sec. 3.4.2 discusses high pole count motors in the context of high speed applications, Sec. 3.4.3 introduced motor design trade-offs characteristic of motors with high pole count and Sec. 3.4.4 discusses how the tooth width and area may be optimized to improve a motor's torque and torque density. Next, Sec. 3.5 provides electro-magnetic FEA verification of the results of Sec. 3.4 and Sec. 3.6 describes the development and fabrication of motor prototypes, designed according to the proposed guidelines and methodology. Finally, Sec. 3.7 describes the possible motor scaling modes and discusses the challenges and limitations related to the practical implementation of high torque motors.

Ch. 4 is concerned with the design and prototyping of high torque, compact, and lightweight gearboxes for robotic applications. Sec. 4.2 is concerned with the analysis, design and manufacturing of the Wolfrom Gearbox and introduces important practical improvements. This gearbox is attractive due to its wide range of reduction ratios. Sec. 4.3 describes the development of a novel Bearingless Planetary Gearbox which is the main contribution of the chapter. Detailed strength analysis and manufacturing considerations are included in order to outline its advantages in terms of torque, weight, compactness and manufacturing readiness. The gearbox is unique for its floating components and lack of carrier and bearings.

Ch. 5 is concerned with the analysis, design, and prototyping of rotary planar springs for robotics applications such as rotary series elastic actuators. Sec. 5.2

proposes a systematic planar rotary spring modeling and analysis procedure. A new mathematical model for multi-armed rotary springs with significant lattitude in the arm design is presented (Sec. 5.2.2). Two methods for spring mass reduction, based on composite materials or *cutouts*, are introduced (Sec. 5.2.4). The design, manufacturing and testing of two spiral spring prototypes based on the proposed analytical model are described (Sec. 5.2.6 and Sec. 5.2.7). Sec. 5.3 discusses internal spring arm contacts. A systematic model of arm contacts is first introduced (Sec. 5.3.1). Then, a complete spring torsional analysis algorithm that accounts for arm contacts is presented (Sec. 5.3.2). Sec. 5.4 presents a consistent optimization-based spring design procedure. The optimization-based approach is first motivated (Sec. 5.4.1). Then, a complete optimization-based spring design algorithms is presented (Sec. 5.4.2). Finally, the design, analysis and testing of an aluminum spring prototype are described (Sec. 5.4.3).

Ch. 6 describes actuator prototypes that feature components developed according to the approaches of Ch. 3, Ch. 4 and Ch. 5. Sec. 6.2 describes an actuator that features a $1:10$ reduction ratio bearingless planetary gearbox. Sec. 6.3 describes a series elastic actuator that features a $1:101$ reduction ratio bearingless planetary gearbox and an elastic element designed according to Ch. 5. Sec. 6.4 describes a series elastic actuator which is used in the tether management system of the Axel rover developed at the NASA Jet Prop. Lab. [36].

Chapter 2

ROBOT DYNAMICS SENSITIVITY

2.1 Introduction

This chapter defines and analyzes the dynamics sensitivity of multi-limbed robots and shows how their actuator designs impact this sensitivity. It is shown that the reflected inertia of a multi-limbed robot's actuators may improve the condition number of the generalized mass matrix, thus, reducing its sensitivity to joint torque errors. Both open chain manipulators (Sec. 2.2), and limbed/legged robots (Sec. 2.3) are considered and some important differences are outlined. These lead to implications regarding robot design with geared actuators and series elastic actuators (Sec. 2.4). Example robot models are analyzed in Sec. 2.5.

A crucial design aspect that is usually neglected in robot design is the robot's generalized mass matrix dependence on the actuators' characteristics. This chapter provides a brief derivation of a robot's inverse dynamics using Newton-Euler recursive algorithm. The classical result for an open chain manipulator [37–39], is extended to a floating base dynamics formulation for limbed and legged robots. The close form dynamics equations allow a natural robot generalized mass matrix decomposition that reveals the dependence of its condition number on the actuator properties, e.g. actuator reflected inertia.

The condition number of a robot's mass matrix is of great significance for torque controlled robots because it determines how joint torque errors are propagated to joint acceleration errors. A high condition number signifies that relatively small joint torque errors in a subset of the robot's joints may lead to unexpected large acceleration errors in a possibly different subset of joints. This is demonstrated in Sec. 2.5, where mass matrix analysis is provided for a 12 DOF quadruped robot model and for RoboSimian (see Sec. 1.1). In the case of high mass matrix condition number, fast robot motion or heavy loading of its end effectors may lead to large unstable oscillations that span most of the robot's joints under closed loop control. Therefore, a robot's generalized mass matrix condition number provides a strong indication of the robot's dynamic capabilities.

The derivations begins with the assumption of geared motor type actuators, that is, the gearbox output is rigidly connected to the output link with no added compliance.

SEAs are considered in Sec. 2.4. Fig. 2.1 shows an example two-link robot manipulator with joints driven by geared motors. The analysis of this section uses screw theory and the notation developed in [40].

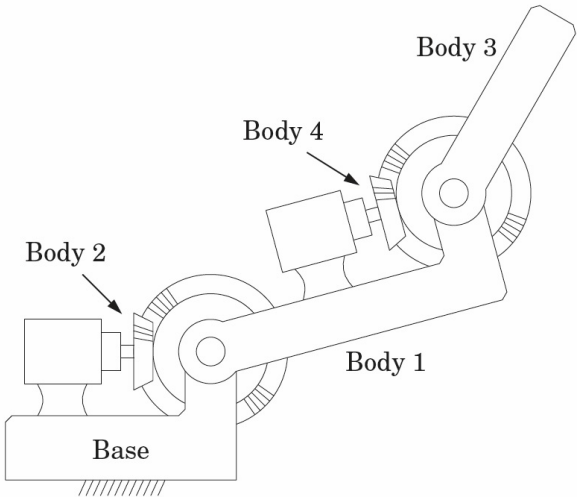

Figure 2.1: A two-link robot arm driven by gearmotors [37] ©2008 Springer.

2.2 Open Chain Manipulator Inverse Dynamics

First, an open chain manipulator that consists of rigid body links connected by one-degree of freedom revolute joints is considered. Fig. 2.2 shows the structure

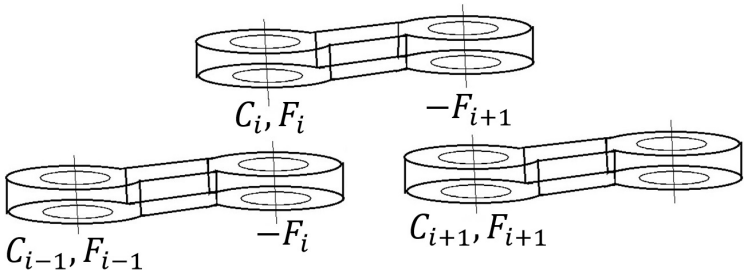

Figure 2.2: Open chain manipulator structure.

of such manipulator. There are n links, C_i is the frame fixed to link i such that its z-axis is aligned with the i^{th} joint axis, and F_i is the wrench between link i and link $i-1$. The base is denoted with index 0 and the end-effector is denoted with index $n+1$.

The following definitions are used in the rest of the chapter:

- τ_i is the i^{th} joint torque,
- $g_{i-1,i}$ is the rigid body transformation of frame C_i relative to frame $C_i - 1$,
- ξ_i is the i^{th} joint twist,
- θ_i is the i^{th} joint angle,
- M_i is the i^{th} link generalized inertia matrix,
- V_i is the i^{th} link velocity.

The base acceleration is defined as $\dot{V}_0 = A_g$ because in the case of a manipulator, the base acceleration is used to account for gravity.

The Newton-Euler recursive dynamics algorithm is given by [37, 38]:

- *Forward Recursion*:

$$\begin{aligned} V_i &= Ad_{g^{-1}{}_{i-1,i}} V_i + \xi_i \dot{\theta}_i \\ \dot{V}_i &= \xi_i \ddot{\theta}_i + Ad_{g^{-1}{}_{i-1,i}} \dot{V}_i - ad_{\xi_i \dot{\theta}_i} (Ad_{g^{-1}{}_{i-1,i}} V_i). \end{aligned} \tag{2.1}$$

- *Backward Recursion*:

$$\begin{aligned} F_i &= Ad^T_{g^{-1}_{i,i+1}} F_{i+1} + M_i \dot{V}_i - ad^T_{V_i} M_i V_i \\ \tau_i &= \xi_i^T F_i. \end{aligned} \tag{2.2}$$

The adjoint transformation, $Ad_{g_{i,j}}$ transforms twists and wrenches from reference i frame to reference frame j [40]. For a given twist $\xi = \begin{bmatrix} v & \omega \end{bmatrix}^T$,

$$ad_\xi = \begin{bmatrix} \hat{\omega} & \hat{v} \\ 0 & \hat{\omega} \end{bmatrix}.$$

As shown in [39], the Newton-Euler recursive dynamics formulation may be written in a matrix form:

$M_{dyn}\ddot{\theta} + KA_0 + LF_{n+1} + C = \tau$,

where

$$\begin{aligned} M_{dyn} &= \xi^T G^T \mathbb{M} G \xi \\ K &= \xi^T G^T \mathbb{M} G P_0 \\ L &= \xi^T G^T P_t^T \\ C &= \xi^T G(\mathbb{M} G(P_0 A_g + ad_{\xi\dot{\theta}} P_0 V_0 + ad_{\xi\dot{\theta}} \Gamma V) + ad_V^T \mathbb{M} V). \end{aligned} \tag{2.3}$$

The various matrices in Eq. (2.3) have the following definitions:

$$V = \begin{bmatrix} V_1 \\ \vdots \\ V_n \end{bmatrix} \in R^{6n},\ \dot{\theta} = \begin{bmatrix} \dot{\theta_1} \\ \vdots \\ \dot{\theta_n} \end{bmatrix} \in R^{n},\ F = \begin{bmatrix} F_1 \\ \vdots \\ F_n \end{bmatrix} \in R^{6n},\ \xi = \begin{bmatrix} \xi_1 & 0 & 0 \\ 0 & \ddots & 0 \\ 0 & 0 & \xi_n \end{bmatrix} \in R^{6n \times n}$$

$$P_0 = \begin{bmatrix} Ad_{g_{0,1}}^{-1} \\ 0 \\ \vdots \\ 0 \end{bmatrix} \in R^{6n \times 6},\ P_t = \begin{bmatrix} 0 \\ \cdots \\ 0 \\ Ad_{g_{n,n+1}}^{-1} \end{bmatrix}^T \in R^{6 \times 6n},\ \tau = \begin{bmatrix} \tau_1 \\ \vdots \\ \tau_n \end{bmatrix} \in R^{n},$$

$$\mathbb{M} = \begin{bmatrix} M_1 & 0 & \dots & 0 \\ 0 & M_2 & \dots & 0 \\ \vdots & \vdots & \ddots & \vdots \\ 0 & 0 & \dots & M_n \end{bmatrix},\ G = \begin{bmatrix} I & 0 & \dots & 0 & 0 \\ Ad_{g_{1,2}}^{-1} & I & \dots & 0 & 0 \\ \vdots & \vdots & \ddots & \vdots & \vdots \\ Ad_{g_{1,n}}^{-1} & Ad_{g_{2,n}}^{-1} & \dots & Ad_{g_{n-1,n}}^{-1} & I \end{bmatrix},$$

$$\Gamma = \begin{bmatrix} 0 & 0 & \dots & 0 & 0 \\ Ad_{g_{1,2}}^{-1} & 0 & \dots & 0 & 0 \\ \vdots & \vdots & \ddots & \vdots & \vdots \\ 0 & 0 & \dots & Ad_{g_{n-1,n}}^{-1} & 0 \end{bmatrix},\ ad_{\xi\dot{\theta}} = \begin{bmatrix} -ad_{\xi_1\dot{\theta}_1} & 0 & \dots & 0 \\ 0 & -ad_{\xi_2\dot{\theta}_2} & \dots & 0 \\ \vdots & \vdots & \ddots & \vdots \\ 0 & 0 & \dots & -ad_{\xi_n\dot{\theta}_n} \end{bmatrix},$$

$$ad_V^T = \begin{bmatrix} -ad_{V_1}^T & 0 & \dots & 0 \\ 0 & -ad_{V_2}^T & \dots & 0 \\ \vdots & \vdots & \ddots & \vdots \\ 0 & 0 & \dots & -ad_{V_n}^T \end{bmatrix}, \tag{2.4}$$

where $\mathbb{M}$, G, Γ, $ad_{\xi\dot{\theta}}$ and $ad_V^T \in R^{6n \times 6n}$.

As discussed in [37], Eq. (2.3) can be very sensitive. This is demonstrated by showing that 0.5% error on the joint torques may lead to more than 40% error on the joint accelerations of an example 6 DOF planar arm that has identical joints and links. This sensitivity may be explained by considering the manipulator's generalized mass matrix, M_{dyn}. M_{dyn} is a symmetric positive definite matrix [40] that can have a very high condition number in some configurations, especially for manipulators with many DOF. For symmetric positive definite matrices, the condition number is defined as $\kappa(M_{dyn}) = \frac{\sigma_1(M_{dyn})}{\sigma_n(M_{dyn})} = \frac{\lambda_{max}(M_{dyn})}{\lambda_{min}(M_{dyn})}$, where $\sigma_j(M_{dyn})$ is the j^{th} singular value, and $\lambda_{min}(M_{dyn})$ and $\lambda_{max}(M_{dyn})$ are the minimum and maximum eigenvalues, respectively. Thus, if $\kappa(M_{dyn})$ is large, small torque errors

may propagate to large acceleration errors, and in this case, Eq. (2.3) becomes an ill-conditioned problem for the accelerations. In this case, injecting relatively small magnitude torque in the joint space direction of the minimum eigenvalue of the mass matrix may lead to very large accelerations in the same joint space direction.

In the derivation of Eq. (2.3), the actuator reflected inertia is neglected. In order to introduce its dynamics effects, let I_i be the i^{th} joint reflected inertia and $I = diag(I_1, \ldots, I_n)$. The updated backward recursion from Eq. (2.2) is given by:

$$\begin{aligned} F_i &= Ad^T_{g^{-1}_{i,i+1}} (F_{i+1} - I_{i+1}\xi_{i+1}\ddot{\theta}_{i+1}) + M_i\dot{V}_i + \xi_i I_i \ddot{\theta}_i - ad^T_{V_i} M_i V_i \\ \tau_i &= \xi_i^T F_i. \end{aligned} \tag{2.5}$$

Thus, the updated mass matrix in Eq. (2.3) becomes:

$$M_{rob} = M_{dyn} + \xi^T I \xi = M_{dyn} + I. \tag{2.6}$$

All robot joints are assumed to be either revolute or prismatic, otherwise $\xi^T I \xi = I$ is not valid. Next, of main interest is how I affects the condition number, $\kappa(M_{rob})$. Due to the fact that both M_{dyn} and I are positive definite, the condition number of M_{rob} is bounded by:

$$\kappa(M_{rob}) \leqslant \frac{\lambda_{max}(M_{dyn}) + \max\limits_i I_i}{\lambda_{min}(M_{dyn}) + \min\limits_i I_i}. \tag{2.7}$$

Eq. (2.7) suggests that the reflected actuator inertia may be used to modify the condition number of the mass matrix, and thus, the sensitivity of the dynamics problem described in Eq. (2.3).

For example, if one designs the actuators so that they all have the same reflected inertia, which is equal to the maximum eigenvalue of the mass matrix ($I_1 = \cdots = I_n = \lambda_{max}(M_{dyn})$), then $\kappa(M_{rob}) \leqslant 2$. This condition may often be achieved using geared motors with low to mid reduction ratio.

For manipulators with "stiff" actuators, that, is actuators that feature high reduction gearboxes, it is usually the cases that $\lambda_{max}(M_{dyn}) \ll \min\limits_i I_i$. Then, $M_{rob} \approx I$ and the actuators' reflected inertia overshadows the manipulator dynamics. This effect may be used to explain the high positional accuracy of "stiff" manipulators. Due to their high reflected inertia, disturbances and unmodeled dynamics have little effect on the joint acceleration, that is, the dynamics coupling between the joints is effectively eliminated. Thus, high gain local joint controllers can be introduced that lead to

high accuracy positioning control. However, the high actuator reflected inertia leads to high impedance ($M_{rob} \approx I$ and I may be quite large), thus, the loading and forces that results from contacts of the manipulator with the environment may be very high and unexpected impacts may lead to substantial damage.

2.3 Limbed and Legged Robot Inverse Dynamics

This section considers limbed and legged robots that are constructed by attaching k open chain manipulator limbs (legs and/or arms) to a central body (a floating base). Most bipedal and quadruped robots may be modeled in this way. The equations of motion for such robots may be derived by extending the backwards recursion in the Newton-Euler algorithm to the floating base. For the j^{th} limb, the variables and matrices in Eq. (2.3) and Eq. (2.4) are given with superscript j. The floating base acceleration is defined as $\dot{V}_0 = A_0 + A_g$ so that gravity is again compensated for, while A_0 is the actual acceleration of C_0. Let M_0 be the generalized inertia matrix of the central body. Then, extending the backward recursion to the floating base leads to the Newton-Euler equation for the central body:

$$M_0 A_0 - Ad_{V_0}^T M_0 V_0 + \sum_{j=1}^{k} Ad_{g_{0,1}^j}^{-T}(F_1^j - \xi_1^j I_1^j \theta_1^j) + M_0 A_g = 0. \tag{2.8}$$

Expanding and rewriting leads to the robot dynamics equations:

$$(M_0 + \sum_{j=1}^{k} M_0^j) A_0 + \sum_{j=1}^{k} K^j \ddot{\theta}^j + \sum_{j=1}^{k} L_0^j F_{n+1}^j + C_0 + \sum_{j=1}^{k} C_0^j = 0 \tag{2.9}$$

$$\begin{aligned} (K^1)^T A_0 + (M^1 + I^1)\ddot{\theta}^1 + L_1 F_{n+1}^1 + C^i &= \tau^1 \\ &\vdots \\ (K^k)^T A_0 + (M^k + I^k)\ddot{\theta}^k + L^k F_{n+1}^k + C^k &= \tau^k. \end{aligned} \tag{2.10}$$

Where,

$$\begin{aligned} M^j &= (\xi^j)^T (G^j)^T \mathbb{M}^j G^j \xi^j,\ K^j = (P_0^j)^T (G^j)^T \mathbb{M}^j G^j \xi^j,\ L^j = (\xi^j)^T (G^j)^T (P_t^j)^T, \\ C^j &= (\xi^j)^T G^j (Ad_{Vj}^T \mathbb{M}^j V^j + \mathbb{M}^j G^j (P_0^j A_g + Ad_{\xi^j \dot{\theta}^j} P_0^j V_0 + Ad_{\xi^j \dot{\theta}^j} \Gamma^j V^j) \\ M_0^j &= (P_0^j)^T (G^j)^T \mathbb{M}^j G^j P_0^j,\ L_0^j = (P_0^j)^T (G^j)^T (P_t^j)^T, \\ C_0^j &= (P_0^j)^T (G^j)^T (Ad_{Vj}^T \mathbb{M}^j V^j + \mathbb{M}^j G^j (P_0^j A_g + Ad_{\xi^j \dot{\theta}^j} P_0^j V_0 + Ad_{\xi^j \dot{\theta}^j} \Gamma^j V^j)) \\ C_0 &= -Ad_{V_0}^T M_0 V_0 + M_0 A_g. \end{aligned} \tag{2.11}$$

Eq. (2.9) describes the actuated dynamics and Eq. (2.10) describes the unactuated dynamics of the robot. Then, the robot's generalized mass matrix is:

$$M_{rob} = \underbrace{\begin{bmatrix} M_{cen} & K^1 & \dots & K^k \\ (K^1)^T & M^1 & 0\dots & 0 \\ \vdots & \vdots & \ddots & \vdots \\ (K^k)^T & 0 & 0\dots & M^k \end{bmatrix}}_{M_{dyn}} + \begin{bmatrix} 0 & 0 & \dots & 0 \\ 0 & I^1 & 0\dots & 0 \\ \vdots & \vdots & \ddots & \vdots \\ 0 & 0 & 0\dots & I^k \end{bmatrix}, \tag{2.12}$$

where, $M_{cen} = M_0 + \sum_{j=1}^{k} M_0^j$ is the inertia matrix of the robot (all the links and central body) in the given configuration w.r.t C_0. Similar to open chain manipulators, the mass matrix M_{dyn} may have a very high condition number, $\kappa(M_{dyn})$. Let $K = \begin{bmatrix} K^1 & \dots & K^k \end{bmatrix}$, $M_{lim} = diag(M_1, \dots, M_k)$, $I_{lim} = diag(I_1, \dots, I_k)$. M_{rob}, M_{dyn}, M_{lim} and M_{cen} are symmetric positive definite [40] and have complete set of orthogonal eigenvectors that span their respective joint space. Then, M_{rob} can be factored using the Schur decomposition:

$$\begin{aligned} M_{rob} &= \begin{bmatrix} M_{cen} & K \\ K^T & M_{lim} \end{bmatrix} + \begin{bmatrix} 0 & 0 \\ 0 & I_{lim} \end{bmatrix} \\ &= \begin{bmatrix} \underline{1} & 0 \\ K^T M_{cen}^{-1} & \underline{1} \end{bmatrix} \begin{bmatrix} M_{cen} & 0 \\ 0 & M_{lim} - K^T M_{cen}^{-1} K \end{bmatrix} \begin{bmatrix} \underline{1} & M_{cen}^{-1} K \\ 0 & \underline{1} \end{bmatrix} + \begin{bmatrix} 0 & 0 \\ 0 & I_{lim} \end{bmatrix} \\ &= \underbrace{\begin{bmatrix} \underline{1} & 0 \\ K^T M_{cen}^{-1} & \underline{1} \end{bmatrix}}_{Y^T} \underbrace{\begin{bmatrix} M_{cen} & 0 \\ 0 & M_{lim} + I_{lim} - K^T M_{cen}^{-1} K \end{bmatrix}}_{X} \underbrace{\begin{bmatrix} \underline{1} & M_{cen}^{-1} K \\ 0 & \underline{1} \end{bmatrix}}_{Y}. \end{aligned} \tag{2.13}$$

Defining X and Y matrices according to Eq. (2.13) leads to $\kappa(M_{rob}) \leqslant \kappa(Y)^2 \kappa(X)$, therefore,

$$\kappa(M_{rob}) \leqslant \kappa(Y)^2 \frac{max(\lambda_{max}(M_{cen}), \lambda_{max}(M_{lim} + I_{lim} - K^T M_{cen}^{-1} K))}{min(\lambda_{min}(M_{cen}), \lambda_{min}(M_{lim} + I_{lim} - K^T M_{cen}^{-1} K))}. \tag{2.14}$$

Alternatively:

$$\begin{aligned} &\underbrace{\begin{bmatrix} \underline{1} & 0 \\ -K^T M_{cen}^{-1} & \underline{1} \end{bmatrix}}_{Y^{-T}} \begin{bmatrix} M_{cen} & K \\ K^T & M_{lim} + I_{lim} \end{bmatrix} \underbrace{\begin{bmatrix} \underline{1} & -M_{cen}^{-1} K \\ 0 & \underline{1} \end{bmatrix}}_{Y^{-1}} = \\ &\qquad \underbrace{\begin{bmatrix} M_{cen} & 0 \\ 0 & M_{lim} + I_{lim} - K^T M_{cen}^{-1} K \end{bmatrix}}_{X}. \end{aligned} \tag{2.15}$$

Therefore:

$$\kappa(M_{rob}) \geqslant \kappa(Y^{-1})^{-2} \frac{max(\lambda_{max}(M_{cen}), \lambda_{max}(M_{lim} + I_{lim} - K^T M_{cen}^{-1} K))}{min(\lambda_{min}(M_{cen}), \lambda_{min}(M_{lim} + I_{lim} - K^T M_{cen}^{-1} K))}. \quad (2.16)$$

Eq. (2.14) and Eq. (2.16) provide upper and lower bounds for the robot mass matrix condition number as a function of the actuator reflected inertia matrix I_{lim}. The matrix K describes how the actuated dynamics in Eq. (2.9) affects the unactuated dynamics in Eq. (2.10) and vice versa. Thus, the matrices $M_{cen}^{-1}K^1 \ \ldots \ M_{cen}^{-1}K^k$ describe how joint angle accelerations of each of the limbs propagate to acceleration of the total robot mass and inertia. The matrices $(K^1)^T M_{cen}^{-1} K^j \ \ldots \ (K^2)^T M_{cen}^{-1} K^j \ \ldots \ (K^k)^T M_{cen}^{-1} K^j$ describe how the resulting accelerations of the total robot mass and inertia, due to accelerations of the joints in the j^{th} limb, map to torques in the joints of all robot limbs. Therefore, for most robot designs that have at least two limbs and significant fraction of their mass concentrated in their central base, one can expect that $\|K^T M_{cen}^{-1}\|$ and $\|K^T M_{cen}^{-1} K\|$ are low (in most cases $\|K^T M_{cen}^{-1}\|, \|K^T M_{cen}^{-1} K\| << 1$). Then, Eq. (2.14) and Eq. (2.16) suggest that the robot's generalized mass matrix condition number may be approximated as:

$$\kappa(M_{rob}) \approx \frac{max(\lambda_{max}(M_{cen}), \lambda_{max}(M_{lim} + I_{lim}))}{min(\lambda_{min}(M_{cen}), \lambda_{min}(M_{lim} + I_{lim}))}. \quad (2.17)$$

Eq. (2.17) suggests that similar to open chain manipulators, a proper choice of the actuators' reflected inertia may improve a robot's generalize mass matrix condition number, $\kappa(M_{rob})$, by improving the condition number of the actuated dynamics portion, which corresponds to the limbs. However, the portion of the mass matrix that corresponds to the unactuated dynamics remains mostly unaffected by the actuators. Thus, unlike manipulators, the condition number of the mass matrix of limbed or legged robots always depends explicitly on the robot's mechanical design regardless of the actuators' properties, and Eq. (2.17) suggests that the unactuated dynamics portion of the mass matrix, M_{cen}, places lower bound, given by $\kappa(M_{cen})$, on the robot mass matrix condition number, $\kappa(M_{rob})$. Furthermore, if the actuators' reflected inertia is very high: $\max_{i,j}(I_i^j) >> \lambda_{max}(M_{cen}), \lambda_{max}(M_{lim})$, which is the case with high reduction ratio "stiff" gearmotors, Eq. (2.17) suggests that the robot's mass matrix condition number $\kappa(M_{rob})$ may be quite high as in this case:

$$\kappa(M_{rob}) \approx \frac{\max_{i,j}(I_i^j)}{\lambda_{min}(M_{cen})}.$$

Thus, unlike open chain manipulators, high actuator reflected inertia, may have negative effect on the legged or limbed robot's mass matrix condition number.

This observation may be used to explain why humanoid or limbed robots built with high reduction ratio harmonic drives are predominantly controlled under static equilibrium.

In summary, the simple analysis of this section suggests that as far as the dynamics of limbed or legged robots is concerned, the actuator reflected inertia has profound implication on the achievable robot performance in dynamic applications. Unlike open chain manipulators, both low and high reflected actuator inertia results in increased dynamics sensitivity that may propagate and significantly amplify joint torque errors. Furthermore, Eq. (2.17) suggests that for a given robot, the actuator design may be tuned so that the robot's generalized mass matrix condition number, $\kappa(M_{rob})$, is minimized, and thus, the robot's joint torque sensitivity is reduced to a minimum. Thus, as far as geared motors are concerned, one should expect optimum dynamic performance to be achieved with actuators that feature reduction ratios in the low to mid range.

2.4 Robots with Series Elastic Actuators

As discussed earlier, series elastic actuators are typically constructed by attaching a compliant element between the load and the output of a high reduction gearbox that is driven by a small sized motor. The following definitions for the i^{th} joint in the j^{th} limb are used in this section:

- μ_i^j is the joint friction coefficient,
- ζ_i^j is the actuator friction coefficient,
- Θ_i^j is the actuator output angle,
- S_i^j is the stiffness values of the compliant element.

The actuated robot dynamics of Eq. (2.1) and the unactuated robot dynamics of Eq. (2.2) become:

$$(M_0 + \sum_{j=1}^{k} M_0^j)A_0 + \sum_{j=1}^{k} K^j \ddot{\theta}^j + \sum_{j=1}^{k} L_0^j F_{n+1}^j + C_0 + \sum_{j=1}^{k} C_0^j = 0 \tag{2.18}$$

$$\begin{aligned} (K^1)^T A_0 + M^1\ddot{\theta}^1 + L_1 F_{n+1}^1 + C^i &= S^1(\Theta^1 - \theta^1) - \mu^1\dot{\theta}^1 \\ &\vdots \\ (K^k)^T A_0 + M^k\ddot{\theta}^k + L^k F_{n+1}^k + C^k &= S^k(\Theta^k - \theta^k) - \mu^k\dot{\theta}^k. \end{aligned} \tag{2.19}$$

$$\begin{aligned} I^1\ddot{\Theta}^1 + \zeta^1\dot{\Theta}^1 &= \tau^1 + S^1(\theta^1 - \Theta^1) \\ &\vdots \\ I^k\ddot{\Theta}^k + \zeta^k\dot{\Theta}^k &= \tau^k + S^k(\theta^k - \Theta^k). \end{aligned} \tag{2.20}$$

Eq. (2.18) describes the actuated dynamics and Eq. (2.19) describes the unactuated dynamics of the robot, which is coupled to the actuator dynamics of Eq. (2.20) through the elastic elements. In this case, the robot's generalized mass matrix is $M_{rob} = M_{dyn}$ (M_{dyn} is defined in Eq. (2.12)), which suggests that the condition number, $\kappa(M_{rob})$, is no longer affected by the actuator reflected inertia. Thus, as far as the robot's dynamics is concerned, the elastic elements effectively eliminate the

actuators' reflected inertia. As previously discussed M_{dyn} would normally have a large condition number, especially in the case of high DOF robots. Therefore, one should expect SEA robots to suffer from high sensitivity and significant dynamic performance limitations due to joint oscillatory behavior under closed loop control, which results from the SEA characteristic elasticity. Eq. (2.19) suggests that improving a SEA robot's dynamic performance may be achieved by:

- Increasing the SEA stiffness which may lead to reduced amplitude of oscillations. However, this also leads to degraded force control resolution.
- Increasing the joint friction which may lead to damping of oscillations. However, this also leads to increased losses and potential heating issues.

Dynamics sensitivity issues are reported in [15] regarding NASA-JSC Valkyrie which is a series elastic actuated humanoid robot with 44 DOF. In the article, the sensitivity of the robot's control system to the dynamics model is attributed to low friction of SEA joints. However, as shown in this section, the joint torque sensitivity of the SEA robots is an intrinsic dynamics problem that may not be solved by the addition of joint friction or SEA stiffness increase. These measure only "mask" the fundamental dynamics limitations.

2.5 Example Robot Dynamics Calculations

This section provides examples of how the actuator reflected inertia affects a robot's generalized mass matrix condition number. A 12 DOF quadruped is first considered, followed by an analysis of RoboSimian's mass matrix.

2.5.1 Quadruped robot example

In order to demonstrate how the reflected actuator inertia affects a limbed robot's dynamics, a simple dynamic model of a 12 DOF quadruped robot is considered. The schematic model is shown in Fig. 2.3. The central body is modeled as a solid box with mass of $20Kg$ and the leg links are modeled as solid cylinders with mass $4Kg$ for the upper link and $1Kg$ for the lower link, thus 50% of the robot's mass is concentrated in its legs. The condition number of the mass matrix of the robot in the configuration of Fig. 2.3 is $\kappa(M_{rob}) = \kappa(M_{dyn}) = 2161$ (if the reflected inertia of the actuators is neglected). Such high condition number suggests that one should expect high sensitivity: small joint torque errors will propagate to high acceleration errors. Thus, "hidden" oscillatory dynamics modes may limit the robot dynamic performance under close loop joint control. However, if one assumes that all joint actuators are identical and have reflected inertia of $I_i^j = 2Kg/m^2$, the mass matrix condition number becomes $\kappa(M_{rob}) = 25.8$. In this case the bounds from Eq. (2.14) and Eq. (2.16) lead to $15.34 \leqslant \kappa(M_{rob}) \leqslant 32.85$ and the approximation of Eq. (2.17) leads to $\kappa(M_{rob}) \approx 22.4$. If all joint actuators are again identical but have reflected inertia of $I_i^j = 200Kg/m^2$, the mass matrix condition number becomes $\kappa(M_{rob}) = 109.1$. In this case the bounds from Eq. (2.14) and (2.16) lead to $74.47 \leqslant \kappa(M_{rob}) \leqslant 159.51$ and the approximation of Eq. (2.17) leads to $\kappa(M_{rob}) \approx 108.9$. These results suggest that Eq. (2.17) closely approximates the robot's generalized mass matrix condition number and provides significant qualitative insight into the significance of the actuator reflected inertia for the robot dynamic performance.

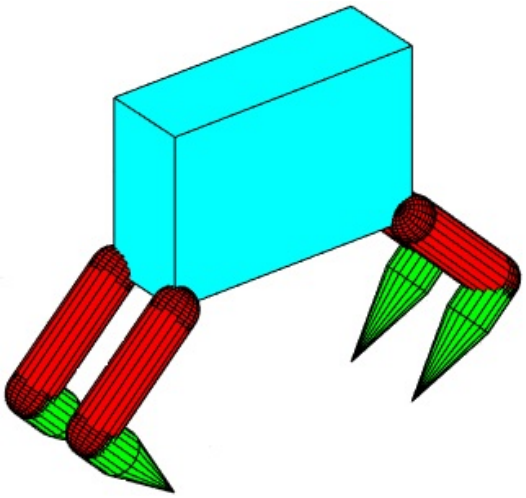

Figure 2.3: Quadruped robot model.

Fig. 2.4 shows some of the robot's eigenvalues and their corresponding eigenvectors

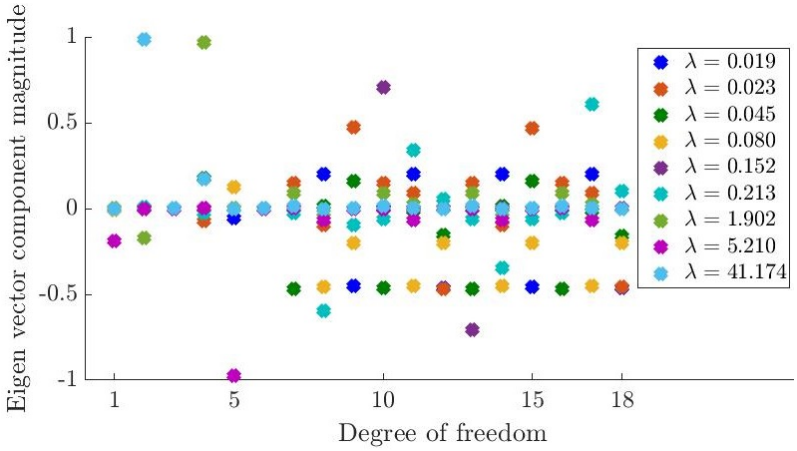

(a) No actuator reflected inertia.

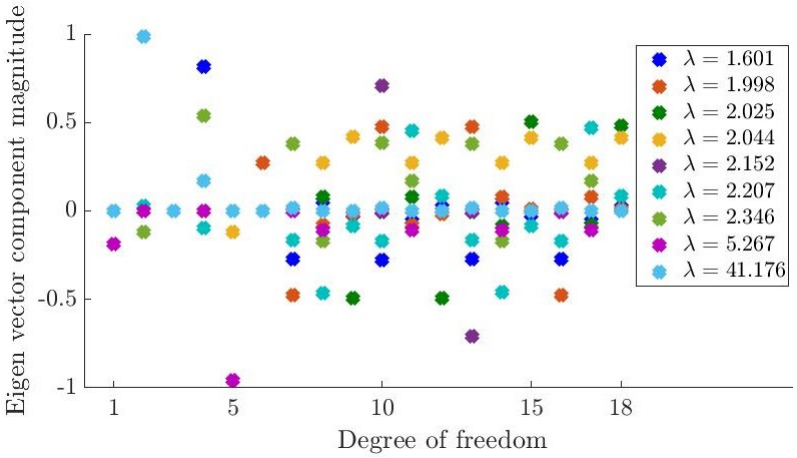

(b) Actuator reflected inertia of $2\frac{Kg}{m^2}$.

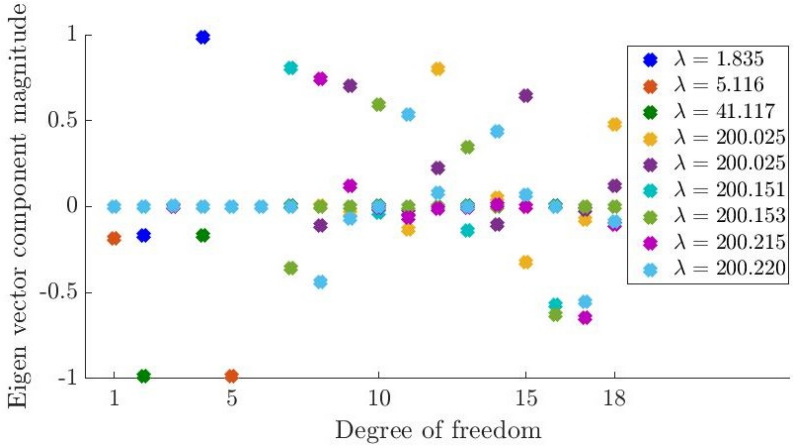

(c) Actuator reflected inertia of $200\frac{Kg}{m^2}$.

Figure 2.4: Representative eigenvectors of the generalized mass matrix of the quadruped robot model of Fig. 2.3 for different values of the actuator reflected inertia. The corresponding eigenvalues are in the range from the smallest to the maximum. All actuators are assumed identical.

for three cases:

- actuators with no reflected inertia (see Fig. 2.4a).
- actuators with identical reflected inertia of $2\frac{Kg}{m^2}$ (see Fig. 2.4b).
- actuators with identical reflected inertia of $200\frac{Kg}{m^2}$ (see Fig. 2.4c).

As may be observed in Fig. 2.4a, when the actuators have no reflected inertia, eigenvalues of the generalized mass matrix that are orders of magnitude smaller than the maximum eigenvalue, have corresponding eigenvectors that span multiple DOFs. Therefore, small magnitude torques (that may be due to commanded joint torque errors) along these eigenvector directions in the joint space may lead to high magnitude accelerations along the same direction in the joint space. These joint space eigenvectors may cause oscillations and even instability under close-loop control, thus, severely limiting the robot achievable performance, regardless of the high and low level control strategies.

Fig. 2.4b shows that when the actuator reflected inertia is larger than the minimum eigenvalue and smaller than the maximum eigenvalue of the unactuated robot mass matrix, M_{cen}, the robot's mass matrix condition number, $\kappa(M_{rob})$, is at minimum and is determined solely by the robot design. Such reflected inertia levels may be achieved with low to mid reduction ratio actuators (see Sec. 1.1). For this quadruped example, a significant part of the robots mass is concentrated in the central body and the distal links in the limbs are quite light which leads to a large condition number of the actuated robot mass matrix, $\kappa(M_{cen})$, as the robot's inertia (in all directions, regardless of the configuration) is significantly smaller than its mass.

Finally, Fig. 2.4c shows that high actuator reflected inertia, characteristic with high reduction ratio actuators, may still lead to large mass matrix condition number of the robot. Therefore, one may expect whole body oscillations and instability if the robot is close-loop controlled in dynamic locomotion because the robot dynamics sensitivity is solely due to the robot unactuated dynamics. However, under quasi-static control, the robot would work well as the unactuated dynamics is in stable equilibrium, in this case. Furthermore, Fig. 2.4c suggests that the actuated dynamics is quite decoupled due to the high reduction ratio actuators which is characteristic for manipulators (see Sec. 2.2).

2.5.2 RoboSimian

This section considers RoboSimian's (see Sec. 1.1) generalized mass matrix in the configuration shown in Fig. 2.5 which corresponds to a quadruped locomotion stance. Fig. 2.6 shows some of the robot's eigenvalues and their corresponding eigenvectors for three cases:

- actuators with no reflected inertia (see Fig. 2.6a).
- actuators with identical reflected inertia of $4\frac{Kg}{m^2}$ (see Fig. 2.6b).
- actuators with identical reflected inertia of $200\frac{Kg}{m^2}$ (see Fig. 2.6c).

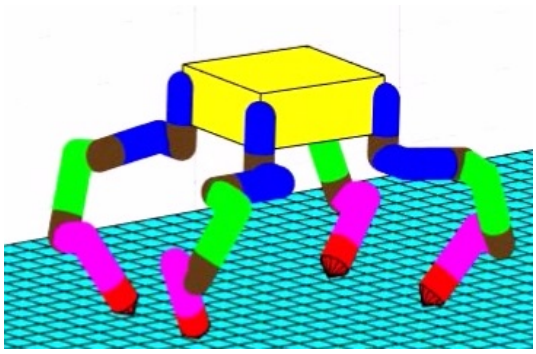

Figure 2.5: RoboSimian locomotion stance model.

If the actuators have no reflected inertia, the robot's generalized mass matrix condition number is $\kappa(M_{rob}) = 5.2 \times 10^4$ and the limbs mass matrix, M_{lim}, has condition number, $\kappa(M_{lim}) = 1030$. Such high condition numbers suggest extremely sensitive robot dynamics. Fig. 2.6a suggests that due to the high number of links in each limb (7 DOF), there are multiple joint space eigenvectors of the mass matrix with large number of non-zero DOF components that have very small corresponding eigenvalues. Therefore, actuators with no reflected inertia, such as SEA, may be unsuitable robot designs with such high complexity.

On the other hand, due to the large number of joints, it may not be possible to design shock tolerant, backdrivable actuators with reflected inertia that is larger than the minimum eigenvalue and smaller than the maximum eigenvalue of the unactuated robot mass matrix, M_{cen}. Nevertheless, Fig. 2.6b suggests that the robot's mass matrix condition number may still be improved significantly (see Eq. (2.17)), if actuators with identical reflected inertia of $4\frac{Kg}{m^2}$ are used, which may be achieved with mid reduction ratio actuators. In this case, $\kappa(M_{rob}) = 27.3$.

Finally, Fig. 2.6c suggests that for robots with high number of joints in their limbs, high reduction ratio actuators may lead to favourable generalized mass matrix condition number. For actuator reflected inertia of $200\frac{Kg}{m^2}$, $\kappa(M_{rob}) = 24.1$ for the RoboSimian model in the configuration of Fig. 2.5.

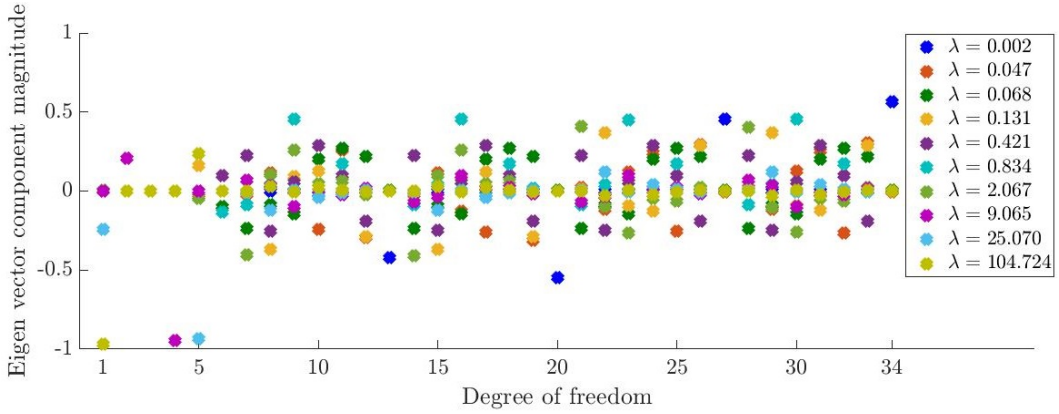

(a) No actuator reflected inertia.

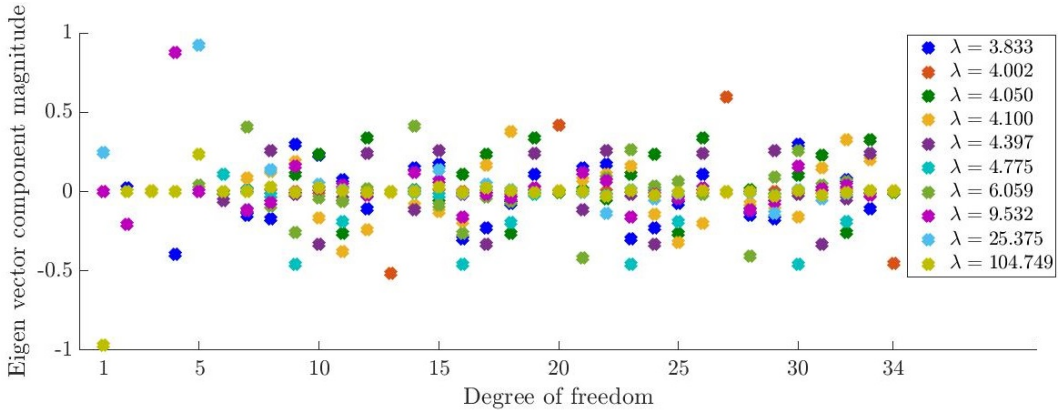

(b) Actuator reflected inertia of $4\frac{Kg}{m^2}$.

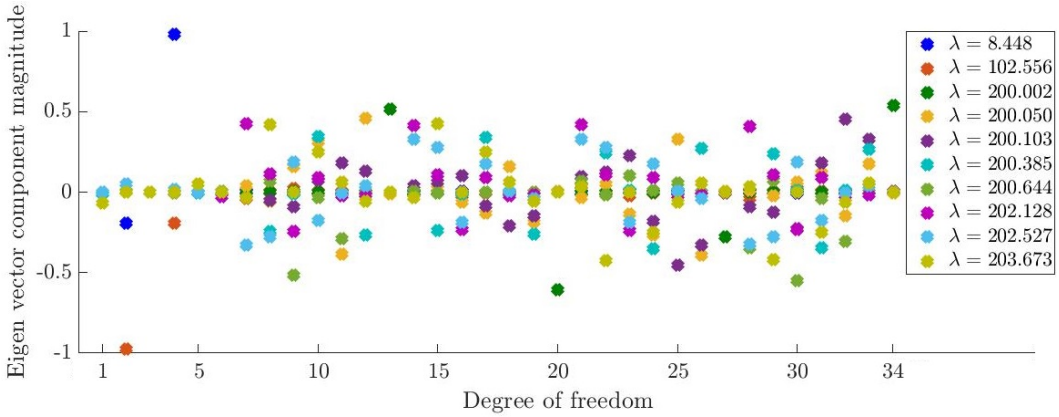

(c) Actuator reflected inertia of $200\frac{Kg}{m^2}$.

Figure 2.6: Representative eigenvectors of Robosimian's model generalized mass matrix for different values of the actuator reflected inertia. The corresponding eigenvalues are in the range from the smallest to the maximum. All actuators are assumed identical.

2.6 Conclusion

This chapter analyzes robot dynamics sensitivity and discusses how actuators may impact it. It is shown that for both manipulators and multi-limbed robots, actuator reflected inertia may reduce this sensitivity significantly by reducing the generalized mass matrix condition number. Due the compliance in SEAs, actuator dynamics is separated from the robot dynamics and the intrinsic robot dynamics sensitivity is unaffected by the actuators. Even though, increasing the SEA stiffness and friction may improve the performance, the sensitivity is not affected and the fundamental performance limitations persist regardless of the control strategy. Therefore, the analysis suggests that the low to mid reduction ratio geared motor in the dual actuation architecture, which is proposed in Sec. 1.2, may be designed to minimize the robot's intrinsic dynamics sensitivity which may lead to significant dynamic performance advantage compared to SEAs.

Chapter 3

DESIGN OF BRUSHLESS-DC OUTER ROTOR MOTORS WITH DOUBLE-LAYER CONCENTRATED WINDING

3.1 Introduction

This chapter is concerned with the design and prototyping of high performance permanent magnet motors. The dependence of a motor's losses on its speed and load motivate the formulation of application-specific design requirement, guidelines and performance metrics. The three applications considered in this chapter are electric vehicles, drones, and robotic joint actuation (which is of primary interest).

The advantages of outer rotor motors with concentrated widnings are outlined and a flux-linkage model predicting their performance is derived. The analytic model is used to gain insight into how the pole and slot count affect motor performance. Next, the performance of high pole count motors is analyzed and motor design trade-offs are introduced. These analyses motivate the formulation of application-specific guidelines and performance metrics. The main objective of the chapter is to introduce consistent methods for improving the motor torque and torque density, primarily in terms of robotic joint actuation applications. Electro-magnetic FEA provides verification of the analytic results presented in the chapter. Motor prototypes are designed and machined in-house according to the proposed guidelines and methodology. The prototypes' performance is characterized, and the results show good agreement with FEA predictions. The performance of the developed prototypes is compared to high cost, off-the-shelf frameless motors.

Finally, motor scaling modes are described and analyzed in terms of outer rotor motors with concentrated windings. These allow the performance of scaled version of an existing design to be rapidly predicted without the usage of computationally expensive FEA. The scaling modes discussion provides a complementary motor design trade-offs analysis and outlines the challenges in implementing motors with high torque and torque density in robotic applications.

3.1.1 Permanent Magnet (PM) Synchronous Motors

Permanent magnet motors find increasing application by replacing induction motors in numerous devices due to their weight, size and efficiency advantages. Furthermore, in some cases traction permanent magnet motors (or motors optimized for toque production) may be used as a replacement of the complete geared induction motor systems.

The two most widely used rotary motor types are the radial and axial ones. Coreless (ironless) and slotless motors are not considered in this thesis due to their low torque density resulting from their large air gap, and thus, low air gap flux. Such motors are advantageous in high speed applications that involve high electrical frequencies as they do not have stator core losses. Axial motors may have advantages in certain applications but are still relatively rare mainly due to their manufacturing challenges [41]. The axial flux flow in these motors requires circumferential lamination, which is difficult and costly to manufacture [42]. A thorough review of the various permanent magnet axial flux motor designs reported in literature may be found in [43]. Axial motors may be designed in various configurations: one stator - one rotor, two stators - one rotor, one stator - two rotors, etc. Radial flux and axial flux (two stators - one rotor) motor structure comparison is described in [44]. It is found that the axial flux motor is superior only when the ratio between motor outer stator diameter and length is low, and when the ratio between the motor outer diameter to inner diameter is high. A torus slotless axial motor which is designed to be coupled directly to the wheel of EV scooter is described in [45]. The dual rotor or dual stator configurations of axial motors pose severe structural requirements, design constraints and may significantly affect robotic joint packaging. Therefore, axial motors are not considered further in this thesis.

This chapter is concerned with the design of radial surface mount permanent magnet (SMPM) motors due to their modeling, analysis, simulation and manufacturing readiness. Furthermore, the radial motors' cylindrical shape is very attractive for coupling to shafts, gearboxes, joints, etc (within typical robotic applications). The main motor staror winding schemes are distributed and concentrated. In concentrated winding, the coils of each of the phases are *concentrated* around different stator teeth, while in distributed windings, the coils are equally distributed in the slots [46]. The design aspects of permanent magnet motors with concentrated windings are reviewed in [41, 47]. The theory of the operation of concentrated winding motors, their advantages and challenges are discussed in [48–51]. The performance

of motors with single and double layer windings are compared in [52]. Designs with irregular distribution of slots are introduced in [50]. Design of motors with concentrated windings for low speed applications is discussed in [53]. A design study of low speed direct drive SMPM motors is presented in [54]. High speed application of PM motors is discussed in [55]. Cogging torque minimization techniques are described in [56, 57]. Torque ripple is discussed in [58]. PM motors used in hybrid electric vehicles (HEV) are reviewed in [59]. The design of permanent magnet motors with concentrated windings in the context of electric vehicles (EVs) is discussed in [60, 61]. Core (or iron loses) are discussed in [62–64], in the context of PM motors in [65–67] and rotor core losses are considered in [68–70].

Interior permanent magnet (IPM) motors are attractive due to the possibility of wide speed range of constant power operation [71–73]. The reason is the improved flux weakening capability (driving a motor beyond its rated speed through injection of direct current) of these machines due to their higher direct inductance and the existence of reluctance torque (direct current torque) [71–73]. Flux weakening and reluctance torque are outside of the scope of this thesis and are not further discussed. IPM motors suffer from higher mass and rotor inertia due to the additional amount of iron used in their rotors which makes them unattractive for dynamically intensive applications like robotics. Nevertheless, higher air gap flux densities may be achieved in IPM motors using flux concentration [54, 74, 75]. For this reason, IPM motors are only briefly considered in this chapter with the goal of showing they have no significant torque and torque density advantages.

Finally, motor scaling rules are discussed in [76–78]. These may be quite useful in predicting the performance of a scaled version of an existing motor design.

The aforementioned prior works are primarily concerned with the generic modeling and design of motors for general application. In contrast, this chapter considers the application-specific design and trade-offs of outer rotor motors with concentrated windings. The objective is to show that given a particular application, one may design such motors with superior performance compared to what is available off-the-shelf, provided the intrinsic motor design trade-offs are leveraged. Of main focus is motor design for robotic joint applications.

3.1.2 Contributions and Chapter Structure

Sec. 3.2 discusses the application-specific motor design requirements for electric vehicles, drone and robotic joint actuators. Sec. 3.3 describes the structure of permanent magnet motors and outlines the advantages of outer rotor motors with concentrated windings. Sec. 3.3.3 describes a flux linkage model for these motors which is used in the derivation of the analytic design trade-offs and guidelines of Sec. 3.4. Sec. 3.4.1 describes how a motor's slot count affects its performance, Sec. 3.4.2 discusses high pole count motors in the context of high speed applications, while Sec. 3.4.3 introduces motor design trade-offs characteristic of motors with high pole count, and Sec. 3.4.4 discusses how the tooth width and area may be optimized to improve a motor's torque and torque density. Next, Sec. 3.5 provides electro-magnetic FEA verification of the results of Sec. 3.4 and Sec. 3.6 describes the development and fabrication of motor prototypes, designed according to the proposed guidelines and methodology. Sec. 3.7 describes the possible motor scaling modes and discusses the challenges related to the practical implementation of high torque motors. Finally, Sec. 3.8 briefly describes motor failure modes.

3.2 Application-specific Motor Design Consideration

This section provides a brief and simplified motor loss discussion that motivates examining motor operating conditions in three distinct applications: electrical vehicles or EVs (Sec. 3.2.1), drones (Sec. 3.2.2) and robotics (Sec. 3.2.3). Thus, the objective of the section is to examine ways to improve motor performance w.r.t. a particular application, especially robotic joint actuation.

In order to understand the basic trade-offs in motor design, first motor operating losses need to be discussed. The majority of the power losses in permanent magnet motors may be attributed to copper losses in the coils and core (or iron) losses in the stator. Core losses are due to changes of the magnetic field in the stator electrical steel lamination (see Sec. 3.3.3). Fig. 3.1 shows schematically the dependence of the losses on the motor operating conditions. Disregarding nonlinear, high-order effects, copper losses are dependent only on the motor loading (current in the windings) while core losses are dependent only on the motor speed. For some motor designs, skin and proximity effects may lead to significant copper loss increase at high speeds and the armature reaction may lead to core loss increase at high loading. Depending on the motor topology, rotor losses (due to harmonics in the windings magnetomotive force) may also be nontrivial (see Sec. 3.3.2). Their significance is, however, not due to their size but due to the fact that they occur in the rotor, which may not be readily cooled in some designs. Nevertheless, the simplified loss relations described in Fig. 3.1 provide a sufficient loss components dependence that may be advantageous in application specific motor design consideration.

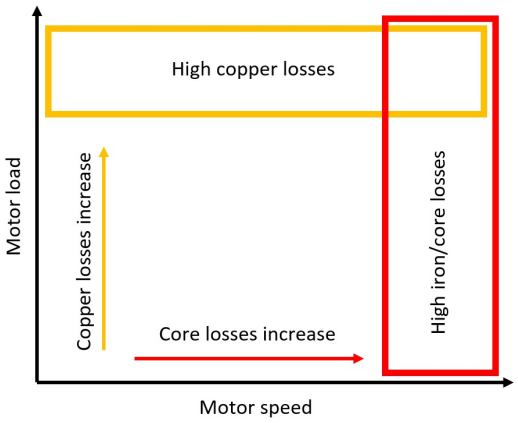

Figure 3.1: Motor losses in terms of load and speed.

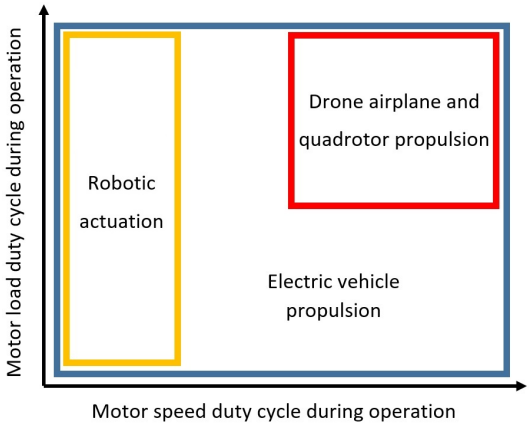

Figure 3.2: Operating duty cycle of motors depending on the application.

The usefulness of this simple loss model may be demonstrated by considering three general permanent magnet motor applications: electric vehicles (EV) propulsion, airplane or quadrotor drone propulsion, and robotics actuation (for manipulators, legged or limbed robots, etc.). In each of these applications the operating conditions of the permanent magnet motors are characterized by different speed and load duty cycles. That is, during a complete operation cycle, motors spend different fraction of time at high load and high speed conditions. Fig. 3.2 shows a simplified plot of the characteristic load and speed duty cycles for the three applications considered in this chapter. In the context of this chapter, robotics refers to applications that feature actuated joints, usually comprised of motors coupled with gearboxes, that are characterized by their limited range of motion (typically less than a full rotation of the gearbox output).

3.2.1 Motors Designed for EV Applications.

Depending on the terrain, EV motors may be loaded at any level and speed for an arbitrary amount of time, and thus, they need to be equally *efficient* at:

- high load and at any motor velocity, which may occur when the vehicle is climbing hills at different speeds.
- low load and at any motor velocity, which may occur when the vehicle is traveling on level terrain at different speeds.

Therefore, EV motors need to perform well in both variable speed and variable load conditions, independently. Comparing these requirements to the simplified loss relations of Fig. 3.1 suggests that efficient EV motors need to have relatively low core losses. That is, the motor may not dissipate excessive amount of power (as heat) to simply run at no load or low load. The motor weight is generally a small fraction of the vehicle's mass (plus the payload), therefore, in the design of EV motors, it is acceptable to trade-off motor size and mass in order to increase the vehicle propulsion efficiency, and thus, its travel range. This argument may be used to explain the relatively large size and mass of EV motors. The definition and characterization of the mass vs. core loss design trade-off is one of the contributions of this chapter (see Sec. 3.4).

3.2.2 Motors Designed for Drone Applications.

During operation, the permanent magnet motors in electric airplanes and quadrotors are responsible for sustaining the flight by overcoming air friction and gravity, respectively. Thus, these motors are mostly operated at high speed and at high load condition. As far as the performance is concerned, only the motor efficiency at high power is important.

On the other hand, reducing the motor weight allows for direct increase of the vehicle's payload capability as the actuation system usually accounts for a large portion of the total weight, therefore, the motor power density and high load efficiency are crucial performance metrics.

This simple analysis suggests that an electric aircraft's propulsion efficiency is only dependent on the total motor operating losses rather than the individual loss components. Therefore, high power density motor topologies that feature relatively high core losses may significantly boost overall vehicle performance as long as their efficiency is adequate at high power levels. Examples of such motors may be seen in Fig. 3.3. Consulting the motors' data sheets reveals that the core loss may account for as much as 50% of the total loss at motor rated power for these designs. On the other hand, at rated load these motors may achieve torque densities as high as $10\frac{Nm}{kg}$. Here torque density of a motor is defined as the rated torque divided by the mass of the motor active components (stator lamination, magenets, rotor yoke and windings). In this chapter, rated torque is defined in terms of rated copper loss at stall and this torque metric choice is motivated and further discussed in the following section.

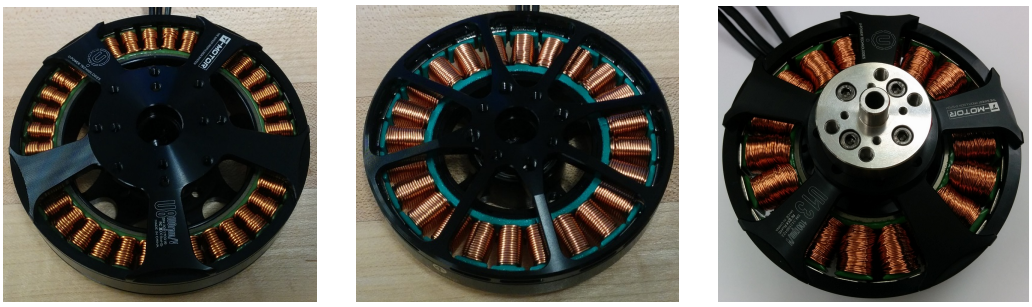

Figure 3.3: High efficiency permanent magnet motors by T-motor used for high power, heavy lifting quadrotors and airplane drones [79].

3.2.3 Motors Designed for Robotics Applications.

The final actuation category of Fig. 3.2 is of main interest in this chapter and this thesis in general. The high torque density requirements in robotic actuation usually leads to the coupling of permanent magnet motors with mid to high reduction ratio gearboxes.

For robotic applications, the torque production *efficiency* and torque *density* are the important motor characteristics. Both of these are somewhat ambiguous and need concrete definition in the context of this chapter.

Conceptually, a torque production efficiency needs to quantify how well the motor produces torque. In [4], this is achieved using the *motor constant*, which is defined as the torque squared per unit ohmic or copper loss. The motor constant, according to this definition, is sometimes included in motor datasheets.

This chapter adopts a slightly different approach that is motivated from the intended use of the motors as part of enclosed robotic joints. For this application, a driving motor is enclosed in a cover or housing and the amount of heat that may be sustainably dissipated by the joint system is determined by the housing (and potentially a cooling system), rather than the motor properties. Then, the maximum amount of heat that the motor can generate is expected to be constrained to a particular value independent of the motor design. Therefore, in the context of a robotics application, it is sensible to compare motor candidates or design motors in terms of nominal or rated stall copper loss, P_{cu}. This motivates the adoption of the following definitions in this chapter:

- A motor's rated torque is given in terms of a rated copper loss at stall, P_{cu}, which is the torque that the motor delivers when the output is stationary and P_{cu} power is dissipated as heat.
- Torque density is defined as the rated torque divided by the motor active mass (the combined mass of the stator, rotor, magnets and copper in the motor).

Robotic joints generally have very limited range of motion (less than a full rotation in most cases), therefore, the high speed duty cycle is quite limited and the core loss contribution to the total loss, in the motor operating cycle, is expected to be relatively small since the motors never operate continuously at high speed. In addition, higher joint speeds are usually achieved while the joint is relatively unloaded. This situation occurs, for example, throughout the swing phase in legged robot locomotion, as well

as fast end-effector translations motions between object placement and object pick-up in robotic manipulation. Therefore, increased AC copper losses (due to skin and proximity effects) at high speed may also be acceptable in these applications. This simple analysis suggests that increasing the permanent magnet motor torque density at the expense of higher core losses at high speed may be quite advantageous in applications where low mass and high compactness robotic actuation is desired. Such applications may be found in limbed or legged robotics, manipulation, etc. As discussed in Sec. 1.1, whole body manipulators such as RoboSimian are of primary interest in this thesis. The torque and torque density (according to the definition above) of the joint motors in these applications is of major importance. For example, the maximum payload of a robotic manipulator at the end-effector may be determined from the maximum stall torque that each of the joints can sustain and the manipulator forward kinematic.

As discussed in Ch. 1 and Ch. 2, mid reduction geared actuators may have significant advantages in terms of reducing a robot's dynamics sensitivity. Such actuators based on high torque density, compact motors may compete with the traditional high reduction ratio harmonic drives coupled with small high speed motors and ultimately replace them for robotic applications. The main advantages of mid reduction ratio geared motors are:

- their improved *backdrivability*, that may allow high bandwidth and accurate torque control without a dedicated torque sensor. In this case, the motor load current may be used as a direct torque measurement. For example, in the absence of singularities, the end-effector forces may be estimated using the joint motor currents and the forward manipulator dynamics without any additional sensors.

- in their improved dynamic *responsiveness*. The actuator's significantly lower reflected inertia, combined with the high actuator torque capability may improve efficiency in high performance dynamic robotic applications. The significance of the actuators reflected inertia for the robot dynamics sensitivity is elaborated in Ch. 2.

- in their reduced actuator noise generation. The reduced gearing and motor speeds may significantly improve the robotic system operational noise. This is further discussed in Ch. 4.

3.3 Outer Rotor BLDC Motors with Concentrated Winding.

A brushless permanent magnet (PM) motor is comprised by a stator (the stationary part that contains the windings) and a rotor (the rotating part that contains the magnets). This section begins with a consideration of radial inner and outer rotor motors (Sec. 3.3.1), followed by discussion of the most widely used winding schemes (Sec. 3.3.2). The advantages of outer rotor motors (outrunners) with concentrated windings are discussed. Next, an analytic motor model (Sec. 3.3.3) is outlined and used to gain useful motor design insights in Sec. 3.4.

This thesis is primarily concerned with the design of SMPM motors due to their manufacturing readiness and simplicity. Furthermore, these motors have lighter rotors with lower inertia, which is quite useful for robotic actuators featuring low to mid reduction ratio gearboxes. Finally, their modeling is simplified due to their nonsalient rotor structure. Salient machines (such IPM) have varying reluctance depending on their rotor orientation [80]. IPM motors are only briefly considered in Sec. 3.4.4 and it is shown theoretically that higher torque and torque density may be achieved using magnet flux concentrated poles designs. Nevertheless, in Sec. 3.5.4, it is shown that the higher rotor mass of such IPM motors offsets their potential advantages for the applications considered in this thesis.

Only three-phase motors in star configuration subject to three-phase balanced currents are considered. Even though, the delta winding configuration has attracted considerable attention in the drone industry due to its simplified manufacturing, it is not considered in this chapter due to the possible occurrence of circulating currents that cannot be controlled [42, 47]. Thus, the motors considered in this chapter have windings that consist of three phases that represent the coils between one of the motor terminals and a neutral point where the phases meet. Each phase is characterized by its resistance and inductance, and generates back electromotive force (back-EMF or bEMF) when the rotor spins.

3.3.1 Outer and Inner Rotor Motors.

The most widely used radial permanent magnet motors have are the inner rotor and outer rotor (outrunner). Fig. 3.4 shows schematically the construction of inner and outer rotor motors [81].

Provided the air gap thickness is small (distance between magnets and stator teeth), the rotor in-plane thickness is significantly smaller than the stator in-plane thickness. Therefore, for the same motor outer diameter, outer rotor motors have significantly

higher torque than inner rotor motors. This follows from the fact that the produced torque is approximately proportional to the square of the air gap diameter (see Fig. 3.4) as further discussed in Sec. 3.7. For both motor structures increasing the length of the teeth (designated by l_t in Fig. 3.6) or equivalently the slot depth leads to decrease of the electrical resistance of the phases due to the increased copper area of the slots. However, in the case of inner rotor motors, increasing the slot depth also leads to air gap radius decrease, and thus, torque decrease. This inherent trade-off between the slot depth and air gap radius which is characteristic of inner rotor motors, does not apply in the case of outer rotor designs. Therefore, high compactness motors with large torque capability are possible if the outrunner construction is adopted.

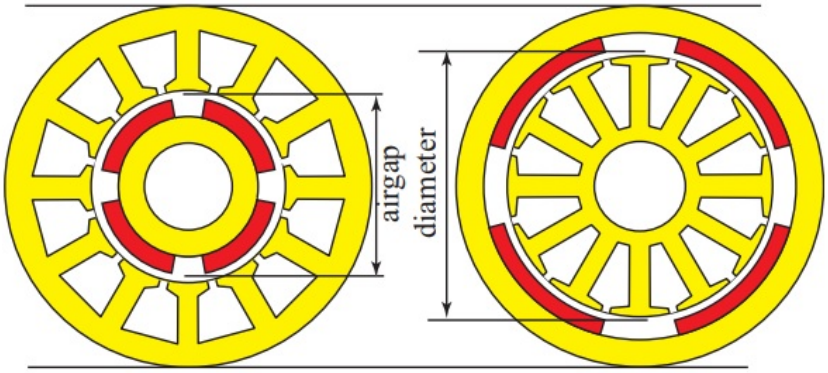

Figure 3.4: Structure of surface mounted permanent magnet inner and outer rotor motors [81]. The permanent magnets are coloured in red. Left: inner rotor motor. Right: outer rotor motor (outrunner). The stator is constructed by teeth and slots (between the teeth) that contain the winding conductors. See also Fig. 3.6.

From a manufacturing point of view, outrunner motors are advantageous as the magnets may simply be glued to the rotor yoke even in high speed applications. This is not the case with inner rotor motors, which usually require a non-magnetic sleeve to retain the magnets and support the centrifugal magnet forces [55]. The presence of a sleeve further deteriorates the produced torque due to the possibly increased air gap thickness and motor rotor inertia. Therefore, for applications where the motor inertia is to be minimized, outrunners have clear advantage (when the size of the rotor is the same).

Finally, outer rotor motors with their fixed stator on the inside, allow for the introduction of central support shaft that may be used for cabling and bearing support in robotic joints. Sensors, like encoders may also be integrated in the stator interior.

3.3.2 Motor Winding Types.

The windings of PM motors consist of coils made of magnet wire (copper or aluminum wire covered with enamel isolation). The most widely used winding configurations are the distributed, single layer concentrated and double layer concentrated ones. Distributed winding represents the majority of industrial permanent magnet synchronous motors. Fig. 3.5 shows a frameless motor with distributed windings used in the MIT cheetah [30]. Fig. 3.3 shows double layer concentrated winding motors designed for quadrotors. In double-layer winding all stator teeth have coils around them, while in single layer windings only half of the teeth are wound. Single layer winding is rare due to its more trapezoidal bEMF, greater axial length, higher rotor losses, and lower slot fill factors (in case of cost effective manufacturing) [48, 49, 82, 83].

Figure 3.5: Stator of distributed winding frameless motor [30] ©2015 IEEE.

Compared to double layer, single layer windings have advantages in their higher winding factor (the concept of winding factor is fundamental for motors with concentrated windings and is described in Sec. 3.3.3), higher inductance and better fault-tolerance at the cost of higher armature reaction (magnetic field generated by the current in the coils), higher magnetomotive force (MMF) harmonic content and may require substantially thicker stator yoke [52, 82, 84]. For these reasons single layer concentrated windings are not considered further in this thesis.

The main advantages of double layer concentrated windings compared to distributed windings are [41]:

- higher power density, torque density, efficiency and compactness due to short windings end turns and higher possible slot fill factor [48]. The conductors in the slots of concentrated winding motors that correspond to a given phase do not all produce maximum torque (this phenomena is quantified by the winding factor, discussed in Sec. 3.3.3) [48, 49]. However, if the slot-pole combination is selected according to the approach discussed in Sec.

3.3.3, the corresponding torque reduction is significantly minimized and the aforementioned advantages may be realized.

- lower manufacturing cost. Concentrated winding motors may be readily wound using low cost fan winding machines (outrunners) and needle winding machines (inner rotor motors).
- lower cogging torque due to the fractional number of slots per pole per phase. [48, 49].

The key challenges characteristic of concentrated winding motors are related to [41]:

- rotor losses due to MMF harmonics of the coils [51].
- vibrations and noise due to unbalanced magnetic forces [49].

The magnitude of the rotor losses generally comprise a small fraction of the total loss, especially if rotor yoke lamination is used. Magnet eddy current losses may be reduced through magnet segmentation [68]. Furthermore, rotor losses are generally low in high pole count motors due to the relatively small magnet size and low armature reaction (further discussed later in the section). The outrunner topology is beneficial in allowing better rotor loss heat dissipation [48]. If motor topology with slot symmetry is utilized, no unbalanced radial magnetic forces exist (slot symmetry is described in Sec. 3.3.3). These considerations motivate interest in outer rotor motors with concentrated windings and high pole count.

Outrunner permanent magnet motors with concentrated winding are also characterized with high manufacturing readiness even without specialized motor manufacturing equipment, which greatly facilitates prototyping. The coils may readily be wound by hand if a reasonable winding fill factor is assumed, even when a higher number of wire strands are used.

3.3.3 Double Layer Concentrated Winding Outer Rotor Motor Modeling

A large number of sources in the literature (see Sec .3.1.1) describe PM motor modeling, however, these prior works present models that are usually quite general and complex, and cannot be readily used to gain design insights for outer rotor motors with concentrated windings. Thus, the objective of the derivation in this section is to obtain a reduced order model that describes sufficiently well the characteristics of outer rotor motors with double layer concentrated windings, and is simple enough

to lead to clear analytic motor design trade-offs and practical motor design insights (described in Sec. 3.4). Higher order effects that are ignored in this section are either discussed in the following section or characterised using electro-magnetic FEA in Sec. 3.5.

Concentrated winding outrunner motors are defined by the geometry shown in Fig. 3.6. As discussed in the previous section, the conductors comprising each of the phases of motors with concentrated windings do not all produce maximum torque. To model this effect, a motor winding factor, C_w, is typically introduced in the literature. This winding factor quantifies the difference between the motor torque produced by the conductors belonging to a phase with the torque that would have been produced with the same number of conductors that carry the same amount of current but all produce maximum torque. The derivation and modeling that leads to the introduction and calculation of C_w is quite involved and is not required in order to understand any of the concepts in this chapter, therefore, it is not included here and the interested reader is encouraged to consult [48, 49, 51]. Clearly, in the case of concentrated windings, $C_w \leq 1$, and one's goal is to maximize C_w. The value of C_w is heavily dependent on the motor slot per pole per phase, Q_{pp}. The closer the value of Q_{pp} is to $\frac{1}{3}$, the higher the winding factor [48, 49, 51]. As a comparison, distributed windings have unit slot per pole per phase and $C_w = 1$. In the literature, motors with Q_{pp} that is not an integer are sometimes referred to as fractional-slot.

Only magnetically balanced motors are to be considered, therefore, a minimum symmetry is required in the pole-slot choice. Otherwise, the unbalanced radial forces may cause increased vibration and noise [49, 51, 81]. The motors of interest in this chapter, fall in the following general family that is characterized with high winding factor ($C_w \geq 0.933$ [48, 49, 51]):

$$\begin{aligned} Q &= 12 + k_q 6 \qquad P = Q \pm 2 \\ q &= k_s Q \qquad p = k_s P, \end{aligned} \tag{3.1}$$

where q and p are the motor slot and pole count, respectively. Q and P are the slot and pole count of the motor base

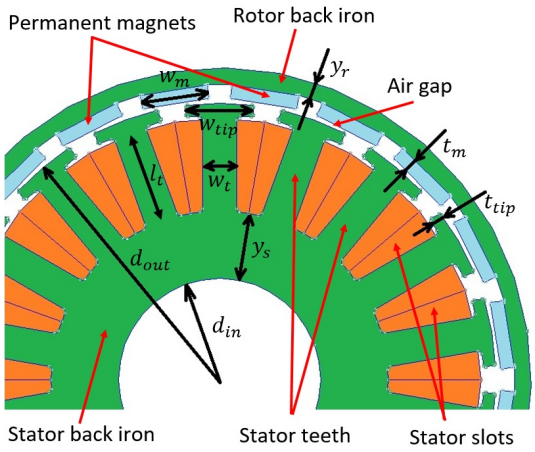

Figure 3.6: Structure of a permanent magnet outer rotor motor with concentrated windings. The stator slots contain the phase winding conductors.

topology of minimum symmetry (defined by the non-negative integer k_q in Eq. (3.1)) and the coefficient $k_s \geq 1$ is an integer that defines the motor symmetry. That is, the motor can be split up in $2k_s$ parts (like "cake" slices) and each of these parts may produce torque independently. Motors with higher k_q and lower k_s have higher winding factors and lower theoretical cogging torque as cogging torque is minimized by maximizing the lowest common multiple of q and p [48, 49, 51]. However, [82] suggests that motors with lower k_s (or lower symmetry) also have higher rotor losses.

For initial design, the winding factor may be taken as constant ($C_w = 0.94$ [48, 49, 51]) for the motors featuring the topology described by Eq. (3.1). Even though, other topologies with high winding factors exist (see Eq. (3.22)), the one in Eq. (3.1) may be used as a representative for the analysis purposes of this section.

It is useful to define the motor rotor orientation in terms of mechanical degrees (denoted by θ_m) and electrical degrees (denoted by θ_e) because in a single mechanical rotor rotation there are $\frac{p}{2}$ electrical cycles [42]. Therefore, $\theta_m = \frac{p}{2}\theta_e$. This chapter extensively uses the concept of electrical degree.

Motors with the construction of Fig. 3.6 and slot-pole combination described by Eq. (3.1), exhibit sinusoidal bEMF with few low-magnitude harmonics provided the magnet width is around 120 electrical degrees. This corresponds to approximately $\frac{2}{3}$ of the rotor surface being covered with permanent magnets, while approximately $\frac{1}{3}$ of the rotor surface is equally distributed between the magnets to create physical separation between them (see Fig. 3.6). Reducing the magnet width leads to reduced torque and increased torque ripple. On the other hand, increasing the magnet width towards 180 electrical degrees causes increasing flux leakage between adjacent magnets and/or the tooth tips, which worsens the torque ripple with no significant increase in the produced torque. The effect of the magnet width of the motor torque performance is analyzed using FEA in Sec. 3.5.1. Once the other motor dimensions are determined, the tooth tip width, w_{tip}, may be optimized using electro-magnetic FEA in order to minimize the cogging torque, torque ripple, etc, as shown in Sec. 3.6.1.

Flux-linkage model for motor torque and bEMF induced voltage

Let N_{turns} be the number of winding turns per stator tooth, assuming no parallel paths. That is, the windings comprising a given phase are made of a single long magnet wire that is wound around all the teeth belonging to the phase. Parallel paths (magnet wires that belong to the same phase and travel around the teeth in parallel)

are treated as wire strands, and thus, the phase magnet wires are modeled as a single Litz wire. Therefore, in this chapter, the windings may not have parallel paths but may have strands. This modeling approach is quite useful as it avoids introduction of magnet wire gauge (measure of wire size) in the trade-off analysis.

The phase flux linkage (the flux linked by the coils of a motor phase winding) is given by [80]:

$$\begin{aligned} \psi(\theta_m) &= -\Psi cos(\frac{p}{2}\theta_m) \\ \Psi &= \frac{q}{3} N_{turns} C_w B_q c_l l_m w_t, \end{aligned} \tag{3.2}$$

where Ψ is the peak value of the phase flux linkage, B_q is the peak flux density in the teeth, l_m is the motor out-of-plane thickness, w_t is the in-plane thickness of the teeth (see Fig. 3.6) and c_l is the lamination fill factor. For a given air gap, a_g (typically $.5mm$ to $1mm$), magnet thickness, t_m, and magnet residual flux density or remanence, B_r, the maximum air gap flux density may be simulated using electromagnetic FEA or approximated using the models of [42, 85] (See Eq. (3.18)). Then, assuming the rotor yoke thickness y_r is sufficient so that the yoke is not saturated, the air gap flux density may be used to choose w_t so that B_q is in the range $1.6T$ to $1.8T$ (maximum value with no saturation) for the case of electrical steel laminated stator.

The phase bEMF voltage may be found by differentiating the flux linkage in Eq. (3.2) w.r.t. θ_m [80]. The phase induced voltage is then given by:

$$\begin{aligned} V_{phase} &= K_{ph} \omega_m sin(\frac{p}{2}\theta_m) \\ K_{ph} &= \frac{C_w}{6} pq N_{turns} B_q c_l l_m w_t, \end{aligned} \tag{3.3}$$

where K_{ph} in the phase bEMF constant and $\omega_m = \frac{d\theta_m}{dt}$ is the motor mechanical rotational speed. Then assuming balanced three-phase brushless-DC motor driving (three-phase balanced sinusoidal phase currents), the motor torque may be found, using the equivalence between the motor torque and bEMF constants [80]:

$$T_m = K_t I_m = \frac{3}{2} K_{phase} I_m, \tag{3.4}$$

where I_m is the motor synchronous current (which is equal to the peak of the slot currents under the assumptions and definitions in this section) and $K_t = \frac{3}{2} K_{ph}$ is the synchronous motor torque constant given by:

$$K_t = \frac{C_w}{4} pq N_{turns} B_q c_l l_m w_t \tag{3.5}$$

Eq. (3.5) describes how the motor structure determines its torque production per unit synchronous current. From the geometry of Fig. 3.6, the slot area may be approximated as:

$$A_{slot} = \frac{\pi}{q}\left(\left(\frac{d_{out}}{2} - t_{tip}\right)^2 - \left(\frac{d_{in}}{2} + y_s\right)^2\right) - w_t l_t, \tag{3.6}$$

where d_{in} and d_{out} are the stator inner and outer diameters, respectively, y_s is the stator yoke thickness, t_{tip} is the tip tooth thickness, and l_t is the stator tooth length (which is equal to the slot depth) and is given by $l_t = \frac{d_{out}}{2} - t_{tip} - \frac{d_{in}}{2} - y_s$.

The motor slot resistance is:

$$R_{slot} = N_{turns}^2 \frac{\sigma l_m}{c_f A_{slot}}, \tag{3.7}$$

where σ is the winding resistivity and c_f is the bare copper slot fill factor (usually in the range $0.3 - 0.4$ for low cost manufacturing). The factor N_{turns}^2 appears in Eq. (3.7) because in the slot there are N_{turns} magnet wires, connected in series, each with $\frac{A_{slot}}{N_{turns}}$ area. Then, the motor phase resistance is:

$$R_{phase} = \frac{4q}{3}\left(k_c \frac{2\pi r_w}{l_m q} + 1\right) R_{slot}, \tag{3.8}$$

where k_c is a winding coefficient that quantifies the winding end turns' length [48] and r_w is the average radius of the windings and may be approximated as:

$$r_w = \frac{\frac{d_{out}}{2} - t_{tip} + \frac{d_{in}}{2} + y_s}{2}. \tag{3.9}$$

The synchronous motor resistance R_s and terminal resistance R_{term} are:

$$R_s = \frac{3}{2} R_{phase} \quad \text{and} \quad R_{term} = 2R_{phase} \tag{3.10}$$

The terminal resistance, R_{term}, is included here mainly because it is the resistance parameter that can always be experimentally measured and is usually quoted in motor datasheets.

Eq. (3.4) suggests that in order to calculate the motor output torque, one requires the motor synchronous current, I_m. As discussed in Sec. 3.2, motor torque is defined w.r.t. the rated copper loss at stall, P_{cu}. This is particularly advantageous for robotic applications (see Sec. 3.2). Furthermore, the performance of different motor designs may be compared in a systematic way, provided the same copper loss at stall, P_{cu}, is assumed. The synchronous current I_m is:

$$I_m = \sqrt{\frac{P_{cu}}{R_s}}. \tag{3.11}$$

The phase currents are assumed to be balanced sinusoids with amplitude I_m. Then, the motor rated torque is:

$$T_s = \frac{C_w}{4} pqB_q c_l l_m w_t N_{turns} \sqrt{\frac{P_{cu}}{R_s}}. \tag{3.12}$$

Eq. (3.12) describes how the design parameters affect the produced motor torque for a given value of copper loss at stall, P_{cu}, and is thus, extensively used in the rest of the chapter.

The motor phase self-inductance is defined:

$$L_{sf} = \frac{\frac{q}{3} N_{turns}^2}{R_m + R_g} \tag{3.13}$$

where R_m and R_g are the air gap and magnet reluctance, respectively, given by [42]:

$$R_m = \frac{t_m}{\mu_R \mu_0 w_m l_m} \qquad \text{and} \qquad R_g = \frac{a_g}{\mu_0 w_m l_m}, \tag{3.14}$$

where μ_0 and μ_R are the permeability of free space and relative permeability of the magnets, respectively. The phase self-inductance quantifies the the phase winding MMF-generated flux that "travels" from the stator, through the rotor and back to the stator in the closed magnetic circuit. On the other hand, the phase leakage inductance quantifies the phase winding MMF-generated flux that "leaks" between the teeth and may be approximately calculated using the method described in [42] for the geometry in Fig. 3.6 by:

$$L_{kg} = \frac{q^2}{3} N_{turns}^2 (\mu_0 l_m) \Bigg(\underbrace{\frac{t_{tip}}{2\pi d_{out} - q w_{tip}}}_{\text{due to tips of teeth}} + \underbrace{\frac{l_t}{2\pi (d_{in} + y_s + \frac{l_t}{2}) - q w_t}}_{\text{due to bodies of teeth}} \Bigg) \tag{3.15}$$

Then, the motor phase inductance is:

$$L_{ph} = L_s + L_{kg}. \tag{3.16}$$

In Eq. (3.16), the end turns contributions to the inductance are neglected which is easily justified by the tightly packed end turns of outrunner motors (see Fig. 3.3).

The motor synchronous inductance is [80]:

$$L_s = \frac{3}{2} L_{ph}. \tag{3.17}$$

Generally, motor inductance is not characterized as an important design parameter. However, when motors with high pole count are considered, the motor inductance may become a limiting factor. This point is further discussed in Sec. 3.4.2, where important insights are gained regarding how the motor inductance components (self-inductance versus leakage inductance) affect the high pole count motor performance. Eq. (3.16), Eq. (3.17) and Eq. (3.14) suggest that reducing the air gap and magnet thickness and increasing the magnet width lead to inductance increase.

The reluctance expressions of Eq. (3.14) may be used to find the peak of the air gap flux density [42, 85]:

$$B_g = \frac{R_m}{R_m + R_g} B_r. \tag{3.18}$$

The armature reaction, that is, the magnetic field flux and flux density in the air gap at the tip of a stator tooth due to the current in its phase winding are characterized by the following amplitudes [80]:

$$\begin{aligned} \Phi_c &= \frac{N_{turns} I_m}{R_g + R_m} \\ B_c &= \frac{(\mu_R \mu_0 l_m) N_{turns} I_m}{t_m + \mu_R a_g}, \text{ respectively.} \end{aligned} \tag{3.19}$$

Eq. (3.19) is used in Sec. 3.4.2 to describe how the motor pole count affects saturation and rotor losses.

For a rated bus voltage, V_{rated}, and rated speed, ω_{rated}, determined by the desired motor application, the number of turns per tooth may be calculated as:

$$N_{turns} = \frac{V_{rated}}{\frac{C_w}{2\sqrt{3}} pq B_q c_l l_m w_t \omega_{rated}}. \tag{3.20}$$

Thus, the rated speed, ω_{rated}, corresponds to the maximum theoretical speed at no load. For a given magnet wire gauge, the strands may be calculated from the slot fill factor and slot area:

$$N_{strands} = \frac{c_f A_{slot}}{N_{turns} d_{wire}}, \tag{3.21}$$

where d_{wire} is the bare copper wire diameter. Eq. (3.20) and Eq. (3.21) suggest that in most cases V_{rated}, c_f and d_{wire} (or the magnet wire gauge) may need to be modified so that N_{turns} and $N_{strands}$ are natural numbers corresponding to a physically realizable motor design.

Finally, additional motor designs similar to those defined by Eq. (3.1) may be derived using:

$$\begin{aligned} Q &= 9 + k_q 3 \qquad P = Q \pm 1 \\ q &= k_s Q \qquad p = k_s P \end{aligned} \tag{3.22}$$

For these motors $k_s \geq 2$, otherwise unbalanced radial motoring forces occur. However, designs with $k_s = 2$ in Eq. (3.22) may also be derived using Eq. (3.1). Therefore, for the purposes of initial design, it is sufficient to consider only the motors defined by Eq. (3.1).

Space vector modulation (SVM) and field oriented control (FOC)

This chapter is only concerned with electro-mechanical design of high performance motors and does not consider the design of the driver circuitry and its control. However, it is useful to briefly restate some of the assumptions in this section in terms of vector control for readers that are familiar with the concept. In this chapter, three phase balanced motor driving refers to three phase sinusoidal currents with zero direct-axis component of the current space vector. Thus, the synchronous current, I_m, corresponds to the quadrature direction current. Knowledge of SVM and FOC is not necessary to understand the content of this chapter, therefore, these concepts are not further described here. The interested reader is encouraged to consult the excellent SVM and FOC reviews in [42, 74, 80].

Motor loss modeling

In addition to the copper loss at stall, P_{cu}, the velocity dependent core losses and AC copper losses need to be taken into account. The core loss is traditionally separated into hysteresis, eddy current and excess loss:

$$P_{co} = P_h + P_e + P_a = K_h f B^2 + K_e f^2 B^2 + K_a f^{1.5} B^{1.5}, \tag{3.23}$$

where f is the sinusoidal excitation frequency and B is the corresponding flux density amplitude. K_h, K_e, K_a are the hysteresis, eddy current and excess loss coefficients. In the case of non-sinusoidal excitation, Fourier analysis techniques in combination with Eq. (3.23) may be used to estimate the core loss [62]. In motors, the shape of the excitation is heavily dependent on the motor construction and varies significantly within the motor components. The magnetic excitation may also be characterized by high order harmonics.

Given the high order dependence of the core losses on the flux excitation amplitude (see Eq. (3.23)), the core loss in the yoke may be reduced by an order of magnitude compared to the core loss in the teeth, provided the stator yoke thickness y_s in the range of $1.5w_t$ to $2w_t$. As one may observe in Fig. 3.7, for such designs, the flux density levels in the yoke are reduced significantly as the flux from the teeth "splits up" which is characteristic of motors with concentrated windings. In this case the teeth account for the majority of the motor core loss, and thus, the core loss is proportional to the teeth length, l_t (or equivalently, to the slot depth).

Up to this point in the chapter, copper losses are considered independent of the motor speed. However, proximity and skin effects may lead to a substantial copper loss increase at higher speeds in motors with high pole count. The modeling technique of these effects described in [42] is particularly useful for the case of outrunner motors with concentrated windings. Without repeating the analysis in [42], proximity and skin effects are proportional to f_e^2, where f_e is the electrical frequency which is related to the mechanical rotational speed ω_m by:

$$f_e = p\omega_m/(2\pi). \tag{3.24}$$

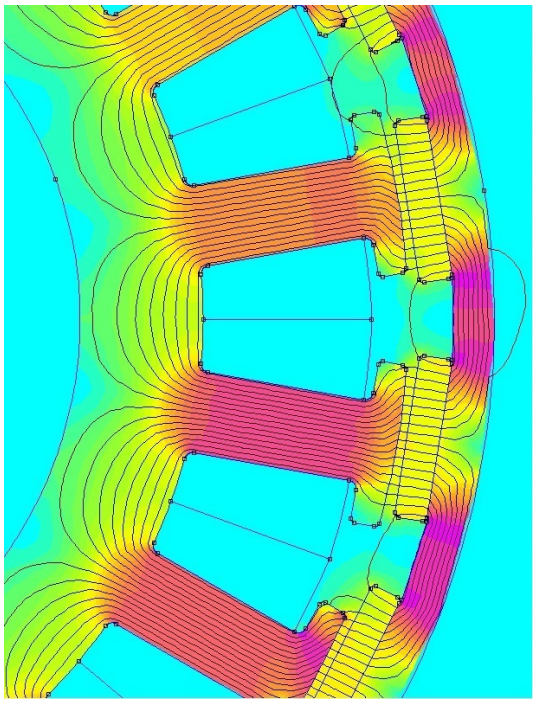

Figure 3.7: Flux density distribution in a motor. Darker colours correspond to higher flux density.

These parasitic losses may be suppressed by reducing the magnet wire gauge (and thus, increasing the number of strands) and decreasing the slot depth.

From motors perspective, the fundamental core loss frequency f in Eq. (3.23) is given by the electrical frequency f_e.

Rotor losses in motors with concentrated windings are significantly higher than the rotor losses in motors with distributed windings due to the presence of MMF harmonics [68–70]. The expressions for the armature reaction and MMF in Eq. (3.19) are quite useful in determining how the motor design parameters affect the rotor losses, as discussed in the following section.

3.4 Motor Design Insights, Trade-offs and Guidelines

The analytic model of Sec. 3.3.3 may be used to gain valuable insight into the design of outer rotor motors with concentrated windings. The objectives of this section are:

- to determine how the critical outer rotor motor design parameters affect performance (slot count in Sec. 3.4.1, pole count in Sec. 3.4.3 and teeth width in Sec. 3.4.4).
- to show that no fundamental limitations prevent employing motors with high pole count in high speed applications (Sec. 3.4.2).
- to formulate high level motor design trade-offs concerning motor torque, torque density, compactness, efficiency, etc. in Sec. 3.4.3.
- to develop a set of application specific motor design guidelines, motivated by the introduced design trade-offs, that may be beneficial for the development of high performance actuators in Sec. 3.4.5.
- to motivate the choice of a design metrics that allows consistent motor performance comparison in Sec. 3.4.6.

3.4.1 Effect of the Slot Count on the Motor Torque

Eq. (3.1) and Eq. (3.22) suggests that for a given number of poles, p, air gap size, magnet size and grade, etc., multiple valid options for the number of slots, q, may exist that lead to motor designs with high winding factor, C_w, and have the same main dimensions (d_{in}, d_{out}, y_s, y_r), teeth shape and size, etc. Prior motor design works in the literature do not provide clear guidelines how the number of slots affects a motor's performance and suggest that only the winding factor and cogging torque consideration suffices [49, 51]. This section introduces a novel geometry based slot factor, $C_q(q)$, which may be used to rapidly determine which value for q leads to the outer rotor motor design with the highest torque. The analysis of this section leads to useful trade-off insight related to choice of the motor slot count.

Starting with Eq. (3.6) and rearranging leads to:

$$A_{slot} = C_{A_s} \frac{1 - C_{A_q} q}{q}, \tag{3.25}$$

where $C_{A_s} = \pi\left(\left(\frac{d_{out}}{2} - t_{tip}\right)^2 - \left(\frac{d_{in}}{2} - y_s\right)^2\right)$ and $C_{A_q} = \frac{w_t\left(\frac{d_{out}}{2} - t_{tip} - \frac{d_{in}}{2} - y_s\right)}{\pi\left(\left(\frac{d_{out}}{2} - t_{tip}\right)^2 - \left(\frac{d_{in}}{2} - y_s\right)^2\right)}$.

Clearly, $C_{A_s} > 0$ and $C_{A_q} > 0$ for outer rotor motors with concentrated windings (Fig 3.6). Next, combining Eq. (3.10) and Eq. (3.7), leads to:

$$R_s = C_R N_{turns}^2 \Big(1 + C_{k_c} q\Big) \frac{1}{A_{slot}}, \tag{3.26}$$

where $C_R = \frac{4\sigma k_c \pi r_w}{c_f}$ and $C_{k_c} = \frac{l_m}{k_c 2\pi r_w} = 0.171 \frac{l_m}{r_w}$ for double layer concentrated windings [48]. Clearly, $C_R \geq 0$ and $C_{k_c} \geq 0$. Then, combining Eq. (3.26) and Eq. (3.25), leads to:

$$R_s = C_R C_{A_s} N_{turns}^2 \frac{q(1 + C_{k_c} q)}{1 - C_{A_q} q}, \tag{3.27}$$

Finally, combining Eq.(3.27) and Eq. (3.12) leads to:

$$T_s = \underbrace{C_w \sqrt{C_q(q)}}_{\text{function of } q} \times \underbrace{\frac{\sqrt{P_{cu}}}{4\sqrt{C_R C_{A_s}}} p B_q c_l l_m w_t}_{\text{independent of } q} \tag{3.28}$$

where $C_q(q) = \frac{q(1 - C_{Aq} q)}{(1 + C_{k_c} q)}$.

Eq. (3.28) shows that $T_s \propto C_w \sqrt{C_q(q)}$, and therefore, the slot factor, $C_q(q)$, may be used to determine which motor would deliver most torque among the motors that have the same main dimensions, teeth and pole count, p.

Further insight may be gained for motor designs characterized with high pole count and reasonable out-of-plane thickness. These are of main interest in the later sections of the chapter. For Neodymium Iron Boron (NdFeB) Magnets with energy product larger than 32 MGOe (NdFeB magnets of grades higher than N32), and for any reasonable choice of the motor slot depth, the following lower bound may be derived from the geometry of Fig. 3.6 and Eq. (3.25):

$$C_{A_q} \geq \frac{0.3}{p}. \tag{3.29}$$

Differentiating C_q in Eq. (3.28) w.r.t. q leads to $\frac{dC_q}{dq} = \frac{1 - C_{A_q} q(2 + C_{k_c} q)}{(1 + C_{k_c} q))^2}$. Then, substituting the lower bound from Eq. (3.29) shows that

$$1 - [C_{A_q} q(2 + C_{k_c} q)]|_{q=p} < 1 - 0.3(2 + 0.171 \frac{p l_m}{r_w}).$$

Therefore, $\frac{dC_q}{dq}|_{q=p} < 0$ provided $\frac{p l_m}{r_w} > 7.8$. This condition is satisfied for most motors with higher number of poles, reasonable width to diameter ratio and reasonable

slot depth. Then, it may be concluded that for such motor designs, it is beneficial to choose the motor designs with $P = Q + 2$ in Eq. (3.1) and $P = Q + 1$ in Eq. (3.22), as these motors would deliver higher torque for the same rated copper loss, P_{cu}. These motors would also have lower mass due to the usually low slot fill factor and would be easier to manufacture due to the lower number of teeth to wound.

For the very rare case of thin motors with large diameter, low number of poles and shallow slots, it might be the case that $\frac{dC_q}{dq}|_{q=p} > 0$. These motors could benefit form having higher number of slots. However, such motors are of little practical use due to their relatively high winding end turns resistance, which results in torque disadvantage. In the rest of the chapter only motors whose design satisfies $P = Q+2$ in Eq. (3.1) or $P = Q + 1$ in Eq. (3.22) are considered.

This analysis also suggests that outrunner motors could benefit from higher symmetry (higher k_s) due to the corresponding lower number of slots. On the other hand, motors with lower symmetry (or lower k_s) have lower cogging torque and simpler manufacturing as the slots of a given phase "cluster" together [81]. Thus, lower values of k_s result in phase slot clusters that may be continuously wound. This illustrates a fundamental motor design trade-off related to the motor cogging torque requirements. In application such as robotics where low cogging torque is usually desired, motors with lower symmetry may be preferred. On the other hand, in application such as quadrotors the cogging torque is not important and higher symmetry designs are advantageous.

The slot clusters associated with a given phase may be wound in parallel rather than series. Thus, these motor designs are constructed from a number of identical motor segments (or "cake" slices) that produce torque in parallel from electrical stand point. The winding connections of such a motor construction are sometimes referred to as parallel circuits in the literature. The maximum number of parallel circuits possible is given by $2k_s$. Parallel circuits are useful as they allow reduction of the number of strands or the gauge of the windings magnet wire in high power motors wired for low voltage.

Provided the stator yoke, y_s, is thick enough so that the flux levels in the yoke are significantly lower than those in the teeth (see losses discussion in Sec. 3.3.3 and Fig. 3.7), the majority of the core loss is generated in the teeth. In this case, the core loss is proportional to the number of slots, q. Therefore, motors with lower slot count may also benefit from lower core loss, and thus, better high power efficiency.

Finally, Eq. (3.13), Eq. (3.17) and Eq. (3.20) suggest that $L_{sf} \propto \frac{1}{q}$. Therefore, motors with lower slot count also feature higher self-inductance, which may be beneficial in some cases. Motor inductance is further discussed in the following section.

3.4.2 High Pole Count Motors in High Speed Applications

Traditionally, motors with high pole count are considered suitable only for low speed traction or direct drive applications [55, 60, 81]. However, there is no hard limitation that prevents their use in high speed applications even when used with BLDC drivers with 120° commutation.

To show this, consider the effects of changing the number of poles while the stator outer diameter, teeth length and magnet thickness are fixed. First, Eq. (3.1) and Eq. (3.22) suggest that approximately $q \propto p$. From the geometry of Fig. 3.6, it can be shown that the product qw_t is approximately constant, therefore, $w_t \propto \frac{1}{q}$. Then, Eq. (3.5) suggests the motor torque constant is $K_t \propto p$. Next, Eq. (3.20) suggests that the number of turns is $N_{turns} \propto \frac{1}{p}$ as the rated motor voltage, V_{rated}, and speed, ω_{rated}, are preserved. However, the combined magnet and air gap reluctance is $R_m + R_g \propto p$ from Eq. (3.14) because $w_t \propto \frac{1}{q}$ and approximately $q \propto p$. Therefore, substituting these in Eq. (3.13) suggests that approximately $L_{sf} \propto \frac{1}{p^2}$. Also Eq. (3.15) suggests that $L_{kg} \approx const$, that is, increasing the number of poles does not affect the phase leakage inductance. The characteristic structure of the outrunner motor (see Fig. 3.6) suggests that at low pole count the motor phase inductance is dominated by the self-inductance component, due to the rapidly increasing distance between the teeth and the resulting large gap between the tooth tips. The scaling of the inductance components with number of poles of the motor has important implications, as discussed below.

The total phase slot area is approximately constant and the motor resistance is not significantly affected by changing the pole count. In practice, Eq. (3.26) suggests that the motor resistance decreases with increasing the number of poles due to reduction of the windings end turns, however, this effect may be ignored for the purposes of this discussion.

The following conclusions may be drawn from the above analysis:

- increasing the pole count, p, up to a threshold value, p_L, which is characterized by $L_{sf} = L_{kg}$, improves the motor reactive power and power factor.

  This follows from the fact that the inductive phase impedance at a motor mechanical speed ω_r is given by $X_L = 2\pi L_{ph} f_e = 2\pi(L_{sf} f_e + L_{kg} f_e)$, and $L_{sf} \propto \frac{1}{p^2}$, while $L_{kg} = const$ and $f_e \propto p$ (see Eq. (3.24)). Therefore, X_L decreases for $L_{sf} > L_{kg}$. The reactive power decreases, while the active power is approximately preserved, which leads to power factor increase.

  On the other hand, if the pole count is further increased beyond p_L, then $L_{sf} < L_{kg}$ and X_L increases which deteriorates the motor reactive power and power factor.

- increasing the pole count, p, leads to decrease of the motor electrical open loop time constant, τ_e. This follows form the fact that $\tau_e = \frac{L_{sf}+L_{kg}}{R_{ph}}$. However, increasing p beyond p_L leads to asymptotic convergence of $\tau_e \rightarrow \frac{L_{kg}}{R_{ph}}$. The time constant is a crucial parameter determining the motor current and torque ripple in 120° commutation, sometimes referred to as BLDC in the literature. If the time constant is too large compared to the commutation switching frequency, BLDC may lead to increased motor losses due to the open loop commutation. In such cases, the motor inductance becomes a performance limiting factor. However, if FOC is utilized instead, the time constant is not of major importance due to the closed loop phase current control.

From practical motor design perspective, the tooth tip thickness scales with the magnet size so that the flux density levels are preserved, therefore, the tooth tip contribution to the leakage inductance in Eq. (3.15) scales with $\frac{1}{p}$. Eq. (3.15) suggests that the teeth body contribution to the leakage inductance may be reduced by decreasing the length of the stator teeth and or (equivalently reducing the slot depth). Therefore, motors of arbitrary high pole count may be designed to have favourable reactive power, power factor and electrical open loop time constant provided the leakage inductance is not dominant.

As demonstrated with the aid of electro-magnetic FEA in Sec. 3.5.3, torque degradation occurs when flux leakage levels in the motor components increase due to increasing of the motor pole count. The relative increase of the phase leakage inductance compared to the phase self-inductance, is an indication of such increase

in the flux leakage levels. Therefore, outer rotor motors that have relatively high leakage inductance are not usually practical. The flux leakage issues and their suppression are further discussed in Sec. 3.5.3.

Eq. (3.16), Eq. (3.14) and Eq. (3.18) suggest that the motor self-inductance, L_{sf}, may be increased by decreasing the air gap thickness, a_g, without modifying the air gap flux density, B_g, provided the magnet thickness, t_m, is decreased correspondingly. Thus, the motor self-inductance may be manipulated directly by changing the air gap thickness and magnet thickness. Usually, the size of the air gap is chosen as small as possible given the manufacturing and assembly tolerances.

This analysis also suggests that motors intended for high speed applications that have high number of poles are characterized by high electrical frequency and low inductance which are both challenging for the driver circuitry. The high electrical frequency requires fast control, especially for FOC. The low inductance may lead to large current ripple, and increased copper losses and requires high PWM frequency and possibly additional filtering. Increasing the motor phase inductance may be used to reduce PWM current ripple. On the other hand, reducing the motor phase inductance may be used to reduce the motor time constant and improve the high speed commutation.

The rotor yoke thickness, y_r, (see Fig. 3.6) is determined by the magnet strength and width so that the rotor yoke is not saturated, that is, the yoke reluctance does not limit the airgap flux density. Therefore, for a given magnet grade, the motor rotor inertia is proportional to the magnet thickness, t_m. Thus, there are important design trade-offs to consider in the choice of the air gap thickness, magnet grade, thickness, width etc. in applications that benefit from lower motor inertia.

Finally, an important motor aspect that is usually overlooked in PM motors is the armature reaction. The assumptions and approximations from earlier in the section suggest that $N_{turns} \propto \frac{1}{p}$ and the motor delivers the same torque regardless of its pole count, p, for a given values of the synchronous current, I_m. Therefore, the windings MMF is inversely proportional to p, and Eq. (3.19) leads to $\Phi_c \propto \frac{1}{p^2}$ and $B_c \propto \frac{1}{p}$. Therefore, increasing the number of poles leads to significant reduction in the motor armature reaction. Dynamic robotic applications that are characterized by the occurrence of large forces due to impacts or contacts with the environment, such as legged robots, require actuators that can sustain loads many times their rated torque for short time intervals [30]. Under high winding MMF, the permanent magnets of a SMPM motor may be partially demagnetized, which causes permanent motor

damaged and loss of performance. Furthermore, magnetic saturation of the teeth due to the windings MMF may cause increased torque ripple and reduced torque, which limits the motor peak torque capability. The windings MMF also introduces flux density harmonics in the teeth that may lead to a substantial contribution to the motor core losses and especially to the rotor losses as previously discussed. Therefore, it may be concluded that motors with high pole count may have significant advantages in terms of dynamic robotic applications due to their reduced windings MMF or equivalently reduced armature reaction (see Eq. (3.19)). In fact, $B_c \propto \frac{1}{p}$ suggests that the peak torque is $T_{peak} \propto p$. However, similar to the phase inductance discussion above, increased levels of flux leakage may lead to deviation from this analytic conclusion and lower than expected performance (see Sec. 3.5.1).

3.4.3 Performance Trade-offs Related to Motor Pole Count

Increasing the motor pole count, p, may lead to significant motor mass and rotor inertia reduction. On the other hand, the motor electrical speed, f_e, is proportional to the number of poles, p, (see Eq. (3.24)), which suggests that motors with high number of poles may suffer from excessive core losses (see Eq. (3.23)). This section discusses this design trade-off from a practical perspective to motivate advantageous high torque density motor designs.

Similar to the previous section, consider the effect of increasing the number of poles p, while the motor inner and outer diameters, d_{in} and d_{out}, are preserved (see Fig.3.6), and the magnet grade, thickness and air gap remain the same. Following the assumptions of Sec. 3.3.3, increasing the pole count, p, causes proportional decrease of the magnets width, w_m. Smaller magnets require thinner rotor yoke so that the flux density levels in the yoke remain the same as suggested by the flux density distribution in Fig. 3.7 . Therefore, the rotor yoke mass and inertia proportionately decrease with increasing pole count, p. The magnet mass remains the same as the total amount of magnet material is not reduced provided the air gap thickness is preserved. Then, for a given motor size and magnet thickness, increasing the pole count beyond some threshold value is expected to have limited effect on the rotor mass and inertia.

The teeth width, w_t, and teeth tip thickness, t_{tip}, and width ,w_{tip}, are determined by the magnet width as discussed in Sec. 3.3.3. Therefore, these variables are proportionately decreased with increasing pole count. Thinner teeth require thinner stator yoke so that the flux density levels in the yoke are the same. The total

teeth mass remains approximately the same provided the teeth length is unaltered. However, the yoke mass is proportionately decreased with an increasing number of poles. The thinner stator yoke and tooth tips also lead to higher slot area (Eq. (3.6)), and thus, lower slot resistance (Eq. (3.7)). Therefore, increasing the motor pole count may lead to significant torque density increase.

The mass of the stator usually comprises a major part of the total motor weight. To demonstrate the effect of the pole count increase on the stator mass, consider an outer rotor motor construction with 14 poles that has 25% of its stator mass contributed to the teeth. Such weight distribution would be typical for low pole count motors. Fig. 3.8 show the stator mass reduction associated with increasing the motor pole count, p. The figure suggests that increasing the motor pole count beyond a threshold value leads to small mass reduction in a diminishing returns fashion. Further advantages of increasing the pole count are related to the resulting thinner teeth tips and stator yoke which improves the motor compactness, and shorter windings end turns which also improves the motor axial length and reduces the motor resistance.

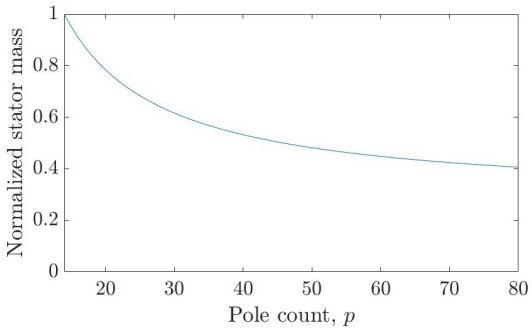

Figure 3.8: Plot of normalized motor stator mass against pole count.

Increasing the motor pole count, however, leads to core loss increase. Eq. (3.23) and Eq. (3.24) suggest that the core loss components scale by:

$$P_h \propto p \qquad P_e \propto p^2 \qquad P_a \propto p^{1.5} \tag{3.30}$$

provided consistent flux density levels are achieved by all designs. The AC component of the copper loss also scales quadratically with the electrical frequency as shown in [42]. Thus, increasing the number of poles may significantly deteriorates the core and copper losses. However, under the assumption that the stator yoke is thick enough so that the majority of the core losses are generated in the teeth, high efficiency motor designs with high pole count are still possible.

For example, consider a $q = 12$ slot, $p = 14$ pole motor that operates at 95% efficiency at a given angular velocity with equal core and copper loss contributions to the total loss. Eq. (3.30) suggests that if the motor poles are increased to $p = 28$, the motor efficiency at the same speed and load would be at least 90%. However, Fig.

3.8 suggests that the motor with $p = 28$ poles has almost 40% lower mass than the $p = 14$ pole motor. Thus, depending on the application the $p = 28$ pole motor may have considerable performance advantages as discussed in Sec. 3.2. Furthermore, reducing the teeth length leads to proportional reduction in the motor core loss which may be used as means to balance the copper and core loss contributions to the total loss in order to maximize the motor performance.

3.4.4 Torque and Torque Density Dependence on the Shape of the Teeth

As described in Sec. 3.3.3, the width of the teeth is chosen so that the flux density in the teeth is in the range of $1.6T$ to $1.8T$. The function of the tooth tip is to realize consistent air gap thickness along the magnet width and concentrate the flux in the tooth to the desired flux density level as shown in Fig. 3.7. The air gap flux depends on the magnet thickness, width, strength, etc. As shown in Sec. 3.5.1, magnet flux leakage limits the maximum air gap flux density that may be realized. Thus, there is a practical limit to the maximum flux in the teeth in the case of surface mount permanent magnets. However, higher air gap flux density may be achieved by flux concentration in some interior permanent magnet (IPM) rotor designs [54, 75]. Therefore, the analysis of this section assumes the desired flux density levels may be achieved for arbitrary width of the teeth. The objective of this section is to investigate how the width of the teeth affects the torque and torque density under these assumptions. Thus, the analysis also implicitly provides insight into how the magnet shape and strength affect the motor performance.

Combining, Eq. (3.7), Eq. (3.10) and Eq. (3.12) leads to:

$$\begin{aligned} T_s \propto \frac{w_t}{\sqrt{R_s}} \propto w_t\sqrt{A_{slot}} \propto w_t\sqrt{A_{tot} - l_t w_t}, \\ A_{tot} = \frac{\pi}{q}\Big(\big(\frac{d_{out}}{2} - t_{tip}\big)^2 - \big(\frac{d_{in}}{2} - y_s\big)^2\Big), \\ l_t = \big(\frac{d_{out}}{2} - t_{tip} - \frac{d_{in}}{2} - y_s\big) \end{aligned} \tag{3.31}$$

where A_{tot} is the combined area of the a slot and a tooth (the region, enclosed by the yellow contour in Fig. 3.9). Then, $\frac{dT_s}{dw_t} = \frac{2A_{tot} - 3l_t w_t}{2\sqrt{A_{tot} - l_t w_t}}$ and $\frac{dT_s}{dw_t} \geq 0$ provided $k_{area} = l_t w_t \leq \frac{2}{3}A_{tot}$, where k_{area} is the ratio of the tooth body area to slot area. Therefore, the maximum torque is achieved when the area of the tooth body is approximately twice the area of the slot.

However, in order to preserve the desired flux density levels, teeth with wider body require thicker stator yoke which both lead to mass increase as the mass density of

the slots is much lower than the mass density of the teeth and the yoke (due to the lower copper fill factor). Therefore, it is beneficial to consider how the motor torque density is affected by varying the width of the teeth.

As discussed in Sec. 3.3.3 and visualized in Fig. 3.7, the rotor yoke thickness, tooth tip width, tooth body width and stator yoke are all proportional to the magnet width so that the prescribed flux density levels in these regions may be realized. Let k_{fe} be the ratio of the combined mass of the rotor, the stator teeth and yoke, to the mass of the body of the teeth. Typically, k_{fe} is in the range $k_{fe} = [2, 5]$, although higher values are possible for low performance designs. Then, with the aid of Fig. 3.9 and Eq. (3.7), the motor mass may be approximated as:

$$M_m \approx q\Big(\underbrace{k_{cu}\rho_{cu}(A_{tot} - w_t l_t)}_{\text{mass of windings}} + \underbrace{k_{fe}\rho_{fe} w_t l_t}_{\text{mass of steel and magnets}} \Big), \tag{3.32}$$

therefore,

$$M_m \propto k_{cu}\rho_{cu}A_{slot} + (k_{fe}\rho_{fe} - k_{cu}\rho_{cu})k_{area}$$

where $k_{cu} = (k_c \frac{2\pi r_w}{l_m q} + 1)c_f$, and ρ_{fe} and ρ_{cu} are the densities of electrical steel and copper, respectively.

The coefficient k_{cu} takes into account the mass of the winding end turns and the slot copper fill factor. For the practical designs considered in this chapter, k_{cu} is in the range $k_{cu} = [0.3, 1.0]$. The lower values correspond to motors with low slot fill factor, high number of poles and high out-of-plane relative thickness. The higher range of values correspond to motors with high slot fill factor, low number of poles and low relative out-of-plane thickness. The motor torque density is then:

$$T_\rho \propto \frac{k_{area}\sqrt{1 - k_{area}}}{k_{cu}\rho_{cu} + (k_{fe}\rho_{fe} - k_{cu}\rho_{cu})k_{area}} \tag{3.33}$$

Fig. 3.10 shows plots of normalized torque against k_{area} for different values

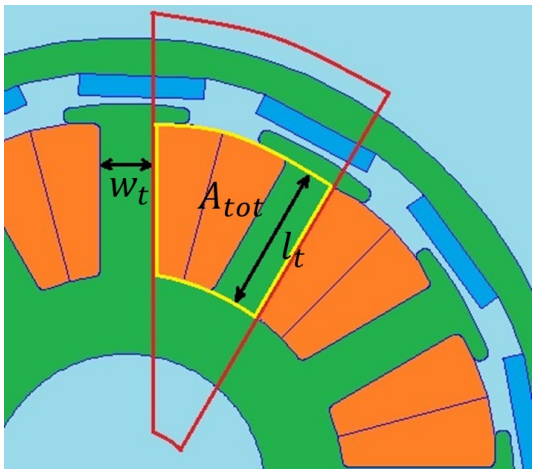

Figure 3.9: Motor structure. The combined area of a slot and a tooth body is enclosed in the yellow contour. The combined weight of the magnet and steel material enclosed by the red contour scales proportionally to the weight of the tooth body.

of k_{fe} and k_{cu}. The plots suggest that motors with low k_{fe} benefit from having stator teeth with wider bodies. Such motors usually have higher number of poles and thinner stator yoke. On the other hand, motors with higher values of k_{cu}, also benefit from having stator teeth with wider body. However, these usually have low number of slots, and thus, it is not readily possible to design motors with high value of k_{cu} and low value of k_{fe} at the same time. Therefore, for most practical motor designs the highest torque density would be achieved for k_{area} in the range $0.3-0.4$, which may be readily realized with high strength surface mount rare earth magnets and deep enough slots.

As discussed before, some IPM rotors designs lead to air gap flux density increase through flux concentration. The plots of Fig. 3.10 suggest that these may be used to achieve higher torque density with shallow slots, and thus, compact stator design. Furthermore, the analysis earlier in this section suggests that these also could have higher torque. However, in order to achieve flux concentration, the magnets in IPM rotors need to be radially oriented rather than circumferentially oriented as in SMPM rotors. The increased thickness and mass of such IPM rotor leads to increased motor outer diameter and output inertia. Therefore, IPM motors are not expected to practically have significant torque and torque density advantages. To this end, the performance of an IPM motor is compared to the performance of a SMPM motor of same outer diameter in Sec. 3.5.4.

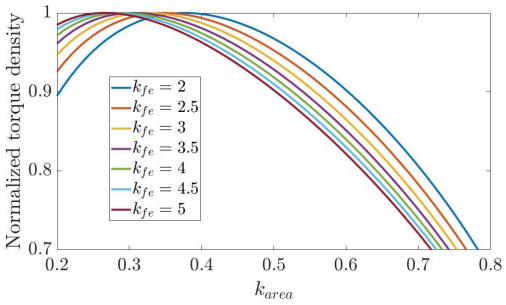

(a) $k_{cu} = 0.4$

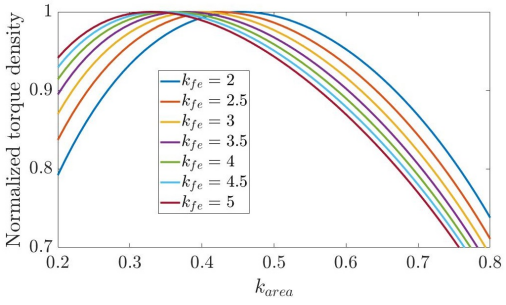

(b) $k_{cu} = 0.7$

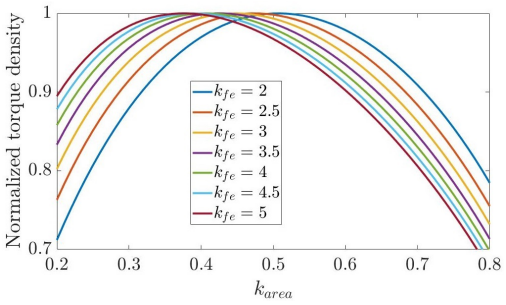

(c) $k_{cu} = 1.0$

Figure 3.10: Plots of normalized motor torque against k_{area} for different values of k_{fe} and k_{cu}

From a practical point of view, the analysis of this section suggests that the slot depth and teeth size may be optimized using the model of Sec. 3.3.3 and iterative FEA for maxim torque density given motor design

constraints.

3.4.5 Application Specific Design Guidelines

The motor performance trade-off analysis that was summarized above, motivates the following general application specific design guidelines:

- For applications that are not weight sensitive such as EVs, motors with lower pole count and deeper teeth are preferred because:
  - They deliver higher torque for the same air gap diameter and stator axial length. Thus, they require less electrical steel for their construction.
  - They have low core and AC copper loss, and thus, are efficient at all speed and load duty cycles.
  - They have higher inductance and may be driven with cheaper and less sophisticated off-the-shelf electronics due to the low electrical frequency.
- For applications that are weight sensitive and require operation at high load and speed duty cycles such as drones, motors with higher pole count and shallower teeth are preferred because:
  - They have significantly higher torque densities with good efficiency which offsets the required higher driver complexity and cost due to the high electrical frequency.
  - They have higher compactness at the cost of higher slot current density due to the lower slot area. The increased void space in the stator may be used for bearings, sensors, etc.
- For application that are weight sensitive but operate at low to high load and low speed duty cycles such as robotics (see Sec. 3.2), motors with higher pole count are preferred because:
  - They have significantly higher torque densities which offsets the higher driver complexity and cost.
  - When packaging and compactness are crucial and higher torque with lower air gap diameter is preferred, deeper slots may be used as the core loss and AC copper loss contributions over a cycle may be quite limited.
  - Shallower slots may be used so that space is available in the motor interior for motor bearings, sensors, brake, etc.

3.4.6 Motor Design Performance Metrics

The discussion in this section suggests the following application specific performance metrics:

- EVs:
  - Core loss at maximum rated speed and no load. The core losses in the stator are primarily due to the motion of the permanent magnets and the armature reaction contribution to the losses is, generally, low. The motor *idle* current is, generally, a good measure of the motor core loss.
  - Rated torque according to Eq. (3.12).
- Drones:
  - Rated torque according to Eq. (3.12).
  - Corresponding torque density.
  - Efficiency at rated speed and rated torque.
- Robotics:
  - Rated torque according to Eq. (3.12).
  - Corresponding torque density.
  - Cogging torque. In dynamic applications where backdrivability is important, the motor cogging torque may be a major design factor.

3.5 Verification of the Analytic Model and Design Approach

This section provides verification of the analytic results of Sec. 3.3.3. First, Sec. 3.5.1 verifies one of the major flux linkage model assumptions related to how the flux in the teeth varies when the rotor magnets width is varied. Next, Sec. 3.5.2 demonstrates the effectiveness of the slot factor in determining the motor that produces the highest torque among all motors of same dimensions and number of poles. Next, Sec. 3.5.3 discussed the trade-offs, characteristic of motor designs with high pole count. The design guidelines of Sec. 3.3.3 are also verified. Sec. 3.5.4 compares the performance of an IPM motor and a SMPM motor that have the same other diameter, in order to demonstrate that IPM motors do not have significant advantages in terms of torque density.

For all motor designs, $M15$ electrical steel laminated stators and rotors are assumed. The corresponding lamination factor is $c_l = 0.95$, which is standard for .35mm thick lamination sheets. For the windings, AWG 24 magnet wire with slot fill factor, $c_f = 0.32$, is assumed and NdFeB magnets are assumed.

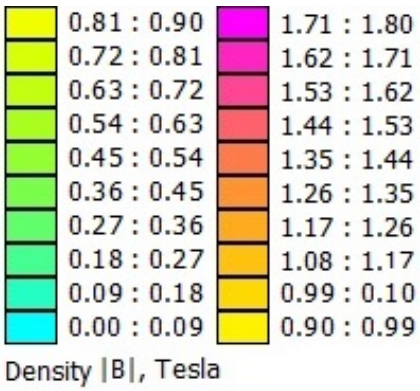

Figure 3.11: Colour bar of magnetic flux density for all FEA simulations in this chapter.

The 2D electro-magnetic FEA analysis results of this section are generated with FEMM software [86]. The generic motor geometry of Fig. 3.6 is coded to allow rapid and parallelizable analysis. Fig. 3.11 shows the magnetic flux density colour bar corresponding to all electro-magnetic FEA simulations.

3.5.1 Magnet Width Effect on Motor Torque

This section uses electro-magnetic FEA to show how varying the magnet width affects the motor phase bEMF. In the literature, it is often suggested that the motor torque and bEMF are proportional to the total air gap flux. However, in the case of outrunner motors, magnet flux leakage may lead to increased torque ripple and even reduced torque when the magnet width approaches the pole pitch.

Eq. (3.2) is valid only if the flux linkage of the windings around each of the teeth is approximately sinusoidal. Otherwise, the bEMF phase voltage waveform would be distorted. When the motor is driven with three phase balanced sinusoidal currents, useful torque is produced only by the synchronous (or fundamental) frequency

harmonic of the bEMF phase voltage [42, 80]. The higher order harmonics produce torque ripple and their amplitude should be minimized.

To see how the magnet width affects the motor performance, a motor with $p = 20$ poles, $q = 18$ slots and stator outside diameter of $d_{out} = 90mm$ is considered. The air gap is set to $a_g = 0.5mm$, and the magnet thickness is $t_m = 2mm$. First, the magnet width and tooth tip width are varied while the width of the teeth and yoke of both the stator and rotor are constant and large enough so no saturation occurs even for the widest considered pole magnets. Thus, the effect of increasing the magnet width beyond 120 electrical degrees may be observed and analyzed.

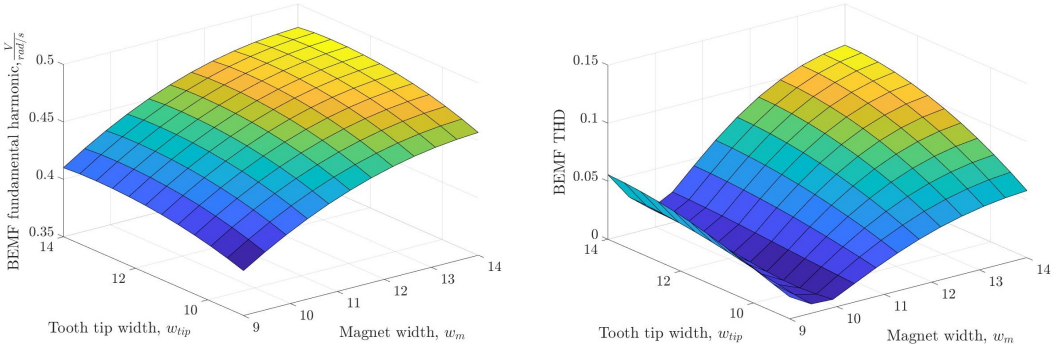

Figure 3.12: Amplitude of the fundamental frequency (on left) and THD (on right) of the motor phase bEMF for a range of values for the magnet width, w_m, and tooth tip width, w_{tip}, both in mm.

Fig. 3.12 shows plots of the magnitude of the fundamental frequency harmonic and total harmonic distortion (THD) of the bEMF phase voltage for a range of values for the magnet width and tooth tip width. The plots show that increasing the

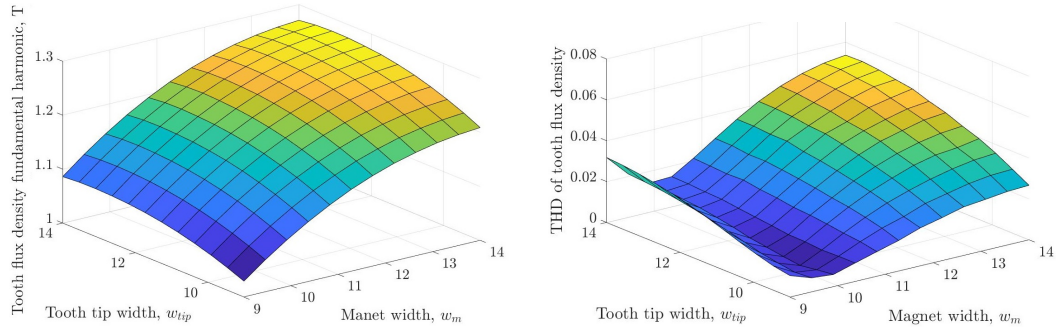

Figure 3.13: Amplitude of the fundamental frequency (on left) and THD (on right) of the flux density in the center of a motor stator tooth for a range of values for the magnet width, w_m, and tooth tip width, w_{tip}, both in mm.

magnet width beyond 120 electrical degrees (which in this case corresponds magnet width of around $w_m = 9.4mm$) leads to an increase in the amplitude of the bEMF fundamental frequency with rapidly decreasing rate. The increased flux leakage

between adjacent magnets, when their width increases and the gap between them decreases, limits the maximum flux density in the stator teeth as shown in the plot of the amplitude of the fundamental frequency harmonic of the flux density in center of the tooth in Fig. 3.13.

Fig. 3.12 shows that the bEMF THD is minimized for magnet width of around 120 electrical degrees. The correlation between the THD plots in Fig. 3.12 and Fig. 3.13 suggests that an increase of the flux density THD is responsible for the increased bEMF THD characteristic of the motors with wider magnets. The

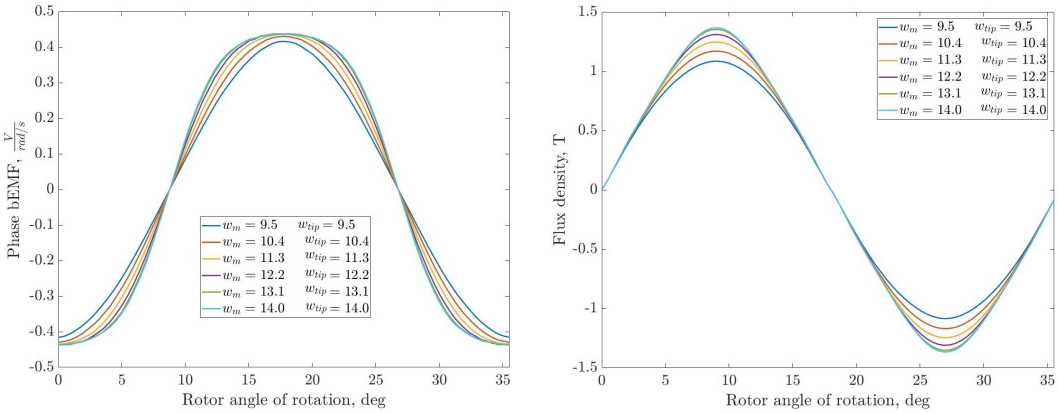

Figure 3.14: Motor phase bEMF (on left) and tooth flux density (on right) for a range of values for the magnet width, w_m, and tooth tip width, w_{tip}, both in mm.

plots in Fig. 3.14 show that the maximum flux density at the center of the teeth increases with increasing magnet width and tooth tip width, however, the distorted flux density waveforms result into increasingly trapezoidal bEMF when the effects of the individual phase windings are superimposed. From the equivalence between the torque and bEMF constants, it may then be concluded that for three phase balanced sinusoidal currents driving, increased bEMF THD causes increased torque ripple, and thus, should be avoided.

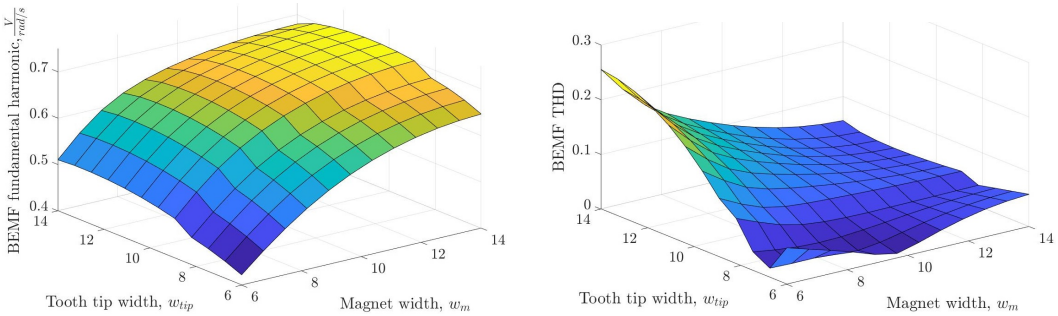

Figure 3.15: Amplitude of the fundamental frequency (on left) and THD (on right) of the motor phase bEMF for a range of values for the magnet width, w_m, and tooth tip width, w_{tip}, both in mm. The body width of the teeth is chosen such that saturation occurs.

It is also beneficial to consider the effect of varying the magnet width and tooth tip width when the tooth body width is such that saturation occurs when the magnet width is increased beyond 120 electrical degrees. Fig. 3.15 shows plots of the amplitude of the fundamental frequency harmonic and total harmonic distortion (THD) of the bEMF phase voltage for this case. The plots show that reducing the magnet width below 120 electrical degrees leads to rapid reduction of the phase bEMF constant and increase in the bEMF THD. On the other hand,

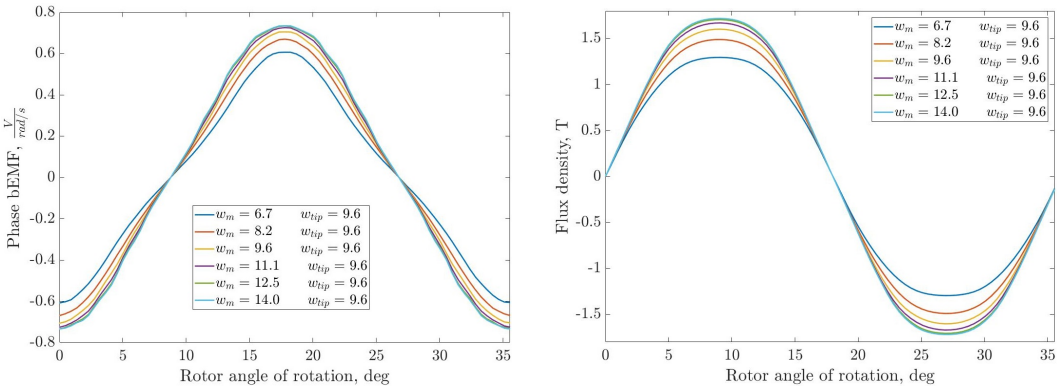

Figure 3.16: Motor phase bEMF (on left) and tooth flux density (on right) for a range of values for the magnet width, w_m, and representative tooth tip width, both in *mm*. The body width is chosen such that saturation occurs.

due to the fact that saturation occurs, the bEMF THD is low when the magnet width is increased beyond 120 electrical degrees. The effect of saturation on the phase bEMF waveform and tooth flux density may be observed in Fig. 3.16. Fig. 3.15 and Fig. 3.16 suggest that approximately sinusoidal bEMF with low THD may be achieved in motors with full pitched magnets with no gap between them. Even though, such motors would have heavy rotors with large inertia, they may be advantageous because of their simplified rotor manufacturing and assembly, and their lower cogging torque [57] due to the improved interaction between the magnet edges and the slots.

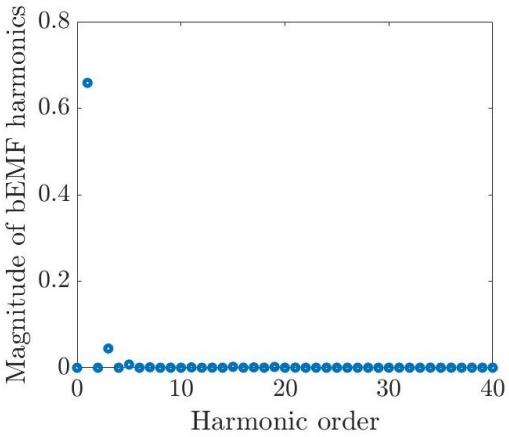

Figure 3.17: Plot of phase bEMF harmonic content of the motor design corresponding to the yellow curves in the plots of Fig. 3.15.

Finally, the yellow curves in the plots of Fig. 3.16 correspond to a motor design

with magnet width of 120 electrical degree and tooth tip width equal to the magnet width. The bEMF harmonic content and FEA simulation of this design are shown in Fig 3.18i and Fig. 3.17,respectively. The motor features quite sinusoidal bEMF with a low amplitude third harmonic. Thus, this motor has advantages in its better torque production, lower mass, lower inertia and lower amount of magnet material used compared to the other motor designs.

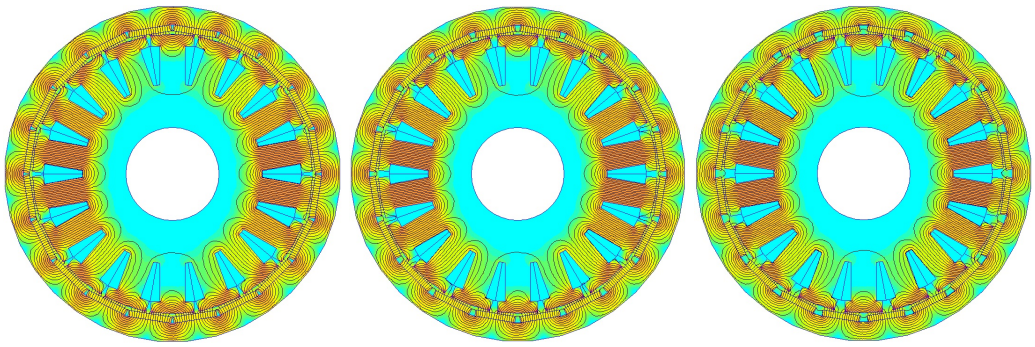

(a) $w_m = 14$, $w_{tip} = 14$ (b) $w_m = 13.1$, $w_{tip} = 13.1$ (c) $w_m = 12.2$, $w_{tip} = 12.2$

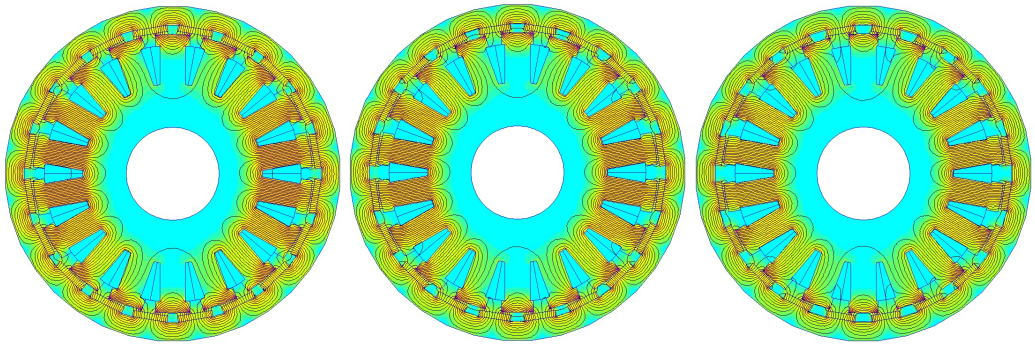

(d) $w_m = 11.3$, $w_{tip} = 11,3$ (e) $w_m = 10.4$, $w_{tip} = 10.4$ (f) $w_m = 9.6$, $w_{tip} = 9.6$

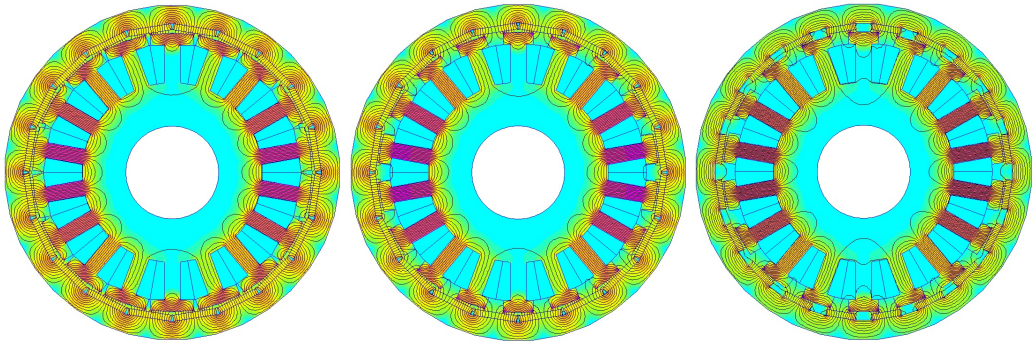

(g) $w_m = 14$, $w_{tip} = 14$ (h) $w_m = 14$, $w_{tip} = 9.6$ (i) $w_m = 9.6$, $w_{tip} = 9.6$

Figure 3.18: FEA simulations, showing the flux density levels in the motor for different values for the magnet width, w_m, and tooth tip width, w_{tip}, both in mm.

Fig. 3.18 shows electro-magnetic FEA simulations of the flux density in some of

the motor designs used in generating the plots of this section. The phase bEMF of these motor designs are shown in Fig. 3.14 and Fig.3.16. One can clearly observe how the flux leakage limits the flux density in the teeth regardless of the magnet width: despite the different magnet widths, the motors in Fig. 3.18a, Fig. 3.18b, Fig. 3.18c, Fig. 3.18d and Fig. 3.18e have almost the same flux density levels in the teeth of their stators. The increased flux density in the rotors of motors with wider magnets suggests that these motors require thicker yoke, and thus, would have significantly higher inertia when optimized.

3.5.2 Slot Factor Analysis Verification

In Sec. 3.4.1, it is shown that the slot factor $C_q(q)$ (see Eq. (3.28)) may be used to rapidly compare the rated torque, T_s, (see Eq. (3.12)) of possible motor designs that have the same pole count, main dimensions, teeth shape and size, slot copper fill factor, etc. Furthermore, the analysis suggests that motors with lower number of teeth (higher symmetry) may have torque and core loss advantages.

Property or dimension	Low q motor	High q motor
Rated power loss at stall, P_{cu}	$100W$	$100W$
Number of poles, p	28	28
Number of slots, q	24	30
Slots per pole, per phase, Q_{pp}	0.286	0.357
Winding factor, C_w [48, 49]	0.933	0.951
Slot factor, $C_q(q)$	4.9	4.5
$C_w\sqrt{C_q(q)}$	2.065	2.017
Rated torque, T_s	5.56Nm	5.44Nm
Active total mass	$593g$	$607g$
Torque density	$9.37\frac{Nm}{Kg}$	$8.97\frac{Nm}{Kg}$

Table 3.1: Characteristics of two motors that have the same number of poles, $p = 28$, and main dimensions but different number of slots.

This section provides verification of the analytic slot factor results (Sec. 3.4.1) by first considering two motors that have inner and outer stator diameters given by $d_{in} = 50mm$ and $d_{out} = 90mm$, respectively and same number of poles, $p = 28$, but different number of slots. One of the motors has $q = 24 < p$ slots and the other has $q = 30 > p$ slots. For both motors, the air gap is set to $a_g = 0.5mm$, and the magnet width and thickness are given by $w_m = 7.25mm$ and $t_m = 2mm$, respectively. Table 3.1 summarizes the characteristics of the two motor designs and Fig. 3.19 displays

FEA simulations of the two motors that show the flux densities in the various parts of the motors. The motor rated torque in Table 3.1 corresponds to the average torque produced by the motor over a complete electrical rotation at $P_{cu} = 100W$ copper loss.

The values for the slot factor $C_q(q)$ and the values for $C_w\sqrt{C_q(q)}$ of the two motors suggest that the motor with $q = 24$ slots would delivers more torque than the motor with $q = 30$ slots even though the motor with $q = 24$ slots has lower winding factor. The FEA simulation results confirm this prediction. The motor with $q = 24$ slots also has slightly lower mass, and thus, better torque density as predicted by the slot analysis of Sec. 3.4.1.

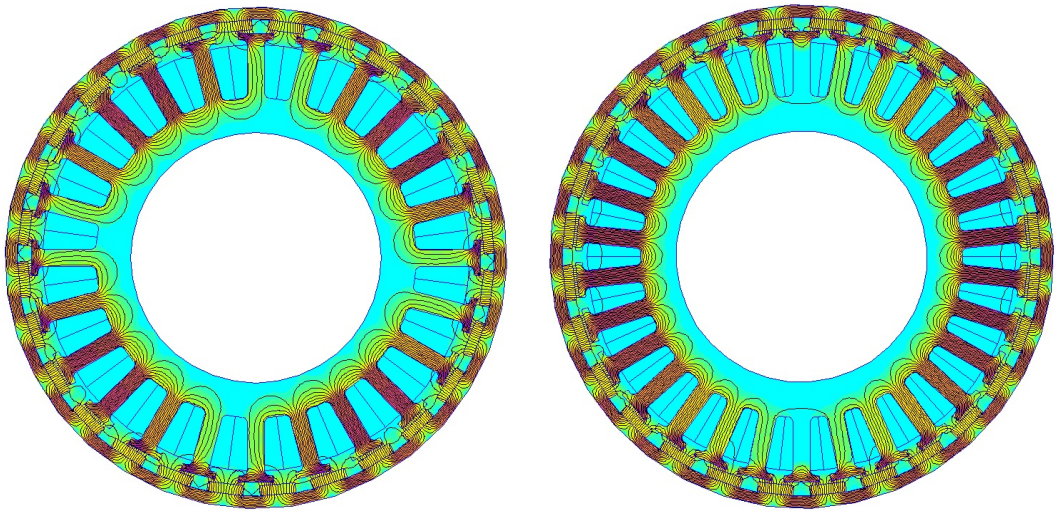

Figure 3.19: Electro-Magnetic FEA simulation of the two motors of Table 3.1. The motor with $q = 24$ slots is shown on the left and the motor with $q = 30$ slots is shown on the right.

The lower winding factor for the motor with $q = 24$ slots is due to the higher symmetry of this design ($k_s = 2$ in Eq. (3.1)) compared to the motor with $q = 30$ slots ($k_s = 1$ in Eq. (3.1)). The symmetry differences are evident in the flux density distributions of Fig. 3.19. The teeth comprising a phase are concentrated in two regions for the motor with $q = 30$ slots and in four regions for the motor with $q = 24$ slots. Consequently, the motor with $q = 24$ may have more parallel circuits. On the other hand, due to the higher number of teeth, the motor with $q = 30$ would have shorter winding end turns and shorter axial length and lower cogging torque due to the minimum symmetry.

Fig. 3.20 slows a plot of the flux density at the center of a stator tooth for both motors for a complete electrical cycle of 360 electrical degrees. As can be observed from

the plot, the flux densities in the teeth of the two motors have the same amplitude and very similar shape, therefore, the core loss generated by a single tooth in either motor would be similar for a given rotor speed. Furthermore, Fig. 3.19 suggests that the flux density levels in the stator yoke would also be similar. Therefore, the motor with $q = 24$ slots would have substantially lower (approximately 20%) core loss than the motor with $q = 30$ slots.

For completeness, two motors with high pole count of $p = 56$ that again have the same inner and outer diameters but different number of slots are also considered. Unlike the previous example, however, both motors have $q < p$. Table 3.2 summarizes the characteristics of the two motor designs and Fig. 3.21 displays FEA simulations of the two motors that show the flux densities in the various parts of the motors. The values for the slot factor $C_q(q)$ and the values for

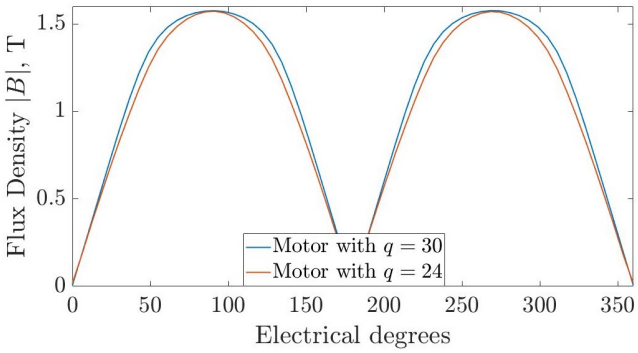

Figure 3.20: Flux density at tooth center for the two motors with $q = 24$ and $q = 30$ slots.

Property or dimension	Low q motor	High q motor
Rated power loss at stall, P_{cu}	$100W$	$100W$
Number of poles, p	56	56
Number of slots, q	48	54
Slots per pole, per phase, Q_{pp}	0.286	0.321
Winding factor, C_w [48, 49]	0.933	0.954
Slot factor, $C_q(q)$	9.57	9.44
$C_w\sqrt{C_q(q)}$	2.89	2.87
Rated torque, T_s	8.57Nm	8.51Nm
Active total mass	$710g$	$713g$
Torque density	$12.06\frac{Nm}{Kg}$	$11.93\frac{Nm}{Kg}$

Table 3.2: Characteristics of two motors that have the same number of poles, $p = 56$, and main dimensions but different number of slots. Flux lines are not shown due to the small stator tooth size.

$C_w\sqrt{C_q(q)}$ successfully predict the torque characteristics of the two motors. In this examples, the two motors have almost identical rated torques and torque densities, however, the motor with lower number of teeth has lower (approximately 12%) core

losses, while the motor with higher number of teeth has lower cogging torque.

In conclusion, this section verifies the slot count analysis of Sec. 3.4.1 and demonstrates a practical design trade-off related to the motor core losses and cogging torque.

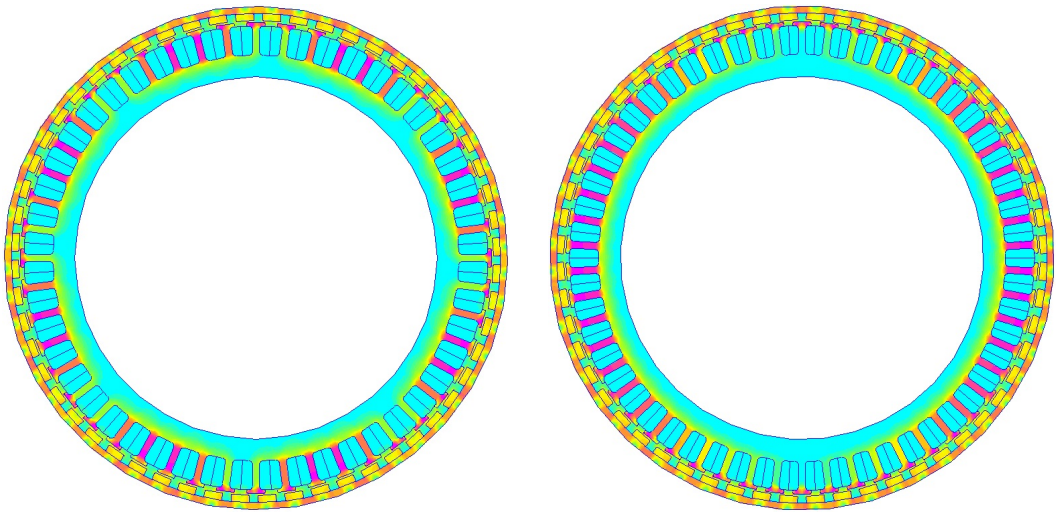

Figure 3.21: Electro-Magnetic FEA simulation of the two motors of Table 3.2. The motor with $q = 48$ slots is shown on the left and the motor with $q = 54$ slots is shown on the right. Flux lines are not shown due to the small size of the teeth.

3.5.3 Design Trade-offs Verification

In Sec.3.4.3, the trade-offs related to high pole count motors are discussed. This section provides electro-magnetic FEA verification that high torque density, high efficiency motors may be achieved, provided high pole count designs are adopted. However, it is shown that magnetic flux leakage limits the motor performance when the number of poles is increased beyond some threshold value.

Similar to the previous sections, different motor designs with the same outer stator diameter, $d_{out} = 100mm$, and magnet width of 120 electrical degrees are considered. All designs also feature the same magnet thickness and air gap thickness, and therefore, the same amount of permanent magnet material. Using FEA, the torque, torque density and efficiency of the motor designs with pole-slot configurations given by Eq. (3.1) are estimated, while the pole count, p, and stator inner diameter, d_{in}, are varied.

Core losses are estimated by:

- recording the flux values in all FEA mesh elements in the iron components for a range of values of the rotor rotational angle.
- finding the flux frequency content in these elements using FFT.
- adding the contributions of the flux harmonics in these elements to the total core loss contributions according to the frequency domain loss approach of [62, 66]. The values for the loss coefficients, K_h, K_e and K_a of Eq. (3.23) are taken from [62].

Magnet eddy current losses are estimated following the approach of [70]. AC copper losses are estimated following the approach of [42]. Rated torque is defined in terms of $P_{cu} = 100W$ power loss at stall. The rated motor speed is $4000RPM$.

Fig. 3.22 shows the FEA simulation results. Fig. 3.22a and Fig. 3.22c show that increasing the motor pole count, p, up to a threshold value that depends on the motor inner diameter leads to motor torque and torque density increase, however, increasing p beyond this threshold leads to a torque and torque density decrease. The model of Sec. 3.3.3 fails to predict this torque reduction due to the fact that magnetic flux leakage is ignored. The two main sources of flux leakage are:

- between the magnets, and between the magnets and the stator teeth. This leakage increases with increasing p while the stator outer diameter is preserved, because the distance between the magnets decreases relative to the magnet and air gap thicknesses, and leads to reduction of the total magnet air gap flux, and thus, also leads to reduction of the flux density in the teeth (see Fig. 3.22b).
- between the bodies of the teeth. As p increases while the stator inner diameter is preserved, the distance between the teeth decreases and the magnet leakage out of the teeth bodies increases which leads to decreasing flux density in the teeth towards the stator yoke. This tooth flux decrease can be clearly observed in Fig. 3.22b which shows the magnetic flux distribution in a motor design with high pole count and deep slots. While tooth body flux leakage occurs in all motors, when p is low, the distance between the teeth is large and the flux reduction along the stator teeth is limited (around 4% near the stator yoke for the motor in Fig. 3.22d)

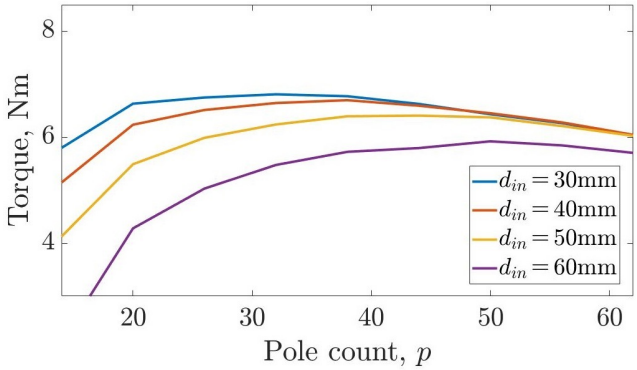

(a) Torque plot.

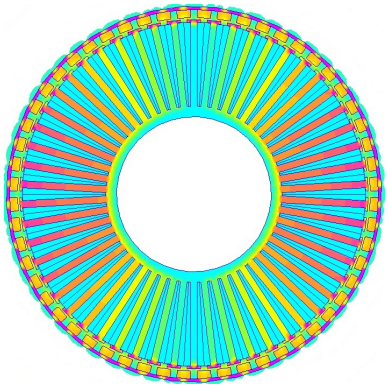

(b) p = 62, q = 60, d_{in} = 40mm.

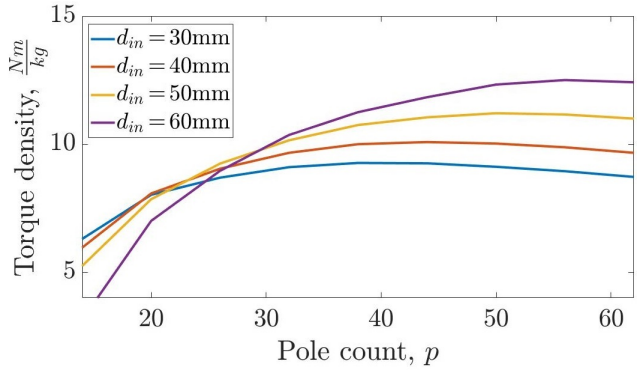

(c) Torque density plot.

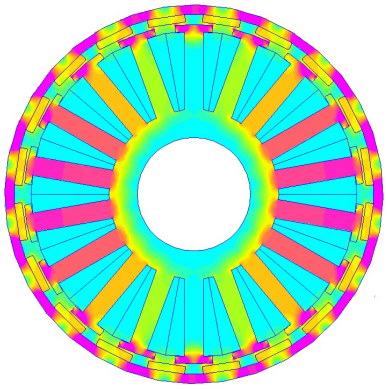

(d) p = 20, q = 18, d_{in} = 30mm.

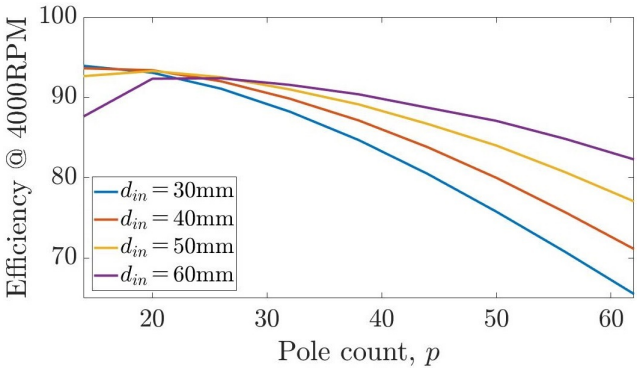

(e) Efficiency plot.

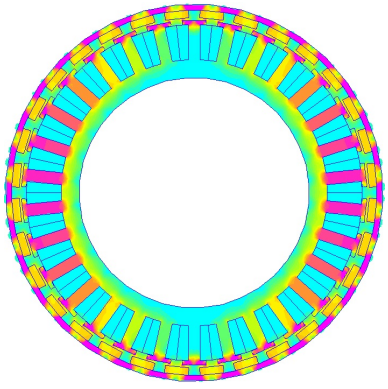

(f) p = 38, q = 36, d_{in} = 60mm.

Figure 3.22: FEA simulation results comparing motors that have the same stator outer diameter. The plots on the left show how the number of poles affects the motor torque, torque density and efficiency for different stator inner diameters. The figures on the right show the flux density distribution in representative motor designs.

The torque density plot in Fig. 3.22c and the efficiency plot in Fig. 3.22e show that high torque density, high efficiency motor designs are possible even with high number of poles, provided the slot depth is reduced so that the tooth flux leakage is limited. An example of such motor design is shown in Fig. 3.22f. It has mass of $0.509Kg$ and rated torque of $5.72Nm$ at $P_{cu} = 100W$, and thus, has torque density of $11.25\frac{Nm}{Kg}$.

At rated speed of $4000RPM$ and rated torque, the motor efficiency is 91.2%. Fig. 3.23 shows a plot of the motor losses as a function of the motor speed. As may be observed from the plot, at rated speed around 50% of the total losses may be attributed to core losses. The increase of the copper losses due to proximity and skin effect is also evident at higher speeds. As discussed in Sec. 3.4.2 and Sec. 3.3.3, the magnet and rotor core losses are quite low as the rotor is laminated and the stator armature reaction of motors with high pole count is small.

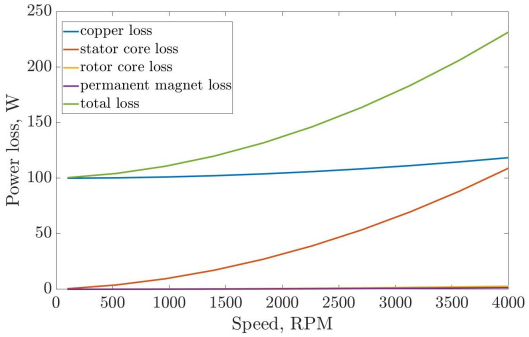

Figure 3.23: Motor losses as a function of motor speed for the design of Fig. 3.22f.

Fig. 3.24 shows how the motor inductance varies with increasing pole count. It may be observed that the motor inductance converges to a given value which corresponds to the leakage inductance. Furthermore, increasing the stator inner diameter leads to a decrease of the length of the stator teeth which causes reduction of the leakage inductance. Therefore, the FEA simulation results confirm the phase inductance analysis of high pole count motors in Sec. 3.4.2.

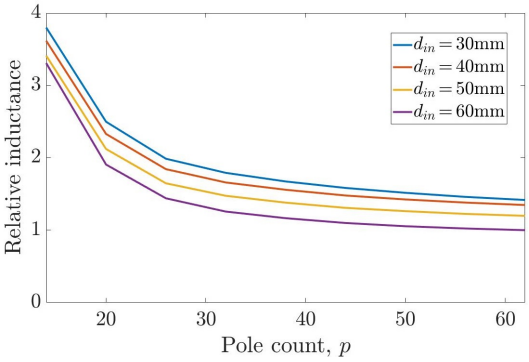

Figure 3.24: Motor normalized inductance as a function of the pole count for different values of the motor inner diameter.

3.5.4 FEA Comparison of SMPM and IPM Motors

This section uses FEA to compare the performance of an IPM motor and a SMPM motor that have the same outer diameter, and number of poles and slots. The slot depth of both motors is FEA optimized for highest torque density following the approach of Sec. 3.4.4. Table 3.3.3 summarizes the characteristics of the two motors and Fig. 3.25 shows FEA simulations of the flux density distribution in the motors.

Property or dimension	SMPM	IPM
Rated power loss at stall, P_{cu}	$100W$	$100W$
Number of poles, p	32	32
Number of slots, q	30	30
Rated torque, T_s	$11.16Nm$	$11.01Nm$
Active total mass	$1044g$	$1048g$
Torque density	$10.69\frac{Nm}{Kg}$	$10.50\frac{Nm}{Kg}$
Stator mass	$799g$	$707g$
Rotor mass	$245g$	$341g$
Rotor inertia	$0.0011\frac{Kg}{m^3}$	$0.0014\frac{Kg}{m^3}$

Table 3.3: Characteristics of a SMPM motor and IPM motors that have the same outside diameter, and pole and slot count. The slot depth of each motor is FEA optimised for maximum torque density (see Sec. 3.3.3).

The two motors have similar performance, even though the air gap diameter of the SMPM motor is higher and the flux levels in the teeth of both motors are identical as can be observed in Fig. 3.25. Furthermore, the mass of the stator of the IPM motor is lower (13%) than the mass of the stator of the SMPM motor. As shown in the tooth width analysis of Sec. 3.4.4, this is due to the fact that the teeth of the IPM motor are wider.

However, the rotor of the IPM motor is significantly (30%) heavier than the rotor of the SMPM motor. As may be observed in Fig. 3.25, the amount of iron used in the rotor of the IPM motors is minimized as much as possible. In fact, physically practical design of the rotor of the IPM motor would be heavier as additional structural support material would be required to constrain the magnets and steel segments. On the other hand, the SMPM motor rotor is significantly easier to manufacture and does not require further structural support apart from epoxy to fix the magnets to the yoke. The reason for the significant difference in the mass of the rotors of the two motors is related to the difference in the flux paths. At most half

of a pole magnet flux passes through the yoke section of the SMPM rotor. On the other hand, in the IPM rotor the flux of two magnets is concentrated in the iron pole segment between them. Therefore, the amount of iron is significantly increased in the IPM rotor, in addition to the increased amount of magnetic material which is required to increase the airgap flux. Furthermore, the magnet leakage in the case of the IPM rotor is also substantially higher as shown in Fig. 3.25.

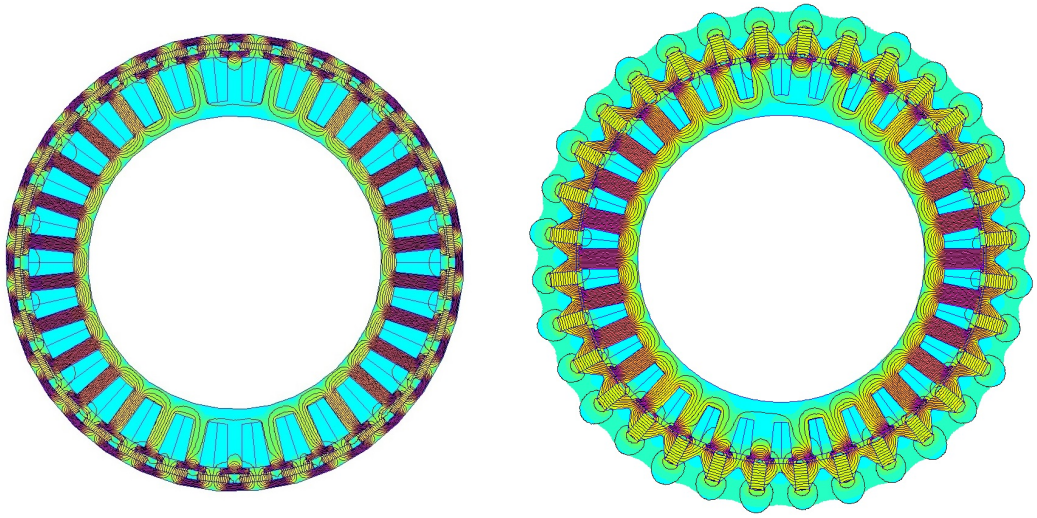

Figure 3.25: Electro-magnetic FEA simulations of a SMPM motor and an IPM motor that have the same outer diameter. The characteristics of the motors are compared in Table 3.3.

In conclusion, the FEA simulations of this section show that the intrinsically higher mass and size of IPM rotors offsets the potential torque advantageous due to the higher possible air gap flux in such motors. In addition, similar torque density levels may be achieved with identically sized SMPM motors that have significantly lighter rotors. Therefore, IPM motors offer no advantageous w.r.t. the design goals and intended applications considered in this thesis.

3.6 Motor Prototypes

This section discusses the design of SMPM motor prototypes according to the approach described in Sec. 3.4. The first set of motors, described in Sec. 3.6.1, is intended for EV applications. A 60 pole motor prototype that has very high torque density and is designed for drone and robotics applications is described in Sec. 3.6.2. The performance of the designed motors is compared to high end off-the-shelf frameless motors in Sec. 3.6.3.

For all motors:

- Neodymium Iron Boron (NdFeB) Magnets are used for the rotor poles.
- 29 gauge M15 electrical steel is used for the rotor and stator lamination.
- laminations were cut using abrasive water jet machining.
- 24 gauge magnet wire used for the windings.
- 6061 aluminum is used for any non-active motor components.

3.6.1 EV Prototypes

This section describes EV brushless dc motor prototypes designed and manufactured in-house. Unlike [60, 61], the motors are not designed for direct drive application, but are intended to be coupled with a gearbox. The maximum desired speed of the motors is set to $4000RPM$. Due to the intended use of the motors, the cogging torque is to be minimized, otherwise, the gearbox amplification of the cogging torque would lead to significantly reduced backdrivability of the actuator.

Early prototypes

The first set of prototypes use the 20 pole - 18 slot motor configuration with $90mm$ outer stator diameter [48, 49]. This configuration is chosen due to its intrinsically low cogging torque and high winding factor. The pole magnet size is $20mm \times 10mm \times 2mm$ with air gap of $0.5mm$. Both motors have no parallel circuits. Fig. 3.26 shows the first prototype. Fig. 3.27 shows the second prototype which has improved compactness as the bearings are installed in the stator interior. The rotor of the second prototype (see Fig. 3.27) has poles consisting of segmented magnets. This leads to substantial reduction of the magnet eddy currents associated with concentrated winding motors [68]. However, circumferential pole segmentation represents a magnetically unstable configuration which leads to manufacturing and

reliability issues. Thus, the intrinsic mechanical stability characteristic of outer rotor motors may not be sufficient and the rotor might require a retaining sleeve.

Figure 3.26: First EV motor prototype.

Figure 3.27: Second EV motor prototype.

Compared to FEA performance predictions, both prototypes exhibit lower bEMF constants (around 10%) and higher resistance (around 8%) due to:

- lower lamination factor caused by burrs at the edges (similar issues with waterjet machined laminations are reported in [87]), inability to achieve uniform pressure, excessive glue build-up, etc.
- longer winding end turns due to irregularity of turns.
- low manufacturing and lamination assembly accuracy.
- excessive varnish (covering the sharp edges on the stator), required to prevent stator phase shorting.

The idle current (measure of no load losses, and thus, very good indication of the core losses) of both motors is around $2.3A$ (around $100W$ of power loss at $44V$) and is somewhat higher that FEA loss predictions shown in Fig. 3.28. This may be caused by reduced resistance between the lamination layers due to the waterjet burrs, which leads to increased eddy currents. Also the measured loss includes friction due to air resistance and the bearings.

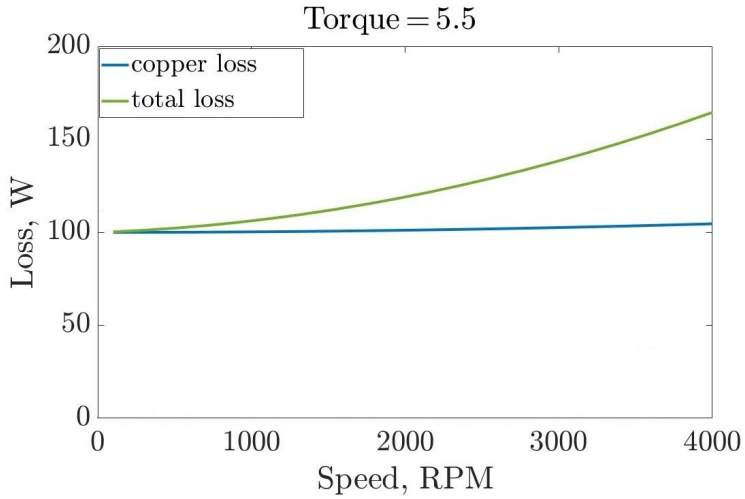

Figure 3.28: Early EV prototype FEA losses prediction as a function of motor speed at load of $5.5Nm$.

Final prototype

In order to improve the motor axial compactness, reduce core loses and increase the motor inductance without deteriorating the torque performance, an alternative motor design is adopted:

- a 14 pole - 12 slot configuration is used to reduce electrical frequency.
- the outer motor diameter is increased and axial length decreased to preserve torque level.
- the motor is FEA optimized to minimize the cogging torque.

Techniques for minimizing the motor cogging torque are presented in [56, 57]. Due to the corresponding manufacturing complexity and performance trade-offs, skewing, variable pole arc width, magnet shifting, notches (auxiliary slots), auxiliary teeth, etc. are not used. Instead the pole pitch and tooth tips width are chosen so that the cogging torque is as small as possible. Due to the fact that no hard motor overall diameter constraints need to be met for the intended application, the pole pitch may be varied while the magnet width is preserved by modifying the stator outside diameter. This approach has the advantage that the tooth width may be determined directly from the magnet width so that the flux in the tooth body is at the desired levels.

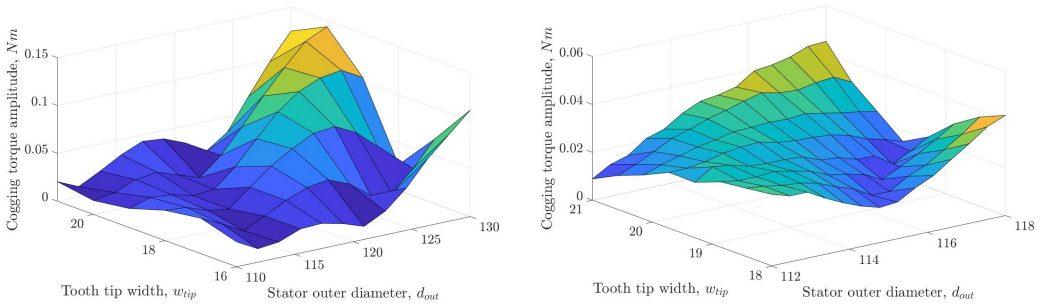

Figure 3.29: Motor cogging torque plots for a range of values for the stator outer diameter, d_{out}, and the tooth tip width, w_{tip}, both in mm. The right plot focuses on a design region of lower cogging torque.

The pole magnets have the following dimension: $3/4in \times 1/2in \times 1/8in$. Fig. 3.29 shows plots of the motor cogging torque as a function of the stator outer diameter and tooth tip width. Consistent regions of minimum cogging torque may be identified in the plots. The higher resolution plot of Fig. 3.29 may be used to select the motor design with lowest cogging torque.

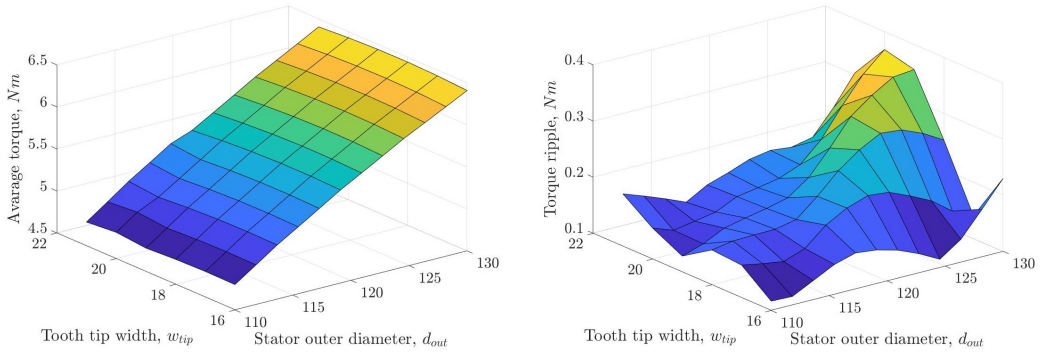

Figure 3.30: Motor average torque (on left) and motor torque ripple (on right) for a range of values for the stator outer diameter, d_{out}, and the tooth tip width, w_{tip}, both in mm.

Fig. 3.30 shows a plot of the motor rated torque (for $P_{cu} = 100W$) and torque ripple as functions of the stator outer diameter and tooth tip width. The torque ripple plot shows that the designs of low cooging torque in Fig. 3.29 also have low torque ripple. The approximately linear torque increase with increasing stator outer diameter that may be observed in the average torque plot of Fig. 3.30 is due to the approximately linear slot area increase. However, as shown in Fig. 3.31, the torque density of the motor actually decreases slightly with increasing stator outer diameter. This is expected, as the total air gap flux is the same for all motors.

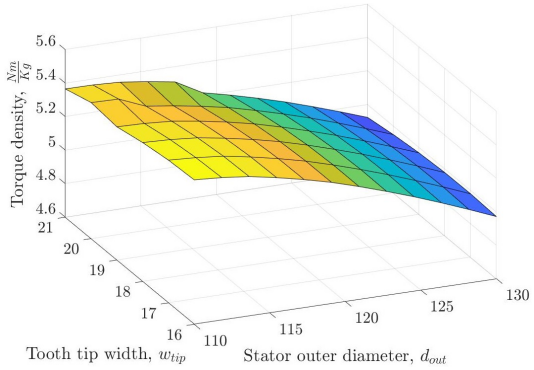

Figure 3.31: Motor torque density for a range of values for the stator outer diameter, d_{out}, and the tooth tip width, w_{tip}, both in mm.

The motor design of minimum cogging torque in Fig. 3.29 is chosen and prototyped. Fig. 3.32 shows photographs of the prototype. Improved lamination, cutting and finishing largely eliminate the practical manufacturing issues of the early EV prototypes, discussed in the previous section. The sheets are glued together to form the lamination first and waterjet cut afterwards. CNC machining is used to chamfer the sharp edges so that lower amount of varnish may be applied.

The prototype's cogging torque is around $.08Nm$ which is low but significantly higher than the FEA prediction. Furthermore, there is significant variation in the magnitude of the cogging torque with the rotor orientation. The discrepancy is

most likely due to manufacturing inaccuracies caused by the light rotor aluminum structure which flexed during machining. The rotors of future prototypes will be designed with improved structural rigidity and accuracy. At speed of approximately 4000 RPM the motor has $1.8A$ no load current which suggests low core loss which is one of the main design objectives. The author believes that a prototype of improved mechanical design and better accuracy on the components would have even lower no load current The resistance is 0.041Ω which is 3% higher compared to the FEA prediction.

Figure 3.32: Final EV motor prototype that uses the 14 pole - 12 slot configuration to improve the motor core losses.

Fig. 3.33 shows comparison of FEA simulation and experimental data for the phase-to-phase bEMF voltage of the motor at approximately $3500RPM$. Due to the tight packaging the neutral point phase connection is not available for oscilloscope measurement. As may be observed from the plot the experimental measurements agrees to around 98% with the FEA prediction. These experimental result confirm the validity of the analytic modeling and FEA simulation of this chapter.

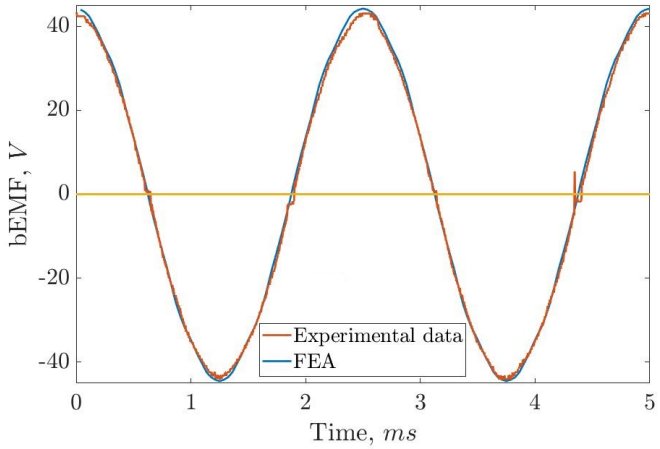

Figure 3.33: Phase-to-phase bEMF voltage wave form for the motor of Fig. 3.32 at $3500RPM$. FEA simulation prediction is compared to measured experimental data.

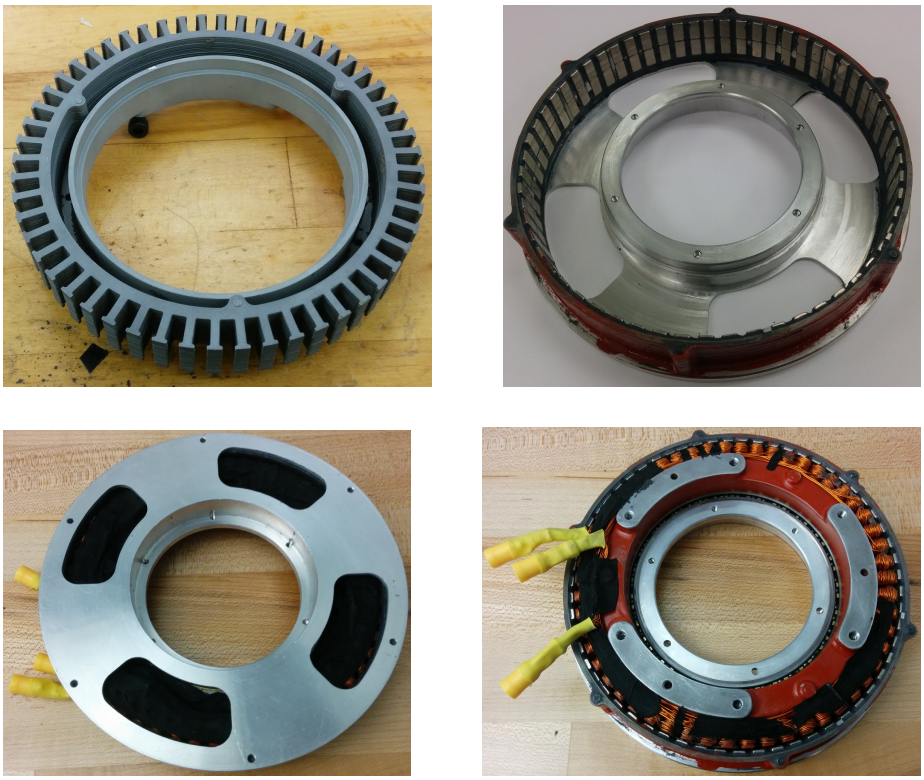

Figure 3.34: Robotics motor prototype that has 60 poles and 54 slots.

3.6.2 Drone/Robotics Prototype

This section describes a robotics/drone brushless dc motor prototypes designed and manufactured in-house. To demonstrate the torque density advantages of high pole count motor designs, the prototype has 60 poles and 54 slots. The stator outer diameter is $142mm$ and the pole size is $20mm \times 5mm \times 2mm$.

Fig. 3.34 shows photographs of the prototype. The prototype was manufactured in a similar fashion to the early EV prototypes of the previous section and also exhibits lower bEMF constants (see Fig. 3.36) and higher resistance (around 8%). The idle current at 2200RPM is around 4.6A with 1.3A due to friction in the assembly. This suggest core loss of around 150W, which is higher than FEA loss prediction shown in Fig. 3.35 for that speed. Similar to Sec. 3.6.1, the increased loss may be caused by reduced resistance between the lamination layers due to the waterjet burrs, which leads to increased eddy currents.

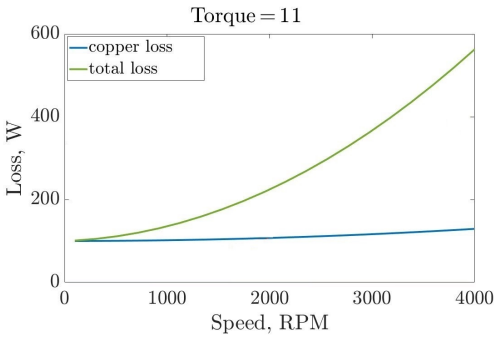

Figure 3.35: Robotics motor prototype FEA losses prediction as a function of motor speed at load of 11Nm.

Fig. 3.36 shows comparison of FEA simulation and experimental data for the phase-to-phase bEMF voltage of the motor at approximately 1000RPM. Due to the tight packaging the neutral point phase connection is not available for oscilloscope measurement. As may be observed from the plot the experimental measurements shows 8% lower bEMF constant than the FEA prediction similar to the early EV prototypes of the previous section.

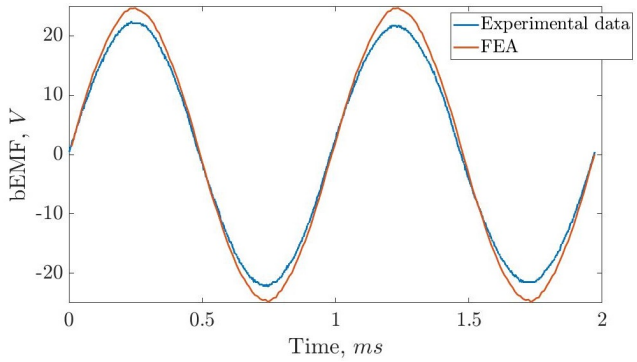

Figure 3.36: Phase-to-phase bEMF voltage wave form for the motor of Fig. 3.34 at 1000RPM. FEA simulation prediction is compared to measured experimental data.

The motor prototype of this section is used as a proof of concept to motivate further development of high pole count motors for robotic applications.

3.6.3 Comparison with Commercially Available Motors

This section shows comparison of the motor prototypes, described in this section, with off-the-shelf high performance frameless motors. To provide a more complete

representation of the available motors, high performance drone motors are also included. In calculating the motor torque density, only the mass of the motor's active components is taken into account (magnets, rotor back iron, stator iron core and windings). In order to achieve full consistency, the motors are compared by their torque and torque density at stall power loss of $100W$. Fig. 3.37 shows a plot of torque density against torque of the considered motors. As may be observed, the EV motors of this section have performance similar to the best available off-the-shelf frameless motors. However, the EV motors of this section have significantly lower manufacturing cost due to their concentrated windings outer rotor design as discussed in Sec. 3.3. On the other hand, the robotics motor exhibits unmatched torque density which demonstrates the main advantage of high pole count motor designs.

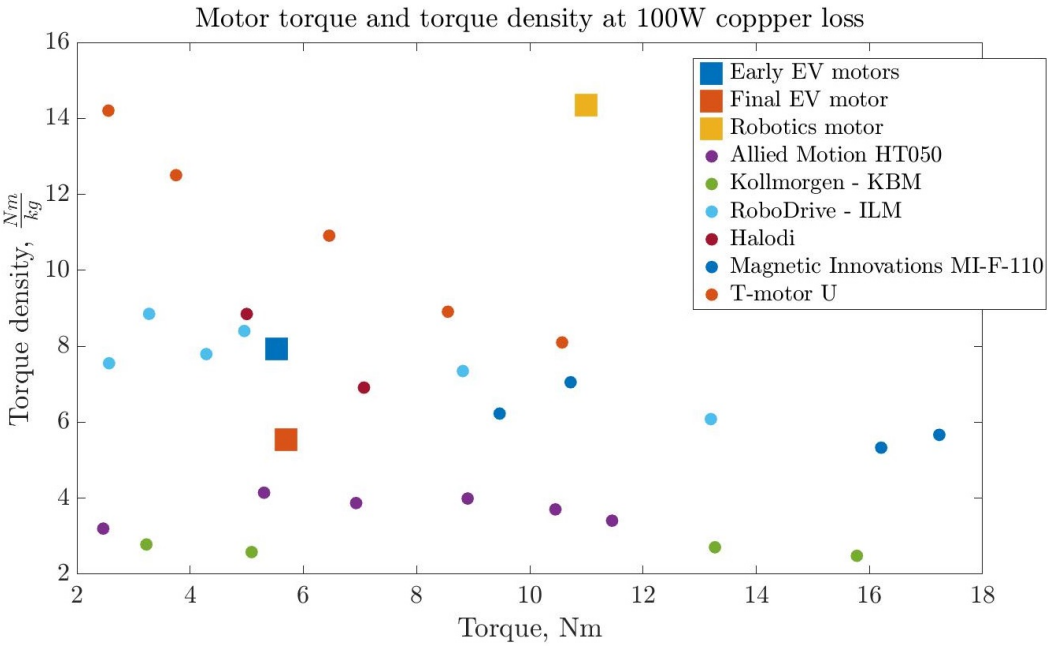

Figure 3.37: Performance comparison of the motors (square symbol) developed in this section with off-the-shelf high performance frameless motors.

As may be observed in the plot, the commercial motors follow a trend of decreasing torque density with increasing motor torque (motors with higher torque also have larger size). The following section explains this trend by considering the possible motor scaling modes. It is shown that radial and axial scaling of a motor design always lead to torque density decrease and the introduced *pole* scaling represents the only means of increasing both the torque and torque density of a motor design.

3.7 Scaling Modes of PM Motors with Concentrated Windings

This section discusses motor scaling in terms of outrunner motors with concentrated windings. The fundamental scaling modes discussed in [76–78] are simplified and focused to outrunner motors with concentrated windings using the model of Sec. 3.3.3. An additional motor scaling mode (briefly discussed in [4]) is also described and compared to the classical ones.

In [76–78], the effects of phase rewinding, and axial and radial scaling on the PM synchronous motor properties and performance are described. Rewinding (Sec. 3.7.1) refers to changing of the number of turns and wire strands so that the motor bEMF constant may be modified while the wire gauge and slot fill factor are preserved. Axial scaling (Sec. 3.7.2) represents consistent variation of the out-of-plane thickness of all motor components, while the in-plane motor dimensions are preserved. Radial scaling (Sec. 3.7.3) represents proportional change of all in-plane motor dimensions, while the motor out-of-plane thickness is preserved. An alternative radial-type scaling mode (discussed in [4]) represents modification of the motor pole count while the motor out-of-plane thickness, and the teeth shape and dimensions are preserved. This scaling mode (Sec. 3.7.4) is defined to as *pole scaling* in this thesis. Fig. 3.38 show the geometrical effect of the three scaling modes.

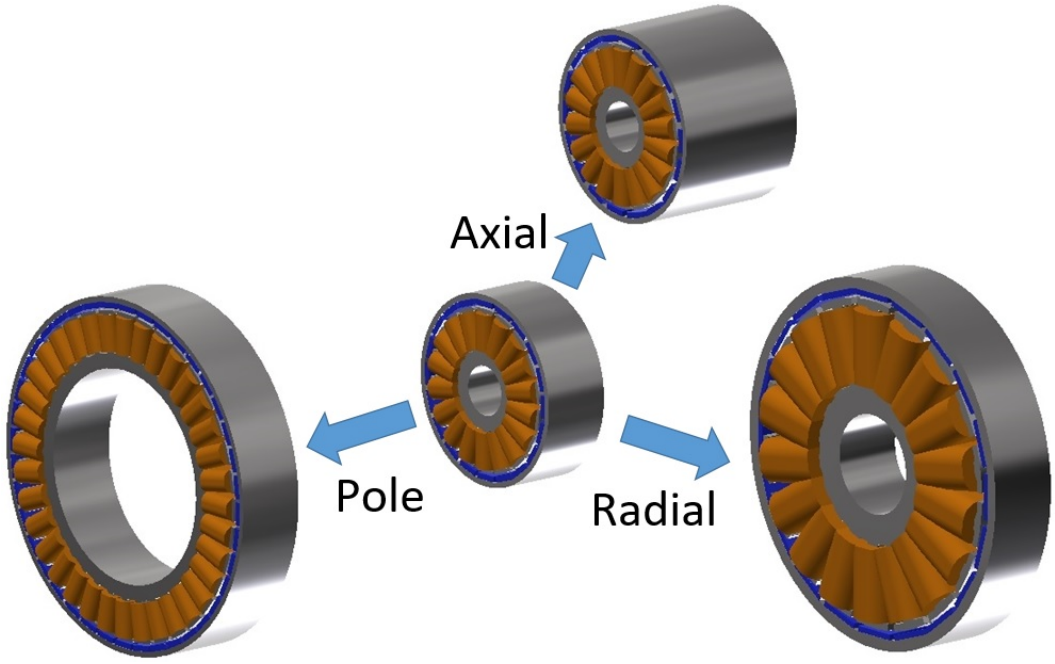

Figure 3.38: Motor scaling modes. The referent motor is a 20 pole-18 outer rotor motor. The pole scaled motor has 40 pole-36 slot motor configuration, which is quite popular in the drone industry (see Fig. 3.3.)

The main objective of this section is to describe how the scaling modes affect the motor torque performance (defined in terms of rated copper loss at stall, P_{cu}) and motor core loss. The results are appoximate and allow the performance of a scaled version of an existing outer rotor motor to be approximately predicted without the use of electro-magnetic FEA, which may be quite useful in the early design stage of a motor, actuator or even a whole robotic system. For the motors considered in this chapter, especially when driven with three phase balanced currents, core saturation due to excessive load is unlikely to occur due to the low armature reaction. Therefore, unlike [76–78], in this chapter, the scaled motor flux is not necessarily the same as the referent (unscaled) motor flux in all motor components.

In addition, as discussed in Sec. 3.2, this chapter aims to motivate and enable the substitution of high gear ratio actuators with torque-optimized high performance motors coupled with low to mid reduction ratio gearboxes in dynamic robotic applications. To this end, the motor bEMF constant, and thus, rated voltage are preserved in all scaling modes. The challenges of driving the resulting high torque motors are described in Sec. 3.7.6.

In the following analysis, the values associated with the referent (unscaled) motor are designated with square brackets ($[*]$).

3.7.1 Motor Rewinding

Rewinding refers to the consistent modification of all teeth windings so that the slot fill factor is preserved. Motor rewinding generally occurs when an application requires changing the motor rated voltage. In this thesis, the rewinding factor k_W is defined as:

$$k_W = \frac{N_{turns}}{[N_{turns}]}. \tag{3.34}$$

As discussed in Sec. 3.3.3, parallel paths are treated as strands, and thus, the number of strands does not appear in Eq. (3.34). For the rewound motor, the synchronous resistance and inductance are [77]:

$$R_s = {k_W}^2[R_s] \qquad L_s = {k_W}^2[L_s]. \tag{3.35}$$

The teeth flux linkage and back-emf constant (both implicit function of the rotor position) are [77]:

$$\Psi = k_W[\Psi] \qquad K_E = k_W[K_E]. \tag{3.36}$$

When operating at the rated copper loss the rewound motor has current and torque [77]:

$$I_s = \left(\frac{P_{Cu}}{R_s}\right)^{1/2} = \frac{1}{k_W}[I_s] \qquad T_s = K_E I_s = [T_s]. \tag{3.37}$$

The results of Eq. (3.35), Eq. (3.36) and Eq. (3.37) may be readily derived using the model of Sec. 3.3.3. The mass, iron losses and torque density are the same in the referent and rewound motors. While, rewinding does not affect the motor performance, it has profound effect on the driver system. For example, rewinding a motor so that it may achieve twice its rated speed at the rated bus voltage requires $k_W = 0.5$. Eq. (3.35) suggests that the rewound motor has synchronous inductance and synchronous resistance four times lower than the referent machine. Therefore, the inverter needs to operate at twice the PWM frequency to ensure similar current ripple levels (same percentage of rated current). Furthermore, lower phase resistance increases the danger of catastrophic failure of both the driver and motor under fault conditions (such as miscommutation or short circuit).

For the axial, radial and pole scaling below, rewinding is extensively used so that the motor rated voltage (bEMF constant) is preserved in the scaling.

3.7.2 Axial Scaling

Axial scaling refers to the consistent variation of all motor active components in the out-of-plane direction with a coefficient k_A, while the in-plane geometry is preserved:

$$k_A = \frac{l_m}{[l_m]}. \tag{3.38}$$

Let k_W be the rewinding factor. Then for the scaled motor, the peak phase flux linkage and bEMF constants are [77]:

$$\Psi = k_W k_A[\Psi] \qquad K_E = k_W k_A[K_E]. \tag{3.39}$$

Eq. (3.39) may be derived using Eq. (3.2) and Eq. (3.5) and suggests that the motor bEMF constant is preserved if $k_W = \frac{1}{k_A}$. Combining Eq. (3.16), Eq. (3.17), Eq. (3.14) and Eq. (3.35) leads to:

$$L_s = \frac{1}{k_A}[L_s]. \tag{3.40}$$

Let $C_{sc} = \frac{2\pi k_c[r_w]}{[l_m][q]}$, then combining Eq. (3.7), Eq. (3.8), Eq. (3.10) and Eq. (3.35) leads to:

$$R_s = \frac{1}{k_A^2}\left(\frac{C_{sc} + k_A}{C_{sc} + 1}\right)[R_s]. \tag{3.41}$$

Then, the scaled motor current and torque are given by (see Eq. (3.12) and Eq. (3.11)):

$$I_s = k_A\sqrt{\frac{C_{sc}+1}{C_{sc}+k_A}}[I_s] \qquad T_s = k_A\sqrt{\frac{C_{sc}+1}{C_{sc}+k_A}}[T_s]. \tag{3.42}$$

Finally, the mass, iron losses and torque density are:

$$\begin{aligned} M_m &\approx k_A[M_m] \qquad J_m = k_A[J_m] \\ P_{co} = k_A[P_{co}] \qquad T_\rho &\approx \sqrt{\frac{C_{sc}+1}{C_{sc}+k_A}}[T_\rho]. \end{aligned} \tag{3.43}$$

The mass, inertial and core losses increase proportionately due to the geometry of axial scaling. Eq. (3.42) and Eq. (3.43) suggest that when $k_A > 1$ (the motor axial length is increased), the motor torque is increased, however, the motor torque density is decreased. Furthermore, given that $C_{sc} \propto \frac{[r_w]}{[l_m][q]}$, motor axial thickness increase is most favourable for thin, radially large motors with low pole count.

3.7.3 Radial Scaling

Radial scaling refers to the proportional variation of all motor active component dimensions in the plane with coefficient k_R while no variation occurs in the out-of-plane direction ($l_m = [l_m]$).

$$k_R = \frac{d_{out}}{[d_{out}]} = \frac{d_{in}}{[d_{in}]} = \frac{w_t}{[w_t]} = \frac{r_w}{[r_w]} = \frac{t_m}{[t_m]} = \frac{a_g}{[a_g]} = \dots \tag{3.44}$$

Let k_W be the rewinding factor. Then for the scaled motor, the peak phase flux linkage and bEMF constants are [77]:

$$\Psi = k_W k_R[\Psi] \qquad K_E = k_W k_R[K_E]. \tag{3.45}$$

Eq. (3.45) may be derived using Eq. (3.2) and Eq. (3.5) and suggests that the motor bEMF constant is preserved, provided $k_W = \frac{1}{k_R}$. Eq. (3.14) suggests that for radial scaling $R_m = [R_m]$ and $R_g = [R_g]$. Then, combining Eq. (3.16), Eq. (3.17) and Eq. (3.35) leads to:

$$L_s = \frac{1}{k_R^2}[L_s]. \tag{3.46}$$

In radial scaling $A_{slot} = k_R^2[A_{slot}]$. Then, combining Eq. (3.7), Eq. (3.8) and Eq. (3.10) leads to:

$$R_s = \frac{1}{k_R^4}\Big(\frac{k_R C_{sc}+1}{C_{sc}+1}\Big)[R_s]. \tag{3.47}$$

Then, the scaled motor current and torque are given by (see Eq. (3.12) and Eq. (3.11)):

$$I_s = k_R^2\sqrt{\frac{C_{sc}+1}{K_R C_{sc}+1}}[I_s] \qquad T_s = k_R^2\sqrt{\frac{C_{sc}+1}{K_R C_{sc}+1}}[T_s]. \tag{3.48}$$

Finally, the mass, rotor inertia, iron losses and torque density are:

$$\begin{aligned} M_m &= k_R^2[M_m] \qquad J_m \approx k_R^3[J_m] \\ P_{co} &= k_R^2[P_{co}] \qquad T_\rho = \sqrt{\frac{C_{sc}+1}{k_R C_{sc}+1}}[T_\rho]. \end{aligned} \tag{3.49}$$

The mass, inertial and core loss scaling in Eq. (3.49) follow from the geometry of radial scaling, that is, the areas of all motor regions (slot, stator teeth, stator yoke, magnets, rotor yoke, etc.) are proportional to k_R^2.

Eq. (3.14) suggests that if the air gap and magnet thickness are preserved rather than scaled, then $R_m = \frac{1}{K_R}[R_m]$, $R_g = \frac{1}{K_R}[R_g]$ and the scaled self-inductance is:

$$L_{sf} = \frac{1}{k_R}[L_{sf}]. \tag{3.50}$$

Eq. (3.50) suggests that the scaling of the motor self-inductance may be improved if the air gap and magnet thickness are preserved in radial scaling. However, the leakage inductance remains unaffected as Eq. (3.15) is independent of the magnet shape and air gap thickness. The scaled rotor inertial may be approximated by $J_m \approx k_R^2[J_m]$ as the magnet thickness and rotor yoke thickness are also preserved in this case. Therefore, the motor torque per unit inertia may be approximately preserved in radial scaling provided the magnet thickness and air gap thickness remain constant rather than scaled. However, as discussed in Sec. 3.5.3, if the air gap is comparable to the width of the gap between the poles, increased magnet leakage may lead to torque reduction. Therefore, in the case of constant air gap, the scaling results of this section are valid provided the flux leakage is not significantly changed due to the scaling.

3.7.4 Pole Scaling

In pole scaling the teeth shape, air gap size and pole shape are preserved while the number of poles is modified. Let k_P be the pole scaling coefficient such that $p = k_P[p]$, (clearly p is an even non-negative integer, which constrains the possible values of k_P). The motor out-of-plane thickness remains unaltered ($l_m = [l_m]$). As

before, let k_W be the rewinding factor. The geometry of pole scaling suggest that the magnet flux leakage levels are identical in both the referent and scaled motors. Then, assuming the motor winding factor and the slot per pole per phase number, Q_{pp}, are approximately preserved, Eq. (3.5) suggests that:

$$\Psi \approx k_W k_P^2[\Psi] \qquad K_E \approx k_W k_P^2[K_E], \tag{3.51}$$

as $q \approx k_p[q]$ (see Eq. (3.1) and Eq. (3.22)). Then, the bEMF constant is preserved if $k_W = \frac{1}{k_P^2}$. The slot area and the length of the windings end turns are also approximately preserved, therefore, Eq. (3.8) suggest that $R_{phase} \approx k_W k_P[R_{phase}]$. Then the synchronous resistance is approximately:

$$R_s \approx \frac{1}{k_P^3}[R_s]. \tag{3.52}$$

Similarly, Eq. (3.16) and Eq. (3.17) suggest that:

$$L_s \approx \frac{1}{k_P^3}[L_s]. \tag{3.53}$$

Then, the scaled motor current and torque are given by (see Eq. (3.12) and Eq. (3.11)):

$$I_s \approx k_P^{3/2}[I_s] \qquad T_s \approx k_P^{3/2}[T_s]. \tag{3.54}$$

From the geometry of pole scaling (also see Fig. 3.6), it can be shown that the motor mass, rotor inertia and torque density approximately scale as:

$$M_m \approx k_P[M_m] \qquad J_m \approx k_P^2[J_m] \qquad T_\rho \approx \sqrt{k_P}[T_\rho]. \tag{3.55}$$

Eq. (3.55) provides an alternative view point to the advantages of motors with high pole count. Unlike the other motor scaling modes, in the case of pole scaling the comparison between the referent and scaled motor core losses is quite difficult due to the differences in the frequency dependence of the core loss components. Nevertheless, Eq. (3.23) suggests that the scaled motor core losses may be upper bounded by:

$$P_{co} \leq k_P^3[P_{co}] \tag{3.56}$$

The equations in this section are approximations and are valid only under the assumptions of Sec. 3.3.3.

3.7.5 Scaling Laws Discussion

Eq. (3.43), Eq. (3.49) and Eq. (3.55) demonstrate and quantify the limitations characteristic to designing motors that have both high torque and high torque density. Increasing the motor size by radial or axial scaling leads to torque density decrease. This trend may be clearly observed in Fig. 3.37. Eq. (3.43) and Eq. (3.49) suggest that radial scaling is more favourable for motors with high pole count and axial scaling is more favourable for motors with low pole count as $C_{sc} \propto \frac{1}{q}$. Which may be explained by the fact that axially scaling up a motor, reduces the resistance of the windings end turns relative to the overall motor resistance (see Eq. (3.41)) while radially scaling up a motor, increases the resistance of the windings end turns relative to the overall motor resistance (see Eq. (3.47)).

Only pole scaling may be used to increase both the torque and torque density of an existing motor design. However, Eq. (3.55) suggests that the higher torque density comes at the price of increased core losses. Therefore, the scaling analysis of this section confirms the analysis and conclusions of Sec. 3.4.3.

The geometry of Fig. 3.6 suggests that pole and radial scaling lead to motors with the same air gap diameter provided the scaling coefficients are the same ($k_R = k_P$). Comparing Eq. (3.48) and Eq. (3.54) suggests that radial scaling leads to higher torque in this case. Therefore, it is beneficial to compare the torque of radially scaled motor with a pole scaled motor with the same airgap diameter which is also axially scaled so that the two motors have identical mass. From Eq. (3.43), Eq. (3.49) and Eq. (3.55) the mass of the two motors is:

$$\begin{aligned} M_m &= k_R^2[M_m] \text{ for the radially scaled motor and} \\ M_m &= k_A k_P[M_m] \text{ for the pole/axial scaled motor.} \end{aligned} \tag{3.57}$$

If $k_P = k_R > 1$ then $k_A k_P = k_R^2$, provided $k_A = k_R$. Then from Eq. (3.43) and Eq. (3.55) the torque of pole/axial scaled motor is:

$$T_s = k_R^2 \sqrt{\frac{C_{sc} + 1}{\frac{C_{sc}}{k_R} + 1}} [T_s] \tag{3.58}$$

Comparing, Eq. (3.49) and Eq. (3.58) suggests that pole/axial scale motor has $\sqrt{\frac{k_R C_{sc}+1}{\frac{C_{sc}}{k_R}+1}}$ higher torque which is solely due to the shorter windings end turns of motors with higher pole count. This coefficient may be used to determine the benefits of pole scaling compared to radial scaling when the scaled motor size is constrained. Due to the fact that $C_{sc} \propto \frac{1}{q}$, the toque advantage of pole scaling diminishes as the pole count of the referent motor increases.

By visually comparing the windings end turns of the prototypes of Fig. 3.32 and Fig. 3.34, one can readily appreciate the significance of Eq. (3.58).

3.7.6 Challenges Related to Robotics Application of High Torque Motors.

As previously discussed, the majority of current robotic systems feature relatively small sized, high speed motors coupled with high reduction gearboxes. The scaling modes analysis of this section, is helpful to outline the challenges in substituting current robotic actuators with high torque motors coupled with low to mid reduction gearboxes.

In this context, consider substituting an actuator that consists of a small motor coupled with a high reduction gearbox, for example a harmonic or a cycloidal drive (see Sec. 4.1.1) with reduction ratio higher than 1 : 100. Eq. (3.49) and (3.43) show that increasing the motor's torque n_s times by axial and/or radial scaling results in a motor of high mass and size (at least n_s times higher). On the other hand, decreasing the reduction ratio of a gearbox n_s times does not necessarily lead to substantial reduction of its mass, if any. This follows from the fact that the output of the low to mid reduction gearbox substitute needs to support identical loads as the high reduction gearbox. Thus, it is clear that it is not really possible to achieve the same torque and torque density levels of high reduction actuators with low reduction gearboxes coupled with large motors of regular design. Nevertheless, Eq. (3.55), the analysis of Sec. 3.4.3, FEA simulations of Sec. 3.5.3 and prototype of Sec. 3.6.2 show that high pole count motors may be designed to achieve torque densities substantially higher than the motors that are currently available off-the-shelf (see also Sec. 3.6.3).

The bus voltage in legged and limbed robotic systems is usually limited due to safety reasons and battery size limitations. Eq. (3.41), Eq. (3.40), Eq. (3.47) and Eq. (3.40) suggest that large motors wired for low voltage are also characterized with small inductance and resistance which are both challenging from a drivers perspective. Furthermore, Eq. (3.52) and Eq. (3.53) suggest that high pole motors have substantially lower resistance and inductance than low pole motors of the same size. These observations are confirmed by the FEA simulations of Sec. 3.5.3 and the characteristics of the prototypes of Sec. 3.6. Therefore, novel motor driver systems may be necessary to fully realize the potential of high pole count motors.

3.8 Failure of PM Outer Rotor Motors with Concentrated Windings

This section briefly discusses the main causes of motor failure, which may be either mechanical or electrical in nature.

3.8.1 Mechanical Motor Failure

Motor mechanical failure may occur when one or more of its components are mechanically damaged.

Presence of relatively small particles in the air gap may lead to magnet surface scratches and even magnet cracks. On the other hand, relatively large particles may lead to rotor jamming, magnet detachment and permanent stator and rotor damage. Motors with high pole count have narrow magnets, and thus, relatively small air gap in order to minimize the magnetic flux leakage between the magnets, and between the magnets and the teeth (see Sec. 3.5.3). Therefore, these motors are susceptible to damage due particles and should be shielded from the environment.

Excessive motor heating may lead to thermal motor failure. This may be caused by motor overload, insufficient heat dissipation or failure of the driver circuitry. Temperatures exceeding 150° may cause:

- separation of glued components, e.g. failure of the bond between the stator aluminum support and stator core, laminations separation (in the case of glued laminates), magnet detachment from rotor back iron, failure of the bond between the rotor back iron and rotor aluminum support, etc.
- electrical failure caused by magnet wire isolation melting (see below), e.g. phase shorting, shorting of conductors in the slots, etc.
- magnet demagnetization caused by operation at increased temperature.

Motor bearing failure in robotics joint actuators is rare. Provided a minimal symmetry exists in the motor pole - slot combination (see Sec. 3.3.3), no unbalanced motor radial forces exist. Manufacturing inaccuracies may still lead to small radial and axial forces caused by the interaction of the magnets with the teeth and the coils, however, these usually have very small magnitude and may not lead to bearing failure. On the other hand, in some applications such as drone actuation, motor bearings may need to support significant loads that are external to the motor, such as axial force due to propeller thrust, etc. These applications require careful motor

bearing design to ensure premature motor failure does not occur due to excessive motor bearing loads.

3.8.2 Electrical Motor Failure

Electrical motor failure usually results from mechanical damage or thermal motor failure (discussed above) and is characterized by a substantial change of the resistance and bEMF of some of the phases due to occurrence of an undesired electrical connection. For example, melting of the magnet wire enamel insulation could cause detrimental shorting between two phases in a slot. Motors with single layer concentrated windings have an advantage, as the coils belonging to different phases are electrically insulated [82]. On the other hand, mechanical damage or melting of the stator core varnish insulation could lead to shorting between the phases through the stator core. Such phase shorting leads to significant motor performance degradation characterized by increased current consumption, excessive heating, noise due to current ripple, etc.

Motor electrical failure may also occur due to demagnetisation of the permanent magnets. This may be caused by overload (excessive current in the coils) or motor driver failure. Higher motor operational temperature increases the chance of demagnetization especially for high grade NdFeB magnets [42]. As discussed in Sec. 3.4.2, motors with higher pole count have lower armature reaction, thus, can deliver safely significantly higher peak torque without danger of demagnetization or magnetic saturation of the stator core.

Finally, as shown in Sec. 3.7.6, high torque motors have low resistance and inductance. For such motors, miscommutation or failure of the driver circuity may lead to excessive current that causes demagnetization of the permanent magnets or thermal motor failure. Therefore, drivers for large torque motors require improved safety features and robustness.

3.9 Conclusion

This chapter is concerned with the design of application-specific high performance motors with the focus on robotic joint actuation. Based on a flux-linkage model, valuable insights are gained regarding how the motor design parameters affect its performance, and in particular, its torque, torque density, efficiency, etc. The analysis shows that:

- magnet width of 120° leads to minimum bEMF total harmonic distortion or equivalently minimum torque ripple. Increasing the magnet width beyond this value leads to little increase in the bEMF fundamental harmonic amplitude due to increased magnet leakage.
- for a given motor pole count, multiple valid values may exist for the slot count. Lower values for the slot count may lead to slightly increased torque and torque density, significantly reduced core losses and allow higher number of parallel circuits. Higher values lead to motor designs of lower cogging torque. Also the slot count analysis suggests that motor designs with higher slot than pole count have no advantages and should be avoided.
- increasing the pole count may lead to significant motor torque density increase. Provided the stator yoke is thick enough, the majority of the core losses are generated in the teeth, and thus, high efficiency high pole count motor designs with shallow slots are possible. A pole count analysis shows that no fundamental limitations prevent the use of such motors for high speed applications.
- the motor torque density may be maximised by adjusting the motor slot depth. A motor tooth width analysis shows that the performance of SMPM motors may not be significantly exceeded by IPM motors in terms of the applications considered in this thesis.

The validity and limitations of the analytic results are demonstrated using FEA and performance characterization of manufactured prototypes.

These insights allow the formulation of clear motor design performance trade-offs, guidelines and metrics which may be quite beneficial in the development of high performance actuators:

- Motors of electric vehicles should be designed with lower pole count and longer stator teeth. Such motor designs deliver higher torque and have lower core losses.
- Drone and robotic joint motors should be designed with higher pole count and shorter teeth. Such motors have significantly higher torque density and good high power efficiency.

Finally, motor design scaling modes are described, analyzed and compared, in order to provide useful tools for rapid scaled motor performance prediction. These scaling modes also provide clear outline of the challenges related to the application of high torque motors in robotic applications. The analysis shows that motors that have both high torque and high torque density may be achieved only by using high pole count.

Chapter 4

ANALYSIS AND DESIGN OF THE BEARINGLESS PLANETARY GEARBOX

4.1 Introduction

As discussed in Ch. 1, high performance legged and mobile manipulating robotic platforms require light weight actuators with high torque density, efficiency, and accuracy. The size, weight, cost, and capabilities of these robotic systems are heavily influenced by the characteristics of their actuators. Furthermore, the actuators' dynamics may have a profound effect on the robot's achievable controlled performance. This chapter introduces a new type of high reduction *Bearingless Planetary Gearbox* which is motivated by the Wolfrom Gearbox, and can achieve a wide range of reduction ratios in a single composite stage. Even though, the novel gearbox is developed primarily with consideration of the intended use in robotics, it is suitable for any demanding application that requires mid to high reduction ratio speed reducers (*e.g.* 10-300). The practical issues which limit the applicability of the Wolfrom Gearbox are discussed and used to motivate the innovations in the chapter. Several advantages of the Bearingless Planetary Gearbox over current approaches in terms of improved robustness, load distribution, manufacturability, and assembly are described. A detailed strength analysis of the Bearingless Planetary Gearbox demonstrates its torque and toque density advantages. In the concept, all gear components float in an unconstrained manner, which is achieved by introducing an additional kinematic constraint that allows the planets to be uniform. With this novel design the planet carrier can be substituted with a secondary sun gear. The resulting gearbox can be readily integrated into compact robotic joints. Its few lightweight components can be manufactured with high accuracy with standard machining techniques.

4.1.1 Speed Reducers Commonly Used in Robotic Applications

The torque density of electric motors is quite low compared to the actuation requirements characteristic of robotic manipulators, mobile manipulation and limbed robotics, etc. To overcome this limitation, high reduction gearboxes are usually employed to achieve high output actuator torques with electric motors. Next, the most widely used speed reducers in robotic applications are reviewed and their advantages

and disadvantages are outlined.

Harmonic drives

Harmonic drives (Fig. 4.1) are widely used in robotic applications that require high torque density, high compactness and positioning accuracy. They have virtually no backlash and have a great advantage in environmentally challenging conditions, such as in space applications, due to the possibility of hermitic sealing [89], [90]. Even though, these gearboxes have only three components, the drive must be manufactured with high accuracy, using complex machining processes. Thus, custom designs of such drives are difficult and expensive to implement. The efficiency is around 70% to 80%, and heating due to friction between the gear teeth, usually limits the performance [90]. Furthermore, intrinsic kinematic errors [91], load hysteresis [92], dry and velocity dependent friction, nonlinear torsional compliance [93], [94], vibration and resonance losses [91], [93], [94], all lead to performance degradation. Thus, nonlinear behavior, instabilities and unexpected fatigue failure are of concern in dynamic applications of harmonic drives with high gain feedback loops.

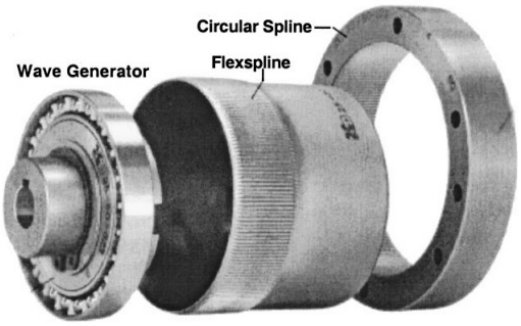

Figure 4.1: Harmonic drive [88] ©2003 IEEE.

Cycloidal drives

Cycloidal drives, like harmonic drives, have high reduction ratios and compact size (see Fig. 4.2). Cycloidal drives permit higher operational torque and efficiencies with lower noise and vibration because the torque is transmitted by roller bearing and only compressive stresses are involved [96]. However, even with precision machining tolerances, backlash and torque ripple caused by reduction ratio fluctuation are

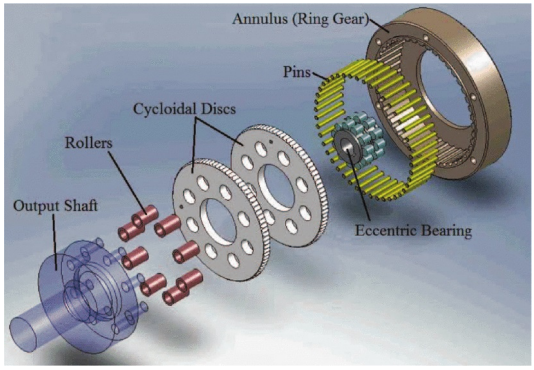

Figure 4.2: Cycloidal drive [95] ©2012 IEEE.

common and unavoidable [96–98]. Thus, custom design with high accuracy for high performance robotic application are both expensive and difficult to manufacture [98].

Single stage planetary gearboxes

Single stage planetary gearboxes (Fig. 4.3) are attractive for their high linearity and efficiency [90]. Gears are standard mechanical components, thus, custom high accuracy gearing can readily be manufactured. However, low backlash or backlash-free epicyclic gearing requires high manufacturing accuracy for all components which can be quite costly. The reduction ratio of the one-stage planetary gearbox is practically limited to the range of 1 : 3 up to 1 : 8 [90]. If higher ratios are desired, then multiple stages can be concatenated. However, the overall size and weight of the gearbox increases substantially in this case. Since the sun gear is typically a small size pinion, the maximum torque that can be generated by a planetary stage is limited by the pinion size, as the other gear components carry much lower loads. This fact explains why planetary gearboxes usually have substantial mass and size, especially in high torque applications.

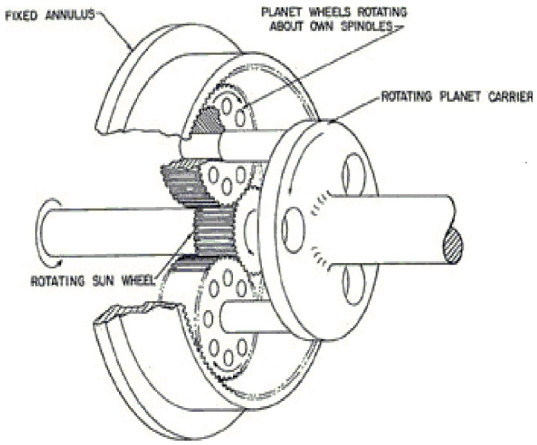

Figure 4.3: One-stage planetary gearbox [99] ©2011 IEEE

Single Stage Compound Planetary Gearboxes

Compound epicyclic gearing finds vast application in vehicle actuation systems (differentials, transmissions, etc.) and mechanical machinery (speed reducers). A modification of the classical planetary gearbox of Fig. 4.3, that has gained recent popularity in the literature, is shown in Fig. 4.4. This sin-

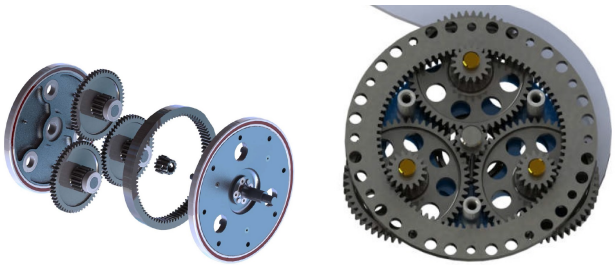

Figure 4.4: Single stage compound planetary gearbox examples ([31] ©2018 IEEE on left and [32] ©2017 IEEE on right).

gle stage compound planetary gearboxes consists of a driving sun gear, a stationary ring gear and compound planets supported by a carrier which is the output. The main advantage of this gearbox is that low to mid reduction ratios can be achieved in a single compund stage. The high linearity and efficiency associated with planetary gearing further promote the gearbox attractiveness. However, achieving high reduction ratios still requires the concatenation of multiple stages. The main disadvantages of this gearbox are related to the higher manufacturing complexity and tolerance requirements associated with the compound planets and the carrier assembly. Furthermore, with higher reduction ratio designs, the planet gears meshing with the ring gear would be pinions and would determine the gearbox load rating. Therefore, the gearbox strength is again determined by a pinion gear's strength, and thus, the gearbox is expected to be disadvantaged in weight and size, for high torque applications.

4.1.2 Contribution and Chapter Structure

The goal of this chapter is to develop a high torque, compact, and lightweight speed reducer that can be efficiently integrated into robotic joints. Of main interest are mid to high range of reduction ratios for application in mid reduction ratio actuators and SEAs (see Ch. 1). The gearbox efficiency, dynamic stability, and positioning accuracy are also of crucial importance for the intended use in robotic actuation. The disadvantages of harmonic and cycloidal drives (described earlier in the section) combined with their prohibitive prototyping cost, makes then unsuitable for the objective of integrating the motor and gearbox into a compact custom design. On the other hand, the planetary gearboxes described in Sec. 4.1.1 are disadvantaged in size, weight and compactness especially when used in high reduction applications.

To achieve the aforementioned design goals, a new type of high performance planetary gearbox is developed, which is based on the Wolfrom Gearbox concept. It has several advantages for robotic applications in terms of torque performance, weight, compactness and manufacturing. While the novel planetary gearbox is suitable for conventional inner rotor motors, some of the designs and prototypes, described in the chapter, are heavily oriented towards outer rotor motors or "outrunner" (see Ch. 3). As discussed in Ch. 3, outer rotor motors have considerable advantages and probably have not had an impact in robotics due to the practical difficulties related to their use with off-the-shelf speed reducers.

The chapter is organized as follows. Sec. 4.2 is concerned with the analysis, design

and manufacturing of the Wolfrom Gearbox and introduces important practical improvements. Sec. 4.3 describes the development of the Bearingless Planetary Gearbox which is the main contribution of this chapter. Detailed strength analysis and manufacturing considerations are included in order to outline its advantages in terms of torque, weight, compactness and manufacturing readiness.

4.2 Analysis of The Wolfrom Planetary Gearbox

This section analyzes the Wolfrom planetary gearbox, and introduces a practical improvement to the design so that the planets may be uniform (Sec. 4.2.2). This uniformity is key for the removal of the gearbox carrier and the introduction of the Bearingless Planetary Gearbox in Sec. 4.3. Brief strength analysis (Sec. 4.2.3) and manufacturing discussion (Sec. 4.2.4) are also included. These motivate the interest in the Wolfrom gearbox and the development of the Bearingless Planetary Gearbox in Sec. 4.3.

4.2.1 Kinematic Layout

The Wolfrom Gearbox is a planetary gearbox that consists of a one sun gear, two ring gears and multitude of planets assembled in a carrier. The concept is first introduced in [100]. The planets, called gear clusters or compound gears [90], consist of two rigidly connected gears. The sun gear is the gearbox input, one of the ring gears is stationary and the other ring gear represents the gearbox output. Fig. 4.5 shows the gearbox layout [90] and a CAD rendering showing the components. Detailed

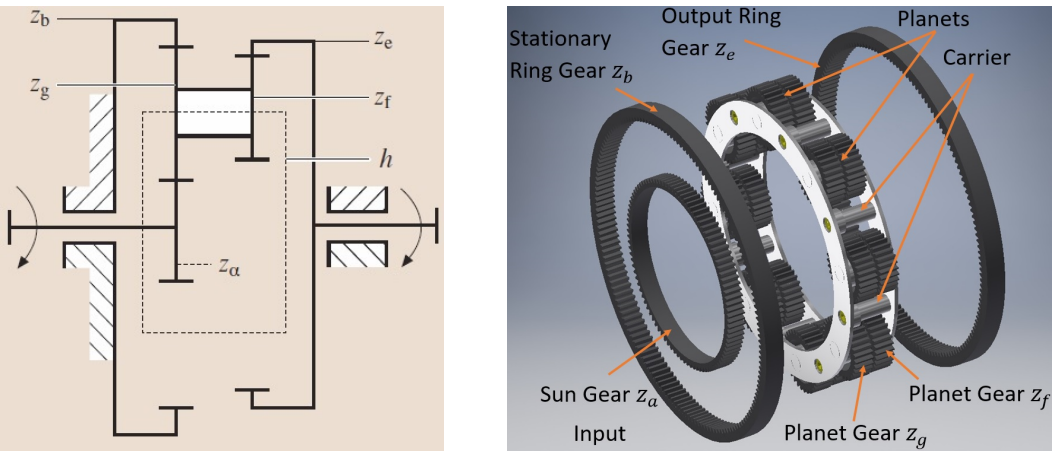

Figure 4.5: Wolfrom planetary gearbox layout [90] ©2009 Springer and CAD rendering.

kinematic description of this layout and similar layouts is presented in [90] and [101]. This gearbox is very attractive as a very wide range of reduction ratios can be

achieved in a single composite stage [90]: from about 1:8 to 1:500 and beyond for some designs. The higher reduction ratios in this range may require a small driving sun gear.

In Fig. 4.5, z_a is the number of teeth of the sun gear, z_b is the number of teeth of the stationary ring gear, z_e is the number of teeth of the output ring gear, and h refers to the planet carrier. The planet gears have z_g and z_f teeth (see Fig. 4.6). The planets must be radially supported by bearings (usually in the carrier). A detailed discussion of bearing units and gearbox bearing design is presented in [90]. To simplify the exposition, the same symbol is used to denote the gear components and their tooth number, as shown in Fig. 4.5. The reduction ratio between the sun gear (gearbox input) and output ring gears is given by [90]:

$$R_{ae} = \frac{(1 + z_b/z_a)}{[1 - z_b z_f/(z_e z_g)]}. \tag{4.1}$$

Generally, the two gears locked together in one planet do not have the same number of teeth $z_f \neq z_g$. If $z_e < z_b$ and $z_f < z_g$, the planet carrier and output ring gear have the same direction of rotation. In this chapter, the gearbox design is restricted to have all gears with the same module, m. Designs with different gear module in the gearbox stages are harder to manufacture and do not necessarily have any advantages. From Fig. 4.5 one can see that meshing of all gearing components requires:

$$\begin{aligned} z_g &= \frac{1}{2}(z_b - z_a) \\ z_f &= z_e - (z_a + z_g). \end{aligned} \tag{4.2}$$

Let p_n denote the number of planets. Then the sun gear cannot mesh with the planet gears unless [90]:

$$(z_a + z_b) \text{ is divisible by } p_n. \tag{4.3}$$

In order to mesh p_n planets without physical interference the following condition also needs to be satisfied:

$$z_g + 2 < (z_a + z_g) \sin\left(\frac{\pi}{p_n}\right). \tag{4.4}$$

The gearbox reduction ratio (Eq. (4.1)) may be split into two components:

$$\begin{aligned} R_{ae} &= R_{ap} R_{pe}, \text{ where} \\ R_{ap} &= 1 + \frac{z_b}{z_a}, \\ R_{pe} &= \frac{z_e z_g}{z_e z_g - z_b z_f}. \end{aligned} \tag{4.5}$$

R_{ap} is the reduction ratio from the sun gear to the planets (or carrier) and corresponds to the reduction ratio of a single stage planetary gearbox. R_{pe} is the reduction ratio from the planets (or carrier) to the output ring gear. If $z_b \approx z_e$, *e.g.* $z_b = z_e - 1$, R_{pe} may be quite large and lead to high reduction ratio alone. Therefore, high reduction ratios (roughly up to $1 : 200$) may be achieved, even when the sun gear number of teeth z_a is relatively large, that is, the sun gear is large in diameter relative to the ring gears. This is in contrast with the single stage and single stage compound planetary gearboxes (see Sec. 4.1) where the sun gear is a pinion. Therefore, a practical advantage of the Wolfrom Gearbox is that an outrunner motor (see Ch. 3) may be incorporated inside the driving sun gear, housed completely in the gearbox interior. Following this approach, gearmotors (the complete system of the gearbox and a motor) with significant compactness and weight advantage may be designed (see Sec. 6.2 and Sec. 6.3).

Fundamental limitations arise in the assembly and manufacturing of the planets. If no additional requirements are imposed, in general, it is not possible to mesh the planet gears z_f and the output ring gear z_e if the planets are identical and are symmetrically positioned. In this case, for assembly it is required that all planets have their gears displaced with respect to each other at a specific angle that reflects their position around the sun gear. For example, let $z_e = z_b - 1$, then if there are $p_n = 5$ planets, the first planet's gears have an aligned tooth, the second planet's gears are displaced by $\frac{1}{5}$ tooth compared to the first one, the third one has its gears displaced by $\frac{2}{5}$ tooth and so on. A further complication is caused by the fact that the two gears of each planet have a different number of teeth, therefore, all planets have to be precisely oriented upon assembly, otherwise the ring gear z_e cannot be meshed with the planet gears z_f. Thus, the planets need assembly features such as alignment holes. These will be further discussed in Sec. 4.3.

4.2.2 Design Requirement for Uniform Planets

In order to significantly improve the manufacturing and assembly of the gearbox, a novel requirement is introduced that allows all planets to be the same:

$$\frac{z_e z_g - z_b z_f}{g} \text{ is divisible by } p_n \tag{4.6}$$

where g is the greatest common divider of $z_e z_g - z_b z_f$ and z_g. If this requirement is met, then p_n planets can be symmetrically positioned around the sun gear z_a. Eq. (4.6) physically means that if a planet in the carrier is meshed with the sun gear and the ring gears, it must be possible to rotate the carrier $s \times \frac{360}{p_n}$ degrees for some

integer s and mesh another planet by just inserting it in the carrier with the same orientation that the first planet had before the carrier was rotated. If it is possible to do this p_n times, all planets can be successfully meshed and the gearbox assembled.

Alternatively, the numbers $\frac{z_e z_g - z_b z_f}{g}$ and $z_a + z_b$ can be used to find the planet positions for unsymmetrical planet configurations. The factorization of $z_a + z_b$ describes every possible planet count in symmetric configuration around the sun gear so that the sun gear can be meshed with the planet gears z_g. Similarly, the factorization of $\frac{z_e z_g - z_b z_f}{g}$ describes every possible planet count in symmetric configuration around the sun gear so that the output ring gear z_e can be meshed with the planet gears z_f. The common possible planet counts in these two sets implicitly indicate all possible planet positions around the sun gear so that the gearbox may be assembled and all gearing components meshed. Then, uniform planets may be inserted in any of these positions. Therefore, a wide range of designs are still possible despite the additional requirement for uniform planets. Initial planets alignment upon assembly is still required. Planet alignment is discussed in Sec. 4.3.

4.2.3 Strength Analysis

Detailed metallic gear strength analysis is available in [90, 102, 103]. Detailed discussion regarding planetary gears design and analysis is given in [90]. For the gearbox layouts shown in Fig. 4.5, the carrier h provides radial support for the planets and the radial loads and moments due to the meshing of the planet gears with the sun and ring gears are balanced by the carrier. Fig. 4.6 shows the meshing forces acting on the planets: F_g is due to the meshing between z_b and z_g, F_f is due to the meshing between z_f and z_e, F_a is due to the meshing between z_g and z_a. The torque that the sun gear z_a carries is low compared to the load carried by the planet gears z_f and z_g due to the high reduction ratio, therefore, F_a is much smaller than F_g, F_f in magnitude. Also $F_f > F_g$ if $z_f < z_g$ (unidirectional rotation of the sun gear z_a and the ring gear z_e) and at equilibrium: $F_f = F_g + F_a$. Then, as far as the strength analysis is concerned, it is enough to consider the meshing between the planet gear z_f and the ring gear z_e, as the meshing loads between the planet gear z_g and the ring gear z_b would be lower in this case. Therefore, it is

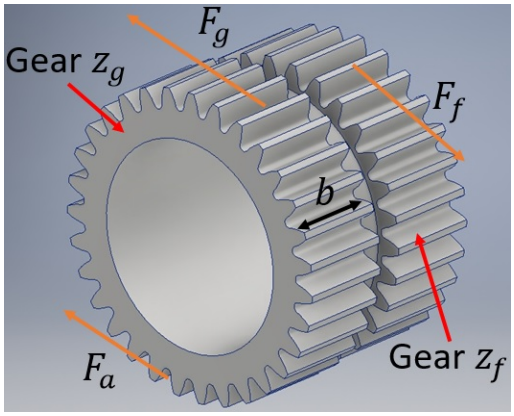

Figure 4.6: Forces in Wolfrom Gearbox.

sufficient to analyze the planet gear z_f for the gearbox strength calculation as the stress in an external gear (sun and planet gears) is larger than the stress in an internal gear (ring gears) due to their meshing [90].

Given an output torque T_e for p_n planets, the force, F_f, and torque, T_f, applied on the planet gear z_f are:

$$F_f = \frac{2T_e}{mp_n z_e} \qquad T_f = \frac{T_e z_f}{p_n z_e}. \tag{4.7}$$

The Hertz stress, σ_H, and bending stress, σ_F, of the teeth of the planet gear z_f are given by [90]:

$$\begin{aligned} \sigma_H &= C_H \sqrt{\frac{T_e(z_e/z_f - 1)}{pm^2 z_e z_f b(z_e/z_f)}} \\ \sigma_F &= C_F \frac{T_e}{pm^2 z_e b}, \end{aligned} \tag{4.8}$$

where C_H and C_F are factors that depend on the loading, material, manufacturing and tooth shape [90] and b is the gear thickness (Fig. 4.6). Let $u_{ef} = \frac{z_e}{z_f}$, $d_e = mz_e$ and $d_f = mz_f$. From Eq. (4.8) it can be seen that:

$$\begin{aligned} \sigma_H &= C_H \sqrt{\frac{1}{d_f}\Big(\frac{u_{ef} - 1}{u_{ef}}\Big)\Big(\frac{T_e}{p_n b d_e}\Big)} \\ \sigma_F &= C_F \Big(\frac{1}{m}\Big)\Big(\frac{T_e}{p_n d_e b}\Big). \end{aligned} \tag{4.9}$$

Eq. (4.9) describes the dependence of the Hertz stress and bending stress on the gear size, module and thickness. The choice of the gear module has little effect on the Hertz stress, while the planet gear diameter, d_f, has little effect on the bending stress.

For a given material choice and manufacturing, the maximum admissible Hertz and bending stresses given by $\sigma_{[H]}$ and $\sigma_{[F]}$ can be determined (see [90, 103, 104]). Then, the gearbox will not fail in its design lifetime, provided $\sigma_H \leq \sigma_{[H]}$ and $\sigma_F \leq \sigma_{[F]}$. In robotic applications, a combination of the peak and continuous torque failure criteria may be an appropriate choice because throughout its life, the gearbox may not be subject to enough maximum loading cycles for fatigue failure to occur. Then Eq. (4.8) leads to:

$$\begin{aligned} T_e &\leq \Big(\frac{\sigma_{[H]}}{C_H}\Big)^2 \Big(\frac{u_{ef}}{u_{ef} - 1}\Big) d_f (p_n d_e b) \\ T_e &\leq \frac{\sigma_{[F]}}{C_F} m (p_n d_e b) \end{aligned} \tag{4.10}$$

Eq. (4.10) suggests that $T_e \propto (p_n d_e b)$, and thus, reveals a major load advantage of this gearbox layout compared to the conventional one-stage planetary gearbox. Since the output of the gearbox is a ring gear and the output torque is proportional to its size, high torques may be supported, as the size of this ring gear may be quite large. In most designs, the value of the module m may be adjusted so that the gear tooth bending strength is not the limiting strength factor. In this case, the maximum gearbox torque is:

$$T_e = \left(\frac{\sigma_{[H]}}{C_H}\right)^2 \left(\frac{u_{ef}}{u_{ef}-1}\right) d_f (p_n d_e b) \tag{4.11}$$

Unlike the single stage compound planetary gearbox of Sec. 4.1.1, the planet gears of the Wolfrom gearbox are not pinions. Thus, the Wolfrom gearbox may have multiple times higher load caring capability than the single stage compound planetary gearbox. In addition, the Wolfrom gearbox feature a single additional ring gear, therefore, its torque density may also be significantly higher.

With the aid of Eq. (4.9) and Eq. (4.10) one can employ a simple iterative general gearbox design procedure. Given a particular application, the gearbox design goals such as maximum torque, speed, weight, etc. and design constraints such as: physical size, motor speed and size, bearings availability, materials ($\sigma_{[H]}$,$\sigma_{[F]}$), manufacturing, lubrication, etc. are first defined. Then iteratively, one can optimize the gear ratio and gear size from the Hertz strength, and optimize the module and gear face width from the bending strength, given the goals and constraints.

4.2.4 Manufacturing and Gearbox Characteristics

The manufacturing of the ring gears and the sun gears involves standard techniques. The main difficulties are related to the planet manufacturing. Fig. 4.7 shows a side view of a planet. The distance between the planet gears is denoted as the *planet gap*. The planets would be conventionally machined through shaping. A review of gear manufacturing is available in [90, 103, 104]. Gear cluster design and manufacturing is also discussed in detail in [90]. The planet gap plays an important role in the manufacturing process [90]. For the purposes of packaging and weight compactness, the gap size

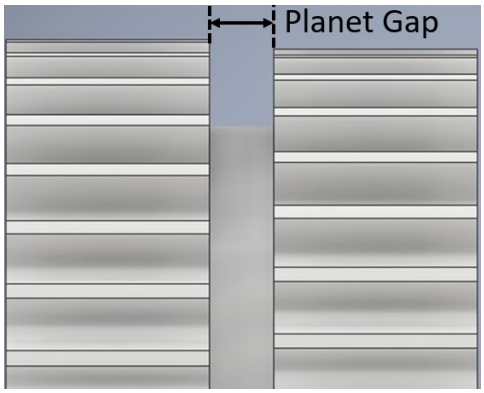

Figure 4.7: Compound planet side view.

should be kept as small as possible. Finishing operations, such as grinding following carbonizing, place additional constraints on gap size selection.

If the gears are cut to their nominal shape, it is very unlikely that it would be possible to assemble the gearbox. To solve this problem, *gear profile correction* is used [103, 104]. The shaping tool applies a *negative shift* by cutting deeper (towards the center) in the gear blanks. The resulting gears have pitch diameters that are smaller than the standard values for the given number of teeth. Thus, the meshing center distances are reduced and the resulting radial backlash makes it possible to assemble the gearbox. A measure of backlash is always required for successful meshing of gears, but high performance designs require low or reduced backslash [103, 104], otherwise anti-backlash mechanism must be introduced.

For high reduction applications, one would choose $z_e = z_b - 1$ to maximize the reduction ratio and, thus, $z_f = z_g - 1$. In this case, the planets need four critical machining operations: bearing hole drilling, alignment feature machining and shaping of the two gears plus possible gear grinding. The machining errors from each step could add-up to a relatively large overall error, requiring a relatively large shift profile to accommodate the errors. These effects lead to an increase in the gearbox noise, backlash, friction and, a drop in efficiency due misalignment and reduction of meshing contact ratio [103]. In general, efficiencies in the range of 0.7 (for high reduction designs) to 0.9 (for low reduction designs) are to be expected [90]. Furthermore, due to the backlash and the fact that the planets are constrained in the carrier, the load is generally not distributed evenly across the planets. In fact, no more than three or four planets carry the load [90]. On the other hand, the manufacturing cost of high precision planets would significantly increase the overall gearbox cost. Thus, similarly to harmonic and cycloidal drives, custom high performance gearbox designs of the type described in this section may also he expensive and difficult to manufacture for robotic applications.

4.2.5 Application in the Gear Bearing Drive

An application of the Wolfrom Gearbox layout in the Gear Bearing Drive is described in [101], [105] and [102]. Fig. 4.8 shows the schematic structure of this design. In the concept, the planets have additional cylindrical extrusions that extend outwards from both planet gears and function as roller bearings. The sun gear and the ring gears have similar roller extrusions. The gears' rolling surfaces in combination with roller rings perform the function of the carrier. However, due

to the fact that the planets, the sun gear and the ring gears are both gears, and bearing rollers, their radial positions are fixed with respect to each other. None of the gear components *float*, and thus, the planet load distribution can be quite uneven and catastrophic failure could occur at loads much lower than the rated ones. Furthermore, unavoidable eccentricity and angular misalignment due to manufacturing tolerance would require higher gear backlash to even assemble the gearbox. Extensive backlash in the meshing could lead to a significant drop in efficiency due to internal forces and misalignments. Using the gearbox as a joint raises addition concerns as side loads and moments are supported by the planets, therefore, friction and efficiency could significantly vary with the joint bearing load. Finally, the gear bearings require high machining accuracy and are quite difficult to manufacture as the roller surfaces also require hardening and grinding otherwise the gearbox life could be substantially reduced. Due to these possibly severe practical limitation of the gear bearing drive, it is not considered further in this thesis.

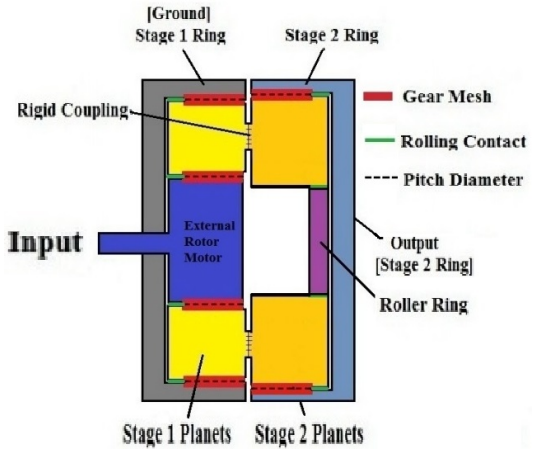

Figure 4.8: Gear Bearing Drive [101] ©2018 Springer.

4.2.6 Modifications of the Wolfrom Gearbox

This section discusses novel modifications to the Wolram gearbox layout described in Sec. 4.2.1. The first gearbox variant features profile corrected gears and is advantageous when very high reduction ratios are desired. The second variant may be suitable for low reduction application with large size motors.

Very High Reduction Double Planetary Row Gearbox

Very high reduction ratios may be achieved if the planetary layout shown in Fig. 4.5 is modified so that $z_f = z_g$ and $z_e = z_b \pm 1$. In this case, $R_{pe} = \frac{z_e}{z_e - z_b} = \mp z_e$, while R_{ap} remains the same. Therefore, the gearbox reduction ratio is given by:

$$R_{ae} = \mp z_e \left(\frac{z_a + z_b}{z_a}\right). \tag{4.12}$$

Eq. (4.12) suggests that reduction ratios beyond $1:1000$ are possible.

However, meshing of all gearing components requires the ring gears and the sun gear to be corrected so that the center distance between the planet gears z_f and the ring gear z_e is the same as the center distance between the planet gears z_g and the ring gear z_b. Corrected gears have pitch diameter that is larger or smaller than the standard value. This may be achieved by modifying the center distance between the blanks and the cutter (shaper, hobber, etc.) from the standard value for uncorrected gears, while the gear is being produced. Details regarding gear profile correction may be found in [103, 104].

For this gearbox design the planets cannot be uniform and the planet gears need to be displaced with respect to each other at a specific angle that reflects their position in the carrier, as described in Sec. 4.2.1. In addition, the requirement of Eq. (4.3) has to be satisfied, otherwise the sun gear z_a cannot be meshed with the planet gears z_g. However, due to the fact that $z_f = z_g$, the planets do not need to be aligned upon assembly and can simply be inserted at their respective positions on the carrier.

Fig. 4.9 shows a 3-D printed prototype of a Wolfrom Gearbox that features corrected gears and has reduction ratio of $1 : 419.2$. All gears have module $m1$.

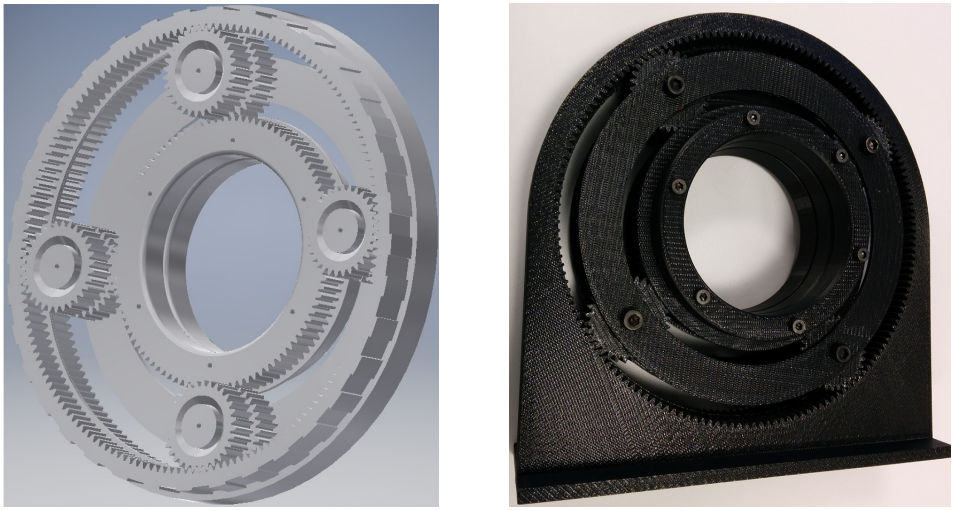

Figure 4.9: Example gearbox design with tooth correction. Left: CAD rendering. Right: 3D printed prototype.

Designs Without a Sun Gear

Wolfrom derived gearbox design without a sun gear is also possible. In this case, the motor drives the planet carrier directly. The physical coupling between the motor and the carrier may be realized in many way. Fig. 4.10 show a CAD rendering and

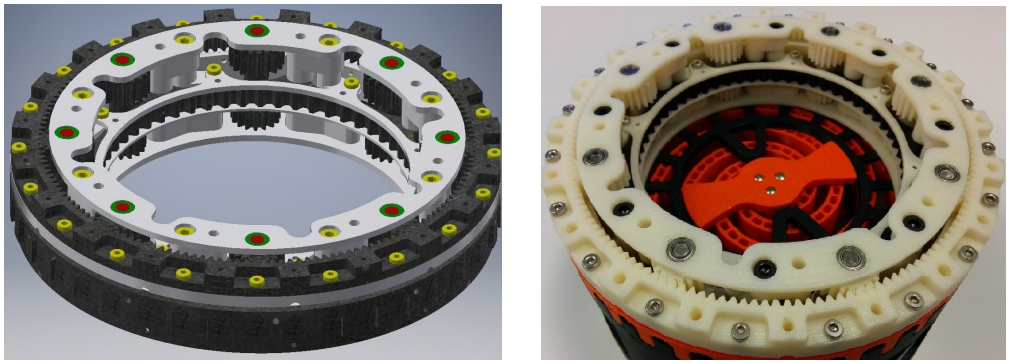

Figure 4.10: Example gearbox design without a sun gear. Left: CAD rendering. Right: 3D printed joint prototype that features the gearbox.

a 3D printed prototype of an early concept design that features a gearbox with no sun gear. It is intended to use an outrunner motor (see Sec. 3.3) to drive the carrier through involute splines. Designs without a sun gear are suitable for low reduction application as well as in some special cases for high reduction applications, provided tooth profile correction is used as described in the previous section. The gearbox reduction ratio is given by R_{pe} (see Eq. (4.5)). The angular velocity of the planets is:

$$\omega_{z_g} = \omega_{mot} \frac{z_b - z_g}{z_g}, \tag{4.13}$$

where ω_{z_g} is the motor angular velocity. Eq. (4.13) suggests that for such designs the planet speed ω_{z_g} may be multiple times the motor speed ω_{mot} if the ring gear z_b has a lot more teeth than the planet gears z_g. On the other hand, high gear tangential velocities may cause increased noise and vibration, lubrication issues and limitation, increased wearing, etc. [103, 104]. Therefore, designs that do not feature a sun gear, and have relatively small number of teeth on the planet gears, may not be suitable for use with high speed motors.

4.3 Bearingless Planetary Gearbox

This section introduces a novel *bearingless planetary gearbox* which is based on the Wolfrom gearbox layout of Sec. 4.2. Sec. 4.3.1 provides an overview of the gearbox structure and advantages. Sec. 4.3.2 provides a detailed strength analysis and Sec. 4.3.3 discusses the possible elimination of the gearbox assembly features. Sec. 4.3.4 describes bearingless planetary gearbox designs with assembled planets.

4.3.1 Kinematic Layout of the Bearingless Planetary Gearbox

In the conventional one stage planetary gearbox, the carrier is the output link and is of critical importance. However, in the planetary layout of Fig. 4.5 the carrier only provides radial and torsional support for the planets and does not transmit any load. The unbalanced radial and torsional loads are mainly due to the meshing forces associated with the planet gears and the ring gears. The carrier assembly consists of many components, some of which can require complex machining and tight tolerances [90]. Furthermore, it adds substantial mass to the gearbox and complexity to the planet design as discussed earlier. Bearing availability for a given design also imposes design constraints. These factors motivate the development of a novel *bearingless planetary gearbox*.

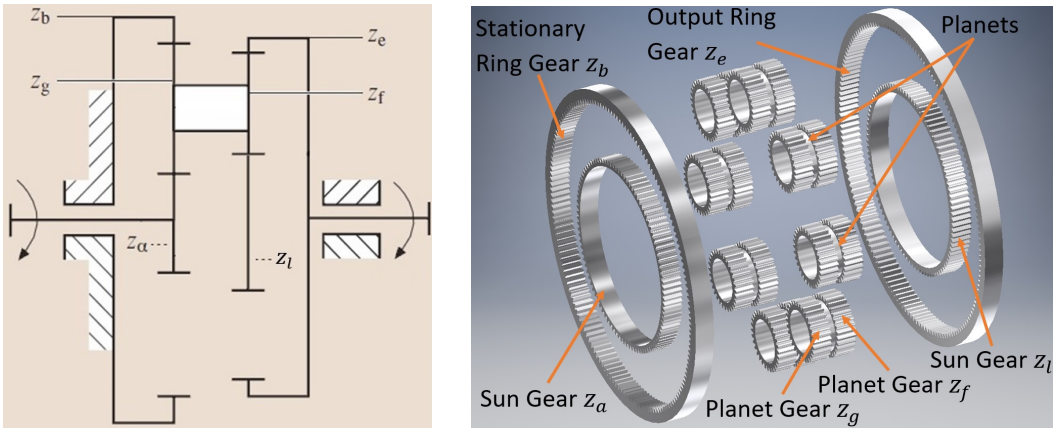

Figure 4.11: The Bearingless Planetary Gearbox kinematic layout (one left) and CAD rendeing (on right).

Fig. 4.11 shows the kinematic layout and example CAD rendering of a bearingless planetary gearbox design. The carrier is eliminated and a secondary sun gear z_l is introduced to provide the necessary support of the gear clusters. This modification can always be done if the planets are identical, which may be realized with the design constraints discussed in Sec. 4.2.2. To show this, let $z_e = z_b - k$ and assume that it is possible to mesh p_n planets. Then p_n is a factor of $z_a + z_b$ and $z_l = z_a + k$.

Therefore, $z_l + z_e = z_a + z_b$, and thus, p_n is a factor of $z_e + z_l$ and the gears of the planetary stage, given by z_l, z_f and z_e, may be meshed.

Eliminating the carrier and introducing the second sun gear, z_l, has the following consequences:

- The planets float freely: they are not constrained in the radial direction except by their meshing with the sun and ring gears. Thus, the load distribution of the planets is improved. The gearbox load rating may also be increased by adding more planets.
- The manufacturing complexity of the planets is reduced, as no bearings are required to mount the planets in a carrier. Therefore, gear cutting and finishing is the only critical step.
- The mass is significantly reduced as all gear components can be constructed with thin sections (see Fig. 4.11).
- The gearbox can be designed with reduced backlash.
- The assembly procedure is significantly improved. The planets can be inserted one by one instead of assembled simultaneously as part of a carrier.
- Designs with cheaper, moderately accurate gears are also possible (for example manufactured using injection molding, sintering, etc.). Applications that are not backlash sensitive, such as those that do not involve bi-direction gearbox driving, may benefit from low a cost bearingless planetary gearbox.

The improved gearbox compactness makes it ideal for integration into robotic joints so that the output ring gear is attached directly to the joint rotor. The possibly large sun gear diameter allows efficient mechanical coupling with the output of high performance outer rotor motors (see Sec. 3.3). Furthermore, the possible introduction of a central joint support shaft with central cabling holes may allow lighter and more compact joint structure.

Fig. 4.12 shows a bearingless planetary gearbox prototype. The gears are made of 4140 steel, have module $m1$ and out-of-plane thickness of $10mm$. All gears were machined on a CNC slotting machine in-house. The gearbox has eight planets and a reduction ratio of 1:101.

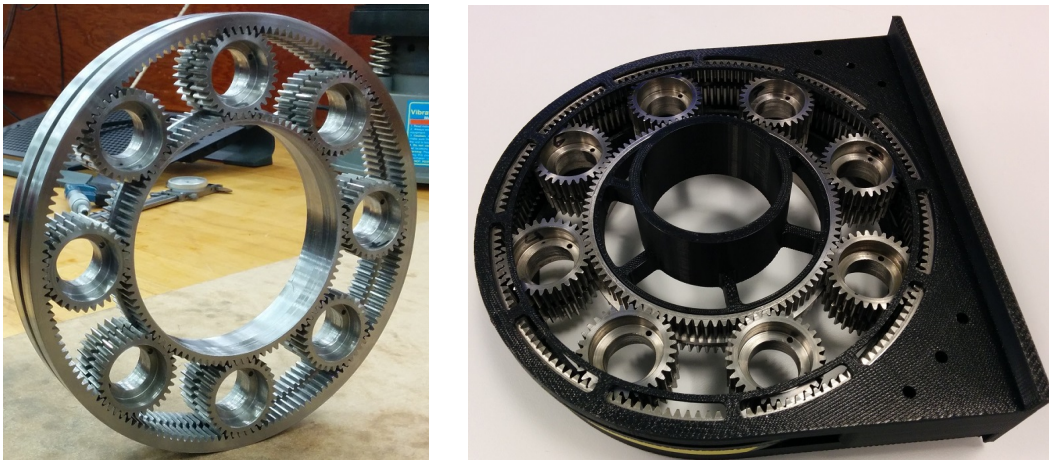

Figure 4.12: Bearingless planetary gear drive prototype. Right: prototype showing the floating nature of all components. Left: prototype in 3D printed case that axially constraints the motion of the gears. The gearbox diameter and width are 170mm and 23.175mm, while the driving sun gear diameter is 90mm. The weight is 1.1 Kg.

The bearingless planetary gearbox consists of two planetary stages that share the same gear cluster planets. A single planetary stage may have efficiency in the range of 0.96-0.98 [90]. Thus, depending on the manufacturing and gearbox design characteristics, it is expected that high efficiencies $\geq$ 0.9 may be achievable in practice. No experimental data confirming this is currently available and the gearbox efficiency characterization is subject of future research.

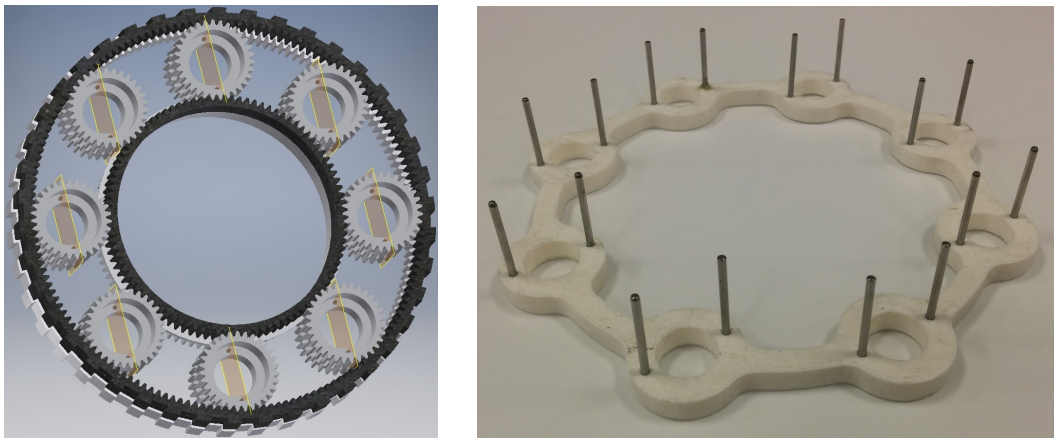

Figure 4.13: Left: CAD rendering showing the planet alignment. Right: assembly alignment part for the prototype show in Figure 4.12.

Eliminating the carrier does not remove the need for planet alignment. Fig. 4.13 shows a CAD rendering of the prototype shown in Fig. 4.12. All planets have the same orientation. In order to achieve this, an alignment part (Fig. 4.13) is used which places the planets in the correct position and orientation during assembly.

4.3.2 Bearingless Planetary Gearbox Strength Analysis

Unlike the Wolfrom gearbox of Sec. 4.2, the bearingless planetary gearbox does not feature a carrier, thus, the sun gears have to balance the radial and out-of-plane torsional loads from the meshing of the planet and ring gears. Hence, new strength analysis and design guidelines are necessary and are provided in this section.

Support of the unbalanced planet radial and torsional loads

In the bearingless planetary gearbox, similar to the Wolfrom gearbox, the largest tangential forces, F_g and F_f, are due to the meshing of the planet gears with the ring gears (see Fig. 4.6) and F_a is much smaller than F_g, F_f in magnitude. Due to the planets' floating nature, the radial loads due to the meshing of a planet gear with a ring gear is supported by the meshing of that planet gear with the corresponding sun gear. Therefore, the planet gears are *pushed* towards the sun gears and two

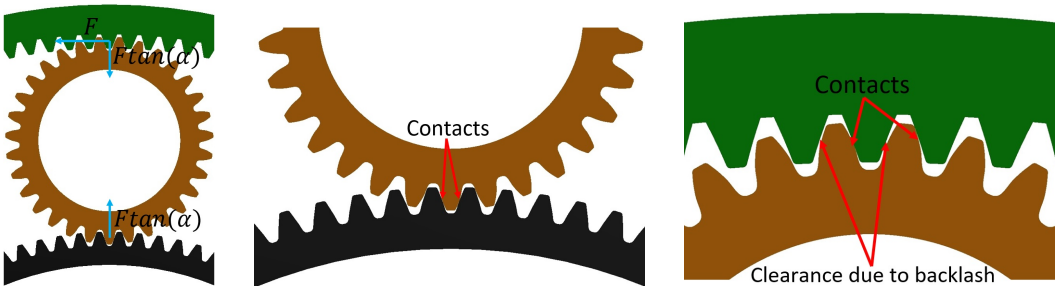

Figure 4.14: Left: plane gear forces due to meshing with ring gear and sun gear in the bearingless planetary gearbox. F is the tangential meshing force (corresponding to F_g or F_f) and α is the gear pressure angle. Middle: two sided contact between a planet gear and a sun gear. Right: clearance in the meshing between the ring gears and the sun gears due to gearing backlash.

sided tooth contact occurs between the sun gears and the planet gears as shown in Fig. 4.14. This two sided contact provides the radial support of the planet gears and the existing gearing backlash manifests into the development of clearance in the meshing between the planet gears and the ring gears as shown in Fig. 4.14. Thus, the number of planet gear tooth faces in contact at the sun gear is twice the number of faces in contact at the ring gear, which suggests that the additional radial load supported by the sun gears should not be sufficient to cause premature failure or extensive wearing. However, in the absence of a carrier, the meshing forces F_g, F_a and F_f (see Fig. 4.6) give rise to an unbalanced out-of-plane couple which has to be balance by the meshing of the planet's gears with the ring gears and the sun gears.

To understand the mechanics of this, two contact models are first considered: uneven one-sided meshing contact between the planet gears and the ring gears, and uneven double-sided contact between the planet gears and the sun gears. Regardless of their distributions, the total meshing contact forces of the planet gears with the sun and ring gears are the same for a given gearbox load and working conditions. Thus, the meshing load between the planet gears and the ring gears may be modeled as the meshing tangential forces, F_f and F_g, applied at the mid-plane of the planet gears and concentrated couples, τ_f and τ_g, of unknown magnitude (see Fig. 4.15). Similarly, the meshing contact between the planet gears and the sun gears may be modeled by concentrated couples, τ_a and τ_l. The sun gear meshing tangential force, F_a is ignored as it it is much smaller than F_g and F_f in magnitude, and thus, the sun gear stresses resulting from it, may be neglected. Then, from equilibrium: $F_f \approx F_g$ (see Fig. 4.6). Due to the two sided contact at the sun gears, the balancing radial forces may be ignored for the purposes of this analysis, provided the sun gears are not smaller than the planet gears. Fig. 4.15 shows the relevant forces and moments due

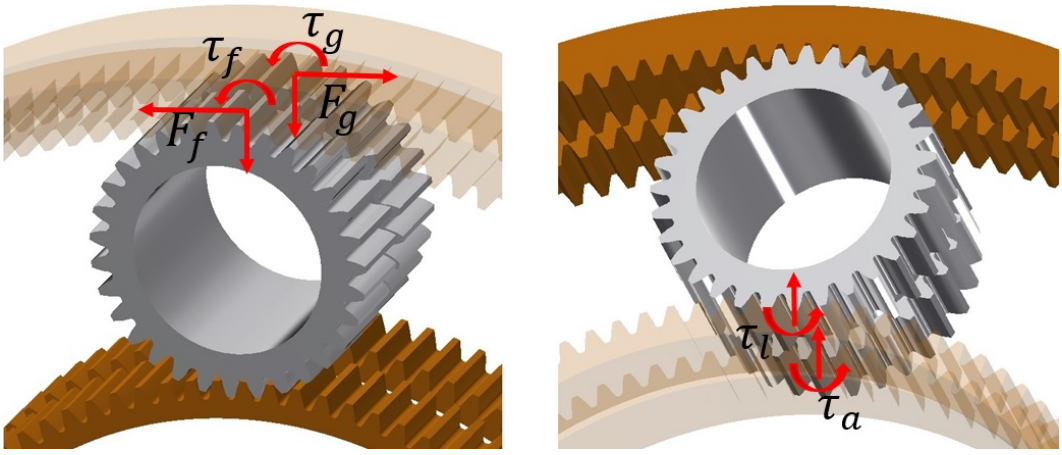

Figure 4.15: Planet meshing contact loads of the bearingless planetary gearbox.

to the gearing measing contacts. There are four unknown couples: τ_g, τ_f, τ_a and τ_l. As far as solid deformation is concerned, the teeth of all gearing components have similar shape and dimensions, thus, their strain response would be quite similar if subject to the same bending and torsional loads. If gears with less than 12 to 15 teeth are used, this assumption may not be valid due to substantial teeth root undercut. Without loss of generality, assume all gears have more than 18 teeth so there is no undercut. Therefore, the principle of super position combined with the principle of minimum potential energy suggests that $\tau_f \approx \tau_f \approx \tau_a \approx \tau_l \approx \frac{(F_g+F_f)b}{8} = \frac{F_f b}{4}$, as $F_g \approx F_f$. Eq. (4.7) and Eq. (4.8) suggest that $\sigma_H \propto \sqrt{\frac{T_e}{b}} \propto \sqrt{\frac{F_f}{b}}$. Then,

neglecting the effect of the planet gap, one should expect the contact pressure distribution, shown in Fig. 4.16, between the planet gears and the ring gears. The maximum value of the distribution (Fig. 4.16) is twice the value of the contact pressure between a planet gear and a ring gear in the equivalent Wolfrom gearbox that has the same planets, ring gears and driving sun gear, and is subject to the same load. Therefore, for a bearingless planetary gearbox design: $\sigma_H \approx \sqrt{2}\sigma_H^w$, where σ_H^w is the maximum gear Hertz stress in the equivalent Wolfrom gearbox. This simple analysis, suggest that the bearingless planetary gearbox may require Hertz stress load derating of more than 30%. In a similar fashion the effect of the meshing couples on the gear bending strength may be analyzed. However, as discussed in Sec. 4.2.3, in most designs, the gear module, m, may be chosen so that the Hertz stress determines the gearbox strength. Therefore, the effect of the meshing couples on the gear bending strength is not further considered analytically.

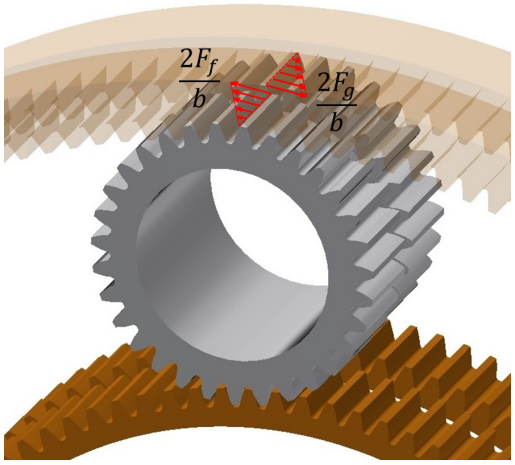

Figure 4.16: Contact pressure distribution in the meshing between the planet gears and the ring gears in the bearingless planetary gearbox, neglecting the effect of the airgap. The peaks of the two distributions for the planet gears z_f and z_g are $\frac{2F_f}{b}$ and $\frac{2F_g}{b}$, respectively.

The analytic strength considerations of this section provide rough approximations and FEA modeling is used as the primary tool for determining the bearingless planetary gearbox strength as discussed in the following section. Nevertheless, the simple analysis provides qualitative understanding of the causes of the uneven stress distributions and how one could improve them. For example, design with ring gears of thin out-of plane thickness may be employed as shown later in the section. Future development of the bearingless planetary gearbox and similar floating component gearboxes will be centered at reducing and eliminating the unbalanced out-of-plane coupling load.

FEA-based strength analysis

The goal of this section is to establish consistent procedures for estimating the bending and Hertz stresses in the bearingless planetary gearbox under load. The bending and Hertz stress expressions in Eq. (4.8) are empirical, therefore, FEA results may not be used directly in these formulas.

This section proposes the introduction of derating constants in Eq. (4.8) that are estimated using FEA so that Eq. (4.8), Eq. (4.9) and Eq. (4.10) may be used with a bearingless planetary gearbox design. First, for a reasonable load, the bending and Hertz stresses in the bearingless planetary gearbox design are FEA estimated. Next, the bending and Hertz stresses in the equivalent Wolfrom gearbox design under the same load are also FEA estimated. Finally, the approximate derating bending and Hertz stress coefficients for the bearingless planetary gearbox are estimated by comparing the FEA results for the two gearbox designs.

This procedure is demonstrated for the gearbox design of Fig. 4.13. Fig. 4.17 shows FEA simulation model and mesh for both the bearingless planetary gearbox design and for the equivalent Wolfrom gearbox design. Mesh control is used to significantly reduce the element size in the areas where tooth contact may occur.

Fig. 4.18 show the FEA simulation results for the stresses in the contact areas between the ring gears and the planet gears for both gearboxes. As expected, uneven contact occurs that causes increased Hertz and bending stresses in the case of the bearingless planetary gearbox. The maximum bending and Hertz stresses for the Wolfrom gearbox are given by approximately $\sigma_F = 70MPa$ and $\sigma_H = 260MPa$, respectively. The maximum bending and Hertz stresses for the bearingless planetary gearbox are given by approximately $\sigma_F = 105MPa$ and $\sigma_H = 400MPa$, respectively. Therefore, one may introduce derating coefficients for the bending and Hertz stresses, given by $\eta_F = 0.65$ and $\eta_H = 0.65$, respectively.

Fig. 4.19 show the FEA simulation results for the stresses in the contact areas between the sun gears and the planet gears for the bearingless planetary gearbox. The couples τ_a and τ_l lead to uneven two sided contact. The figure also shows exaggerated deformation renderings which confirm one sided contact at the ring gears under load and show the resulting torsional planet deformation due to the unbalanced load couple.

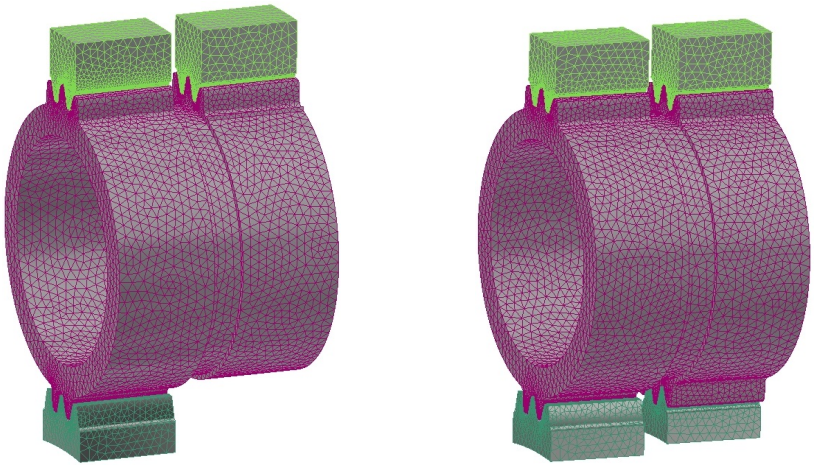

Figure 4.17: FEA model and mesh of Wolfrom gearbox (on left) and bearingless planetar gearbox (on right). For both gearboxes, the sun and ring gears are constrained to rotate around their centers. A load of $25Nm$ is applied to both gearbox ring gears (supported by only one planet). The planet of the bearingless planetary gearbox is floating while the planet of the Wolfrom gearbox is constrained so that it may only rotate around its axis.

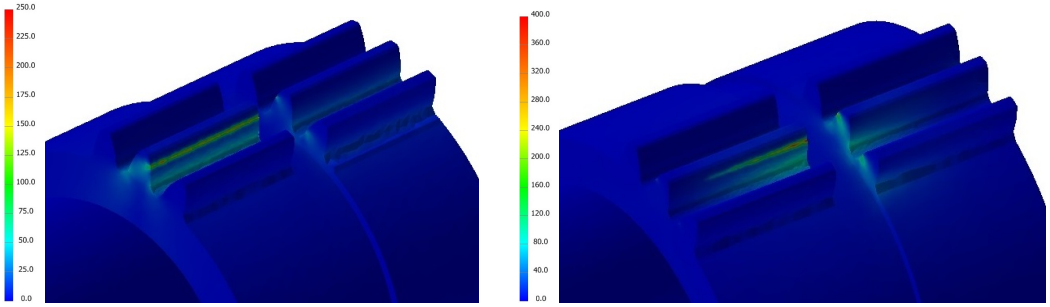

Figure 4.18: FEA simulation results for the stress distribution in the planet gears due to the meshing with the ring gears for the Wolfrom gearbox (on left) and bearingless planetary gearbox (on right). A load of $25Nm$ is applied to both gearbox ring gears (supported by only one planet). The stress in the ring gears is not shown because it is lower than the stress in the planet gears, as predicted by the analysis of Sec. 4.2.3.

In the case of the bearingless planetary gearbox, Eq. (4.9) and Eq. (4.10) become:

$$\begin{aligned} \sigma_H &= \frac{C_H}{\eta_H}\sqrt{\frac{1}{d_f}\left(\frac{u_{ef}-1}{u_{ef}}\right)\left(\frac{T_e}{p_n b d_e}\right)} \\ \sigma_F &= \frac{C_F}{\eta_F}\left(\frac{1}{m}\right)\left(\frac{T_e}{p_n d_e b}\right). \end{aligned} \tag{4.14}$$

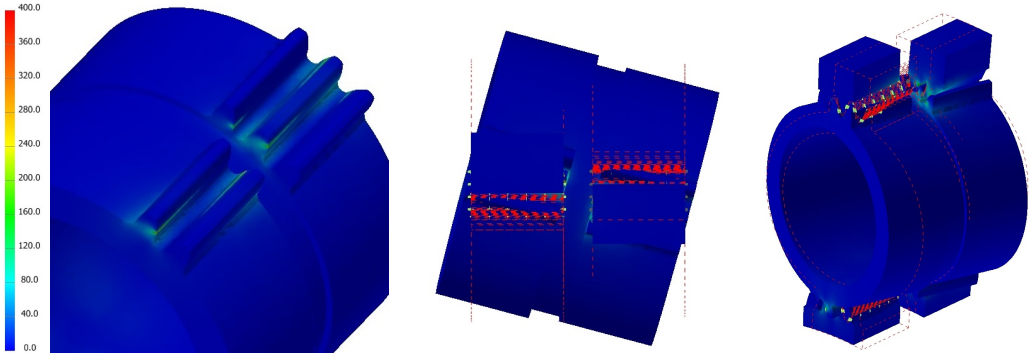

Figure 4.19: FEA simulation results for the stress distribution in the planet gears due to the meshing with the sun gears for the bearingless planetary gearbox (on right). Exaggerated FEA simulation views of the deformation are shown in the middle and on the right.

and

$$T_e \leq \eta_H \left(\frac{[\sigma_H]}{C_H}\right)^2 \left(\frac{u_{ef}}{u_{ef}-1}\right) d_f (p_n d_e b)$$
$$T_e \leq \eta_F \frac{[\sigma_F]}{C_F} m (p_n d_e b), \tag{4.15}$$

respectively. The derating coefficients, $\eta_F = 0.65$ and $\eta_H = 0.65$, are somewhat larger than expected. This is due to the large planet gap of $0.125in$ ($3.175mm$). Reducing the planet gap to $0.1mm$ (which is an unrealistically small value) leads to stress reduction of as much as 10%. Therefore, in the design of the bearingless planetary gearbox one should try to minimize the size of the planet gap as much as possible.

Eq. (4.15) allows one to estimate the maximum torque that the gearbox of Fig. 4.13 may sustain, assuming the load is distributed evenly between all the planets. For refined C 45 steel ($\sigma_{[H]} = 430MPa$ and $\sigma_{[F]} = 356MPa$), the maximum torque is $T_e \approx 125Nm$, calculated from the Hertz stress and $T_e \approx 360Nm$ from the bending stress. On the other hand, face hardened 4340 steel ($\sigma_{[H]} = 1160MPa$ and $\sigma_{[F]} = 705MPa$) leads to maximum torque of $T_e \approx 830Nm$, calculated from the Hertz stress and $T_e \approx 720Nm$ from the bending stress. It is important to note that these are continuous torque ratings without a safety factor or consideration of the working conditions such as maximum speed, lubrication, load distribution, etc. In general, the peak torque ratings would be significantly higher.

Designs with thinner ring gears

The FEA simulation results from the previous section suggest that due to the unbalanced couple, the gearbox load is supported by only part of the faces of the ring gears because of the uneven meshing contact with the planet gears. Therefore, the ring gear out-of-plane thickness may be reduced while the thickness of the other gearing components is preserved, without deteriorating the gearbox torque performance. As previously discussed (see Fig. 4.6), the ring gears support the gearbox output torque, and thus, large tangential forces occur in the meshing between them and the planet gears. Therefore, the ring gears require a relatively large in-plane-thickness and their mass may account for a large portion of the total gearbox mass. Then, reducing their thickness may lead to significant gearbox torque density increase. Fig. 4.20 shows FEA simulation mesh and stress distribution for the bearingless planetary gearbox design of Fig. 4.13 with ring gears of half out-of-plane thickness. In generating the FEA stress distribution in Fig. 4.20, the same torsional loading

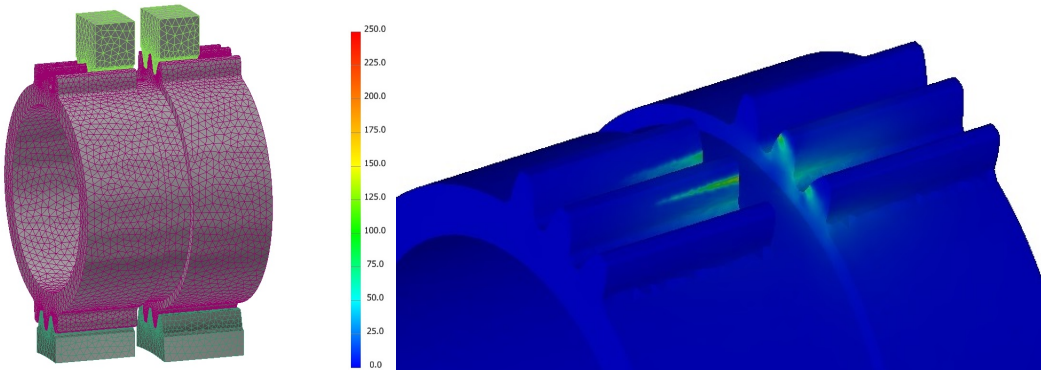

Figure 4.20: FEA simulation model and mesh (on left), and simulation results (on right) for the stress distribution in the planet gears due to the meshing with the ring gears for the bearingless planetary gearbox with thinner ring gears.

is used as for the FEA results of Fig. 4.18. Comparing the stress distributions in Fig. 4.20 and Fig. 4.18 shows that reducing the ring gear out-of-plane thickness by half does not lead to planet bending or Hertz stress increase. Therefore, the FEA simulation results confirm that advantageous bearingless planetary gearbox designs with thinner ring gears are possible.

Choice of number of planets

If the planets are more than four, there is no guarantee that the load will be equally distributed between them despite the advantages of the bearingless planetary gearbox

and regardless of the accuracy of the gears [90]. Nevertheless, even if the load is not evenly distributed, additional planets do increase the life of the gearbox. Then, a lower number of planets with equal load distribution can be assumed at the design stage and the gear material maximum admissible stresses updated to reflect the introduction of more planets [90]. Therefore, the floating nature of the planets would certainly lead to a significant load rating increase if a larger number of planets is utilized.

Furthermore, a higher number of planets is also desirable because they provide the support of the floating components and in the case of thin section sun gears, infinitesimal deformations could lead to improved load distribution as well. The planet performance requires experimental characterization which is subject of future research.

Gear Tangential Velocity

An important gearbox design aspect that has not been discussed yet, is related to the gears' rotational speed. The tangential (or circumferential) velocity of the gears is an important factor that may determine the required manufacturing accuracy for smooth and quiet gearing [90, 103]. In the case of the bearingless planetary gearbox, the sun gear z_a and the planet gear z_g have the same tangential velocity which is the highest gear tangential velocity in the gearbox and is given by:

$$v_a = \frac{(mz_a)\omega_a}{2} \tag{4.16}$$

where ω_a is the angular velocity of the sun gear. For example, spinning the sun gear of the gearbox prototype of Fig. 4.13 at $4000RPM$, results in $v_a \approx 20m/s$. Full load, smooth and quiet operation at this rotational speed require gearing of extra accuracy (class 6) [90, 103].

As far as most robotic applications are concerned, actuators rarely operate at maximum power, even for short amount of time as discussed in Ch. 3. Fast manipulation of relatively light objects or limb swinging in legged robots, are example applications where joints carry minimum loads at high angular speed. On the other hand, slow manipulation of heavy objects or standing and walking in legged robots, are example applications where joints carry excessive loads at low to mid angular speed. Therefore, peak tangential gear velocities exceeding the maximum value for the particular gear class can be allowed in robotic applications provided the peak power and noise levels are acceptable.

However, dynamically challenging and highly repetitive robotic motions, such as running, may involve short time intervals where the actuators are fully loaded at high angular speed so that sufficient energy can be injected into the system while the robot is in contact with the ground. For such applications that require highly repetitive, short peak power intervals, lower gear tangential velocities may be required to avoid excessive gearbox wear and noise.

Therefore, in the case of the bearingless planetary gearbox, the maximum tangential gear velocity can enforce important gearbox design constraints and trade-offs. For example, choosing a design with a large sun gear z_a allows incorporating a high torque outer-rotor motor inside the gearbox that directly drives the sun gear z_a. However, in this case the maximum motor speed may be limited by the condition that the tangential velocity (Eq. (4.16)) should not exceed a maximum allowable value. Alternatively, costly manufacturing or finishing may be required to achieve a successful design.

4.3.3 Removal of the Planet Assembly Features

The planet design of the prototype of Fig. 4.12 has assembly features comprised of holes in the planet interior which serve two purposes:

- they align the planets to their correct orientation w.r.t. each other upon assembly, using the assembly jig of Fig. 4.13.
- they ensure that the orientation of the two planet gears is consistent among all planets (up to the given manufacturing tolerance). *E.g.* the two planet gears have an aligned tooth which is precisely oriented w.r.t. the holes.

Due to the removal of the carrier, the planets need not be simultaneously aligned and assembled in the gearbox. Thus, as long as the orientation of the two planet gears is identical (up to the given manufacturing tolerance) and an alignment tooth is consistently indicated on each of the planets, they may be correctly oriented and assembled by inspection.

As far as manufacturing is concerned, the planets do not require assembly features if both planet gears can be machined without removal of the blank midway. If $|z_f - z_g| \geq 5$ the two planet gears may be cut consecutively from the same side. Thus, the planet blanks do not need to be turned in order to cut both planet gears. However, this is not true if $|z_f - z_g| \leq 4$. Nevertheless, it is still possible to cut both

planet gears without rotating the blank, provided each gear is cut from a different direction, *e.g.* the top gear is cut from above and the bottom gear is cut from below. Such double-sided shaping may be realized by attaching two shaper cutters as shown in Fig. 4.21. In this case, the bottom cutter is used to shape the top gear while the top cutter is used to shape the bottom gear.

Therefore, if the gear teeth are large enough ($m \geq 1mm$) so that the planets may be aligned by inspection upon assembly, they need no assembly features provided the aforementioned manufacturing techniques are adopted. Fig. 4.22 shows bearingless planetary gearboxes which are used in actuator prototypes (see Sec. 6.2 and Sec. 6.3) and are designed, manufactured and assembled without planet assembly features. The average gear normal backlash of the prototypes' components is around $0.03mm$. Normal backlash is calculated by measuring the distance between a specific number of teeth which depends on the gear size and comparing it to tabulated standard values.

Figure 4.21: Compound planet manufacturing using double-sided shaping.

4.3.4 Bearingless Planetary Gearbox Designs With Assembled Planets

The planets need not be comprised of a single solid piece. Instead the two gears may be assembled either directly to each other or mounted on a support part using keys, splines, press fit, frictional joint, etc. The advantages of these alternative planet construction methods are:

- the two planet gears are individually cut and finished which reduces the manufacturing cost and complexity.
- the planets may either be assembled individually using an assembly jig that aligns the two gears to their correct orientation w.r.t each other or rigidly connected once the planet gears are meshed with the ring and sun gears in the formed two planetary stages.

- for some gearbox designs with assembled planets, gears of lower backlash may be used which promotes better contact ratio, leading to smoother meshing and lower wearing as the unavoidable orientation error characteristic of solid planets need not be compensated for.

Figure 4.22: Prototype of the bearingless planetary gearbox with no planet assembly features. The gearbox on the left is a remake of the gearbox of Fig. 4.12 with substantially lower backlash and is used in the actuator prototype of Sec. 6.3. The gearbox on the right has reduction ration of $1 : 10$ and is used in the actuator prototype of Sec. 6.2.

In addition to the aforementioned advantages, assembled planet designs promote rapid gearbox prototyping which may be quite useful at the early prototyping stages of novel complex actuation systems. Manufacturing of low quantity custom design gears is quite costly and usually has long lead times. On the other hand, commercially available gears have large and inconsistent normal backlash. This motivates investigating techniques for backlash-free gearbox prototyping with commercial gears.

Backlash removal in bearingless planetary gearboxes with assembled planets

The amount of backlash in the meshing of two gears may be controlled by adjusting their center distance. Therefore, the backlash in one or a small set of planets contained in a small region around the sun gear may be significantly reduced or effectively removed, if first, the sun gears are displaced so that the center meshing distances between the gears of these planets and the sun and ring gears is minimized (see Fig. 4.23). Once this is done, the gears in each of these planets are rigidly connected to each other using one of the aforementioned methods, *e.g.* using a

frictional joint. Next, the gears in each of the remaining planets are displaced w.r.t. each other so that half of these planets supports torque with no backlash in one of the gearbox rotational directions while the other half supports torque with no backlash in the other direction. Once this is done, the gears of these planets are rigidly connected to each other.

In this bearingless gearbox variant, the planets of minimum meshing center distance ensure that the backlash of the gearbox output is eliminated, while the two sets formed by the rest of the planets ensure constancy of the meshing distances of all gearing components, regardless of the rotational direction.

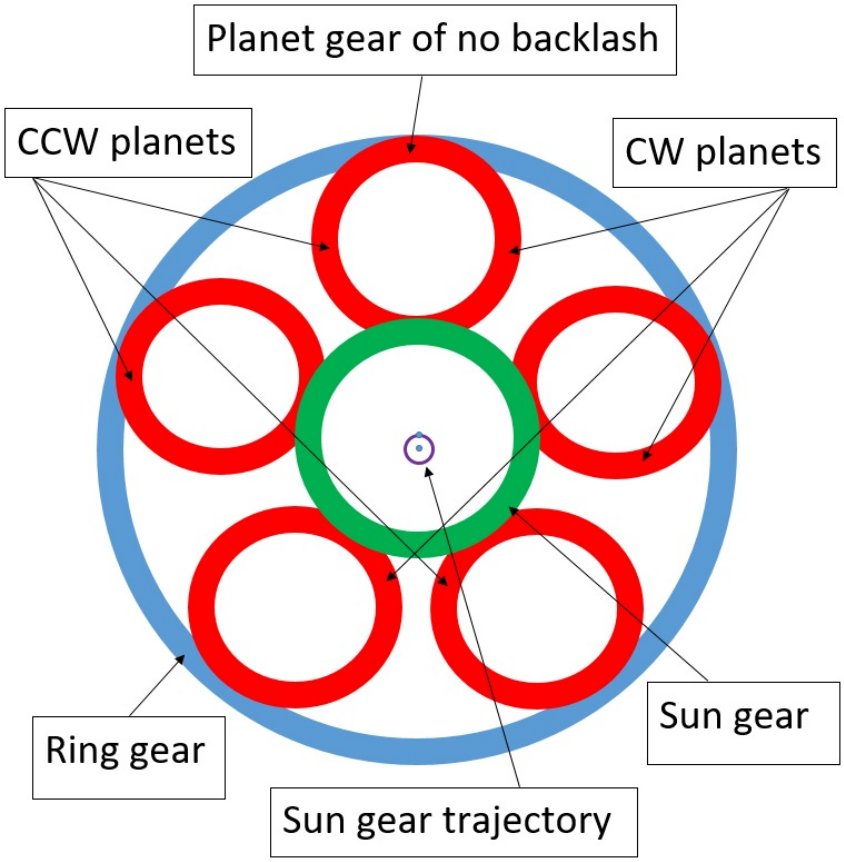

Figure 4.23: Schematic construction of a backlash-free bearingless planetary gearbox with five assembled planets.

Fig. 4.23 shows a schematic construction of a backlash-free bearingless planetary gearbox with five assembled planets. The planets may be split in two set: one that supports torque in the clockwise (CW) direction and one that supports torque in the counter-clockwise (CCW) direction. The two sets share the planet that has minimum gear meshing center distances. The gear meshing center distances of the

rest of the planet gears are larger, and thus, they have lower contact ratio [103]. Too low contact ratio (≤ 1.2) may lead to increased gear wearing, which poses an upper bound on the maximum gearing backlash that may be compensated. Furthermore, three planets that are positioned in irregular fashion around the sun gear share the load in either direction, therefore, one of the planets may end up supporting higher loads than the rest, and thus, wear out faster. Such irregularity is typical for gearboxes with compensated backlash. For these reasons, bearingless planetary gearboxes constructed in this fashion using commercial gears are only suitable for proof of concept prototyping.

As shown by the purple circle in Fig. 4.23, due to the different planet gears meshing center distances, the centers of the sun gears follow a circular orbit around the centers of the ring gears. This eccentricity is particularly important for the driving sun gear which should be coupled to the motor using a flexible coupling to ensure smooth gearbox operation.

Prototype of a beringless planetary gearbox with assembled planets

Fig. 4.24 shows pictures of a bearingless planetary gearbox prototype with assembled planets that features the construction of Fig. 4.23. The gearbox is used as part of SEA tether management system of the Axel rover developed at the NASA Jet Prop. Lab. [36] (see Sec. 6.4). The gearbox has $1:36$ reduction ratio and excellent back-

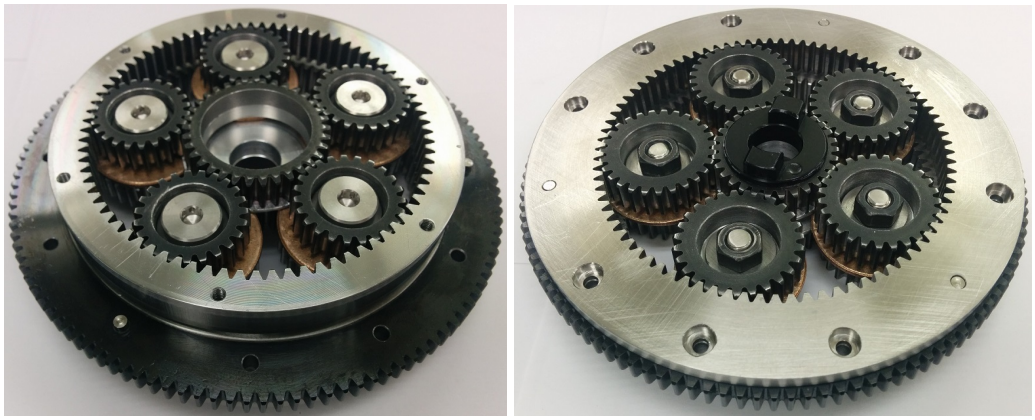

Figure 4.24: Prototype of a bearingless planetary gearbox with assembled planets. It is used in the actuator prototype of Sec. 6.4

.

drivability. Commercial SDP-SI gears featuring in-house modifications were used for the prototype construction. Fig. 4.25 shows a section view of the planet design.

A belleville washer provides compression force ensuring a constant frictional coupling between the two gears. The planet is axially constrained by a thrust bearing.

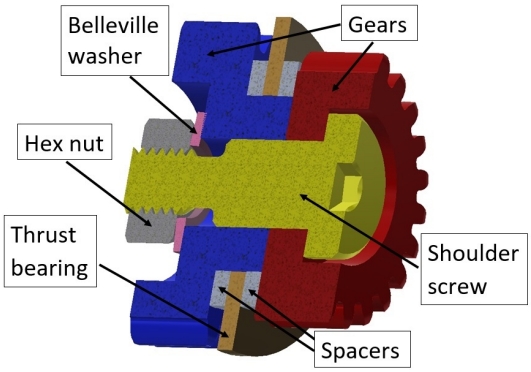

Figure 4.25: Assembled bearingless planetary gearbox planet design.

Despite the large commercial gears' normal backlash in the range from $0.08mm$ to $0.16mm$, the gearbox is backlash-free. This is achieved by assembling the gearbox utilizing a fixture that constrains the sun and ring gears so that one of the planets meshes without backlash with the sun and ring gears as discussed in the previous section. The backlash of the rest of the planets is then removed by displacing the gears in each planet with respect to each other by manually pushing while tightening the nut and flattening the belleville washer.

Thus, the main advantage of this bearingless planetary gearbox variant is that it can be constructed backlash-free with standard gearing components with small post purchase modifications. The planets mass is, however, significantly higher compared to the thin section design of Sec. 4.24. Therefore, the main disadvantages of such designs are the increased gearbox mass and inertia due to the additional planet components and the possibly higher wearing and noise due to the lower contact ratio and increased load on some of the planet gears.

A three-piece flexible coupling connects the driving motor rotor to the driving sun gear. In general, such three-piece couplings are designed to tolerate large shaft misalignment, and are thus, ideal for interfacing the gearbox sun gear with its eccentric motion.

4.4 Conclusion

Motivated by the shortcomings of existing speed reducers used in robotic application, this chapter introduces a novel *Bearingless Planetary Gearbox*. The concept is based on the Wolfrom Gearbox which is first analyzed to demonstrate potential torque density advantages and allow practical design improvements. The novel bearingless planetary gearbox does not feature a carrier and all gearing components float, therefore, its advantages may include improved robustness, load distribution and assembly. The gearbox features low number of light, readily manufacturable components that may be integrated compactly into robotic joints. The chapter concludes with detailed strength analysis and modifications that further improve the gearbox manufacturing readiness and suitability for prototyping of novel actuators and mechanisms.

Chapter 5

ANALYSIS AND DESIGN OF PLANAR ROTARY SPRINGS

5.1 Introduction

The chapter is concerned with the analysis, design, and prototyping of rotary planar springs for robotics applications such as rotary series elastic actuators. Such springs may be suitable for applications that require efficient mechanical energy storage, torsional passive compliance of any kind, misalignment tolerant flexible coupling of components, etc. The first key contribution of this chapter is the development of a mathematical model, based on curved beam theory, that allows rapid design, analysis, and comparison of rotary springs that have arbitrary arm shape. The model may be used to formulate a search algorithm for optimal spring design given a predetermined arm shape. Two spring mass reduction methods via composite arm structures, or arm cutouts are also introduced. The second key contribution is a complete analysis algorithm that allows for rapid spring torsional loading response simulation with possible internal contacts between the spring arms. Typically overload spring protection is achieved by the addition of hard stops which limit the spring maximum displacement. The chapter introduces an alternative approach to overload protection based on arm contacts. The third key contribution is the development of an optimization-based design methodology which maximizes the springs' overall torque density through optimization of the arm profile. The proposed design approach is theoretically motivated and alternative ways of spring optimization are considered. The proposed design and analysis algorithms are validated through nonlinear FEA and mechanical testing of manufactured prototypes.

5.1.1 Previous SEA Rotary Spring Designs

The main job of SEAs is to implement force control and compliance with a prescribed rotary stiffness in order to achieve actuator performance goals (see Sec. 1.1). The compliant elements of rotary SEAs should be able to tolerate small misalignments and side loadings like mechanical flexible couplings. Commercially available couplings are designed to connect an input shaft (*e.g.*, a motor) to an output shaft (*e.g.*, a ball screw rod), and are not designed for applications that require high torque capabilities and lower stiffness.

A great variety of SEA springs can be found in the literature. Fig. 5.1 shows rotary spring designs based on linear springs. In these designs the springs are prestressed to ensure uniformity. As the figure suggests, they also feature high complexity. Rough performance calculations suggest that high torque, low stiffness requirements needed for SEA applications result in linear spring designs that require excessively large and massive assemblies.

Figure 5.1: Linear springs based designs. Left [10] ©2009 IEEE and right [9] ©2005 Springer.

Fig. 5.2 show spiral-based spring designs developed in previous research efforts. The spring shown in Fig. 5.2a is a single spiral wound from a steel strip while the rest of the spiral springs are manufactured from a high grade steel plate through electrical discharge machining. The springs in Fig. 5.2b and 5.2c are based on Archimedean spirals. All the springs in Fig. 5.2a, Fig. 5.2b and Fig. 5.2c are designed using principles of elementary spiral torsion spring theory [106]. The modeling and analysis framework presented in Sec. 5.2.2 is a substantial improvement over these classical, and highly simplified, design models. The spring in Fig. 5.2c is designed by iterative optimization of the shape using Finite Element Analysis (FEA). The springs shown in Fig. 5.2e and Fig. 5.2f are based on the same principle. In these prior works, a spring geometry is chosen, and then modeled in an FEA system. The FEA analysis is iterated in an *ad hoc* way, with small changes to design parameters, until a design which meets performance criteria while satisfying packaging constraints is determined. Among the various designs presented in the literature, of most interest are the planar rotary springs machined from a solid plate, due to their manufacturing advantages.

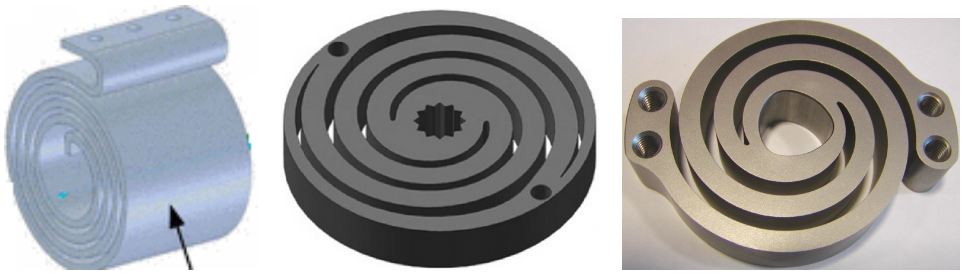

(a) [107] ©2011 IEEE (b) [12] ©2010 IEEE (c) [13] ©2010 IEEE

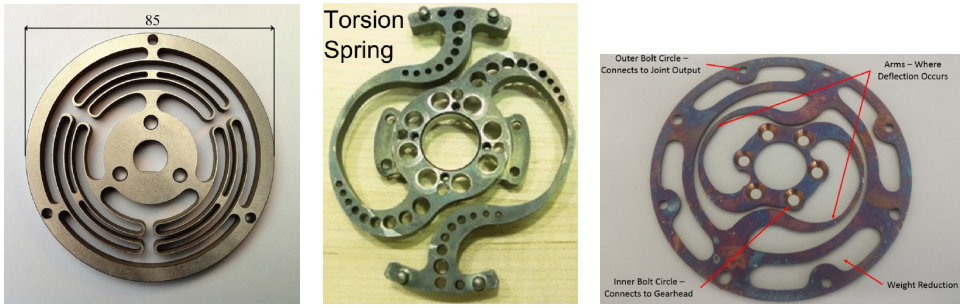

(d) [108] ©2012 IEEE (e) [15] ©2015 Wiley (f) [109] ©2017 IEEE

Figure 5.2: Previous Spiral Spring Designs.

In robotic applications, the actuator torque density is a crucial performance factor. Actuators' weight contributes for a significant portion of a robot's overall weight. Furthermore, mobile and limbed robots need to support their own weight, which poses considerable actuator challenges. SEA compliant elements can have considerable mass, therefore, improving their torque density, by lowering their mass, can substantially impact the overall robotic system performance. In [110], the compliant element shape is FEA-optimized so that its volume utilization or form coefficient is improved. The arm profile thickness variations that can be observed in Fig. 5.2e and Fig. 5.2f, suggest a similar optimization approach, however, no design details are provided in [15] and [16]. To the best of the author's knowledge, no systematic spring design procedure or consistent performance optimization algorithms have been previously introduced in the literature.

5.1.2 Contributions and Chapter Structure

Sec. 5.2 proposes a systematic planar rotary spring modeling and analysis procedure. A new mathematical model for multi-armed rotary springs with significant lattitude in the arm design is presented (Sec. 5.2.2). Two methods for spring mass reduction, based on composite materials or *cutouts*, are introduced (Sec. 5.2.4). By reducing the spring mass, these methods improve the torque density. This is the first rigorous methodology to minimize rotary SEA spring mass without compromising its performance. The design and manufacturing of two spiral spring prototypes based on the proposed analytical model are described (Sec. 5.2.6 and Sec. 5.2.7). The validity of the mathematical model is confirmed through mechanical torsional testing of the prototypes.

Sec. 5.3 discusses internal spring arm contacts. A systematic model of arm contacts is first introduced (Sec. 5.3.1). Then, a complete spring torsional analysis algorithm that accounts for arm contacts is presented (Sec. 5.3.2).

Sec. 5.4 presents a consistent optimization-based spring design procedure. This is the first rigorous method to optimize SEA spring performance. The optimization-based approach is first motivated (Sec. 5.4.1). Then, a complete optimization-based spring design algorithms is presented (Sec. 5.4.2). Finally, the design and analysis of an aluminum spring prototype are described (Sec. 5.4.3). The validity of both the analysis algorithm of Sec. 5.3 and the optimization-based design algorithm are confirmed through FEA and mechanical prototype testing.

5.2 Planar Rotary Spring Modeling

The section begins with a definition of the spring design goals and constraints (Sec. 5.2.1). Next, a mathematical model for rapid analysis and simulation of planar rotary springs is introduced (Sec. 5.2.2). The spring arms may be of an arbitrary shape. A brief discussion of out-of-plane buckling is also provided (Sec. 5.2.3). Next, modeling of composite arm designs is presented (Sec. 5.2.4). The section concludes with a model specialization to spiral arms (Sec. 5.2.5) and the design, and testing of two spring prototypes (Sec. 5.2.6 and 5.2.7).

5.2.1 Spring Structure

Fig. 5.3 shows a general planar rotary spring structure, consisting of arms that meet at inner and outer circles. The arms need not assume a spiral shape. The arm ends can be either pinned or fixed at the inner and outer circles. These attachments can be physically realized in many ways (*e.g.*, the arms can be joined to a solid material center and a solid outer rim). The spring action is realized when the outer circle rotates relative to the inner circle (while their centers remain concentric).

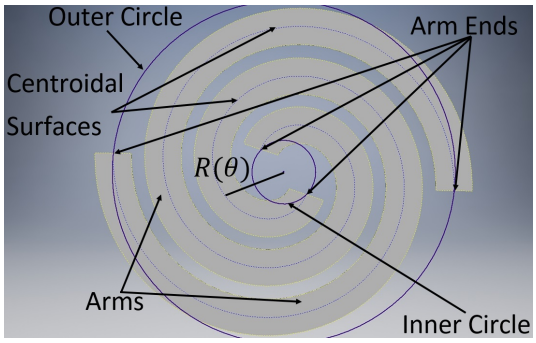

Figure 5.3: Planar rotary spring structure.

A spring design starts with the choice of the inner (with radius R_{in}) and outer (with radius R_{out}) circles. Their sizes are typically a function of mechanical packaging constraints. Next the arm shape (*e.g.*, a spiral) and arm material are determined. A significant portion of the chapter's later sections is devoted to the arm shape design. The stiffness of a planar rotary spring is linearly proportional to its out-of-plane thickness t and can be scaled to satisfy other constraints.

5.2.2 Spring Mathematical Model

The section introduces a mathematical model that is the basis for the planar rotary spring design and analysis methods described in this thesis. Previous planar rotary spring designs utilize elementary spiral spring theory [106] or employ iterative FEA techniques. Instead this section develops a model based on curved beam theory.

The model uses the Euler-Bernoulli theory of elasticity and assumes that the spring material obeys Hooke's law. "Small" deformation strains are also assumed. The spring incorporates n planar arms. Without loss of generality, it is assumed that

$n \geq 2$, and that the arms are arranged in a rotationally symmetric way so that there are no unbalanced radial forces. All the arms are also assumed to be uniform so that it is sufficient to consider only one of them. If this is not the case, the ODE described in Eq. (5.13) can be specialized for each arm. The arm geometry is defined in polar coordinates: $R(\theta)$ for $\theta \in [\theta_{min}, \theta_{max}]$ describes the location of the arm's centroid surface, as shown in Fig. 5.3.

The arm is modeled as a thin curved beam with rectangular cross section, as shown in Fig. 5.4, and assumed to be *slender*. Next, it is necessary to find the neutral surface and eccentricity of the beam. To do so, first the radius of curvature of the beam's centroid surface is found, which is given by:

$$r_c(\theta) = \frac{(R(\theta)^2 + (R(\theta)')^2)^{3/2}}{|R(\theta)^2 + 2(R(\theta)')^2 - R(\theta)R(\theta)''|} \tag{5.1}$$

where the derivatives in Eq. (5.1) are taken with respect to θ. Let $d(\theta) = b(\theta) - a(\theta)$ be the beam's in-plane thickness. From Sec. 5.2.1, recall that t is the beam's out-of-plane thickness (see Fig. 5.4). The inner and outer curvature radii of the beam are $a(\theta) = r_c(\theta) - d(\theta)/2$ and $b(\theta) = r_c(\theta) + d(\theta)/2$. The radius of curvature r_n of the neutral surface and the eccentricity $e(\theta)$ are [111]:

$$\begin{aligned} r_n(\theta) &= \frac{A(\theta)}{\int\int_{A(\theta)} \frac{dA(\theta)}{r}} \\ e(\theta) &= r_c(\theta) - r_n(\theta) \end{aligned} \tag{5.2}$$

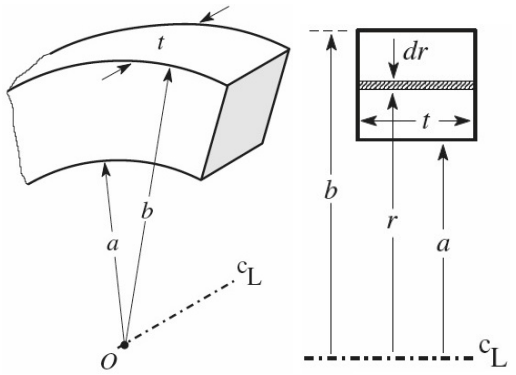

Figure 5.4: Curved beam kinematics [111] ©2011 Springer.

where $A(\theta)$ is the cross-sectional area of the beam. In the case of a rectangular cross section [111]:

$$r_n(\theta) = \frac{b(\theta) - a(\theta)}{ln(b(\theta)/a(\theta))}. \tag{5.3}$$

The coordinates of the centroid surface in the plane are:

$$\begin{aligned} x_c(\theta) &= R(\theta)cos(\theta) \\ y_c(\theta) &= R(\theta)sin(\theta). \end{aligned} \tag{5.4}$$

Then, the coordinates of the neutral surface in the plane are:

$$\begin{aligned} x_n(\theta) &= x_c(\theta) - e(\theta)\frac{y_c(\theta)'}{\sqrt{x_c(\theta)'^2 + y_c(\theta)'^2}} \\ y_n(\theta) &= y_c(\theta) + e(\theta)\frac{x_c(\theta)'}{\sqrt{x_c(\theta)'^2 + y_c(\theta)'^2}}. \end{aligned} \tag{5.5}$$

Combining these formulae, it can be shown that the arc-length parameterization, s, and tangent angle, $\alpha(s)$, of the arm's neutral surface are:

$$\begin{aligned} s(\Theta) &= \int_0^{\Theta} \sqrt{(x_n(\theta)')^2 + (y_n(\theta)')^2} d\theta \\ \alpha(s) &= atan2(y_n(\Theta)', x_n(\Theta)') \end{aligned} \tag{5.6}$$

where $atan2(*,*)$ is the four quadrant arctangent. The derivatives in Eq. (5.5) and Eq. (5.6) are taken with respect to θ. Assuming that the neutral surface is inextensible, the longitudinal and shear strains can be ignored. This is justified as these strains are in general quite low and the resulting stresses and displacements do not strongly affect the arm's behavior [111].

The kinematics of a generalized arm are shown in Fig. 5.5. Let E be Young's modulus of the spring material and L be the length of the arm (with respect to the neutral surface). Clearly, the arm's cross-sectional area, A, and in-plane thickness, d, need not be constant and are functions of s. Of interest is the deformed shape of the spring arm under loading, specified by the forces F_x and F_y acting on the arm end, as shown in Fig. 5.5. The constitutive relation for the deformation of the arm is [111]:

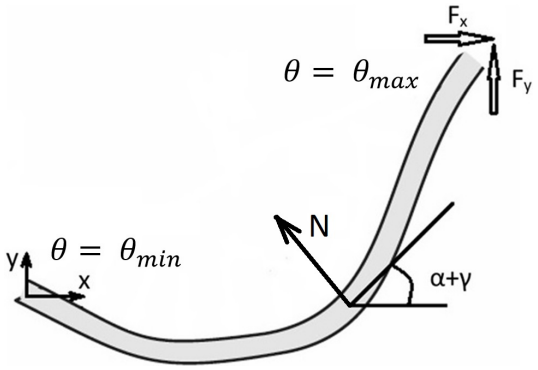

Figure 5.5: Spring arm kinematics.

$$M(s) = (A(s)Ee(s)r_n(s))\frac{d\gamma}{ds} \tag{5.7}$$

where $\gamma(s)$ is the displacement of the arm's neutral surface as shown in Fig. 5.5. From the load balance laws:

$$\frac{dM}{ds} = -N(s) \tag{5.8}$$

where N is the shear force due to the loading. From the geometry of Fig. 5.5:

$$N(s) = -F_x sin(\alpha(s) + \gamma(s)) + F_y cos(\alpha(s) + \gamma(s)). \tag{5.9}$$

Substituting Eq. (5.9) and Eq. (5.8) into Eq. (5.7), leads to the governing equation for the displacement angle $\gamma(s)$, which defines locally how the arm deforms along

its length:

$$\frac{d^2\gamma}{ds^2} = \frac{[F_x sin(\alpha(s)+\gamma(s)) - F_y cos(\alpha(s)+\gamma(s))] - \frac{d(A(s)Ee(s)r_n(s))}{ds}\frac{d\gamma}{ds}}{A(s)Ee(s)r_n(s)}, \quad s \in [0, L]. \tag{5.10}$$

A concrete solution to Eq. (5.10) requires boundary conditions. It is assumed that the proximal end of the spring arm (at $\theta = \theta_{min}$, or equivalently $s = 0$) is stationary and subject to either a pinned or a fixed boundary condition. For the fixed boundary condition, $\gamma(0) = 0$, and for the pinned one, $\frac{d\gamma(0)}{ds} = 0$. $\Delta\beta$ is defined as the displacement angle of the arm's distal tip, as shown in Fig. 5.6. Then the displacement (x_{dis}, y_{dis}) of the arm at its end, $\theta = \theta_{max}$ (or equivalently $s = L$), is given by:

$$\begin{aligned} x_{dis} &= R_n cos(\beta_0 + \Delta\beta) \\ y_{dis} &= R_n sin(\beta_0 + \Delta\beta) \end{aligned} \tag{5.11}$$

where $R_n = \sqrt{x_n(L)^2 + y_n(L)^2}$ and $\beta_0 = atan2(y_n(L), x_n(L))$. Thus, this arm end is rotated at an angle $\Delta\beta$ around the spring's geometric center.

If the distal end of the arm is fixed (i.e., its rotational displacement is given) as shown in Fig. 5.6, then $\gamma(L) = \Delta\beta$. Here, without loss of generality, the rotary displacement of the spring is taken to be equal to the rotational displacement of the distal end. If instead, the distal end is pinned, the boundary condition becomes $\frac{d\gamma(L)}{ds} = 0$. In the deformed configuration:

$$\begin{aligned} x_{dis} &= \int_0^L cos(\alpha(s)+\gamma(s))ds \\ y_{dis} &= \int_0^L sin(\alpha(s)+\gamma(s))ds. \end{aligned} \tag{5.12}$$

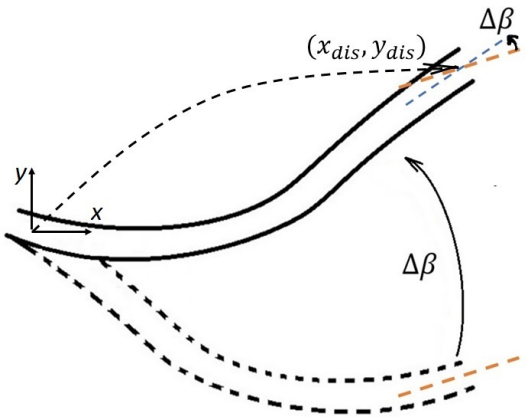

Figure 5.6: Kinematics of the spring arm's deformation.

Eq. (5.10), and its boundary conditions, define an ODE boundary value problem for the deformation of the arm:

$$\begin{aligned}
\frac{d^2\gamma}{ds^2} &= \frac{[F_x sin(\alpha(s)+\gamma(s)) - F_y cos(\alpha(s)+\gamma(s))] - \frac{d(A(s)Ee(s)r_n(s))}{ds}\frac{d\gamma}{ds}}{A(s)Ee(s)r_n(s)} \\
\gamma(0) = 0 \quad &\text{or} \quad \frac{d\gamma(0)}{ds} = 0 \\
\gamma(L) = \Delta\beta \quad &\text{or} \quad \frac{d\gamma(L)}{ds} = 0 \\
\int_0^L cos(\alpha(s)+\gamma(s))ds &= R_n cos(\beta_0 + \Delta\beta) \\
\int_0^L sin(\alpha(s)+\gamma(s))ds &= R_n sin(\beta_0 + \Delta\beta) \\
s \in [0, L].
\end{aligned} \tag{5.13}$$

Eq. (5.13) describes a very general problem with unknowns given by: F_x, F_y, $\Delta\beta$ and the initial condition (which depends on the boundary conditions).

The stress in the arm interior at the point with radius of curvature r is given by [111] (see Fig. 5.4):

$$\sigma(s, r) = E\Big(1 - \frac{r_n(s)}{r}\Big)r_n(s)\frac{d\gamma}{ds} \quad \text{for} \quad r \in [a(s), b(s)]. \tag{5.14}$$

Then, the stresses at the convex (cx) and concave (cv) arm bending surfaces are respectively given by:

$$\begin{aligned}
\sigma_{cx}(s) &= E\Big(1 - \frac{r_n(s)}{a(s)}\Big)r_n(s)\frac{d\gamma}{ds} \\
\sigma_{cv}(s) &= E\Big(1 - \frac{r_n(s)}{b(s)}\Big)r_n(s)\frac{d\gamma}{ds}.
\end{aligned} \tag{5.15}$$

The maximum stress in the arm occurs at the convex arm surface (see Sec. 5.4.1):

$$\sigma_{max} = \max_s(|\sigma_{cx}(s)|) \quad \text{for} \quad s \in [0, L]. \tag{5.16}$$

Design experiments suggest that the use of fixed boundary conditions generally results in a stiffer spring design. Furthermore, when both arm ends are fixed, there are no moving parts and the spring is easier to manufacture.

Eq. (5.13) can be solved to find the initial condition ($\frac{d\gamma}{ds}(0)$ or $\gamma(0)$ depending on the boundary condition at $s = 0$) and forces, F_x and F_y, that must be applied at the arm's end, $s = L$, to achieve $\Delta\beta$ angular displacement of the spring, given the

boundary conditions. Unfortunately, Eq. (5.13) cannot be solved analytically, thus, a numerical shooting method is required.

Once Eq. (5.13) is solved, one can calculate the spring torque and stiffness at the given angular displacement $\Delta\beta$, assuming that there are n identical arms:

$$\tau(\Delta\beta) = n\{\underbrace{[x_{dis}F_y - y_{dis}F_x]}_{\text{deformation forces}} + \underbrace{[A(L)Ee(L)r_n(L)]\frac{d\gamma}{ds}(L)}_{\text{b.c. couple}}\} \tag{5.17}$$

$$K(\Delta\beta) = \frac{\tau(\Delta\beta)}{\Delta\beta}.$$

Eq. (5.17) suggests that the spring torque is due to the arm deformation forces F_x and F_y, and a boundary condition couple. If the distal arm end at $s = L$ is pinned, then $\frac{d\gamma(L)}{ds} = 0$ and the boundary condition couple is zero, therefore, in this case the torque is only due to the arm deformation forces. On the other hand, if this end is fixed, then the spring structure needs to support the deformation boundary condition couple $[A(L)Ee(L)r_n(L)]\frac{d\gamma}{ds}(L)$ at the outer circle. Thus, unlike FEA approaches, this mathematical model allows one to gain significant design insight into the arm loading characteristics.

5.2.3 Out-of Plane Buckling

Out-of-plane buckling can be a concern for springs with a small out-of-plane thickness. Increasing the out-of-plane thickness of the spring minimizes the chances of a buckling failure, but does increase its stiffness. Design experiments suggest that assemblies of thin higher stiffness springs could have lower mass compared to thick springs with the same overall stiffness and maximum loading torque. Therefore, buckling failure prevention poses a design trade-off.

To allow rotary springs to also serve as flexible couplings which can handle small misalignments, the introduction of complex out-of-plane mechanical spring constraint elements is to be avoided. Due to the fact that modeling buckling in curved beams is quite involved and requires additional assumptions [112], buckling is ignored at the modeling stage. However, as rule of thumb the spring's out-of-plane thickness should be approximately the same or larger than the spiral's in-plane thickness. To ensure no buckling occurs, nonlinear buckling FEA can be used at the final design stage. In general, a failure of non-linear static FEA analysis is also an indication of possible buckling problems [113].

5.2.4 Mass Reduction Techniques

This section introduces two different approaches to minimize the deployed mass of a rotary spring. The goal is to significantly reduce the weight of the spring without compromising its characteristics in terms of stiffness and maximum allowable loading. Both approaches are based on the observation that the arm material near the neutral surface does not experience high bending loads.

Composite Material Arms

The use of a sandwich structure (Fig. 5.7) in the arm can lead to significant weight reduction. Practically, a slot along the centroidal surface is cut out and filled with a lighter secondary material. The secondary material experiences low bending load, and primarily ensures that the arm's deformation kinematics remains the same. The trade-off is that the flexural rigidity of the arm slightly decreases.

Let E, ρ and E_s, ρ_s be the stiffness and density of the primary and secondary materials, respectively. Without loss of generality, assume that the two primary layers have the same thickness, given by $\Delta d(s)$ (see Fig. 5.7). Let $d_s(s)$ be the thickness of the secondary material layer. For the bending analysis, the transformed section approach [114] is employed, and thus, instead of the composite arm, a homogeneous primary material arm is constructed so that it has the same flexural rigidity as the composite arm. The transformed arm has the same profile and a new cross-section which is the *transformed section*, shown in Fig. 5.7.

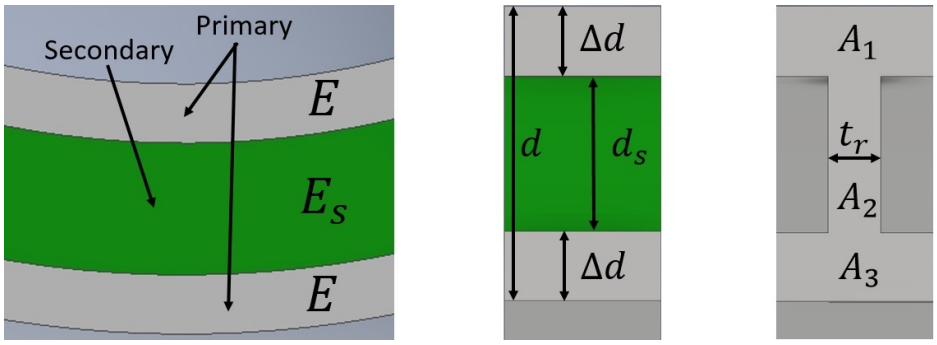

Figure 5.7: Composite material spring arm. The sandwich structure on the left, its cross-section in the middle and its transformed section on the right.

The transformed arm thickness is $t_r = \frac{E_s}{E} t$. If the new cross-section is symmetric (which is always true if the primary layers thickness is the same), $r_c(s)$ remains the same, otherwise the new centroidal surface has to be found and $r_c(s)$ recalculated.

For the transformed arm [111]:

$$A(s) = \sum_i A_i(s), \qquad r_n(s) = \frac{A(s)}{\sum_i \int \int_{A_i(s)} \frac{dA}{r}} \tag{5.18}$$

where $A_i(s)$ is the area of the discrete regions in the transformed cross section, shown in Fig. 5.7. For the structure shown in Fig. 5.7, Eq. (5.18) simplifies to:

$$\begin{gathered} A(s) = t(\frac{E_s}{E}(d(s) - 2\Delta d(s))) + 2\Delta d(s)) \\ r_n(s) = \frac{\frac{E_s}{E}(d(s) - 2\Delta d(s))) + 2\Delta d(s)}{ln(\frac{b(s)}{b(s)-\Delta d(s)}) + \frac{E_s}{E} ln(\frac{b(s)-\Delta d(s)}{a(s)+\Delta d(s)}) + ln(\frac{a(s)+\Delta d(s)}{a(s)})}. \end{gathered} \tag{5.19}$$

Eq. (5.19) allows us to use the arm of Fig. 5.7 with the model of Sec. 5.2.2.

Without loss of generality, assuming d and d_s are constant along the arm, let $k_s = \frac{d_s}{d}$. Then, introducing the sandwich composite structure achieves fractional reduction in the mass of the arm given by:

$$\Delta M \approx (1 - \frac{\rho_s}{\rho})\frac{d_s}{d} = k_s(1 - \frac{\rho_s}{\rho}). \tag{5.20}$$

Therefore, k_s represents the design trade-off between mass reduction and stiffness reduction. From elementary beam theory one can also approximate the fractional decrease in the flexural rigidity of the arm by :

$$\Delta E \approx \frac{(1 - \frac{E_s}{E})(d - 2\Delta d)^3)}{d^3} \approx \frac{1 - \frac{E_s}{E}}{(1 - \frac{\rho_s}{\rho})^3}\Delta M^3. \tag{5.21}$$

Eq. (5.21) and Eq. (5.21) provide basic quantification of the trade-off between mass decrease and flexural rigidity decrease, and thus, can be used to determine the size of the secondary material layer. However, in practice a minimum thickness for the primary layers is determined once the manufacturing method and machining tolerances are determined.

The coefficient $(1 - \frac{E_s}{E})/(1 - \frac{\rho_s}{\rho})^3$ in Eq. (5.21) can be used as secondary material performance metric and should be maximized at the material choice design stage.

Arm Cutouts

The bond between the primary and secondary layers in the sandwich structure are loaded in shear, and thus, are susceptible to failure due to overload or fatigue at loads lower than the primary material rated ones.

As an alternative to the sandwich composite structure, one can introduce *cutouts* in the arm profile (see Fig. 5.8). Support material must be left between the cutouts so that the kinematics of the bending displacement is enforced. The sandwich structure of Fig. 5.7 can be used to approximate the arm with the cutouts by taking $E_s = 0$ and $\rho_s = 0$. Then:

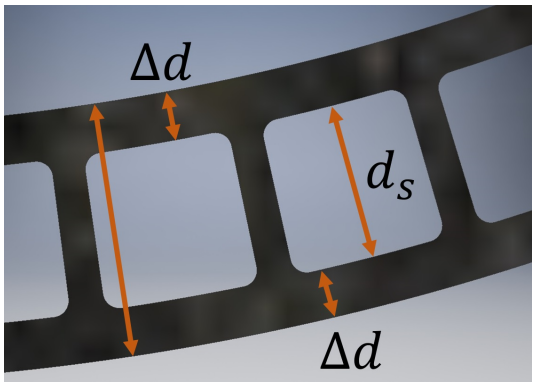

Figure 5.8: Spring arm cutouts.

$$A(s) = 2t\Delta d(s), \qquad r_n(s) = \frac{2\Delta d(s)}{ln[(\frac{b(s)}{b(s)-\Delta d(s)})(\frac{a(s)+\Delta d(s)}{a(s)})]}, \qquad \Delta M \approx \frac{d-2\Delta d}{d} = k_s, \tag{5.22}$$

$$\Delta E \approx \frac{(d-2\Delta d)^3}{d^3} = k_s^3 \approx \Delta M^3. \tag{5.23}$$

Without loss of generality, d and d_s are assumed constant along the arm in Eq. (5.23). The fact that $\Delta E \approx \Delta M^3$ demonstrates the effectiveness of the cutouts in reducing the spring mass without significantly compromising its stiffness. Again, $k_s = \frac{ds}{d}$ represents the design trade-off between mass reduction and stiffness reduction.

Due to their manufacturing advantages and superior performance, weight reduction cutouts are utilized for some of the spring prototypes discussed later in this chapter.

5.2.5 Archimedean Spiral Arm Spring Designs

This section shows how the model developed in Sec. 5.2.2 can be used to design springs with *Generalized Archimedean* spiral arms of constant thickness.

All $n \geq 2$ arms spiral around the spring's geometric center in a rotationally symmetric way (see Fig. 5.3). The proximal spiral ends, where $\theta = \theta_{min}$, are connected to the inner circle with radius R_{in} and the ends, defined by $\theta = \theta_{max}$, are positioned at the outer circle with radius R_{out}. The radii R_{in} and R_{out} typically depend on the packaging requirements for the spring within the overall system design. The equation of the undeformed spiral centerlines is given by:

$$R(\theta) = c\theta^q + R_{in} \qquad \theta \in [\theta_{min}, \theta_{max}]. \tag{5.24}$$

In most cases, the desired spring performance specification is given in terms of maximum torque, τ_{des}, and stiffness ,K_{des}. Then, the maximum spring displacement

can be calculated by $\Delta\beta_{max} = \frac{\tau_{des}}{K_{des}}$. Next, the spring material with density ρ and maximum allowable stress $[\sigma]$ is chosen. If a composite arm design is used, the secondary material layer properties also need to be chosen and arm bending properties determined according to Sec. 5.2.4. The maximum arm stress at maximum displacement, $\Delta\beta_{max}$, is $\sigma_{max} = [\sigma]$ (Eq. (5.16)).

The goal is to find the best spring design that conforms to the packaging constraints. Therefore, given an arbitrary out-of-plane thickness t, the spring with maximum load at spring displacement $\Delta\beta_{max}$ is desired. Once the in-plane design is finalized, t can be scaled to achieve the desired spring stiffness.

Next follows a summary of the spring design parameters and guidelines for their choice:

- The choice of θ_{min} is arbitrary, however, it affects how the spiral arms meet at the inner circle. The value of θ_{min} should be large enough to avoid significantly reduced radius of curvature of the arm's profile in the vicinity of the inner circle. Larger values could deteriorate spring performance.
- Fixed or pinned boundary conditions of the arm ends at the inner and outer circles. All prototype designs presented here use fixed boundary conditions at both ends due to their high manufacturing readiness.
- The coefficient c in Eq. (5.24) is determined by the condition $R(\theta_{max}) = R_{out}$.
- The coefficient q in Eq. (5.24) controls how the spacing between the arms changes along their profiles. The value of q heavily impacts the spring's potential to *self-intersect* during large displacements. As shown in Fig. 5.9, as the spring deflects in either the clockwise or counterclockwise directions, the spiral arms eventually intersect at a particular angle. These intersections limit the largest practical rotation achievable by the design. Design experiments suggest that the spring's performance is maximized if the intersection angles are the same in both rotational directions.

After selecting the parameters described above, two free parameters remain: θ_{max} and the in-plane thickness d. The system in Eq. (5.13) can be solve for a given choice of these parameters with $\Delta\beta = -\Delta\beta_{max}$ for clockwise and $\Delta\beta = \Delta\beta_{max}$ for counterclockwise spring deformation. In this formulation the unknowns are the deformation initial condition $\frac{d\gamma}{ds}(0)$, arm end forces F_x and F_y. The solutions yield a

specific design, whose rotary torque at maximum spring deflection is quantified (see Sec. 5.2.2). In this way, the (θ_{max},d) parameter space can be searched to find the spring which can support the highest torque at maximum displacement. Designs that result in maximum bending stress σ_{max} higher than $[\sigma]$ or spiral intersections (as shown in Fig. 5.9) are discarded. Thus, the performance of all possible springs that have the chosen arm shape and meet at the inner and outer circles is compared to find the one that can carry the highest torque under the given maximum displacement. Other optimality criteria are also possible.

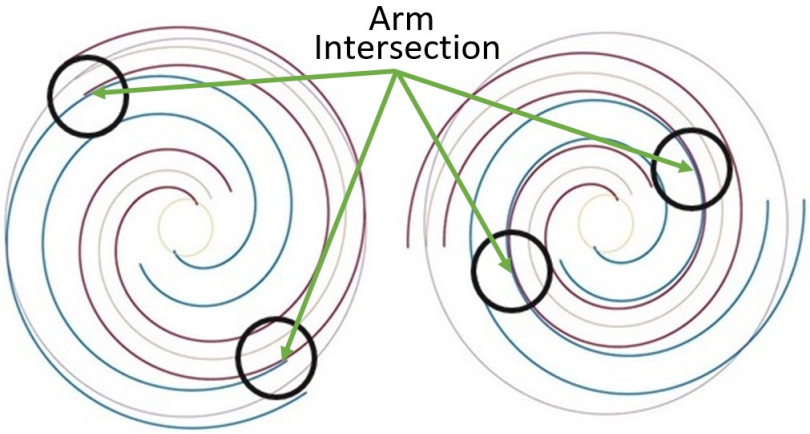

Figure 5.9: Deformations of the spring that cause the arms to intersect.

5.2.6 AR500 Steel Spring Prototype

This section describes the design, manufacturing, and experimental testing of a planar rotary spring that was built to validate the model presented in Sec. 5.2.2, and the mass reduction techniques of Sec. 5.2.4. The section concludes with a comparison of the model and FEA predictions, and the experimental results.

Design

Since the spring spirals are loaded in bending, the arm material's yield strength is of the greatest importance (together with its fatigue strength or endurance limit). For the prototype, TEMco $AR500$ steel [115] was chosen. $AR500$ is a quenched and tempered, through hardened, wear-resistant grade steel. The typical yield strength is $1289MPa$ or $187ksi$. The spring design was based on a maximum allowable bending stress of $[\sigma] = 1100MPa$, so as to include a safety factor.

The inner and outer radii are chosen as $R_{in} = 18mm$ and $R_{out} = 74mm$ so that the spring can be mated with other components in an actuator prototype (see Sec. 6.3). The value $\theta_{min} = 0.2rad$ was taken in order to allow enough physical space for

four spirals without intersection at the spring center. For the given dimensions, the parameter $q = 0.9$ in Eq. (5.24) allows good symmetry in the spring deformation under loading in both directions.

The design target was set to stiffness of $K_{des} \approx 600\frac{Nm}{rad}$ and maximum allowable torque of $\tau_{des} = 200\frac{Nm}{rad}$. This results in maximum allowable angular displacement of $\Delta\beta_{max} = 20°$. Two spirals ($n = 2$) with $\Delta d \approx 2mm$ are used in order to reduce the amount of machining time and to limit the dependence of the spring performance on the machining tolerances, thus, ensuring enough spring rigidity.

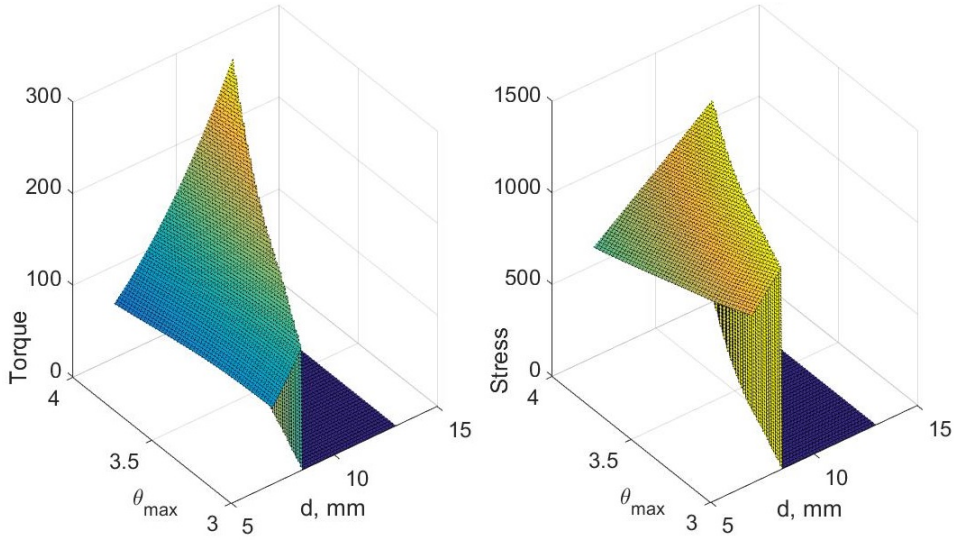

Figure 5.10: Spring design search Results. Left: torque at maximum displacement $\Delta\beta$. Right: maximum bending stress at maximum displacement $\Delta\beta$.

As described in Sec. 5.2.6, the free design parameters are θ_{max} and arm in-plane thickness, d. Eq. (5.13) is solved over a grid of these free parameters in a physically meaningful range, and resulting designs with maximum bending stress higher than $[\sigma]$ are discarded. Fig. 5.10 plots the maximum realized torque versus the free parameters (d, θ_{max}). From the plot one can choose a spring spiral profile for which that the maximum bending stress is $[\sigma]_{max}$ at the maximum displacement $\Delta\beta$.

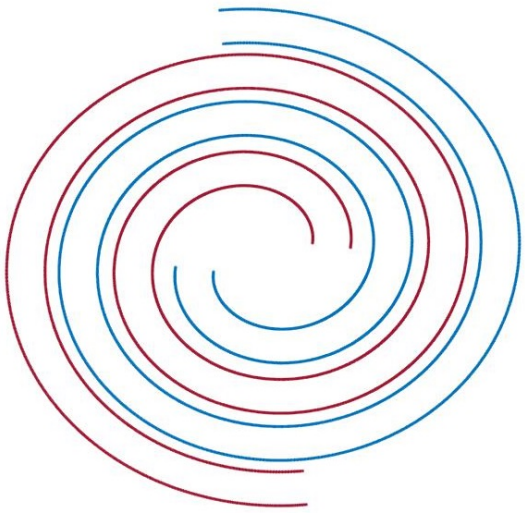

Figure 5.11: $AR500$ spring profile.

Fig. 5.11 shows the chosen spring profile. The corresponding in-plane thickness is $d = 10.7mm$. This design can carry the highest load in the family of all spring designs that conform to the same constraints and material choice, and have the same out-of-plane thickness. All designs that can carry higher loads are infeasible due to spiral intersection at maximum displacement, as depicted in Fig. 5.9. Eq. (5.22) predicts that the spiral weight reduction due to the cutouts is around 60%.

In applications, spring displacements larger than the maximum allowable displacement $\Delta\beta_{max}$ should be prevented (by introducing hard stops) as they would likely result in overload failure in designs like these. Material with thickness $t = 9.525mm$ (or $3/8''$) is used for the prototype manufacturing to meet the required torque and stiffness values.

As described earlier, the mathematical model of Sec 5.2.2 predicts the magnitude of the torque components at the outer circle, particularly the important boundary condition couple of Eq. (5.17). Fig. 5.12 shows the magnitude of this design's loading components. As can be observed, the boundary condition couple has a substantial value, therefore, the spring mounting elements at the outer rim need to be designed so that they can support it.

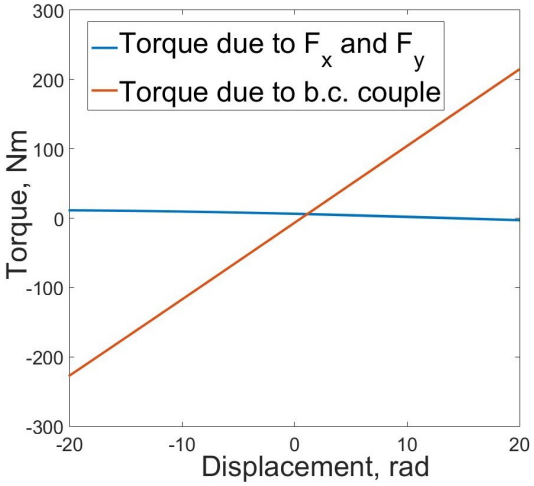

Figure 5.12: Spring torque loading components vs. displacement.

At the final design stage, the chosen profile is imported in a CAD software for the design of the spring mounting elements and introduction of the weight reduction cutouts. Fig. 5.13 shows the spring design. Mounting holes are introduced at both ends of the spirals. The high boundary condition couples motivate the design of the outer mounting holes.

Prototype Manufacturing

Unlike the majority of planar spring prototypes described in the literature, abrasive water jet machining (AWJM) instead of EDM (electrical discharge machining) is used for the prototype manufacturing. AWJM is a grinding process that involves cutting by small particles in a high speed water flow [116] and has the following advantages [116], [117]:

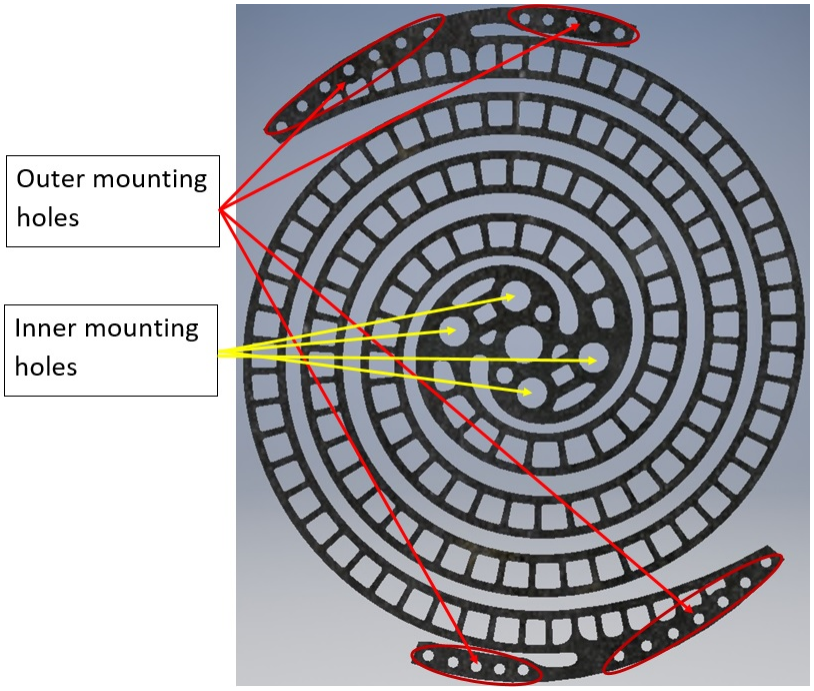

Figure 5.13: *AR*500 Spring design.

- Little fixturing is required due to low cutting forces.
- No heat affected zone (HAZ) and residual stresses are produced, as all of the generated heat is absorbed by the cutting fluid. This is the main advantage of AWJM compared to EDM, laser cutting, plasma cutting, flame cutting, etc. The spring performance heavily depends on the surface properties of the cut faces, as they carry the highest bending stress. The microcracking, embrittlement, thermal stresses [118], and possible chemical embrittlement [119] that can be introduced at the cut surface by EDM may substantially decrease the spring's fatigue strength and result in premature failure. None of these occur with AWJM.
- No start holes are required. This is very important for this design, as the weight reductions cutouts would require substantial prior machining for wire EDM. Furthermore, heavy restrictions may need to be imposed on the cutouts' shape and size due to available tooling.

A main drawback of AWJM is the occurrence of kerf taper on the cut faces. This taper cannot be completely eliminated without a multi-axis cutting head, but can be minimized using strategies described in [117], [120]. Kerf taper is of concern for the spring manufacturing because taper on the spiral out-of-plane faces can cause

unexpected side loads and deformation under spring loading. To reduce the kerf taper, a low stand-off and a submerged machining process with an elongated nozzle was employed. The spring surfaces were also cleaned through sand-blasting.

The spring prototype, machined on a Flow Mach-2b waterjet machine [121], is shown in Fig. 5.14. The arm width difference between the top and bottom of the kerf is around $0.1mm$. Due to manufacturing inaccuracies there is significant variance in the thickness of the spiral profiles that reaches $0.1mm$ at some locations in addition to the kerf. The arm cutouts thickness also varies by up to $0.1mm$. The mounting holes were cut with increased accuracy by reducing the jet speed ($0.03mm$ kerf).

The mass of the spring is $616g$. The CAD estimate of the mass of the spirals is $424g$ with the cutouts and $828g$ without the cutouts. Thus, the cutouts lead to 49% spiral weight reduction which is very close to the model predictions.

Spring Performance Analysis Using The Modeling of Sec. 5.2.2

To estimate the spring's stiffness in the allowable deformation range, Eq. (5.13) can be solved with the prototype's design parameters for a range of values for the displacement $\Delta\beta$: $-\Delta\beta_{max}, -\Delta\beta_{max} + \delta\beta, \ldots, 0, \ldots, \Delta\beta_{max} + \delta\beta, \Delta\beta_{max}$ for some $\delta\beta$. Then Eq. (5.17) can be used to find the torque and stiffness corresponding to each displacement value. The maximum stress at each displacement can be estimated using Eq. (5.16). Model prediction for the torsional response of the prototype shown in Fig. 5.14 are plotted in Fig. 5.18 and Fig. 5.19 and compared to FEA simulation and experimental testing results.

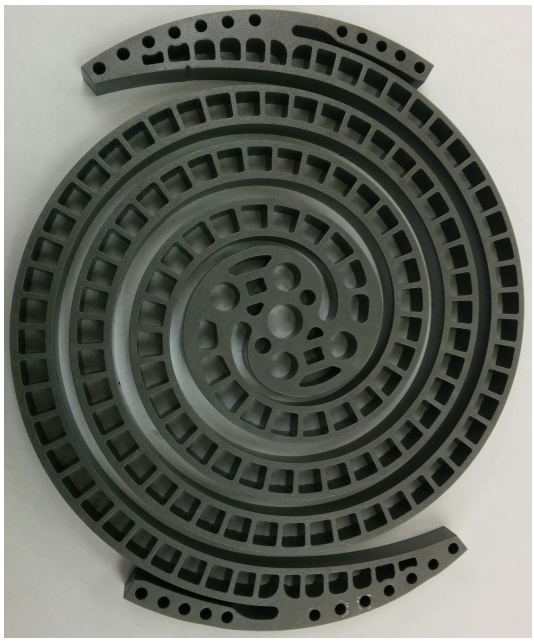

Figure 5.14: AR500 spring prototype.

FEA Analysis

Non-linear static FEA with Autodesk Nastran [113] is used to simulate the spring torsional loading and predict the spring stiffness in the allowable deformation range.

The FEA model uses 2.2 million linear elements, and displacements are introduced by keeping the outer spiral mounting slots fixed, while applying remote forces at the center holes to simulate torque loading. Fig. 5.15 shows FEA simulation of the spring at maximum loading. Non-linear buckling FEA with substantially higher torque load ($400Nm$) is also used to ensure no buckling occurs.

Further nonlinear FEA simulations suggest that the spring can also support moderate axial loads without significant effect on the torsion performance. Therefore, the FEA analysis confirms that the spring can also act as a flexible coupling.

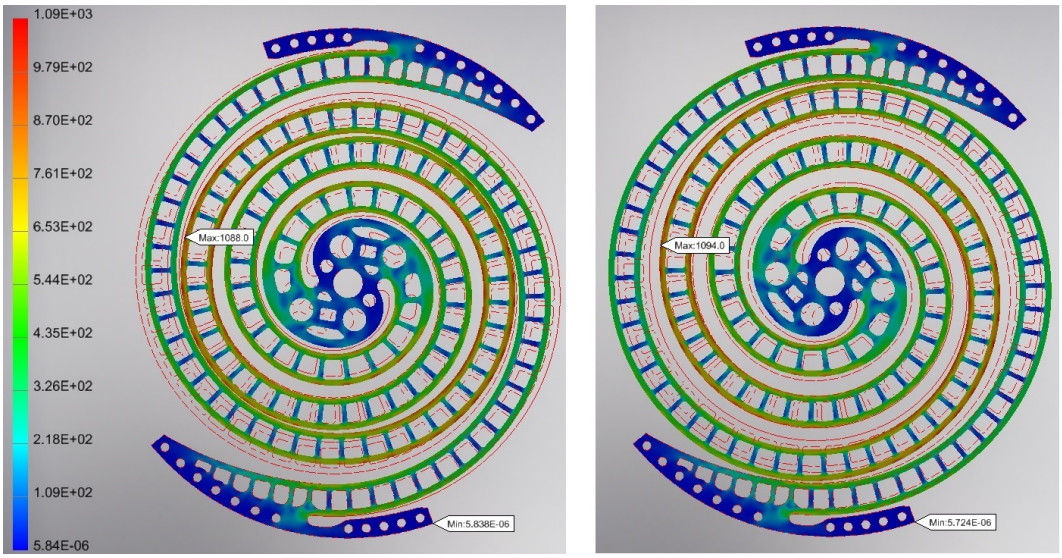

Figure 5.15: FEA $AR500$ spring simulation results at maximum spring torsional loading. Counterclockwise loading on the left and clockwise loading on the right. The colour bar units correspond to stress in MPa.

Experimental Testing

An ADMET mechanical testing machine is used to characterize the torsional properties of the spring prototype. Fig. 5.16 shows the experimental set-up. The machine's capacity does not allow for testing the spring at the maximum design loads. However, it is used to characterize the spring's torsional properties over a wide range of loading conditions.

Comparison of Results and Discussion

Fig. 5.17 shows the experimental data from a torsional test. The loading curve is shown in the right plot. The torque against displacement plot shows that the response is quite linear (over 98%). There is barely noticeable hysteresis that is quite difficult

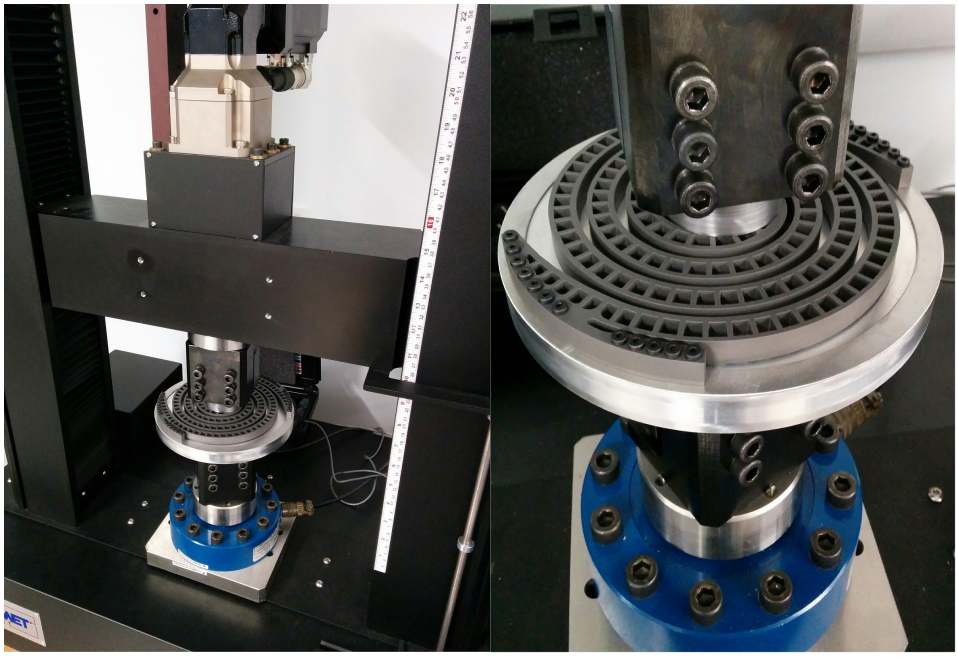

Figure 5.16: *AR*500 spring experimental testing set-up. A close view of the spring on the right and the ADMET testing machine on the left.

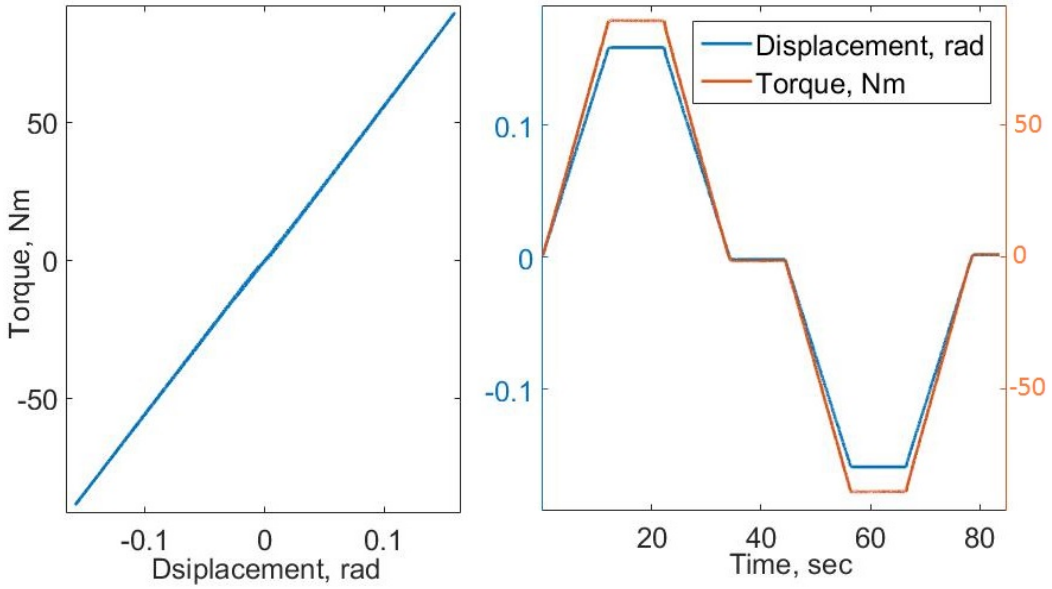

Figure 5.17: *AR*500 spring mechanical torsion test experimental data. A plot of torque against angular displacement on the left and a combined plot of torque and angular displacement against time on the right.

to quantify due to measurement noise. Therefore, the spring mechanical stiffness is quite uniform. The loading curve plot also suggests that the deformation is stable and symmetric. There is less than 1% difference in the stiffness levels depending on the loading direction which is consistent with the analytic model predictions and FEA simulations.

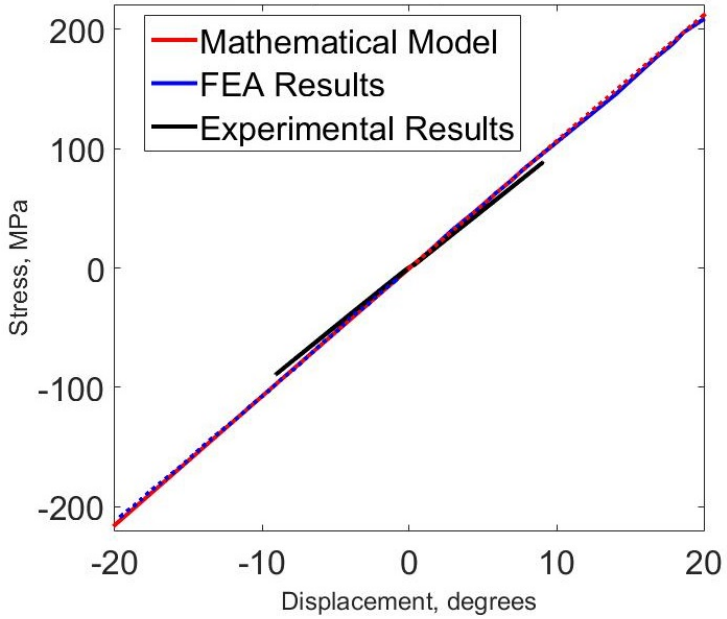

Figure 5.18: Torque against displacement plot for the *AR*500 spring.

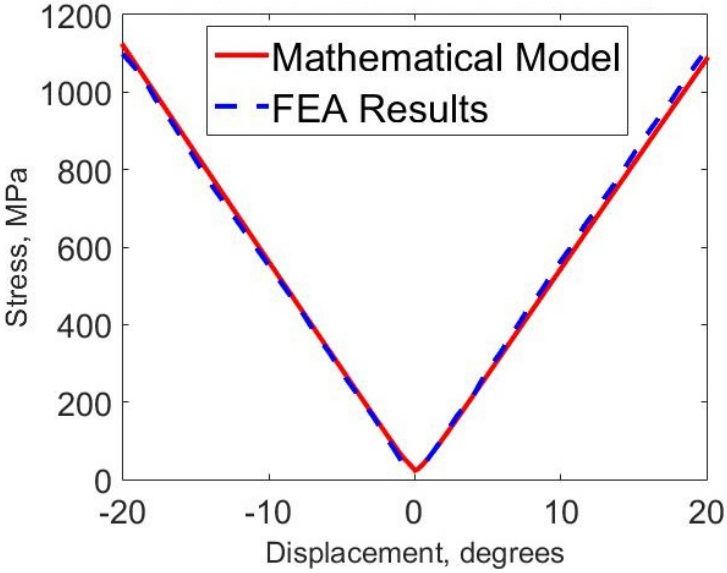

Figure 5.19: Stress against displacement plot for the *AR*500 spring.

The FEA simulation and experimental results confirm the validity of the analytic

model of Sec. 5.2.2. Fig. 5.18 compares the torque against the spring's rotational displacement results from the experimental data with the predictions of the model and FEA.

The FEA results completely agree with the model predictions. The experimental testing results show slightly lower stiffness levels around $560\frac{Nm}{rad}$ compared to the predicted $600\frac{Nm}{rad}$ by the model (less than 7% error).

Fig. 5.19 plots the maximum bending stress vs. displacement. The plot suggests that the FEA and the mathematical model predictions agree to a very high extent. No experimental strain measurements are available to confirm these values.

From elementary beam theory, the flexural rigidity of the arm is proportional to d^3. Therefore, the spring's torsional performance can be very sensitive to the arm profile width d, given that the arms are loaded in bending. The high surface slope in the torque plot of Fig. 5.10, graphically confirms this observation.

The arms' reduced profile width, enlarged cutouts and kerf in some regions, due to the manufacturing inaccuracies discussed earlier are expected to be largely responsible to the small discrepancy between the predictions and the experimental results. Therefore, the manufacturing accuracy and tolerances may affect the spring torsional performance significantly and should be considered at the spring design stage. Further design and experimental issues related to the arm boundary condition enforcement, clamping and attachment of the springs, calibration, etc. may also contribute to the discrepancy between the theoretical predictions and the experimental results.

5.2.7 3D-printed Titanium Spring Prototype

A 3D printed titanium spring is designed following the approach of Sec. 5.2.5 and similarly to the $AR500$ spring design of Sec. 5.2.6. The target stiffness is $100\frac{Nm}{rad}$ with maximum load of $50Nm$, which results in maximum desired displacement of $28.6°$. The spring is used as part of SEA tether management system of the Axel rover developed at the NASA Jet Prop. Lab. [36] (see Sec. 6.4).

Severe packaging constraints motivate a novel dual spring design. The spring consists of two planar rotary springs that share the same solid cylindrical core and are connected in series. Thus, each of the two springs has stiffness twice the desired SEA stiffness. Fig. 5.20 shows the 3D printed titanium prototype and its a cross-sectional view.

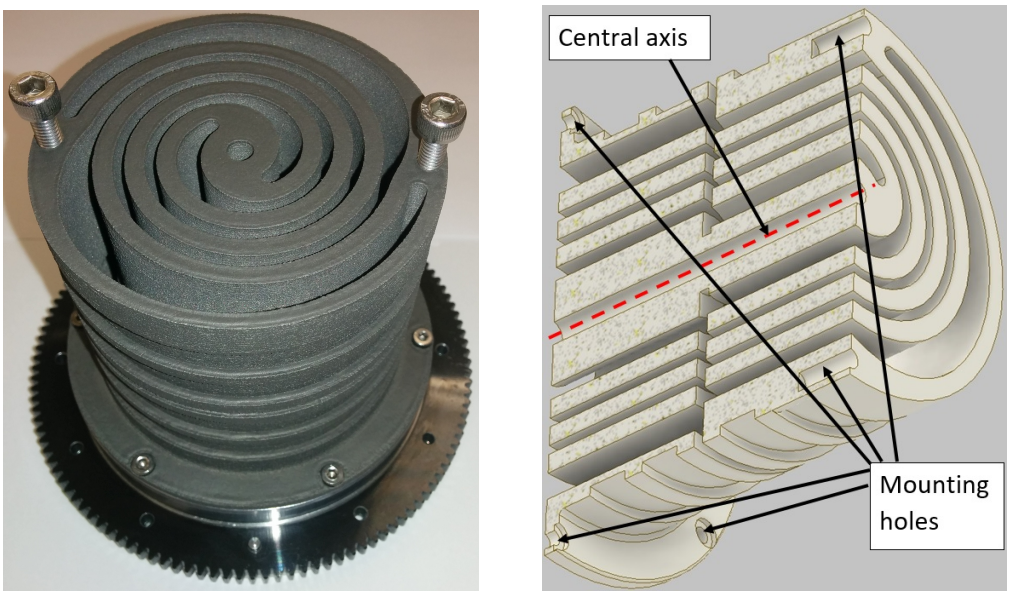

Figure 5.20: Titanium spring prototype on the left and its half section view on the right.

Throughout the design of the spring prototype of Sec. 5.2.5, the central mounting holes' size and their radial positions were identified as a major design constraint driving the spring radial size. Therefore, the main advantage of the novel dual spring design is that the spring arms attach much closer to each other at the spring central axis compared to the arms of designs that have central mounting holes. All mounting holes are instead on the spring circumference as shown in Fig. 5.20. This leads to significantly improved compactness in the radial direction. A further advantage of this design is that all mounting screws carry little shear load, thus, smaller screw sizes can be used.

The titanium spring prototype is designed for maximum admissible stress at maximum displacement, given by the Ti-6Al-4V fatigue strength of $510MPa$. FEA simulations confirm the design's mechanical properties with an error of $\leq 1\%$ on both the stiffness and the stress values, which is identical to the FEA results of Sec. 5.2.5.

No torsional experimental testing data that characterizes the performance of the prototype of Fig. 5.20 is available. However, the experimental testing results of the tether management system that utilizes the prototype suggest that its stiffness is around 94% of the expected value [36]. The lower prototype measured stiffness is expected to be due to manufacturing inaccuracies and additional unmodeled compliance of some of the system components.

5.3 Modeling, Simulation and Analysis of Spring Arm Contacts

Under substantial torsional loads, the spring deformation can lead to contacts between the arms as shown in Fig. 5.9. Up to this point, the maximum torsional displacement of the springs is assumed to be constrained so as to avoid such contacts. For instance, this can be achieved by the introduction of mechanical hard stops. This section considers the possibility that allowing such contacts can be advantageous.

If the maximum spring displacement is not limited, the spring arms may contact each other under loads higher than the rated loads without the occurrence of a catastrophic failure, provided the maximum arm stress does not exceed the material yield strength, σ_y. Thus, if $[\sigma] < \sigma_y$ and the spring is designed so that the arms contact each other at $[\sigma]$, the spring could support significantly higher unexpected overload torque without failure, provided σ_{max} never exceeds σ_y along the arm. This is particularly useful when $[\sigma]$ corresponds to the material fatigue (endurance) strength, for instance.

The titanium spring prototype of Sec. 5.2.7 is designed in this way. The maximum arm bending stress upon arm contacts is given by the materials fatigue limit. Thus, the spring can support overload torques without the need of hard stops.

The implementation of hard stops usually requires the introduction of additional mechanical components and usually imposes unfavourable design constraints, which both may lead to unnecessary actuator size and mass increase. Furthermore, when the actuator is heavily loaded and the spring displacement is close to the maximum allowable displacement, $\Delta\beta_{max}$, substantial actuator performance degradation may be observed due to sudden shocks caused by engaging of the hard stops. This can be avoided without compromising the actuator performance by designing the spring so that under torsional overload, it enters a different deformation mode which is characterized by the occurrence of arm contacts.

The section introduces an arm contact model (Sec. 5.3.1) which is then used in the development of an arm analysis algorithm that can detect and simulate arm contacts (Sec. 5.3.2).

5.3.1 Arm Contact Model

The model introduced in Sec. 5.2.2 assumes that the only external loads applied to the arm are the end forces F_x, F_y and the boundary condition couple. This section shows how to model the effects of arm contacts (see Fig. 5.9 or Fig. 5.21) and how

to include them in the boundary value problem given by Eq. (5.13).

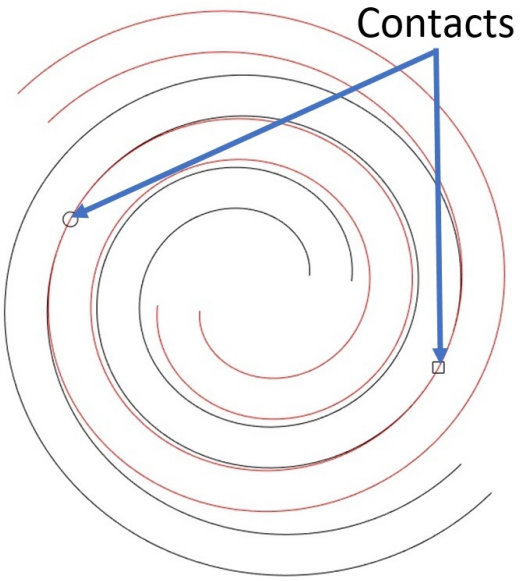

Figure 5.21: Contacting spiral arms.

As before, the arms are assumed to deform in bending only, and when they contact each other, the convex profile of one of the arms contacts the other's concave profile. If the radius of curvature of the concave surface at the contact is larger than that of the convex surface in the considered loading spring range, the contact between the arms can be modeled by a frictionless point contact. This assumption is especially useful if some form of lubrication is provided. Alternatively, friction can be included by rotating the contact force at an angle $\arctan(\mu)$, where μ is the coefficient of friction. To simplify the discussion, frictionless point contact between the arms is assumed.

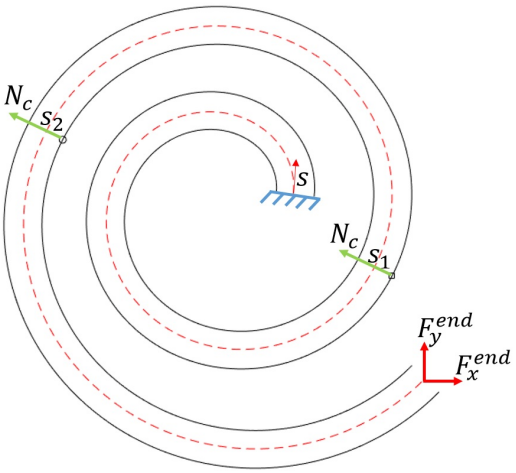

Figure 5.22: Spring arm loading forces.

These assumptions are suitable for spiral arms as their radius of curvature rapidly increases along the profile starting from the spring center. A set of conditions for a general arm shape that ensure two point contacts per arm are, however, difficult to derive. Fig. 5.21 shows the contact points in a two spiral arm example. Without loss of generality, springs with two spiral arms are considered in this section.

These assumptions allow the boundary value problem given by Eq. (5.13) to describe the arm deformation when arm contacts occur. However, in this case, the forces F_x and F_y need to be modified, that is, they are no longer the arm end forces as in Sec. 5.2.2. Instead, F_x and F_y are functions of s and represent the more general arm loading.

Fig. 5.22 shows the arm external forces. Following the frictionless assumption, the

forces at the contact points are given by:

$$\begin{aligned} N_c \begin{bmatrix} -\sin(\alpha(s_1)+\gamma(s_1)) \\ \cos(\alpha(s_1)+\gamma(s_1)) \end{bmatrix} \text{ at } s = s_1 \\ N_c \begin{bmatrix} \sin(\alpha(s_2)+\gamma(s_2)) \\ -\cos(\alpha(s_2)+\gamma(s_2)) \end{bmatrix} \text{ at } s = s_2. \end{aligned} \tag{5.25}$$

The contact forces are internal to the spring, therefore, their magnitudes are equal and given by N_c (see Fig. 5.22).

From the geometry of Fig. 5.22, the arm loading forces are given by:

$$\begin{bmatrix} F_x \\ F_y \end{bmatrix} = \begin{cases} N_c \begin{bmatrix} -\sin(\alpha(s_1)+\gamma(s_1)) + \sin(\alpha(s_2)+\gamma(s_2)) \\ \cos(\alpha(s_1)+\gamma(s_1)) - \cos(\alpha(s_2)+\gamma(s_2)) \end{bmatrix} + \begin{bmatrix} F_x^{end} \\ F_y^{end} \end{bmatrix} & \text{if } s < s_1 \\ N_c \begin{bmatrix} \sin(\alpha(s_2)+\gamma(s_2)) \\ -\cos(\alpha(s_2)+\gamma(s_2)) \end{bmatrix} + \begin{bmatrix} F_x^{end} \\ F_y^{end} \end{bmatrix} & \text{if } s_1 \le s < s_2 \\ \begin{bmatrix} F_x^{end} \\ F_y^{end} \end{bmatrix} & s_2 \le s \end{cases} \tag{5.26}$$

where F_x^{end} and F_y^{end} are the arm end forces (see Fig. 5.22). The spring has $n = 2$ symmetrically arranged arms, therefore, a contact normals symmetry exists which leads to:

$$\alpha(s_1) + \gamma(s_1) = \pi + \alpha(s_2) + \gamma(s_2). \tag{5.27}$$

This observation is used in solving for the contact forces in Sec. 5.3.2. Combining Eq. (5.13) and Eq. (5.26) forms the governing boundary value problem for arm deformation with arm contacts.

5.3.2 Planar Rotary Spring Analysis with Possible Arm Contacts

As shown in Sec. 5.2.5, the analytic model of Sec. 5.2.2 allows for rapid prediction of planar spring torsional properties. Sec. 5.3.1 discussed arm contact modeling, which can be used to augment the planar rotary spring analysis of Sec. 5.2.5, so that arm contacts can be detected and included in the analysis and prediction of torsional

spring performance. The rest of this section assumes that a complete spring design has been achieved and the goal is to characterize its torsional properties with the possible occurrence of arm contacts under load.

When the arms do not intersect, Eq. (5.13) can be readily solved employing a numeric shooting method. However, when there are arm contacts, a simple shooting method implementation can fail. To avoid this, the section formulates a search algorithm combined with a non-linear optimization problem for the analysis of the arm deformation under contacts. The goal is to find arm end forces F_x^{end} and F_y^{end} and initial condition $\frac{d\gamma}{ds}(0)$ that result in a given spring displacement $\Delta\beta$. However, in addition to the these unknowns, N_c is also unknown and needs to be determined in order to characterize the spring torsional performance.

Initial solution and contact detection

First, Eq. (5.13) is solved, assuming no arm contacts occur. As discussed in Sec. 5.2.2, this can be done using a shooting method. Next, the distances between the arms' profiles is calculated to detect any interferences. Fig. 5.23 shows an arm profile interference example. If no interferences are detected, the solution is valid and the algorithm terminates. Otherwise, the corresponding interference regions on each of the profiles are identified (shown in yellow in Fig. 5.23). The mid points (shown in blue in Fig. 5.23) of the interference regions along the arm profile are determined and saved as a variable N^{coord}. This value for N^{coord} is to be used as the initial guess for the arm contact locations. Also, one of the normals at these points (shown in green in Fig.5.23) is saved as a variable N^{dir}. This value for N^{dir} is to be used as the initial guess for the contact force direction. The arm contact forces depend on the deformation angle $\gamma(s)$ (see Eq. (5.25)), therefore, the initial guesses N^{coord} and N^{dir} are not the true arm contact points and contact force direction. The correct values for N^{coord} and N^{dir} are found iteratively.

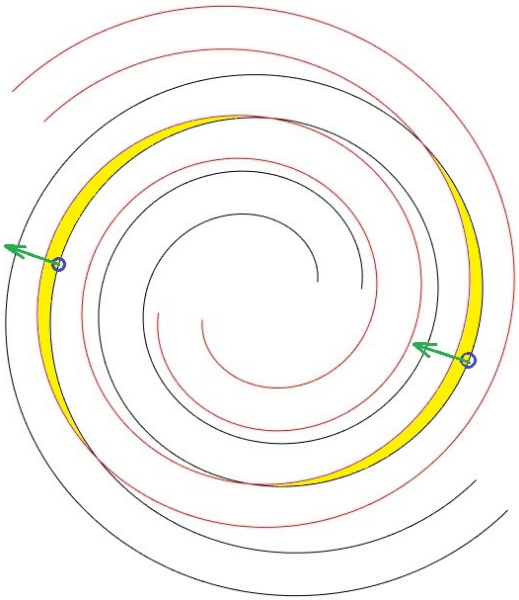

Figure 5.23: Spring arm interference and contacts initial guess.

Solution with arm profile contacts

The approach is based on the assumption that the two contact forces (see Fig. 5.22) act at N^{coord} locations along the arm profile in the N^{dir} direction. Under these assumptions, the arms need to be in contact at the N^{coord} locations and the contact force, N_c, can only be positive (the contact force can only act to push the arms away from each other). Therefore, the value for N_c can be determined by finding the smallest contact force that results in no arm interference or separation at the N^{coord} locations along the arm profile.

For a given spring displacement, $\Delta\beta$, and current values of the N^{coord} and N^{dir} variables, the following non-linear optimization program can be solved:

$$\begin{aligned} \underset{\frac{d\gamma(0)}{ds}, F_x^{end}, F_y^{end}, N_c}{\text{minimize}} \quad & |N_c| \\ \text{subject to} \quad & f_{eq}(\frac{d\gamma(0)}{ds}, F_x^{end}, F_y^{end}, N_c) = 0 \\ & f_{in}(\frac{d\gamma(0)}{ds}, F_x^{end}, F_y^{end}, N_c) \leq 0. \end{aligned} \tag{5.28}$$

Solving Eq. (5.28) gives a valid solution of Eq. (5.13) (with F_x and F_y given by Eq. (5.26)) for the arm displacement $\gamma(s)$ (for $s \in [0, L]$) and the torsional loading that results in spring displacement of $\Delta\beta$ (see Eq. (5.17)).

In calculating the equality constraint function, Eq. (5.10) can be integrated with initial conditions $\gamma(0) = 0$, and current iteration values for $\frac{d\gamma}{ds}(0)$, F_x^{end}, F_y^{end} and N_c to find $\gamma(s)$ for $s \in [0, L]$. The constraint function is used to enforce the boundary conditions and is given by:

$$f_{eq}(\frac{d\gamma(0)}{ds}, F_x^{end}, F_y^{end}, N_c) = \begin{bmatrix} \gamma(L) - \Delta\beta \\ \int_0^L cos(\alpha(s) + \gamma(s))ds - R_n cos(\beta_0 + \Delta\beta) \\ \int_0^L sin(\alpha(s) + \gamma(s))ds - R_n sin(\beta_0 + \Delta\beta) \end{bmatrix}. \tag{5.29}$$

In a similar fashion, the inequality constraint $f_{in}(\frac{d\gamma(0)}{ds}, F_x^{end}, F_y^{end}, N_c)$ ensures that the contact forces are physical (the arms cannot pull each other) and that the arms profiles touch at the contact points N^{coord}.

Iterative solution and stopping criteria

Once the solution of Eq. (5.28) is found, the possibly new arm interference regions are located. The corresponding contact points and contact force direction are saved in $N_{updated}^{coord}$ and $N_{updated}^{dir}$, respectively. The solution to Eq. (5.28) is accepted if

there are no arm interferences. This can be numerically achieved by terminating the algorithm if the minimum of Eq. (5.28) is reached and the following convergence criteria is satisfied:

$$\begin{aligned} |N^{coord} - N^{coord}_{updated}| &\leq \delta^{coord} \\ |N^{dir} - N^{dir}_{updated}| &\leq \delta^{dir} \end{aligned} \tag{5.30}$$

for some integer δ^{coord} and real constant δ^{dir}. Otherwise, N^{coord} and N^{dir} are updated according to:

$$\begin{aligned} N^{coord} &= f^{coord}(N^{coord} - N^{coord}_{updated}) \\ N^{dir} &= f^{dir}(N^{dir} - N^{dir}_{updated}) \end{aligned} \tag{5.31}$$

where f^{coord} and f^{dir} are discrete filters. The use of filters is required to ensure the stability and smoothness of the iterative contact approximation. Both FIR and IIR filters may be used, however, IIR filters are used in generating the spring contact analysis results in this thesis (Sec. 5.4.3).

Once N^{coord} and N^{dir} are updated, Eq. (5.28) is solved again for the updated contacts in an iterative fashion until the contact points and contact direction converge (condition (5.30) is satisfied) or a maximum number of iterations is reached.

Implementation

The algorithm can be implemented using Matlab's fmincom. The algorithm robustness can be significantly improved by utilizing the arm centroidal surfaces to check and update the contact conditions rather than using the arm profiles. This approach allows both coarse and fine arm discretization to be used without unnecessary and costly interpolation.

Validation

The presented algorithm is validated through FEA and torsional load testing of a prototype. The results are presented and discussed in Sec. 5.4.3.

5.4 Optimization-based Design of Planar Rotary Springs

The section describes a novel approach to the design of planar rotary springs which unites the previous arm modeling with nonlinear constrained optimization. The goal is to design the spring with the highest torque density, such that required specifications are met.

Sec. 5.4.1 motivates the optimization approach, Sec. 5.4.2 develops a novel optimization-based design algorithm and Sec. 5.4.3 describes the design of a spring prototype that validates the novel design approach.

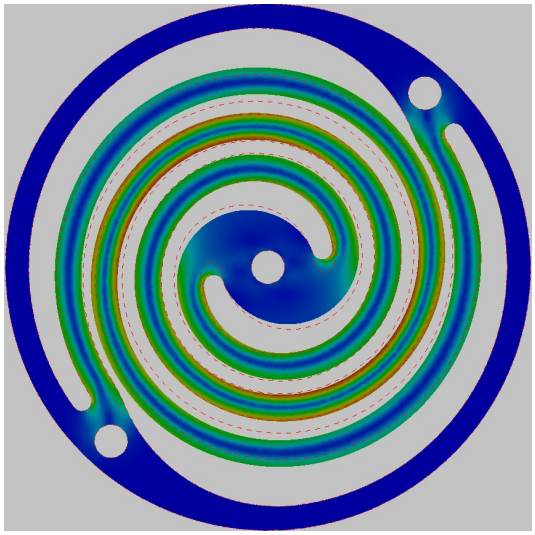

Figure 5.24: FEA torsional simulation of the titanium spring prototype of Sec. 5.2.7

5.4.1 Motivation

Fig. 5.24 shows the FEA torsional simulation of half of the Titanium spring prototype of Sec. 5.2.7. The colours represent stress levels with blue, green, yellow and red corresponding to regions with progressively higher stresses.

The mechanical energy stored in the spring due to the loading is equal to the total strain energy due to the solid deformation. Therefore, regions in the arms that experience lower stresses contribute less to the spring torsional performance. This observation suggest that the spring torque density can be improved by increasing the spring strain energy density. Or equivalently by increasing the stress in areas of lower stress.

Fig. 5.24 shows that the area around the neutral surface carries little stress. This observation was used in Sec. 5.2.4 to motivate the effective weight reduction techniques based on composite arm structure and cutouts.

Tracing the stress levels at either of the two arm profiles shows that the red regions (high stress) are concentrated in relatively small regions. Depending on the spring design, these regions can be as small as 10% to 20% of the total profile length. This observation suggests that significant spring torque density increase is possible if the bending stress along the arm profiles is uniform in all regions.

The section begins with a consideration of the arm strain energy and energy density.

Composite arms are also revisited. The section concludes with discussion of the ways to optimize the arm's shape in order to improve the spring performance.

Arm strain energy density

This section analyzes the arm strain energy and energy density of a torsional spring of the type considered above. It is shown that given an arm deformation gradient $\frac{d\gamma}{ds}$, the strain energy and energy density of the arm are maximized if the stress on the convex arm surface, σ_{cx}, is equal to the maximum admissible stress, $[\sigma]$. This principle is clear, in the case of a straight beam. However, unlike straight beams, for curved beams the centroid surface does not coincide with the neutral surface [111]. Furthermore, the difference between the stresses on the convex and concave arm surfaces increases with increasing the in-plane thickness, d, of the arm (shown below).

In this analysis, the arm's neutral surface is given and the goal is to investigate how varying the in-plane thickness, d, affects the strain energy. This set-up is slightly different from that of Sec. 5.2.2, where the centroidal surface was assumed to be given. The explicit dependence of the variable on s is dropped in the rest of the section to promote clarity. However, derivatives with respect to s are explicitly denoted.

The radius of curvature of the neutral surface r_n can be calculated using Eq. (5.1). Fig. 5.25 shows the arm differential element along the neutral surface arc-length s. For a rectangular cross-section [111]:

$$a = \frac{d}{e^{\frac{d}{r_n}} - 1} \qquad (5.32)$$
$$b = a + d.$$

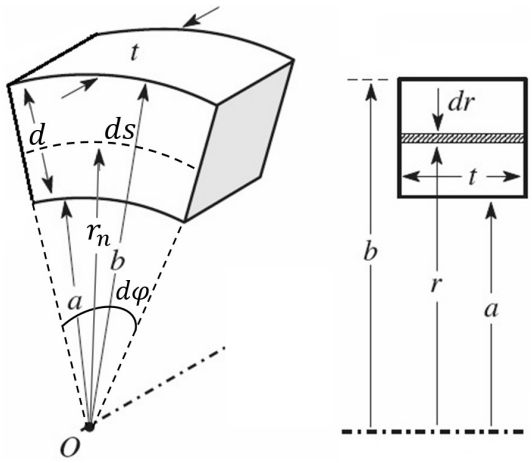

Figure 5.25: Spring arm differential element along the neutral surface.

Eq. (5.32) describes how changing the value of d affects the radii of curvature of the convex and concave surfaces, a and b, respectively, so that the arm neutral surface shape is preserved. That is the radius of curvature of the neutral surface, r_n, is unaffected when the arm thickness, d, is varied. The cross-sectional area and

radius of curvature of the centroid surface are given by:

$$\begin{aligned} A &= (b-a)t \\ r_c &= \frac{b+a}{2}, \end{aligned} \tag{5.33}$$

respectively. The strain energy of the differential element, corresponding to $\frac{d\gamma}{ds}$ is given by:

$$U = \frac{1}{E}\int_a^b [\sigma^2(r)rt]drd\phi = AEr_n e\Big(\frac{d\gamma}{ds}\Big)^2 ds \tag{5.34}$$

where $d\phi = \frac{ds}{r_n}$ (see Fig. 5.25). The mass of the differential element of Fig. 5.25 is:

$$dm = \Big(\frac{b^2-a^2}{2}t\Big)d\phi = \Big(\frac{A(b+a)}{2r_n}\Big)ds. \tag{5.35}$$

By combining Eq. (5.32), Eq. (5.34) and Eq. (5.35), and simplifying the result, it can be shown that the strain energy density, U_m, is given by:

$$U_m \equiv \frac{U}{dm} = \frac{2Er_n^2 e\Big(\frac{d\gamma}{ds}\Big)^2}{b+a} = \frac{Er_n^2\Big(e^{\frac{d}{r_n}}-1\Big)\Big(\frac{d}{2}-r_n+\frac{d}{e^{\frac{d}{r_n}}-1}\Big)\Big(\frac{d\gamma}{ds}\Big)^2}{d(e^{\frac{d}{r_n}}+1)}. \tag{5.36}$$

Let $k_d = \frac{d}{r_n}$ be the arm scaled thickness: clearly $k_d > 0$ for $d > 0$. Then differentiating Eq. (5.36) w.r.t d gives:

$$U_m' = \frac{Er_n^3\Big(e^{\frac{2d}{r_n}}-1-2(\frac{d}{r_n})e^{\frac{d}{r_n}}\Big)\Big(\frac{d\gamma}{ds}\Big)^2}{d^2(e^{\frac{d}{r_n}}+1)^2} = \frac{Er_n^3\Big(\frac{d\gamma}{ds}\Big)^2}{d^2}\Big(\frac{e^{2k_d}-1-2k_de^{k_d}}{(e^{k_d}+1)^2}\Big). \tag{5.37}$$

It can be shown that $e^{2k_d}-1-2k_de^{k_d} > 0$ for $k_d > 0$ by differentiating w.r.t to k_d. Therefore, $U_m' \geq 0$ for $d > 0$. Therefore, it can be concluded that given a deformation gradient $\frac{d\gamma}{ds}$, the strain energy density of the arm increases with increasing d. From Eq. (5.32):

$$a' = \frac{(1-\frac{d}{r_n})e^{\frac{d}{r_n}}-1}{(e^{\frac{d}{r_n}}-1)^2} = \frac{(1-k_d)e^{k_d}-1}{(e^{k_d}+1)^2}, \tag{5.38}$$

where a' is the derivative of a w.r.t. d. It can be shown that $(1-k_d)e^{k_d}-1 < 0$ by differentiating w.r.t. k_d. Then, $a' < 0$, or increasing d leads to a reduction in the value of the variable a. However, $\sigma_{max} \leq [\sigma]$ and from Eq. (5.15) and Eq. (5.16):

$$a = \frac{Er_n^2\frac{d\gamma}{ds}}{Er_n\frac{d\gamma}{ds}+\sigma_{cx}} \geq \frac{Er_n^2\frac{d\gamma}{ds}}{Er_n\frac{d\gamma}{ds}+[\sigma]} \equiv a_{min} \tag{5.39}$$

where a_{min} is the minimum allowable value for a. Therefore, the energy density is maximized if $a = a_{min}$ or equivalently if $\sigma_{cx} = [\sigma]$.

In a similar fashion, it can be shown that $U' > 0$ for $k_d > 0$, where U' is the derivative of U w.r.t. d. Therefore, the strain energy also increases with increasing d, and thus, for a given deformation $\frac{d\gamma}{ds}$, the strain energy is maximized if $\sigma_{cx} = [\sigma]$.

Next, consider the sum of the stresses on the convex and concave surfaces:

$$\sigma_{cx} + \sigma_{cv} = E(2 - \frac{(a+b)r_n}{ab})r_n\frac{d\gamma}{ds} = 2E(\frac{k_d - sinh(k_d)}{k_d})r_n\frac{d\gamma}{ds} \tag{5.40}$$

It can be shown that $k_d - sinh(k_d) < 0$. Therefore, $|\sigma_{cx}| > |\sigma_{cv}|$. Similarly, it can be shown that $(\sigma_{cx} + \sigma_{cv})' < 0$ (derivative with respect to d), and therefore the difference between the stresses on the convex and concave surfaces increases with increasing d.

In conclusion, this section showed that the arm strain energy and strain energy density are maximized if the arm in-plane thickness is maximized, or equivalently if the convex arm surface is subject to the maximum allowable bending stress.

Composite arm modeling

This section supplements composite arm analysis of Sec. 5.2.4 so that composite arms may be used with the optimization-based design algorithm of Sec. 5.4.2.

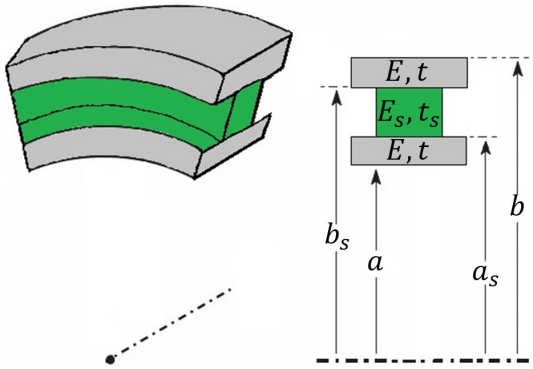

Figure 5.26: Spring composite arm structure.

Fig. 5.26 shows the structure of a general composite arm. The primary material (gray) and the secondary material (green) have stiffness, density and out-of-plane thickness given by E, ρ, t and E_s, ρ_s, t_s, respectively (similar to Sec. 5.2.4).

The arm in-plane thickness is again given by $d = b - a$ and the in-plane thickness of the secondary material layer is $d_s = b_s - a_s$ as shown in Fig. 5.26. For the

composite arm cross-section shown in Fig. 5.26:

$$\begin{aligned} a &= \frac{d}{e^{\frac{d}{r_n}} - 1} \\ b &= a + d \\ a_s &= \frac{d_s}{e^{\frac{d_s}{r_n}} - 1} \\ b_s &= a_s + d_s. \end{aligned} \tag{5.41}$$

The transformed section approach is used in the derivation of Eq. (5.41) (see Sec. 5.2.4). The cross-sectional area, A, and radius of curvature of the centroid surface, r_c, are:

$$\begin{aligned} A &= \Big[d - \Big(1 - \frac{E_s t_s}{Et}\Big) d_s\Big] t \\ r_c &= a + t \frac{\frac{(a_s - a)^2}{2} + (\frac{E_s t_s}{Et})(b_s - a_s)(\frac{b_s + a_s}{2} - a) + (b - b_s)(\frac{b + b_s}{2} - a)}{A}. \end{aligned} \tag{5.42}$$

Eq. (5.34) remains unaltered, while the differential element mass is now given by:

$$dm = \Big(\frac{(b^2 - a^2) - (1 - \frac{t_s \rho_s}{t\rho}(b_s^2 - a_s^2))}{2 r_n} t\rho\Big) ds. \tag{5.43}$$

As described in Sec. 5.2.4, $k_s \equiv \frac{d_s}{d}$ represents the trade-off between mass reduction and stiffness reduction.

Approaches to maximizing the strain energy density

Combining Eq. (5.15) and Eq. (5.32) leads to:

$$\sigma_{cx}(s) = E\Big(1 - \frac{r_n(s)(e^{\frac{d(s)}{r_n(s)}} - 1)}{d(s)}\Big) r_n(s) \frac{d\gamma}{ds}. \tag{5.44}$$

As shown earlier in the section, the strain energy and energy density are maximized if $\sigma_{cx}(s) = [\sigma]$ for $s \in [0, L]$ or along the arm profile. The two design variables in Eq. (5.44) are $r_n(s)$ and $d(s)$. The arm neutral surface curvature radius, $r_n(s)$, can be modified by changing the arm shape. The nonlinear dependence of the curvature radius on the curve coordinates and their first and second derivatives (see Eq. (5.1)), suggests that this modification cannot be achieved locally. Therefore, the entire arm shape needs to be altered, in order to adjust $r_n(s)$ in a region along the arm profile. Note that Eq. (5.1) shows how the radius of curvature of the centroidal surface can be calculated, however, the same equation can be used for the neutral surface,

provided its curve is given in polar coordinates. Unlike the variable $r_n(s)$, the arm in-plane thickness, d, can be modified directly. The value of the variable $d(s)$ may be adjusted in any region while preserving the arm shape, as discussed earlier in the section (see Eq. (5.32)). The dependence of the arm flexural rigidity given by $(A(s)Ee(s)r_n(s))$ on $r_n(s)$ and $d(s)$ in Eq. (5.10) suggests that changing either of the two parameters would have a non-linear effect on $\frac{d\gamma}{ds}$. However, in order to calculate $\frac{d\gamma}{ds}$ along the length of the arm, one needs to solve Eq. (5.13) first. Therefore, the effects of changes in the values of $r_n(s)$ and $d(s)$ on the convex arm stress σ_{cx} in Eq. (5.44) along the arm cannot be predicted unless Eq. (5.13) is solved. Then it can be concluded that optimizing either $r_n(s)$ or $d(s)$ in order to maximize the strain energy and energy density would require solving a nonlinear optimization program. Next the optimization of $r_n(s)$ and $d(s)$ is considered separately.

Modifying the neutral surface curvature radius, $r_n(s)$, while maintaining constant $d(s)$ is equivalent to modifying the shape of a constant in-plane thickness arm. Using a modified version of the algorithm of Sec. 5.4.2, the arm shape can be optimized so that the stress on the convex surface is maximized while $d(s) = const$. This approach has the following disadvantages:

- The selection of an arbitrary inner circle spring diameter is not possible. For a given outer circle diameter, the optimized arm inner circle diameter is determined by the optimization. Thus, the spring design is significantly less flexible.
- Multiple arms cannot be used due to arm intersections.

Fig. 5.27 shows the optimized shape of a two arm spring. The arm shape is determined only by the spring outer circle and material maximum admissible stress. The curves trace the arm neutral surfaces. As can be observed from the figure, the shape of the arms causes in arm interference and the planar spring cannot be manufactured. Furthermore, if the spring in-plane thickness is large enough, the arm might self-intersect, thus, even one arm spring might be unrealizable.

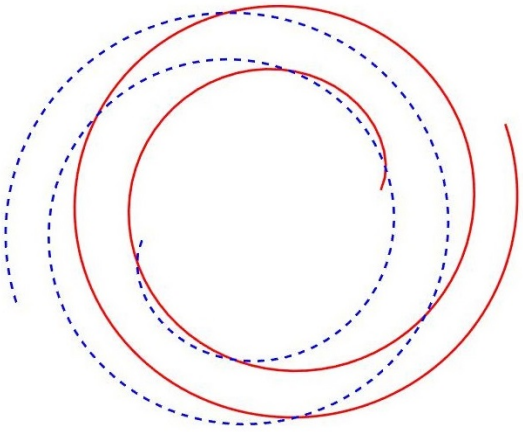

Figure 5.27: Optimized spring shape. The curves trace the arm neutral surfaces.

On the other hand, if the in-plane thickness, $d(s)$, is modified while $r_n(s)$ remains unaltered, the arm shape would be preserved. Thus, if the arm neutral surface is designed so that multiple arms can be positioned symmetrically around the spring center without interference, the arms in-plane thickness may be optimized without the occurrence of arm interference. For example, this is the case for spring arms with spiral neutral surfaces. For this reason, the approach of optimizing $d(s)$ rather than r_n, is adopted in the rest of this work.

5.4.2 Optimization-based Design Algorithm

The section describes a design algorithm that optimizes the arm in-plane thickness so that the arm strain energy density is maximized. The section begins with a brief description of the spring specifications and design procedure. Due to fundamental limitations, the arm performance cannot be independently maximized for rotations in both displacement directions. The optimization algorithm with its bidirectional variant is described in detail, followed by implementation discussion.

Spring Performance Specification and Design Procedure

Similar to Sec. 5.2.5, the spring design starts with a performance specification. As before, desired maximum torque, τ_{des}, and stiffness, K_{des}, are determined. Then, the maximum design spring displacement can be calculated $\Delta\beta_{max} = \frac{\tau_{des}}{K_{des}}$. Next, the spring material is chosen. If a composite section design is employed both the primary and secondary materials need to be determined. The maximum arm stress at maximum displacement, $\Delta\beta_{max}$ (given by σ_{max} in Eq. (5.16)), needs to be $\sigma_{max} \leq [\sigma]$. The size of the inner and outer circles (see Sec. 5.2.2) are assumed to be determined from packaging constraints.

The arm geometry is fully determined by its neutral surface and in-plane thickness. The spring design begins with the choice of the arm neutral surface shape and number of arms, n. In most cases, especially in high torque and low stiffness applications, the arms are chosen to be spiral as discussed in Sec. 5.4.1. Spirals allow for efficient symmetric spring design, since n arms conveniently "spiral" around each other without interference. Given the inner and outer circle, a spiral neutral surface is designed (see Sec. 5.2.5). Unlike Sec. 5.2.5, however, the arm's neutral surface is specified instead of the arms centroidal surface. This approach is motivated be the arm strain energy analysis of Sec. 5.4.1. The rest of the section, assumes that the spring arm neutral surface has been chosen, and is arc-length parameterized (by

s and α). The radius of curvature, $r_n(s)$, is also calculated (see Sec. 5.2.2). Next, the arm in-plane thickness, $d(s)$, is optimized so that $\sigma_{cv}(s) = [\sigma]$, and thus, the arm's strain energy is maximized at $\Delta\beta_{max}$.

Arm In-plane Thickness Optimization

The goal is to optimize the arm profile thickness, $d(s)$, so that the torque and torque density are maximized at the maximum displacement, $\Delta\beta_{max}$. This can be achieved by maximizing the strain energy density or equivalently optimizing $d(s)$ so that the stress at the convex surface is $|\sigma_{cx}(s)| = [\sigma]$, as shown in Sec. 5.4.1. The motivation here is similar to [110], where the shape of a leaf spring is optimized using FEA so that the stress distribution uniformity is improved. However, as will be demonstrated in Sec. 5.4.3, the intuitive approach of reducing $d(s)$ along regions of lower stress, suggested in [110], is found to be inappropriate for the planar springs considered here.

The arm in-plane thickness can be optimized through maximizing the energy density by solving a non-linear optimization program given by:

$$\begin{aligned} \underset{\frac{d\Gamma(0)}{ds}, F, d_{in}}{\text{minimize}} \quad & f\left(\frac{d\Gamma(0)}{ds}, F, d_{in}\right) \\ \text{subject to} \quad & g_{eq}\left(\frac{d\Gamma(0)}{ds}, F, d_{in}\right) = 0 \\ & g_{in}\left(\frac{d\Gamma(0)}{ds}, F, d_{in}\right) \leq 0. \end{aligned} \tag{5.45}$$

Eq. (5.45) is defined in similar fashion to Eq. (5.3.2). Before describing the optimization variables, and the cost and constraint functions, an important practical distinction needs to be made. For the rest of the section, Eq. (5.45) is termed *unidirectional optimization* if the performance of the spring is optimized at the maximum displacement $\Delta\beta_{max}$ only. I.e., spring performance is optimized for displacement in only one of the two torsional directions. The performance of the spring in the other direction is often degraded as shown in Sec. 5.4.3. On the other hand, Eq. (5.45) is termed *bidirectional optimization* when the torque density is maximized for both displacements $\Delta\beta_{max}$ and $-\Delta\beta_{max}$. This directional distinction is important because the torque density of the arm can readily be maximized in the unidirectional case by optimizing $d(s)$ so that $|\sigma_{cx}(s)| = [\sigma]$ everywhere on the convex profile at displacement $\Delta\beta_{max}$, however, this is generally not possible in the case of bidirectional optimization.

In the following, the unidirectional optimization version of Eq. (5.45) is first described. Then, the necessary modifications for the bidirectional optimization are discussed. A brief implementation overview is also provided.

The unidirectional optimization variables are: the deformation angle gradient $\frac{d\Gamma(0)}{ds} = \frac{d\gamma(0)}{ds}$ at the inner circle, the arm end forces, $F = [F_x \quad F_y]^T$, at the outer circle and the in-plane arm thickness at a number of discreet points, $d_{in}(s_k)$ for $k = 1, ..., N_{max}$. Without loss of generality, arm contacts are not considered here. Therefore, F_x and F_y are the arm end forces similar to Sec. 5.2.2. In this implementation, d_{in} is an uniform discretization of $d(s)$, however, other discretization schemes are also possible. The solution of Eq. (5.45) for $\frac{d\gamma(0)}{ds}$ is the initial condition for $\gamma(s)$ in Eq. (5.13) that satisfies the boundary conditions for the arm end forces F, and thus, leads to spring displacement $\Delta\beta_{max}$. The in-plane arm thickness $d(s)$ along the arm profile is found by interpolating the discrete values of d_{in} for $s \in [0, L]$.

In calculating the equality constraint function, $g_{eq}(\frac{d\Gamma(0)}{ds}, F, d_{in})$, first the profile curvature radii a and b are evaluated using Eq. (5.32) o Eq. (5.41) for the current d_{in}. Next A and r_c are evaluated using Eq. (5.33) or Eq. (5.42). Eq. (5.10) can be integrated with the initial conditions $\gamma(0)$ and $\frac{d\gamma}{ds}(0)$ to find $\gamma(s)$ for $s \in [0, L]$. The constraint function is used to enforce the boundary conditions and is given by:

$$g_{eq}(\frac{d\Gamma(0)}{ds}, F, d_{in}) = \begin{bmatrix} \gamma(L) - \Delta\beta_{max} \\ \int_0^L cos(\alpha(s) + \gamma(s))ds - R_n cos(\beta_0 + \Delta\beta_{max}) \\ \int_0^L sin(\alpha(s) + \gamma(s))ds - R_n sin(\beta_0 + \Delta\beta_{max}) \end{bmatrix}. \tag{5.46}$$

Thus, the nonlinear equality constraint, $g_{eq}(\frac{d\Gamma(0)}{ds}, F, d_{in}) = 0$, ensures that $\gamma(s)$ is a valid solution of Eq. (5.13).

Attempting to directly maximize the spring torque and torque density or strain energy and energy density may lead to an unfavorable local minimum. This motivates the strain energy consideration of Sec. 5.4.1. The stress on the convex surface, σ_{cx}, is maximized instead, which may be calculated using Eq. (5.15). The objective function may be defined by:

$$f(\frac{d\Gamma(0)}{ds}, F, d_{in}) = \int_0^L (|\sigma_{cx}| - [\sigma])^2 ds. \tag{5.47}$$

Therefore, $f(\frac{d\Gamma(0)}{ds}, F, d_{in}) = 0$, ensure that the strain energy and energy density are maximized (Sec. 5.4.1). Other cost function definitions are also possible, however, Eq. (5.47) proved to be very stable in implementation with off-the-shelf non-linear solvers.

The nonlinear inequality constraint function $g_{in}(\frac{d\Gamma(0)}{ds}, F, d_{in})$ ensures that the stress in the arm is less than the maximum allowable stress, $[\sigma]$. The constraint can also be used to reduce the stress at the arm ends if stress concentrations are of concern, as discussed in Sec. 5.4.3. In some cases the nonlinear inequality constraint can be omitted in unidirectional optimization especially if the cost function is defined as in Eq. (5.47).

The optimization problem in Eq. (5.45) may be readily solved with off-the-shelf optimization software such as Matlab's fmincon, provided a good initial guess is used. A suitable choice for the initial guess is the solution of Eq. (5.13) for $\Delta\beta_{max}$ with some $d(s) = const$ such that $\sigma_{max} \approx [\sigma]$. Such a solution may be obtained using a shooting method and the approach described in Sec. 5.2.5. Once the solution is obtained, the corresponding values for $\frac{d\Gamma(0)}{ds}$, F and d_{in} can be used to initialize the optimization solver.

The solver performance depends on both the initial guess and the discrete numerical resolution. To improve the speed and accuracy, Eq. (5.45) is consecutively solved with progressively finer discretization using the coarser previous solution as the initial guess. This approach allows one to efficiently find the optimal thickness $d(s)$ such that $\sigma_{cx}(s) = [\sigma]$ for $s \in [0, L]$ in the unidirectional case.

Bidirectional Optimization

Bidirectional optimization seeks to maximize spring performance considering both rotational directions. The optimization variables are $\frac{d\Gamma(0)}{ds} = [\frac{d\gamma_1(0)}{ds} \quad \frac{d\gamma_2(0)}{ds}]^T$ and $F = [F_x^1 \quad F_y^1 \quad F_x^2 \quad F_y^2]^T$, where $\frac{d\gamma_1(0)}{ds}$ and $\frac{d\gamma_2(0)}{ds}$ are the deformation angle gradients at the inner circle, corresponding to spring displacements $\Delta\beta_{max}$ and $-\Delta\beta_{max}$. Similarly, F_x^1, F_y^1 and F_x^2, F_y^2 are the arm end forces corresponding to displacements $\Delta\beta_{max}$ and $-\Delta\beta_{max}$, respectively. In this case the constraint function is given by:

$$g_{eq}(\frac{d\Gamma(0)}{ds}, F, d_{in}) = \begin{bmatrix} \gamma_1(L) - \Delta\beta_{max} \\ \gamma_2(L) + \Delta\beta_{max} \\ \int_0^L cos(\alpha(s) + \gamma_1(s))ds - R_n cos(\beta_0 + \Delta\beta_{max}) \\ \int_0^L cos(\alpha(s) + \gamma_2(s))ds - R_n cos(\beta_0 - \Delta\beta_{max}) \\ \int_0^L sin(\alpha(s) + \gamma_1(s))ds - R_n sin(\beta_0 + \Delta\beta_{max} \\ \int_0^L sin(\alpha(s) + \gamma_2(s))ds - R_n sin(\beta_0 - \Delta\beta_{max}) \end{bmatrix}. \quad (5.48)$$

The nonlinear equality constraint function, $g_{eq}(\frac{d\Gamma(0)}{ds}, F, d_{in}) = 0$, ensures that $\gamma_1(s)$ and $\gamma_2(s)$ are valid solutions of Eq. (5.13), corresponding to $\Delta\beta_{max}$ and $-\Delta\beta_{max}$

displacements, respectively. Like the unidirectional case, the nonlinear inequality constraint ensures that arm stresses do not exceed the maximum admissible stress $[\sigma]$.

In Sec. 5.4.1, it was shown that the strain energy density is maximized if $\sigma_{cx} = [\sigma]$ everywhere along the arm profile. However, this cannot be achieved in bidirectional optimization and the inequality constraint becomes quite important.

5.4.3 7075 Aluminum Spring Prototype

This section demonstrates the effectiveness of the optimization-based spring design approach of Sec 5.4.2 by designing a high performance $7075 - 651$ aluminum spring prototype. The validity of the spring analysis algorithm of Sec. 5.3.2 is also confirmed through FEA and experimental prototype mechanical testing.

Spring Prototype Design

The yield strength of $7075 - T651$ aluminum is approximately $500MPa$. A maximum allowable stress of $[\sigma] = 200MPa$ is chosen, which is slightly higher than the material's endurance limit.

The inner and outer circles have dimensions $R_{out} = 50mm$ and $R_{out} = 15mm$. For manufacturing and demonstration convenience, the out-of-plane thickness of the spring is $t = 10mm$. The maximum design spring displacement is $\Delta\beta_{max} = 20°$.

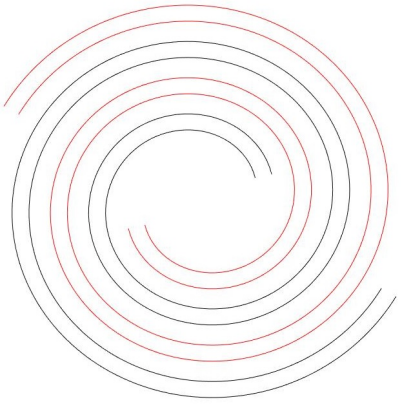

Figure 5.28: Spring shape with constant in-plane thickness.

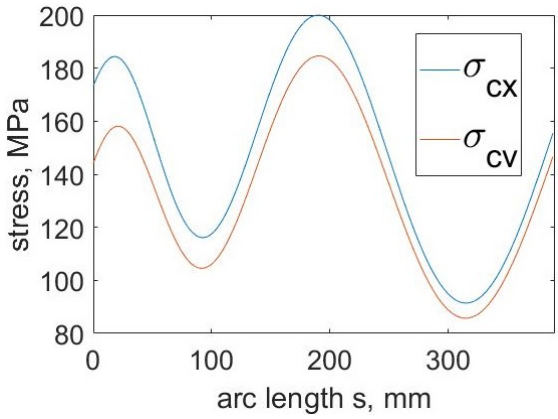

Figure 5.29: Spring arm bending stress at displacement β.

The design begins with finding a spiral spring of constant in-plane thickness $d(s)$, such that the maximum stress in the arms is given by $[\sigma]$ at displacement $\Delta\beta_{max}$. Fig. 5.28 shows the spring profile. Fig.5.29 shows the stress along the arm profile

at displacement $\Delta\beta_{max}$. For this initial design, the arm bending stress is indeed suboptimal. The torque supported at spring displacements $\Delta\beta_{max}$ and $-\Delta\beta_{max}$ is given by $\tau_{\Delta\beta_{max}} = 9.4Nm$ and $\tau_{-\Delta\beta_{max}} = -9.5Nm$, respectively (see Eq. (5.17)). The arms' mass is calculated at $M_{arms} = 103g$.

First, the profile in-plane thickness is optimized using the uni-directional optimization algorithm of Sec. 5.4.2.

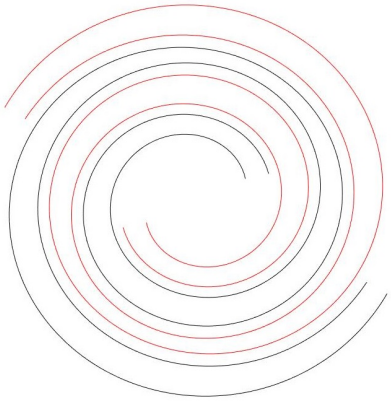

Figure 5.30: Uni-directionally optimized spring shape.

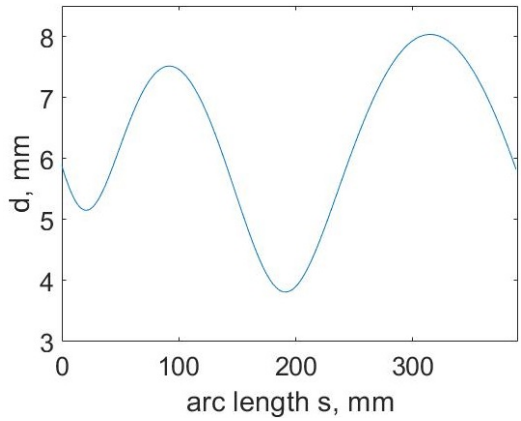

Figure 5.31: Uni-directionally optimized in-plane spring arm thickness d.

The spring is optimized only for $\Delta\beta_{max}$ displacement. Fig. 5.30 shows the uni-directionally optimized spring profile. Fig. 5.31 shows the uni-directionally optimized spring in-plane thickness. The torque supported at spring displacement $\Delta\beta_{max}$ is given by $\tau_{\Delta\beta_{max}} = 23.5Nm$ (see Eq. (5.17)). The arms' mass is calculated at $M_{arms} = 147g$. Thus, the torque and torque density of the arms for displacements $\Delta\beta_{max}$ are increased approximately by 150% and 78%, respectively due to the optimization of the in-plane thickness $d(s)$.

Fig. 5.32 shows the arm profile stresses at maximum displacements $\Delta\beta_{max}$ and $-\Delta\beta_{max}$ for the uni-directionally optimized arm. The figure confirms that in uni-directional optimization, the arm in-plane thickness can readily be optimized so that the bending stress along the convex surface is $\sigma_{cx} = [\sigma]$ for displacement $\Delta\beta_{max}$. However, at displacement $-\Delta\beta_{max}$ there are regions along the arm profile where σ_{cx} is substantially higher than $[\sigma]$. Thus, maximizing the spring performance using the uni-directional optimization leads to an optimal spring torque and torque density in the optimization direction at the expense of deteriorated performance in the other displacement direction.

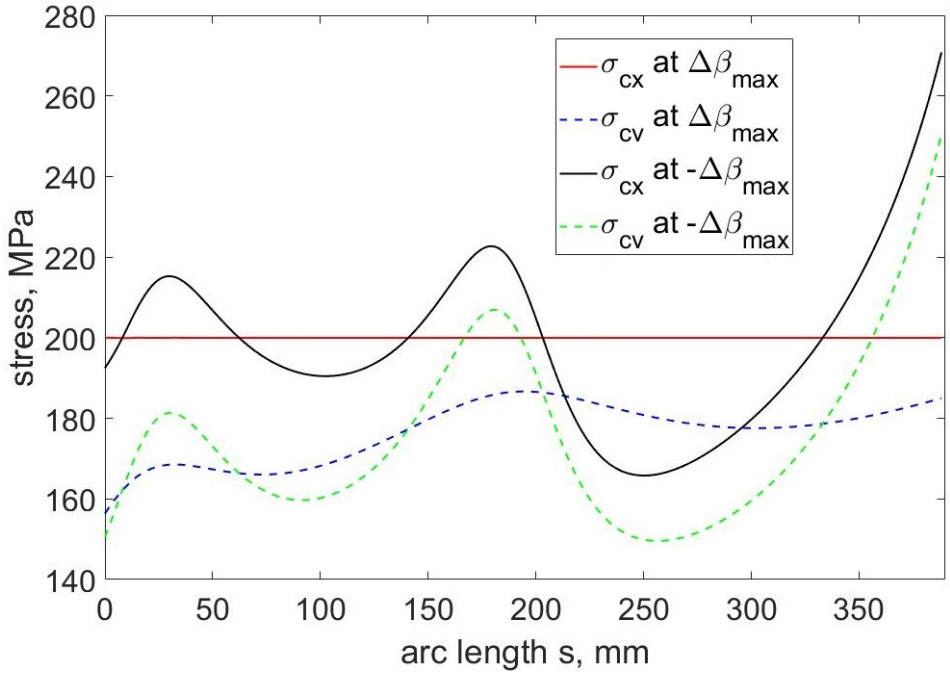

Figure 5.32: Spring arm bending stress for uni-directionally optimized spring at displacements $\Delta\beta_{max}$ and $-\Delta\beta_{max}$.

Next, the profile in-plane thickness is optimized using the bi-directional optimization algorithm of Sec. 5.4.2. Fig. 5.33 shows the bi-directionally optimized spring profile. Fig. 5.34 shows the bi-directionally optimized spring in-plane thickness.

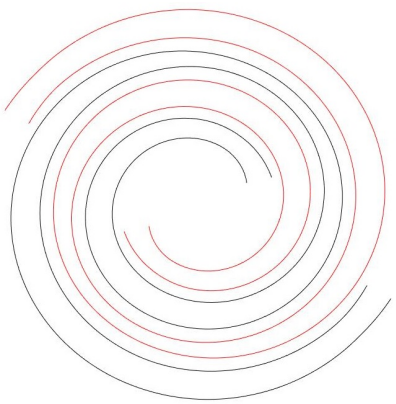

Figure 5.33: Bi-directionally optimized spring shape.

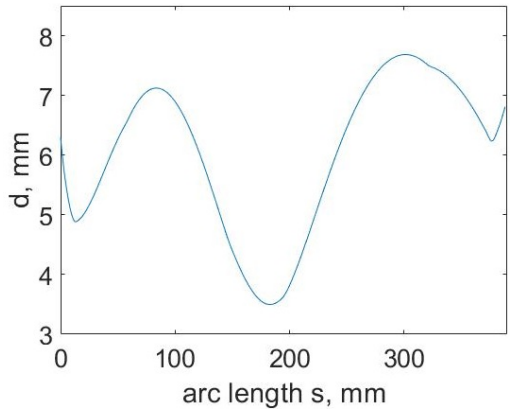

Figure 5.34: Bi-directionally optimized in-plane spring arm thickness d.

The shapes of the uni-directionally optimized and bi-directionally optimized springs are very similar (compare Fig. 5.30 and Fig. 5.33). However, close examination of Fig. 5.31 and 5.34 reveals that the bi-directional spring is slightly thinner in some regions along the arm profile. The increased arm in-plane thickness around the arm

ends for the bi-directionally optimized spring (observed in Fig. 5.34) is a stress concentration prevention measure, which is further discussed later in the section.

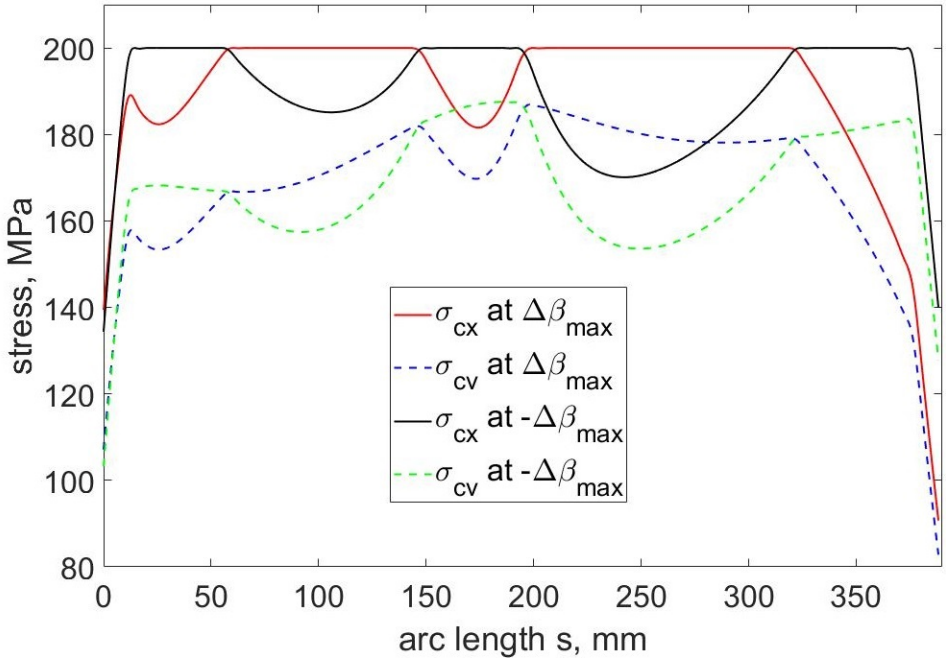

Figure 5.35: Spring arm bending stress for bi-directionally optimized spring at displacements $\Delta\beta_{max}$ and $-\Delta\beta_{max}$.

Fig. 5.35 shows the arm profile stresses at maximum displacements for the bi-directionally optimized arm. Unfortunately, bidirectional optimization cannot yield bending stress equal to the maximum allowable stress everywhere on the convex arm surface. Tracing the convex stress curves in Fig. 5.35 suggest that a directional performance trade-off exists. That is, if the stress in a region along the profile is maximized for spring displaced $\Delta\beta_{max}$, the stress in the same region is lower for spring displaced $-\Delta\beta_{max}$.

The optimization inequality constraint discussed in Sec. 5.4.2 can be modified so that the stress is reduced at the arm ends as demonstrated in Fig. 5.35. Thus, the potential performance limiting stress concentrations at the arm ends can be readily reduced to an acceptable level. This ability to modify the stress in particular regions is quite beneficial from practical design point of view.

The model predicts that the torque carried by the bi-directionally optimized arms at spring displacements $\Delta\beta_{max}$ and $-\Delta\beta_{max}$ are given by $\tau_{\Delta\beta_{max}} = 20.6Nm$ and $\tau_{-\Delta\beta_{max}} = -19.9Nm$, respectively (using Eq. (5.17)). The optimized arms mass is given by $M_{arms} = 140g$. Thus, the torque and torque density of the arms are

increased approximately by 100% and 60%, respectively due to the bi-directional optimization of the in-plane thickness, d.

In order to verify the optimization-based design approach, the spring design which is bi-directionally optimized is selected for manufacturing. The final design step is to add supporting material at the inner and outer circles and provide mounting holes, similar to the prototypes of Sec. 5.2.6 and Sec. 5.2.7. The aluminum spring prototype was CNC machined in-house and is shown in Fig. 5.36.

Figure 5.36: 7075 Al spring prototype.

Spring Analysis and Experimental Validation

The remaining part of the section validates the spring design of Sec. 5.4 and spring analysis algorithm from Sec. 5.3. The design loading conditions for the prototype described in Sec. 5.4.3 are simulated through non-linear FEA with approximately 1.7 million linear elements. However, due to computational resource limitations, contacts are not simulated with such a fine mesh. Instead a coarser mesh with approximately 170 thousand linear elements is used for the contact simulation. The thickness and loadings are significantly scaled down to improve the accuracy in both FEA simulations.

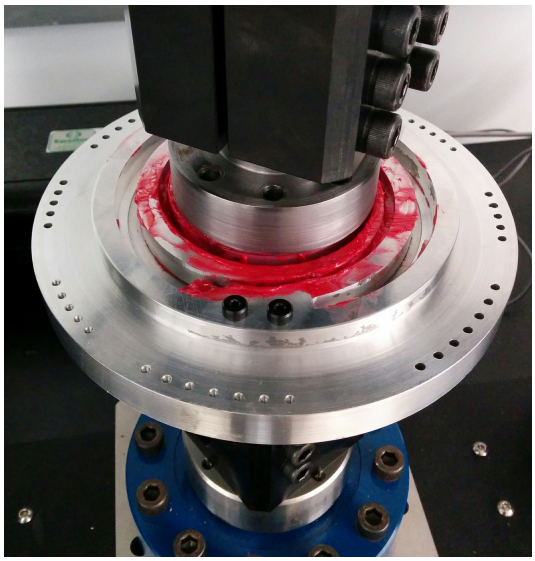

Figure 5.37: 7075 Aluminum spring prototype torsional testing.

Fig. 5.38 shows FEA simulations of the spring torsional design loading which correspond to spring displacements $\Delta\beta_{max}$ and $-\Delta\beta_{max}$, respectively. The FEA simulated stress levels on the arm surfaces completely agree with the model pre-

diction of Fig. 5.35. Furthermore, comparing the FEA simulation results of Fig. 5.24 and Fig. 5.38 reveal the significant advantage of the optimization-based spring design algorithm of Sec. 5.4.2.

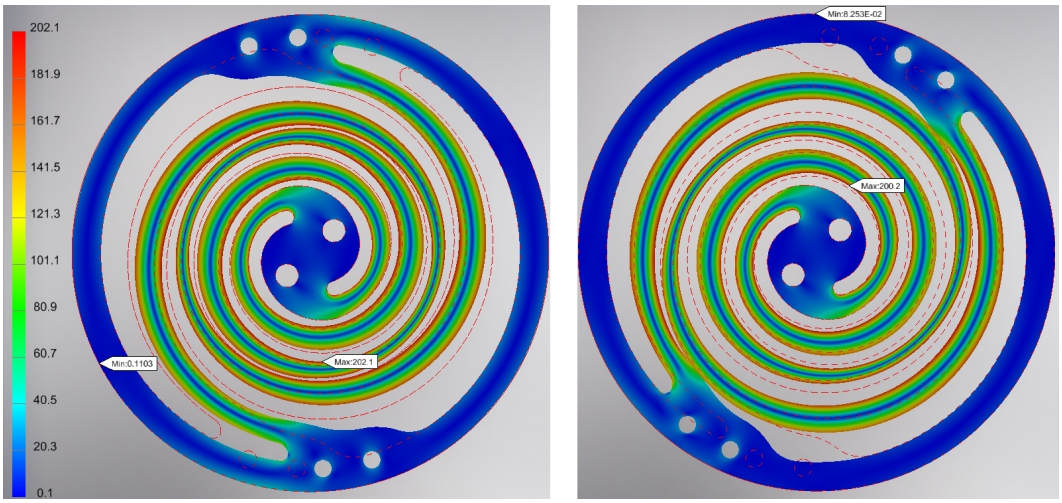

Figure 5.38: FEA simulation results at design spring torsional loading. Counter-clockwise loading on the left and clockwise loading on the right. The colour bar units correspond to stress in MPa.

The torsional properties of the prototype, shown in Fig. 5.36, were characterized with an ADMET mechanical testing machine, similar to Sec. 5.2.6. Fig. 5.37 shows the experimental set-up. Grease was added to decrease the friction between the arms so that the frictionless contact assumption of Sec. 5.3.1 is justified.

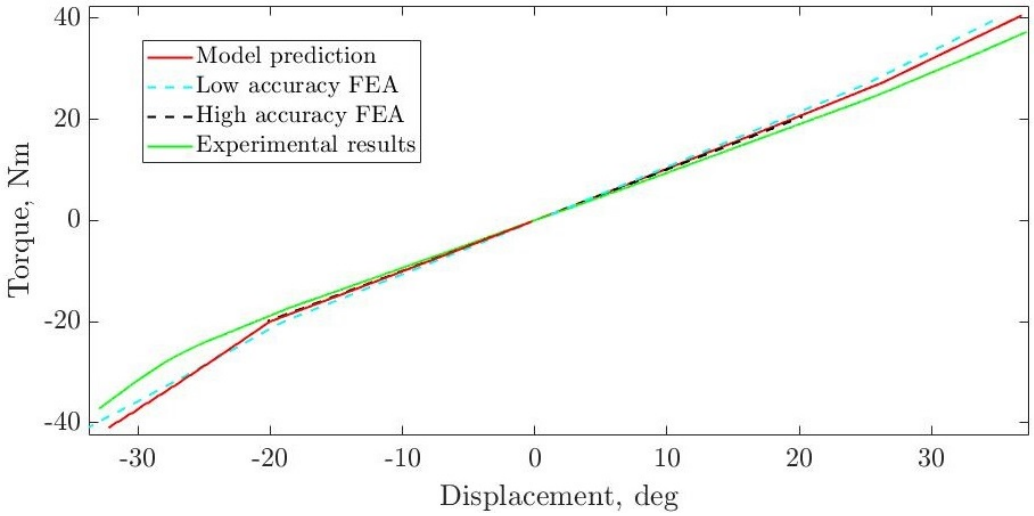

Figure 5.39: Spring torque against displacement plot.

The experimental results and FEA simulation results are compared with the model predictions in Fig. 5.39 and Fig. 5.40.

The fine mesh FEA simulation agrees with the model prediction with a maximum error of around 1% in both the stiffness and stress values. The coarse mesh FEA simulation agrees with the model prediction with a maximum error of around 5.5% in stiffness and 7.5% in stress values.

The experimental results show around 6% lower stiffness levels in the design region (where no arm contacts occur) compared to the model prediction. These results are similar to what is observed in Sec. 5.2.6. The discrepancy is probably due to lower manufacturing accuracy and experimental issues related to the arm boundary condition enforcement, clamping and attachment of the springs, calibration, etc.

With arm contacts at higher loading, the experimental results show around 8% and 12% lower stiffness levels depending on the loading direction. The higher errors (12%) are probably caused by difference in the arm contact conditions at the outer circle in the prototype compared to the modelling. This is unavoidable as the fixed boundary conditions at the outer circle need to be enforced in the prototype. The added material at the outer circle probably causes the contact point to move away from the prediction along the profile.

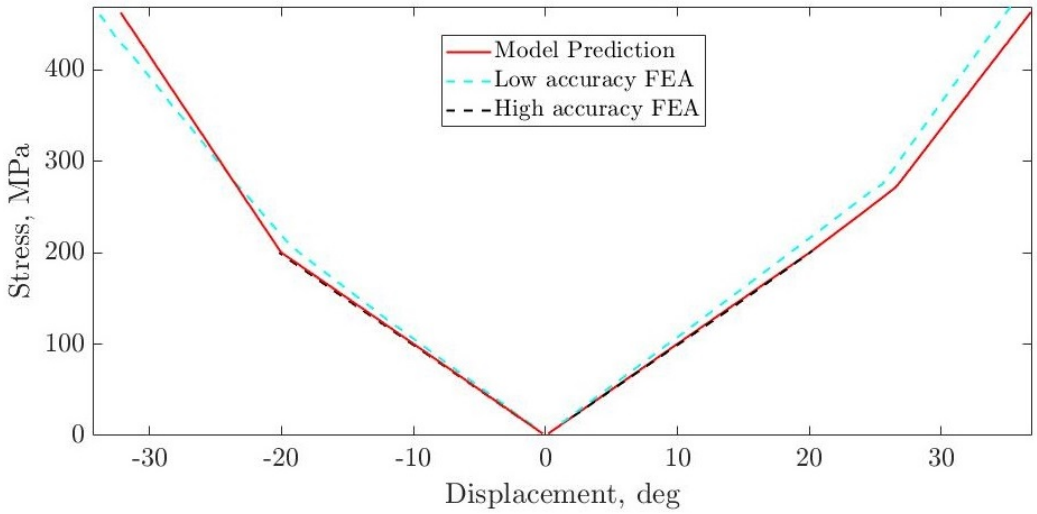

Figure 5.40: Maximum arm bending stress against displacement plot.

In summary, the results of this section, which are analogous to those of Sec. 5.2.6, show the validity of the presented spring optimization-based design and analysis. Furthermore, the arm contact analysis provides a means for rapid spring approximate torsional response prediction under overload conditions. This is quite advantageous because FEA with contacts is quite computationally expensive and can be quite inaccurate as Fig. 5.39 suggests.

Optimization-based design discussion

Comparing Fig. 5.29 with Fig. 5.31 and Fig. 5.34, suggests that the optimal solution for $d(s)$ is quite counter intuitive. As discussed in [110], elementary beam theory suggests that reducing $d(s)$ along regions of low stress, should increase the stress in these regions. Fig. 5.31 and Fig. 5.34 show that this need not be the case. In fact, $d(s)$ increases in the areas of lower stress in Fig. 5.29. This observation demonstrates the main advantage of the optimization-based design approach introduced in Sec. 5.4.2. Furthermore, the nonlinear relationship between the stress and the in-plane thickness, $d(s)$, may be a significant challenge for the iterative FEA-based planar spring optimization procedures previously used in the literature (see Sec. 5.1) and may be the reason why optimal designs such as those presented here, have not been introduced before.

The design example also suggests that both the uni-directional and bi-directional optimization have certain advantages. If the spring is intended for applications that involve loading only in one direction, the uni-directional design optimization allows higher achievable torque and torque density. On the other hand, if the spring is intended for applications where bi-directional loading occurs, the bi-directional design optimization achieves directionally symmetric loading capability.

5.5 Conclusion

The chapter develops a novel mathematical model, based on curved beam theory, that can be used to rapidly design and analyze rotary springs, which are commonly used in SEA systems, as well as mechanical couplings. Techniques and analysis for spring mass reduction through composite structure and cutouts are also introduced. An improved performance analysis algorithm that allows for rapid spring loading response prediction with possible arm contacts is developed. A novel planar spring optimization-based design algorithm which is based on the mathematical model is described. The spring torsional performance is significantly improved through arm profile thickness optimization. A number of mechanical prototypes are designed, analyzed and manufactured according to the novel algorithms and techniques. The proposed design and analysis techniques are validated through FEA and experimental prototype mechanical testing.

Chapter 6

ACTUATOR PROTOTYPES

6.1 Chapter Structure and Contributions

This chapter presents actuator prototypes that feature high torque density motors (Ch. 3), bearingless planetary gearboxes (Ch. 4) and planar rotary springs (Ch. 5). Sec. 6.2 describes an actuator that features a $1:10$ reduction ratio bearingless planetary gearbox. Sec. 6.3 describes a series elastic actuator that features a $1:101$ reduction ratio bearingless planetary gearbox and an elastic element designed according to Ch. 5. The bearingless planetary gearboxes of Sec. 6.2 and Sec. 6.3 are both driven by high torque density outrunner motors that are incorporated into the gearbox interior. These prototypes demonstrate the weight and compactness advantages that may be achieved with custom designs of the bearingless planetary gearbox. Sec. 6.4 describes a series elastic actuator which is similar to the actuator shown in Sec. 6.3 and is used in the tether management system of the Axel rover developed at the NASA Jet Prop. Lab. [36].

6.2 Low Reduction Actuator Prototype

A low reduction bearingless planetary gearbox that has no assembly features (see Sec. 4.3.4) is shown in Fig. 6.1. It is used in the robotic joint prototype of Fig. 6.2. The outrunner motor, driving the prototype is a modified of-the-shelf, high

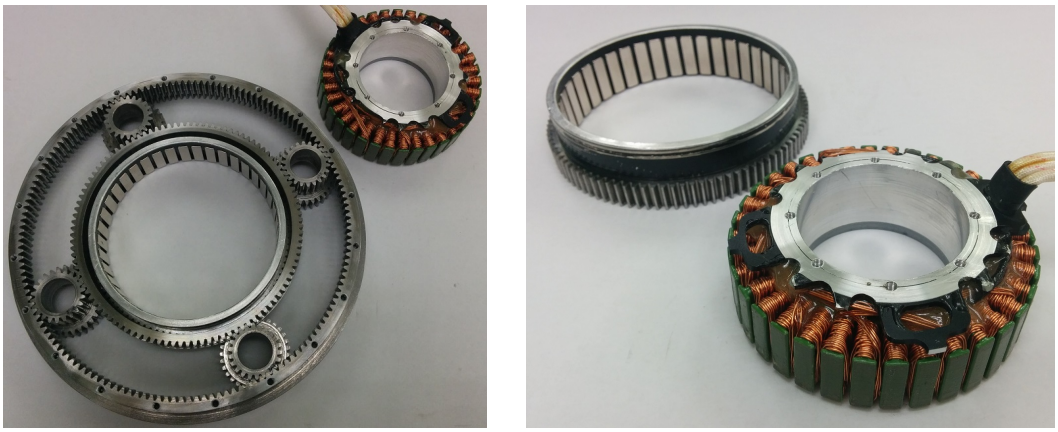

Figure 6.1: Low reduction (1 : 10) bearingless planetary gearbox on left and modified driving outer rotor motor on right. The motor rotor is incorporated into the gearbox driving sun gear.

performance drone motor that has 40 poles and 36 slots (see Fig. 6.1). As shown in Ch. 3, high pole count outer rotor motors with concentrated windings have substantially higher torque density than conventional servo motors used in robotics. In particular, in Sec. 3.5.3 it is shown using electro-magnetic FEA that motors of this particular size and design have optimal torque and torque density at around 40 poles (see Fig 3.22).

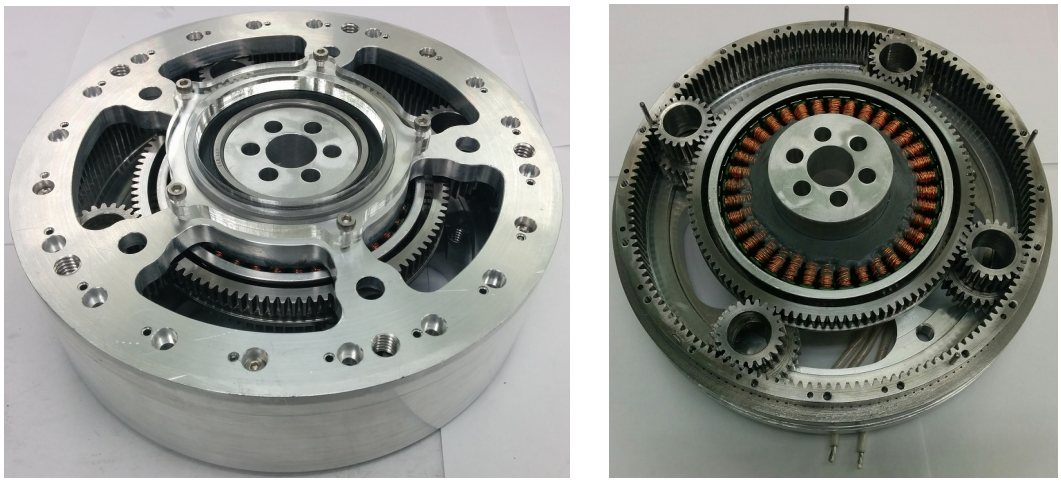

Figure 6.2: Low reduction actuator prototype. On left: complete assembly. On right: with output case removed.

Fig. 6.3 shows CAD section views of the prototype. The unique structure of the bearingless planetary gearbox allows the rotor of the motors to be incorporated into the driving sun gear (see also Fig. 6.1), which promotes significant actuator compactness. The two joint support bearings and the motor bearing are the only bearings in the prototype. The output gearbox ring gear is coupled directly to the

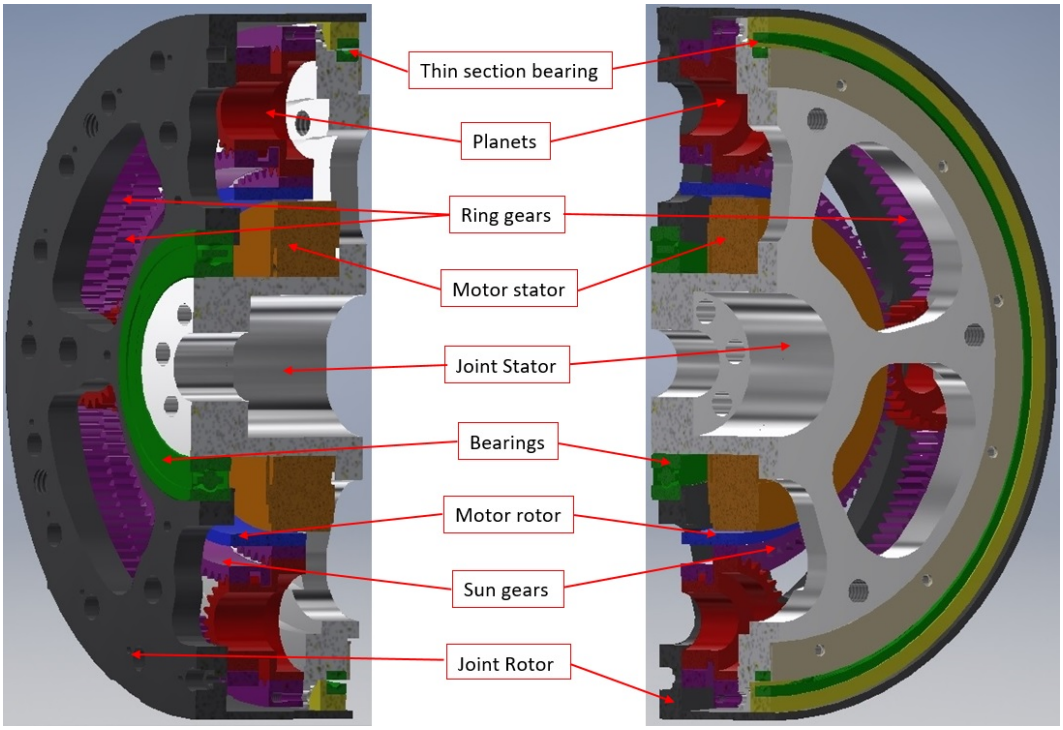

Figure 6.3: Section views the low reduction actuator prototype.

joint output rotor. The large central shaft provides support for the bearings and may be used to guide cables, etc.

The prototype has been tested using off-the-self driver electronics and exhibits excellent backdrivability with minimum backdriving torque of $1.2Nm$ which is mostly due to the amplified motor cogging torque. At $3000RPM$ the motor no load current is $3.2A$. At this speed the motor idle current is around $1.7A$ according to the motor data sheet. Therefore, there is around $70W$ power loss due to gearbox friction. Furthermore, at higher speeds the gearing noise levels increase significantly. The most likely cause for the loss and increased noise are the high tangential speeds of the planet gears due to the large sun gear.

At $3000RPM$ the sun gear tangential speed is around $15\frac{m}{s}$ and as discussed in Sec. 4.3.2, smooth and quiet operation at such high rotational speed requires gears of extra accuracy (class 6) [90, 103]. However, the gears of the prototype shown in

Fig. 6.2 are machined in-house and are of much lower class (probably class 9). Therefore, future prototypes should either have gears of better quality or should be designed to have significantly lower gear tangential speeds by:

- reducing the motor and sun gear size and possibly increasing the number of planets and the gearbox reduction ratio to preserve the actuator rated torque.
- reducing the sun gear size and moving the motor outside of the gearbox.

The prototype shown in this section serves as a proof of concept and improved future prototypes will be extensively tested to verify efficiency, robustness and dynamic loading capability of mid reduction ratio geared actuators based on the bearingless planetary gearbox of Ch. 4. The rated motor torque and the bearingless planetary gearbox strength analysis of Sec. 4.3.2, suggest that if the prototype of Fig. 6.2 is developed with high quality components, it could deliver more than $55Nm$ of continuous torque.

6.3 Bearingless Series Elastic Actuator

A high reduction bearingless gearbox that has no assembly features (see Sec. 4.3.4) is shown in Fig. 6.4. It is used in the bearingless series elastic actuator prototype

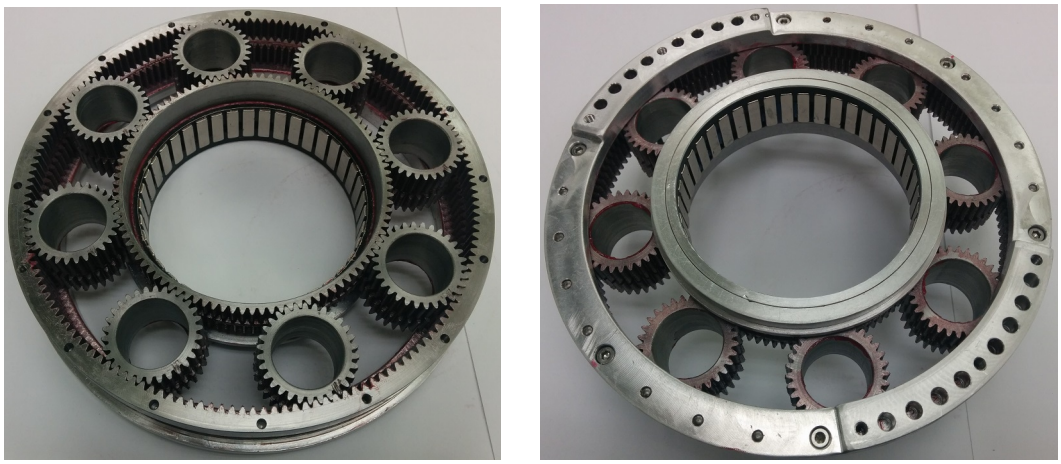

Figure 6.4: High reduction (1 : 101) bearingless planetary gearbox. Similar to Fig. 6.1 the rotor of the driving outrunner is built-in the driving sun gear.

shown in Fig. 6.5. The same outer rotor motor is used for the prototype of this section as the one used in Sec. 6.2 and shown in Fig. 6.1.

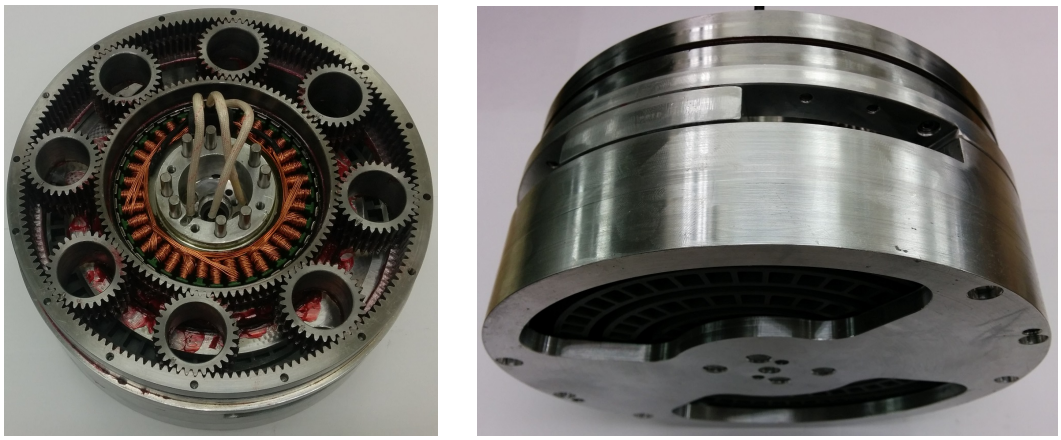

Figure 6.5: Bearingless series elastic actuator prototype. Fig. 6.6 shows the actuator schematic structure.

Fig. 6.6 shows the schematic structure of the actuator. The actuator has no bearings except for the motor bearing. In the design both ring gears are *floating*. Thus, the gearbox is utilized as a differential: the sun gear determines the relative displacement of the two ring gears. The stator of the driving outrunner motor is stationary, while the rotor is rigidly connected to the sun gear as shown in Fig. 6.4. One of the ring gears is the gearbox output and the other ring gear is connect

to the elastic element which is constructed by two of the springs of Sec. 5.2.6, connected in series. The other end of the elastic element assembly is stationary. The advantage of this approach is that it allows for direct measurement of the spring displacement using an encoder or potentiometer (see Fig. 6.6). Most of the SEA designs, reported in the literature (see Sec. 1.1), place the elastic element between the gearbox output and the load. In this case, to measure the elastic element deformation requires two encoder of high resolution. Therefore, the bearingless series elastic actuator design shown in Fig 6.6 has substantial practical advantages as it allows for a more robust and simple way to measure the elastic element deformation.

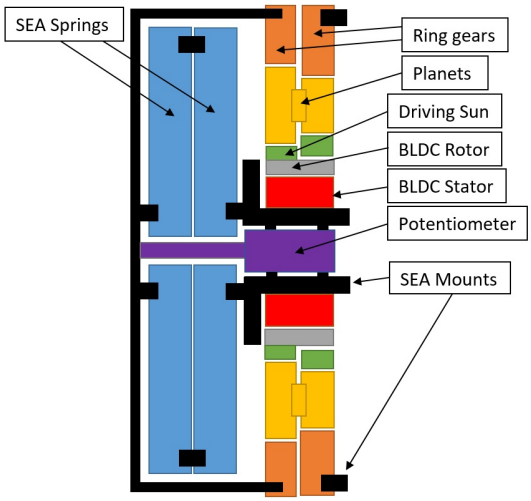

Figure 6.6: Bearingless series elastic actuator structure.

The prototype has been tested using off-the-self driver electronics. At $2000RPM$ the motor no load current is around $4A$. This suggests increased power loss of around $150W$. This is most likely due to the low machining accuracy of the springs, discussed in Sec. 5.2.6. Small eccentricity in the spring mounting holes causes distortion of the gearbox floating structure that creates pressure and misalignment in the meshing of the planets with the ring gears and the sun gears. In future prototypes, this issue may be avoided by flexibly mounting the motor stator so that the driving sun gear also floats. Alternatively, the spring mounting holes may be machined on a CNC mill after the arm profiles are cut using a waterjet machine, in order to improve their accuracy.

Similarly to Sec. 6.2, the gearbox of this section is also subject to high gear tangential speed issues which should be addressed in future prototypes.

The prototype shown in this section serves as a proof of concept and future bearingless SEA prototypes will be developed with full SEA functionally (closed loop force control, position control, etc.) and fully tested. The rated motor torque and the bearingless planetary gearbox strength analysis of Sec. 4.3.2, suggest that if the prototype of Fig. 6.6 is developed with high quality components, it could deliver more than $550Nm$ of continuous torque.

6.4 Series Elastic Actuator of Axel Tether Management System

The bearingless planetary gearbox prototype with assembled planets shown in Fig. 4.24 (Sec. 4.3.4) and the titanium dual spring prototype of Fig. 5.20 (Sec. 5.2.7) are developed for the series elastic actuator of the tether management system of the Axel rover (see Fig. 6.7) developed at the NASA Jet Prop. Lab.

Figure 6.7: Axel rover at field tests. The tether managements system is highlighted in the red circle (middle picture).

Fig. 6.8 show CAD section views and photographs of the primary tension module that houses the bearingless SEA.

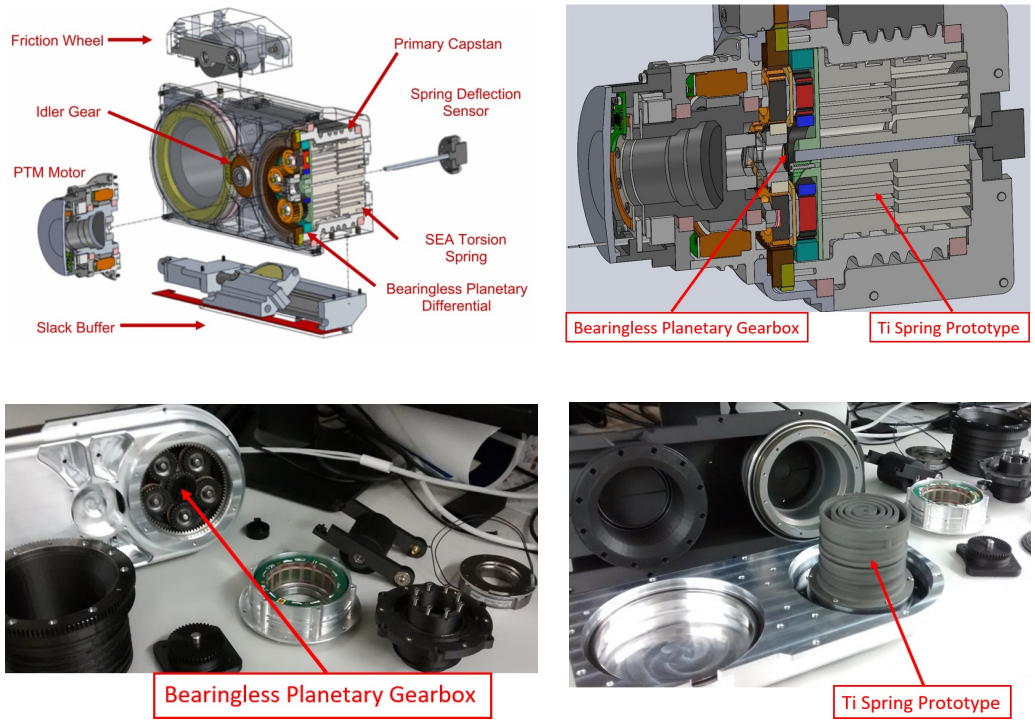

Figure 6.8: Axel primary tension module. Top: CAD section views of mechanism [36] ©2018 IEEE. Bottom: Photographs showing the components.

This section only provides a brief overview of the SEA structure and operation. A complete description of Axel and its tether management system with experimental verification is available in [36].

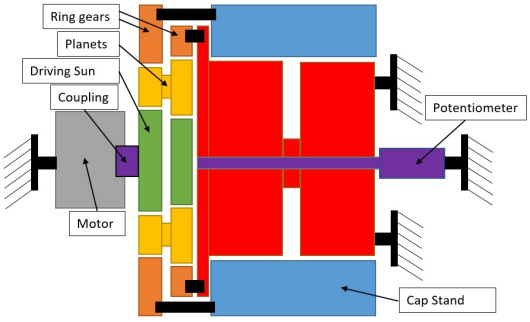

Figure 6.9: Axel SEA structure.

Fig. 6.9 shows the actuator schematic structure which is analogous to the SEA of Sec. 6.3. However, the hard packaging design requirements motivate the novel dual spring design so that it may be compactly positioned in the capstan interior. Similar to the SEA of Sec. 6.3, the differential nature of the bearingless planetary gearbox is exploited in the SEA design of Fig. 6.9 as none of the ring gears are stationary. One of the ring gears is attached to the capstan and the other ring is coupled to the spring. The sun gear (driven by the motor) controls their relative displacement. The simplified structure allows for direct measurement of the spring displacement (similar to Sec. 6.3) because one of its ends is stationary as shown in Fig. 6.9.

The tension management system has been extensively tested for hundreds of hours both using a bench-top test set-up [36] and in field tests (after it was installed on the Axel rover) which provides experimental verification of the performance and robustness of the bearingless planetary gearbox and the rotary planar springs, introduced in this thesis.

Chapter 7

CONCLUSION AND FUTURE WORK

The aim of this thesis is to develop high performance robotic actuation for multi-limbed robots, with possibly high number of degrees of freedom.

A dynamic analysis of such systems (Ch. 2) reveals that the actuators' design, and in particular their reflected inertia, may have significant impact on the robot's dynamics and control sensitivity, which is usually neglected at the robot design stage. The analysis suggests that SEA robots may be subject to fundamental dynamics performance limitation due to the effectively eliminated actuator reflected inertia. It is shown that the SEA springs separates the actuator dynamics from the robot dynamics, thus, the actuator reflected inertia no longer directly affects the robot's generalized mass matrix. On the other hand, the dynamics analysis show that robots that have low to mid reduction ratio actuators at their joints may have substantial dynamics performance advantage compared to robots featuring SEAs, high reduction ratio actuators, etc. The reflected inertia of such actuators may minimize the robot's generalized mass matrix condition number, and thus, reduce the robot dynamics sensitivity to a minimum.

However, the analysis does not exhaustively cover the topic of limbed robot dynamics sensitivity. Future work should include:

- individual actuator design optimization for minimized robot dynamics sensitivity (or maximum robustness).
- robot structure design optimization (link design, actuator placement, etc.).

The shortcomings of existing robotic actuation technologies motivate at least two possible solutions. The first is a novel dual actuation approach, which is proposed in Sec. 1.2, and features a series elastic actuator coupled in parallel with a low reduction geared actuator. However, incorporating two rotary actuators in a single high performance robotic joint requires development of novel high torque density motors (Ch. 3), compact light weight gearboxes (Ch. 4) and weight-optimized rotary springs (Ch. 5). The second solution is a high torque density motor coupled with low-loss, transparent mid-range gearbox.

Ch. 3 is concerned with the design and prototyping of high performance permanent magnet outer rotor motors with concentrated windings. The chapter begins with a discussion of application-specific motor requirements for EVs, drones and robotic joints. The analysis suggests that proper understanding of the motor loss trade-offs may enable the development of motors that have superior performance for a particular application, as compared to available off-the-shelf motors. A flux-linkage based motor model is developed, leading to the derivation of application specific design trade-offs and guidelines with consideration of the motor pole and slot count, slot design, magnet design, etc. Electro-magnetic FEA is used to verify the analytical results. A number of motor prototypes are designed, manufactured and tested to demonstrate the advantages of designing motors optimized for a specific application. The chapter concludes with a description of the possible motor scaling laws and a discussion of the challenges related to the practical implementation of high torque motors.

Ch. 3 argued that interior permanent magnet designs have no advantages compared to surface mount magnet designs for the considered applications. However, they have certain advantages in applications that benefit from field weakening (a technique that allows higher than rated motor speed by injection of direct current) and specialized applications that benefit from large air gap. Therefore, interior permanent magnet motors warrant future analysis, development and optimization using the approach of Ch. 3.

Ch. 3 describes how high torque and torque density motors may be designed, and outlines the major issues with such motors related to their low inductance, resistance, and high electrical frequency. However, the chapter provides no solution to *driving* such motors. This is a major issue that needs to be addressed in future work, as a brushless permanent magnet motor is useless without its driving circuitry. To this end, the author began developing a pulse amplitude modulation (PAM) driver system which consists of a DC-DC buck converter that regulates the voltage of an inverter that is responsible for the motor phase commutation. The resulting system may be capable of driving motors of very low inductance. However, it was found that such driver designs are disadvantaged due to their size: the buck converter stage needs to be designed for maximum theoretical power, even though the motor in a robot joint is not expected to reach this power level even for a short amount of time. Furthermore, the inverter drives the motor with voltage pulses (sometimes referred to as BLDC commutation in the literature) which is sub-optimal for the motors considered in

Ch. 3 due to their sinusoidal bEMF waveform. In order to fully take advantage of such motors, field oriented control (FOC) should be utilized. However, using FOC with PAM drivers leads to significantly increased driver losses. Therefore, it is concluded that PAM driver designs are disadvantaged in driving motors for robotic joint applications. Nevertheless, PAM drivers may be advantageous for high power applications such as drone actuation.

Similar to the analysis regarding motors in Ch. 3, it is possible to formulate application specific motor driver design requirements and trade-offs that could motivate driver designs of superior performance for a given application. Therefore, future motor development work should be focused on application specific motor driver development.

Ch. 4 introduces a novel bearingless planetary gearbox. The development is motivated by the shortcomings of the speed reducers currently used in robotic joint actuators. The novel gearbox has substantial compactness and weight advantage due to its unique floating structure: all gearing components float unconstrained. This is achieved by substitution of the carrier in the classical Wolfrom gearbox with a secondary sun gear. Detailed strength analysis and manufacturing considerations are also provided which outline the gearbox advantages. A major issues for the bearingless planetary gearbox is the existence of an unbalanced planet couple that leads to substantial max gearbox torque derating (more than 30%), and may cause increased noise, wear, etc.

Regardless, of this issue the manufactured gearbox prototypes (Ch. 6) demonstrate the significant advantages and potential of floating component gearboxes such as the bearingless planetary gearbox. Therefore, future development should be focused on gearbox topology modifications that lead to substantial reduction or complete removal of the unbalanced loading.

Ch. 5 is concerned with the analysis, design, and prototyping of rotary planar springs for SEAs. A mathematical model based on curved beam theory is developed to rapidly predict the spring torsional response. Spring mass reduction techniques, based on composite materials or *cutouts*, are introduced. Most of the spring designs that have been previously reported in the literature have dead stops that prevent arm contacts. Ch. 5 proposes an alternative design approach that utilizes spring deformations beyond arm contacts as an overload regime. A systematic model of internal spring arm contacts is developed that allows for rapid prediction of the spring torsional response under contacts. The main contribution of the chapter is

the development of a consistent optimization-based spring design procedure which is motivated by spring arm strain energy consideration. Multiple spring prototypes are designed, manufactured and tested, demonstrating the validity of the described spring analysis and design techniques.

The presented strain energy density approach to the design of the springs may be used in the design of any structural component that is subject to a finite prescribed deformation or prescribed loading that leads to finite deformation. While the spring design methodology is complete, future work could extend the design methodology to novel mechanical coupling components.

Finally, proof of concept actuator prototypes are presented in Ch. 6 to demonstrate the advantages and the potential of the thesis contributions for future development of high performance SEAs and mid reduction geared actuators.

The advances in the design of high torque and high torque density motors of Ch. 3, combined with the high torque, compact and lightweight bearingless planetary gearboxes of Ch. 4, suggest that mid reduction geared actuators may be developed to match the high torque and efficiency of high reduction geared actuators that are currently used in the majority of the robot designs presented in the literature. Such mid reduction ratio actuators may also have significant advantages for limbed or legged robots application in their dynamic performance, especially compared to SEA (see dynamics analysis of Ch. 2). Therefore, future actuator development should be focused on development of high performance systems featuring high torque density outrunners and bearingless planetary gearboxes.

BIBLIOGRAPHY

[1] Claudio Semini et al. "Design of HyQ–a hydraulically and electrically actuated quadruped robot." In: *Proceedings of the Institution of Mechanical Engineers, Part I: Journal of Systems and Control Engineering* 225.6 (2011), pp. 831–849.

[2] Bram Vanderborght et al. "Exploiting natural dynamics to reduce energy consumption by controlling the compliance of soft actuators." In: *The International Journal of Robotics Research* 25.4 (2006), pp. 343–358.

[3] Ian W Hunter, John M Hollerbach, and John Ballantyne. "A comparative analysis of actuator technologies for robotics." In: *Robotics Review* 2 (1991), pp. 299–342.

[4] Sangok Seok et al. "Actuator design for high force proprioceptive control in fast legged locomotion." In: *Intelligent Robots and Systems (IROS), 2012 IEEE/RSJ International Conference on*. IEEE. 2012, pp. 1970–1975.

[5] Gill A Pratt et al. "Stiffness isn't everything." In: *experimental robotics IV*. Springer, 1997, pp. 253–262.

[6] Jerry Pratt, Ben Krupp, and Chris Morse. "Series elastic actuators for high fidelity force control." In: *Industrial Robot: An International Journal* 29.3 (2002), pp. 234–241.

[7] Jonathan W Hurst and Alfred A Rizzi. "Series compliance for an efficient running gait." In: *IEEE Robotics & Automation Magazine* 15.3 (2008), pp. 42–51.

[8] Nicholas Paine, Sehoon Oh, and Luis Sentis. "Design and control considerations for high-performance series elastic actuators." In: *IEEE/ASME Transactions on Mechatronics* 19.3 (2014), pp. 1080–1091.

[9] Seong-Sik Yoon et al. "Safe arm design with MR-based passive compliant joints and visco—elastic covering for service robot applications." In: *Journal of mechanical science and technology* 19.10 (2005), pp. 1835–1845.

[10] Nikolaos G Tsagarakis et al. "A compact soft actuator unit for small scale human friendly robots." In: *Robotics and Automation, 2009. ICRA'09. IEEE International Conference on*. IEEE. 2009, pp. 4356–4362.

[11] Brian T Knox and James P Schmiedeler. "A unidirectional series-elastic actuator design using a spiral torsion spring." In: *Journal of Mechanical Design* 131.12 (2009), p. 125001.

[12] Arno HA Stienen et al. "Design of a rotational hydroelastic actuator for a powered exoskeleton for upper limb rehabilitation." In: *IEEE Transactions on biomedical engineering* 57.3 (2010), pp. 728–735.

[13] Claude Lagoda et al. “Design of an electric series elastic actuated joint for robotic gait rehabilitation training.” In: *Biomedical Robotics and Biomechatronics (BioRob), 2010 3rd IEEE RAS and EMBS International Conference on*. IEEE. 2010, pp. 21–26.

[14] Giorgio Carpino et al. “A novel compact torsional spring for series elastic actuators for assistive wearable robots.” In: *Journal of Mechanical Design* 134.12 (2012), p. 121002.

[15] Nicholas Paine et al. “Actuator Control for the NASA-JSC Valkyrie Humanoid Robot: A Decoupled Dynamics Approach for Torque Control of Series Elastic Robots.” In: *Journal of Field Robotics* 32.3 (2015), pp. 378–396.

[16] Jonathan P Cummings et al. “A compact, modular series elastic actuator.” In: *Journal of Mechanisms and Robotics* 8.4 (2016), p. 041016.

[17] Francesca Negrello et al. “A modular compliant actuator for emerging high performance and fall-resilient humanoids.” In: *2015 IEEE-RAS 15th International Conference on Humanoid Robots (Humanoids)*. IEEE. 2015, pp. 414–420.

[18] Gill Andrews Pratt. “Low impedance walking robots.” In: *Integrative and Comparative Biology* 42.1 (2002), pp. 174–181.

[19] Jerry Pratt and Ben Krupp. “Design of a bipedal walking robot.” In: *Unmanned Systems Technology X*. Vol. 6962. International Society for Optics and Photonics. 2008, 69621F.

[20] Nikos G Tsagarakis et al. “The mechanical design of the new lower body for the child humanoid robot ‘iCub’.” In: *2009 IEEE/RSJ International Conference on Intelligent Robots and Systems*. IEEE. 2009, pp. 4962–4968.

[21] Myron A Diftler et al. “Robonaut 2-the first humanoid robot in space.” In: *2011 IEEE international conference on robotics and automation*. IEEE. 2011, pp. 2178–2183.

[22] Nicolaus A Radford et al. “Valkyrie: Nasa’s first bipedal humanoid robot.” In: *Journal of Field Robotics* 32.3 (2015), pp. 397–419.

[23] Joonbum Bae, Kyoungchul Kong, and Masayoshi Tomizuka. “Gait phase-based control for a rotary series elastic actuator assisting the knee joint.” In: *Journal of Medical Devices* 5.3 (2011), p. 031010.

[24] Nikos G Tsagarakis et al. “Compliant humanoid coman: Optimal joint stiffness tuning for modal frequency control.” In: *2013 IEEE International Conference on Robotics and Automation*. IEEE. 2013, pp. 673–678.

[25] Marco Hutter et al. “HIGH COMPLIANT SERIES ELASTIC ACTUATION FOR THE ROBOTIC LEG SCARL ETH.” In: *Field Robotics*. World Scientific, 2012, pp. 507–514.

[26] Marco Hutter et al. “StarlETH: A compliant quadrupedal robot for fast, efficient, and versatile locomotion.” In: *Adaptive Mobile Robotics*. World Scientific, 2012, pp. 483–490.

[27] Elliott J Rouse, Luke M Mooney, and Hugh M Herr. “Clutchable series-elastic actuator: Implications for prosthetic knee design.” In: *The International Journal of Robotics Research* 33.13 (2014), pp. 1611–1625.

[28] Marco Hutter et al. “Anymal-a highly mobile and dynamic quadrupedal robot.” In: *2016 IEEE/RSJ International Conference on Intelligent Robots and Systems (IROS)*. IEEE. 2016, pp. 38–44.

[29] Lorenzo Baccelliere et al. “Development of a human size and strength compliant bi-manual platform for realistic heavy manipulation tasks.” In: *2017 IEEE/RSJ International Conference on Intelligent Robots and Systems (IROS)*. IEEE. 2017, pp. 5594–5601.

[30] Sangok Seok et al. “Design principles for energy-efficient legged locomotion and implementation on the MIT cheetah robot.” In: *IEEE/ASME Transactions on Mechatronics* 20.3 (2015), pp. 1117–1129.

[31] Toby Elery et al. “Design and benchtop validation of a powered knee-ankle prosthesis with high-torque, low-impedance actuators.” In: *2018 IEEE International Conference on Robotics and Automation (ICRA)*. IEEE. 2018, pp. 2788–2795.

[32] Yanran Ding and Hae-Won Park. “Design and experimental implementation of a quasi-direct-drive leg for optimized jumping.” In: *2017 IEEE/RSJ International Conference on Intelligent Robots and Systems (IROS)*. IEEE. 2017, pp. 300–305.

[33] Paul Hebert et al. “Mobile manipulation and mobility as manipulation—design and algorithms of RoboSimian.” In: *Journal of Field Robotics* 32.2 (2015), pp. 255–274.

[34] John B Morrell and J Kenneth Salisbury. “Parallel coupled actuators for high performance force control: a micro-macro concept.” In: *Proceedings 1995 IEEE/RSJ International Conference on Intelligent Robots and Systems. Human Robot Interaction and Cooperative Robots*. Vol. 1. IEEE. 1995, pp. 391–398.

[35] Michael Zinn et al. “A new actuation approach for human friendly robot design.” In: *The international journal of robotics research* 23.4-5 (2004), pp. 379–398.

[36] Travis Brown et al. “Series Elastic Tether Management for Rappelling Rovers.” In: *2018 IEEE/RSJ International Conference on Intelligent Robots and Systems (IROS)*. IEEE. 2018, pp. 2893–2900. DOI: 10.1109/IROS.2018.8594134.

[37] Roy Featherstone. *Rigid body dynamics algorithms*. Springer, 2014.

[38] Frank C Park, Jihyeon Choi, and SR Ploen. "Symbolic formulation of closed chain dynamics in independent coordinates." In: *Mechanism and machine theory* 34.5 (1999), pp. 731–751.

[39] Scott R Ploen and Frank C Park. "Coordinate-invariant algorithms for robot dynamics." In: *IEEE Transactions on Robotics and Automation* 15.6 (1999), pp. 1130–1135.

[40] Richard M Murray. *A mathematical introduction to robotic manipulation*. CRC press, 1994.

[41] Ayman M El-Refaie. "Fractional-slot concentrated-windings synchronous permanent magnet machines: Opportunities and challenges." In: *IEEE Transactions on industrial Electronics* 57.1 (2010), pp. 107–121.

[42] Duane C Hanselman. *Brushless permanent magnet motor design*. The Writers' Collective, 2003.

[43] M Aydin, S Huang, and TA Lipo. "Axial flux permanent magnet disc machines: A review." In: *Conf. Record of SPEEDAM*. Vol. 8. 2004, pp. 61–71.

[44] Andrea Cavagnino et al. "A comparison between the axial flux and the radial flux structures for PM synchronous motors." In: *IEEE transactions on industry applications* 38.6 (2002), pp. 1517–1524.

[45] Federico Caricchi et al. "Design and construction of a wheel-directly-coupled axial-flux PM motor prototype for EVs." In: *Proceedings of 1994 IEEE Industry Applications Society Annual Meeting*. Vol. 2. IEEE. 1994, pp. 254–261.

[46] V Hrabovcová et al. "Concentrated versus distributed winding in permanent magnet synchronous motors." In: *2017 19th International Conference on Electrical Drives and Power Electronics (EDPE)*. IEEE. 2017, pp. 279–286.

[47] David G Dorrell et al. "A review of the design issues and techniques for radial-flux brushless surface and internal rare-earth permanent-magnet motors." In: *IEEE Transactions on Industrial Electronics* 58.9 (2011), pp. 3741–3757.

[48] Freddy Magnussen and Chandur Sadarangani. "Winding factors and Joule losses of permanent magnet machines with concentrated windings." In: *Electric Machines and Drives Conference, 2003. IEMDC'03. IEEE International*. Vol. 1. IEEE. 2003, pp. 333–339.

[49] Florence Libert and Juliette Soulard. "Investigation on pole-slot combinations for permanent-magnet machines with concentrated windings." In: *International Conference on Electrical Machines (ICEM 04)*. 2004, pp. 5–8.

[50] Jérome Cros and Philippe Viarouge. “Synthesis of high performance PM motors with concentrated windings.” In: *IEEE transactions on energy conversion* 17.2 (2002), pp. 248–253.

[51] Bassel Aslan et al. “Slot/pole combinations choice for concentrated multiphase machines dedicated to mild-hybrid applications.” In: *IECON 2011-37th Annual Conference of the IEEE Industrial Electronics Society*. IEEE. 2011, pp. 3698–3703.

[52] Dahaman Ishak, ZQ Zhu, and David Howe. “Comparison of PM brushless motors, having either all teeth or alternate teeth wound.” In: *IEEE Transactions on Energy Conversion* 21.1 (2006), pp. 95–103.

[53] Pia Salminen et al. “Performance analysis of fractional slot wound PM-motors for low speed applications.” In: *Conference Record of the 2004 IEEE Industry Applications Conference, 2004. 39th IAS Annual Meeting*. Vol. 2. IEEE. 2004, pp. 1032–1037.

[54] Florence Libert and Juliette Soulard. “Design study of different direct-driven permanent-magnet motors for a low speed application.” In: *Proceedings of the Nordic Workshop on Power and Industrial Electronics (NORpie), Trondheim, Norway*. 2004.

[55] Nicola Bianchi, Silverio Bolognani, and Fabio Luise. “Potentials and limits of high-speed PM motors.” In: *IEEE Transactions on Industry Applications* 40.6 (2004), pp. 1570–1578.

[56] ZQ Zhu and David Howe. “Influence of design parameters on cogging torque in permanent magnet machines.” In: *IEEE Transactions on energy conversion* 15.4 (2000), pp. 407–412.

[57] Nicola Bianchi and Silverio Bolognani. “Design techniques for reducing the cogging torque in surface-mounted PM motors.” In: *IEEE Transactions on industry applications* 38.5 (2002), pp. 1259–1265.

[58] Pia Salminen et al. “Torque ripple of permanent magnet machines with concentrated windings.” In: *Proc. International Symposium on Electromagnetic Fields in Mechatronics, Electrical and Electronic Engineering*. 2005.

[59] Massimo Barcaro, Nicola Bianchi, and Freddy Magnussen. “PM motors for hybrid electric vehicles.” In: *2008 43rd International Universities Power Engineering Conference*. IEEE. 2008, pp. 1–5.

[60] Rafal Wrobel and Phil H Mellor. “Design considerations of a direct drive brushless machine with concentrated windings.” In: *IEEE Transactions on energy conversion* 23.1 (2008), pp. 1–8.

[61] James Goss et al. “The design of AC permanent magnet motors for electric vehicles: A design methodology.” In: *2013 International Electric Machines & Drives Conference*. IEEE. 2013, pp. 871–878.

[62] Jemimah C Akiror. "Model for Core Loss Prediction at High Frequency and High Flux Density." PhD thesis. Concordia University, 2012.

[63] Yicheng Chen and Pragasen Pillay. "An improved formula for lamination core loss calculations in machines operating with high frequency and high flux density excitation." In: *Conference Record of the 2002 IEEE Industry Applications Conference. 37th IAS Annual Meeting (Cat. No. 02CH37344)*. Vol. 2. IEEE. 2002, pp. 759–766.

[64] Lotten Tsakani Mthombeni and Pragasen Pillay. "Core losses in motor laminations exposed to high-frequency or nonsinusoidal excitation." In: *IEEE Transactions on Industry Applications* 40.5 (2004), pp. 1325–1332.

[65] K Atallah, ZQ Zhu, and D Howe. "An improved method for predicting iron losses in brushless permanent magnet DC drives." In: *IEEE Transactions on magnetics* 28.5 (1992), pp. 2997–2999.

[66] Dan M Ionel et al. "On the variation with flux and frequency of the core loss coefficients in electrical machines." In: *IEEE transactions on industry applications* 42.3 (2006), pp. 658–667.

[67] Hideo Domeki et al. "Investigation of benchmark model for estimating iron loss in rotating machine." In: *IEEE Transactions on Magnetics* 40.2 (2004), pp. 794–797.

[68] Kais Atallah et al. "Rotor loss in permanent-magnet brushless AC machines." In: *IEEE Transactions on Industry Applications* 36.6 (2000), pp. 1612–1618.

[69] ZQ Zhu et al. "Improved analytical modelling of rotor eddy current loss in brushless machines equipped with surface-mounted permanent magnets." In: *IEE Proceedings-Electric Power Applications* 151.6 (2004), pp. 641–650.

[70] Dahaman Ishak, ZQ Zhu, and David Howe. "Eddy-current loss in the rotor magnets of permanent-magnet brushless machines having a fractional number of slots per pole." In: *IEEE Transactions on magnetics* 41.9 (2005), pp. 2462–2469.

[71] Rukmi Dutta and MF Rahman. "Design and analysis of an interior permanent magnet (IPM) machine with very wide constant power operation range." In: *IEEE Transactions on Energy Conversion* 23.1 (2008), pp. 25–33.

[72] Aimeng Wang, Yihua Jia, and WL Soong. "Comparison of five topologies for an interior permanent-magnet machine for a hybrid electric vehicle." In: *IEEE Transactions on Magnetics* 47.10 (2011), pp. 3606–3609.

[73] M Nasir Uddin, Tawfik S Radwan, and M Azizur Rahman. "Performance of interior permanent magnet motor drive over wide speed range." In: *IEEE Transactions on Energy Conversion* 17.1 (2002), pp. 79–84.

[74] Ramu Krishnan. *Permanent magnet synchronous and brushless DC motor drives*. CRC press, 2009.

[75] Jacek F Gieras. *Permanent magnet motor technology: design and applications*. CRC press, 2009.

[76] Damir Žarko and Stjepan Stipetić. "Criteria for optimal design of interior permanent magnet motor series." In: *Electrical Machines (ICEM), 2012 XXth International Conference on*. IEEE. 2012, pp. 1242–1249.

[77] Stjepan Stipetic, Damir Zarko, and Mircea Popescu. "Scaling laws for synchronous permanent magnet machines." In: *Ecological Vehicles and Renewable Energies (EVER), 2015 Tenth International Conference on*. IEEE. 2015, pp. 1–7.

[78] Stjepan Stipetic, Damir Zarko, and Mircea Popescu. "Ultra-fast axial and radial scaling of synchronous permanent magnet machines." In: *IET Electric Power Applications* 10.7 (2016), pp. 658–666.

[79] T-motors. URL: http://uav-en.tmotor.com/.

[80] James Robert Mevey. "Sensorless field oriented control of brushless permanent magnet synchronous motors." In: (2009).

[81] Florence Meier. "Permanent-magnet synchronous machines with non-overlapping concentrated windings for low-speed direct-drive applications." PhD thesis. KTH, 2008.

[82] Emanuele Fornasiero et al. "Considerations on selecting fractional—slot windings." In: *2010 IEEE Energy Conversion Congress and Exposition*. IEEE. 2010, pp. 1376–1383.

[83] Freddy Magnussen and Heinz Lendenmann. "Parasitic effects in PM machines with concentrated windings." In: *IEEE transactions on industry applications* 43.5 (2007), pp. 1223–1232.

[84] Nicola Bianchi et al. "Design considerations for fractional-slot winding configurations of synchronous machines." In: *IEEE transactions on industry applications* 42.4 (2006), pp. 997–1006.

[85] Stephan Meier. "Theoretical design of surface-mounted permanent magnet motors with field-weakening capability." In: *Master Thesis. Royal Institute of Technology Department of Electrical Engineering Electrical Machines and Power Electronics Stockholm 2001/2002* (2002).

[86] David Meeker. *Finite Element Method Magnetics*. URL: http://www.femm.info/wiki/HomePage.

[87] Şenol Bayraktar and Yakup Turgut. "Effects of different cutting methods for electrical steel sheets on performance of induction motors." In: *Proceedings of the Institution of Mechanical Engineers, Part B: Journal of Engineering Manufacture* 232.7 (2018), pp. 1287–1294.

[88] Rached Dhaouadi, Fathi H Ghorbel, and Prasanna S Gandhi. "A new dynamic model of hysteresis in harmonic drives." In: *IEEE Transactions on Industrial electronics* 50.6 (2003), pp. 1165–1171.

[89] Keiji Ueura and Rolf Slatter. "Development of the harmonic drive gear for space applications." In: *European Space Agency-Publications-ESA SP* 438 (1999), pp. 259–264.

[90] G Antonsson and Karl H Grote. *Springer handbook of mechanical engineering*. 2008.

[91] Fathi H Ghorbel, Prasanna S Gandhi, and Friedhelm Alpeter. "On the kinematic error in harmonic drive gears." In: *Journal of Mechanical Design* 123.1 (2001), pp. 90–97.

[92] RACHED Dhaouadi, FATHI Ghorbel, and Prasanna Gandhi. "Modeling and analysis of hysteresis in harmonic drive gears." In: *Sys. Analysis Model Simul* 1 (2003), pp. 1–14.

[93] Wolfgang Seyfferth, AJ Maghzal, and Jorge Angeles. "Nonlinear modeling and parameter identification of harmonic drive robotic transmissions." In: *Robotics and Automation, 1995. Proceedings., 1995 IEEE International Conference on*. Vol. 3. IEEE. 1995, pp. 3027–3032.

[94] Timothy D Tuttle and Warren Seering. "Modeling a harmonic drive gear transmission." In: *Robotics and Automation, 1993. Proceedings., 1993 IEEE International Conference on*. IEEE. 1993, pp. 624–629.

[95] Naren Kumar, Vladis Kosse, and Adekunle Oloyede. "A novel testing system for a Cycloidal drive." In: *2012 12th International Conference on Intelligent Systems Design and Applications (ISDA)*. IEEE. 2012, pp. 503–507.

[96] Jonathon W Sensinger. "Unified approach to cycloid drive profile, stress, and efficiency optimization." In: *Journal of Mechanical Design* 132.2 (2010), p. 024503.

[97] DCH Yang and JG Blanche. "Design and application guidelines for cycloid drives with machining tolerances." In: *Mechanism and Machine Theory* 25.5 (1990), pp. 487–501.

[98] Karol Seweryn et al. "Optimization of the robotic joint equipped with epicycloidal gear and direct drive for space applications." In: *proceedings of 15th European Space Mechanisms and Tribology Symposium (ESMATS 2013), ESTEC, Noordwijk, Netherlands*. 2013.

[99] Jing Yu and Viliam Makis. "Wavelet analysis with time-synchronous averaging of planetary gearbox vibration data for fault detection and diagnostics." In: *2011 IEEE International Conference on Computer Science and Automation Engineering*. Vol. 1. IEEE. 2011, pp. 417–421.

[100] Frank P Lawler. *Reduction gear drive*. US Patent 2,401,875. 1946.

[101] Elias Brassitos and Constantinos Mavroidis. “Kinematics Analysis and Design Considerations of the Gear Bearing Drive.” In: *Advances in Mechanisms, Robotics and Design Education and Research*. Springer, 2013, pp. 159–175.

[102] Elias Brassitos and Steven Dubowsky. “Compact drive system for planetary rovers and space manipulators.” In: *Advanced Intelligent Mechatronics (AIM), 2015 IEEE International Conference on*. IEEE. 2015, pp. 664–669.

[103] KHK Gears. *Gear Technical Reference*. URL: http://khkgears.net/.

[104] QTC Gears. *Elements of Metric Gear Technology*. URL: http://qtcgears.com/.

[105] Brian Weinberg, Constantinos Mavroidis, and John M Vranish. *Gear bearing drive*. US Patent 8,016,893. 2011.

[106] Jack A Collins, Henry R Busby, and George H Staab. *Mechanical design of machine elements and machines: a failure prevention perspective*. John Wiley & Sons, 2010.

[107] Yiping Liu et al. “Fuzzy controlled hopping in a biped robot.” In: *2011 IEEE International Conference on Robotics and Automation*. IEEE. 2011, pp. 1982–1989.

[108] Fabrizio Sergi et al. “Design and characterization of a compact rotary series elastic actuator for knee assistance during overground walking.” In: *2012 4th IEEE RAS & EMBS International Conference on Biomedical Robotics and Biomechatronics (BioRob)*. IEEE. 2012, pp. 1931–1936.

[109] Dirk Ruiken et al. “uBot-7: A dynamically balancing mobile manipulator with series elastic actuators.” In: *2017 IEEE-RAS 17th International Conference on Humanoid Robotics (Humanoids)*. IEEE. 2017, pp. 676–682.

[110] Eamon Barrett, Matteo Fumagalli, and Raffaella Carloni. “Elastic energy storage in leaf springs for a lever-arm based variable stiffness actuator.” In: *Intelligent Robots and Systems (IROS), 2016 IEEE/RSJ International Conference on*. IEEE. 2016, pp. 537–542.

[111] James R Barber. *Intermediate mechanics of materials*. Vol. 175. Springer Science & Business Media, 2010.

[112] Jiho Moon et al. “Out-of-plane buckling of arches with varying curvature.” In: *KSCE Journal of Civil Engineering* 13.6 (2009), pp. 441–451.

[113] Autodesk. *Nastran*. URL: http://www.autodesk.com/products/nastran/overview/.

[114] Ferdinand P Beer et al. *Mechanics of Materials, McGraw-Hill*. 2006.

[115] TEMco Industrial Power Supply. URL: http://temcoindustrial.com/.

[116] Hwaiyu Geng. *Abrasive Jet Machining in Manufacturing engineering handbook*. McGraw Hill Professional, 2015.

[117] Online Waterjet Resource. URL: http://www.waterjets.org/.

[118] J. Mecer. "EDM's Effect on Surface Integrity part 1 and Part 2." In: *MOLD-MAKING TECHNOLOGY* (2008).

[119] Terrence M Quick. "EDM and the resulting hydrogen embrittlement of maraging steel." In: *JOM* 45.10 (1993), pp. 52–55.

[120] Bachhav Sonawane. "Abrasive Water Jet Machining- A Review." In: *IOSR Journal of Mechanical and Civil Engineering (IOSR-JMCE)* 12.4 (2015), pp. 44–52.

[121] Flow. URL: http://www.flowwaterjet.com/Machines/Mach-2b/.